The Ultrastructural and Abnormal Calcium Handling in Pulmonary Vein Sleeve Cells, Atrial and Ventricular Myocytes During Ageing

Thesis

How to cite:

Masoud, Said (2018). The Ultrastructural and Abnormal Calcium Handling in Pulmonary Vein Sleeve Cells, Atrial and Ventricular Myocytes During Ageing. PhD thesis The Open University.

Version: Version of Record

Link(s) to article on publisher's website:
http://dx.doi.org/doi:10.21954/ou.ro.0000e0ab

The ultrastructural and abnormal calcium handling in pulmonary vein sleeve cells, atrial and ventricular myocytes during ageing

A thesis submission to the Open University for the Degree of Doctor in Philosophy

Said Masoud, BSc

Supervisors:

Dr. Katja Rietdorf
Dr. Martin Bootman
Prof. Fraser McDonald

January 2018

DECLARATION

I declare that the work presented in this thesis is the result of my own work and includes nothing which is the outcome of work performed by other researchers, or in collaboration. This work does not contain any material submitted for a degree, diploma or any other qualification at the Open University. Contributions made by other researchers are fully acknowledged in relevant parts of the thesis.

Said Masoud

January 2018

ABSTRACT

Atrial fibrillation (AF) is the most common sustained cardiac arrhythmia, with age being a significant risk factor. It is well established now that electric activities originating from pulmonary vein sleeve cells (PVCs) initiate AF. Factors that are involved in maintaining AF include structural remodelling and abnormal Ca^{2+} handling in PVCs and atrial myocytes. Whilst structural changes and alterations in the Ca^{2+} homeostasis have been described previously in atrial myocytes, similar studies are still lacking in PVCs. Thus, this thesis investigated structural remodelling and Ca^{2+} handling, particularly in PVCs from 3- and 24month-old mice.

Using immunohistochemical and electron microscopy (EM) studies, this thesis revealed that PVCs just like atrial and ventricular myocytes, express RyR2, Cx40, and Cx43. Whilst RyR2 and Cx43 expressions did not change with age, Cx40 expression was found to deteriorate during ageing. Additionally, EM studies showed significant alterations in mitochondria which increased in size and numbers during ageing. Unlike PVCs, mitochondria in atrial myocytes were enlarged but did not increase in numbers during ageing. Mitochondria in ventricular myocytes did not deteriorate with age.

This study also showed that Ca^{2+} homeostasis in PVCs is disrupted during ageing. PVCs from aged mice had an increased frequency and duration of spontaneous Ca^{2+} waves, with reduced amplitude, less able to follow electrical pacing and had higher basal ROS levels compared to PVCs from young mice.

Additional studies attempted to induce ageing chemically with hydroxyurea (HU) in neonatal rat ventricular myocytes (NRVMs). HU inhibited pacing ability, induced autophagy and increased inducible ROS. Although some changes in chemically ageing

model were similar to those in aged PVCs, further studies are needed to fully establish whether HU can induce ageing in NRVMs.

In conclusion, this study showed that structural remodelling and Ca^{2+} homeostasis differs in PVCs during ageing which may facilitate the occurrence of arrhythmias.

ACKNOWLEDGEMENTS

Firstly, I would like to extend my gratitude to my supervisor, Dr. Katja Rietdorf for her expertise in the lab, encouragement, help and tireless enthusiasm. I would also like to thank my second supervisor Dr. Martin Bootman for his guidance, expertise in the subject and encouragement. They both pushed me to the best of my ability, remained incredibly patient with my set-backs and this thesis would not be possible without their help.

Further to this, I would also like to thank the Open University and Prof. Fraser McDonald for funding this project.

Many sincere thanks to Frances Colyer and Heather Davies for teaching me EM in my first year. I would also like to thank my fellow students Tala and Gaurav for their help in the lab, encouragement and all of the good times that we had during the course of this PhD. Adding to this, I am also grateful to other students at the Open University. In particular, Nadia, Sarah, Sophie, Emily, Mathew, George, Shereen and Conor for their help, interesting talks about politics, coffee breaks and providing much needed distraction when I needed it.

Finally, I would like to thank my family, my lovely mother Maryam, my sister Nadia, my brother Fahmy and lastly but not least my wife, Munawar. She has coped immensely with my constant moaning and stress during the course of this PhD. This PhD will not be possible without her constant encouragement, help and understanding. This thesis is dedicated to my father who passed away in 1996 shortly before he was supposed to start a PhD project in America.

CONFERENCE ITEMS AND PUBLICATIONS

Journal items

Rietdorf, Katja; Masoud, Said; McDonald, Fraser; Sanderson, Michael J. and Bootman, Martin D. (2015). “Pulmonary vein sleeve cell excitation–contraction-coupling becomes dysynchronized by spontaneous calcium transients”. *Biochemical Society Transactions,* 43(3) (pp. 410-416).

Conference items

Masoud, Said; Bootman, Martin D.; McDonald, Fraser and Rietdorf, Katja. (2016-09). Can we use chemical-induction of ageing to develop a model of cardiac ageing*? In: 14th International Meeting of the European Calcium Society* (25-29 September 2016, Valladolid, Spain).

Masoud, Said; Bootman, Martin D.; McDonald, Fraser; MacQueen, Hilary and Rietdorf, Katja. (2016-09). How does fat cause heart diseases? Effects of epicardial adipocytes on cardiomyocyte signalling and contractility *In: 14th International Meeting of the European Calcium Society* (25-29 September 2016, Valladolid, Spain).

Masoud, Said; Bootman, Martin; McDonald, Fraser and Rietdorf, Katja. (2016-03). Chemically inducing ageing in neonatal rat ventricular myocytes In: Evolution brings Ca^{2+} and ATP together to control life and death (16 - 17 March 2016, Kavli Royal Society Centre, Chicheley Hall, Newport Pagnell).

Rietdorf, Katja; Masoud, Said; McDonald, Fraser and Bootman, Martin. (2015). How cells outside the heart can affect the heart beat: The role of pulmonary vein sleeve cells for the development of atrial fibrillation In: Gordon Conference on Calcium Signalling (7-12 June 2015, Newry, Maine, USA).

Masoud, Said; McDonald, Fraser; Bootman, Martin and Rietdorf, Katja. (2015). “Ageing-induced ultrastructural changes of mitochondria of pulmonary vein sleeve cells”, In: Physiology 2015 (6-8 July 2015, Cardiff).

Masoud, Said; Bootman, Martin D.; McDonald, Fraser and Rietdorf, Katja. (2014-10-09). Spontaneous Ca^{2+} signalling and ultrastructural changes in pulmonary vein sleeve cells during ageing – risk factors for atrial fibrillation? In: Calcium Signalling: The Next Generation (9-10 October 2014, London, UK).

Masoud, Said R.; McDonald, Fraser; Bootman, Martin D. and Rietdorf, Katja. (2014-10-09). A comparative study of the ultrastructure changes of atrial myocytes, pulmonary vein sleeve cells and ventricular myocytes during ageing In: Calcium Signalling: The Next Generation (9-10 October 2014, London, UK).

Masoud, Said; Bootman, Martin and Rietdorf, Katja. (2014-06). Spontaneous Ca^{2+} signalling in pulmonary vein sleeve cells increases during ageing. In: Physiology 2014 (30 June - 02 July 2014, London.

Contents

LIST OF FIGURES

LIST OF TABLES

ABBREVIATIONS

I_{CAL} – L-type Ca^{2+} current

I_{K1} – inward rectifier potassium current

I_{KR} – rapid rectifier potassium current

I_{ks} – slow rectifier potassium current

I_{NA} – fast inward sodium current

I_{NCX} – NCX current

I_{TO} – transient outward current

µM - micro-molar

3-MA – 3 methyl adenine

ACE - Angiotensin converting enzyme

AF - atrial fibrillation

ANP – atrial natriuretic peptide

ANT – adenine nucleotide translocator

AP - action potential

ARV/C - arrhythmogenic right ventricular dysplasia/cardiomyopathy

ASPA – Animals Scientific Procedure Act

ATP – adenine triphosphate

AT1R - Angiotensin type 1 receptor

AT2R - Angiotensin type 2 receptor

AUC – area under the curve

AV node - atrioventricular node

Ba^{2+} - Barium

BDMA - benzyl dimethylamine

BSA - bovine serum albumin

Ca^{2+} - Calcium

CICR - Calcium-induced calcium release

CaM – Calmodulin

CaMKII – Calmodulin kinase II

Cl^- - Chloride ion

CRU – Ca^{2+} releasing unit

CsA – cyclosporin A

Cyp D – cyclophilin D

CSQ2 - calsequestrin 2

Cx40 - connexin 40

Cx43 - connexin 43

Cx45 – connexin 45

Ca_v – voltage gated calcium channels

DADs – delayed afterdepolarizations

DDSA - dodecenyl succinic anhydride

DMEM - Dulbecco's Medium Eagle Medium

EADs – early afterdepolarizations

EC-coupling – excitation contraction-coupling

ECG – electrocardiogram

EFS – electrical field stimulation

EM - electron microscopy

FKBP12 - 12 – kDa FK506 binding proteins

FKBP12.6 – 12.6 – kDa FK506 binding proteins

HBSS – Hanks balanced salt solution

HRP- horseradish peroxidase

HU - hydroxyurea

ICLC - Interstitial Cajal like cells

IMM – inner mitochondrial membrane

IP_3 – Inositol 1, 4, 5 trisphosphate

K^+ - potassium ion

LETM1 – leucine-zipper-EF-hand-containing transmembrane protein 1

LSM – laser scanning microscope

MCU – mitochondrial Ca^{2+} uniporter

Mg^{2+} - Magnesium

ml – millilitre(s)

mm - millimetre(s)

mM – millimolar

MN – mitochondrial number

MNA - methyl nadic anhydride

mPTP – mitochondrial permeability transition pore

mRyR1 – mitochondrial ryanodine receptor 1

ms – milliseconds

MS – mitochondrial size

mTOR – mammalian target of rapamycin

mV – millivolts

Na^+ - sodium

NCLX – mitochondrial Na^+/Ca^{2+} exchanger

NCX - Na^+/Ca^{2+} exchanger

NHE – Na^+-proton exchanger

nM - nanomolar

NRVMs – neonatal rat ventricular myocytes

HF - heart failure

Hz - Hertz

LSM - Laser scanning microscope

PB - Phosphate buffer

PBS - Phosphate buffered saline

PFA – paraformaldehyde

PKA – protein kinase A

PLN - phospholamban

PMCA - plasma membrane Ca^{2+}-ATPase

PV – pulmonary vein

PVCs - pulmonary vein sleeve cells

RaM – rapid mode of Ca^{2+} uptake

ROIs – regions of interests

RyRs - Ryanodine receptors

RyR2 - Ryanodine receptor type 2

ROS – reactive oxygen species

RT - room temperature

SA node - sinoatrial node

SEM – scanning electron microscope

SERCA - sarcoplasmic reticulum Ca^{2+}-ATPase

SERCA2a - sarcoplasmic reticulum Ca^{2+}-ATPase type 2

SLN – sarcolipin

SOCE – store operated Ca^{2+} entry

SR - sarcoplasmic reticulum

TBS – Tris buffered saline

TEM – Transmission electron microscope

Tn1 - Troponin 1

TnC - Troponin C

T-tubules - Transverse tubules

UCT - ultra-cut microtome

VOCCs - voltage-operated calcium channels

Chapter 1. Introduction

1.1. Setting the picture: AF, ageing and why they are important issues

Atrial fibrillation (AF) is the most sustained common form of arrhythmias with age becoming a significant risk factor (Kopecky *et al.,* 1987, Go *et al.,* 2001). The prevalence of AF increases strongly with age. Almost all cases occur in people who are 65 years old and above (Hayashi *et al.,* 2002, Nattel *et al.,* 2008). With our ever increasing ageing population, the prevalence of AF is predicted to increase (Teh *et al.,* 2012, Colilla *et al.,* 2013). This reinforces the need to study age-dependent cardiac diseases like AF which are predicted to escalate in the future (Teh *et al.,* 2012, Colilla *et al.*, 2013). It is well established now that ectopic electrical activity originating from pulmonary vein sleeve cells (PVCs) (Sueda *et al.,* 2005; Haissaguerre *et al*., 1998) initiates AF. This thesis explores the effects of ageing mostly in PVCs and the influence of age-dependent changes on facilitating the occurrence of arrhythmias.

1.2. The heart

The heart is a muscular organ that works repetitively and continuously to pump blood to supply the lungs and the body with oxygen. Our understanding of the heart originated in 1628 with William Harvey's finding that the heart is a muscular organ that pumps blood to the body with each heartbeat. This, coupled with the advances in technology in imaging, biochemistry and biophysics of cardiac function have greatly enhanced our understanding of the physiology of the heart and diseases associated with it. The heart rate varies between species in relation to body size; the larger the body the slower the heart rate. The average human heart beats 72 times per minute at rest, whereas a mouse's heart beats on average 450 - 500 times per minute (Janssen and Smits, 2002). The mammalian heart is made up of four chambers; the left and right atria and the left and right ventricles as shown in Figure 1.1 below. The heart consists of many cell types with different properties depending on their spatial and their structural variances (De

Souza *et al.,* 2013). Apart from cardiac myocytes, the heart tissue contains non-myocyte cells including fibroblasts, endothelial cells, smooth muscle cells and conducting cells in the sino atrial (SA) node (Kwak 2013). The major types of cardiac myocytes are atrial myocytes and ventricular myocytes (De Souza *et al.,* 2013), but a third myocyte type can be found in the pulmonary veins which are labelled below in Figure 1.1. These are called pulmonary vein sleeve cell (PVC). This thesis will mainly focus on studying PVCs, atrial and ventricular myocytes.

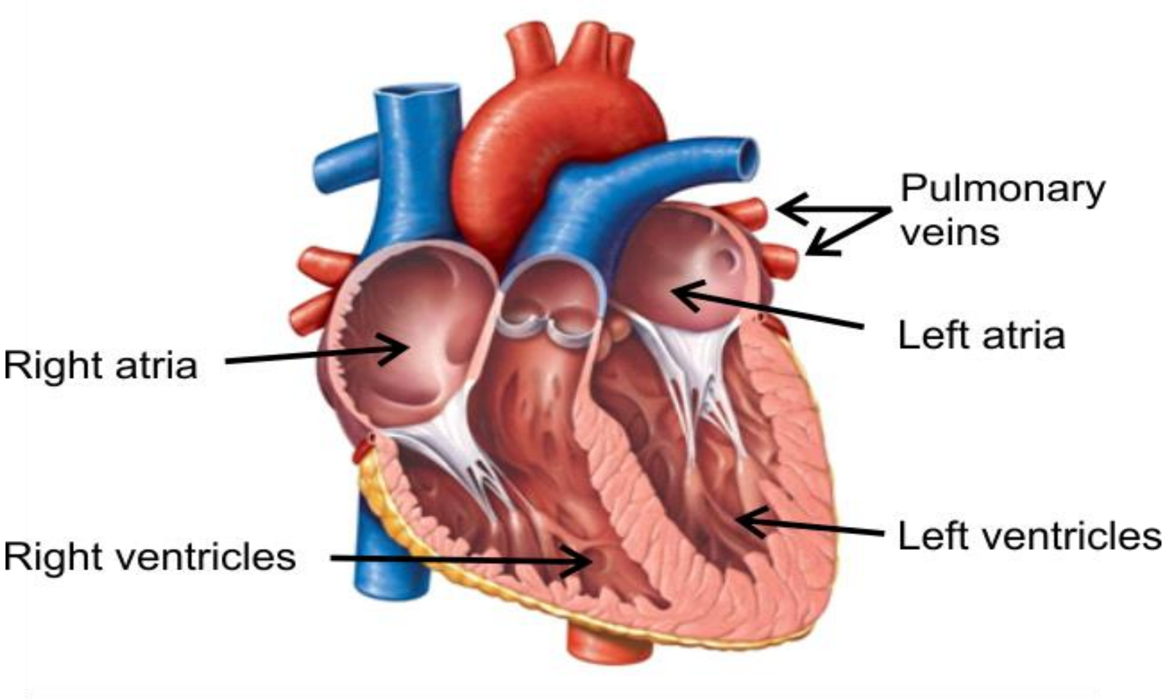

Figure 1.1. The structure of the heart. The basic structure of the heart showing the four chambers and pulmonary veins. From http://classconnection.s3.amazonaws.com/250/flashcards/2024250/jpg/human-heart-diagram-unlabeled-i41349297592107.jpg.

1.3. Pulmonary vein sleeve cells (PVCs)

In 1876, Brunton and Fayrer observed an independent pulsation of a rabbit pulmonary vein after all motion had ceased in the heart (Cheung 1981). It is well known now that a layer of striated muscle is present in the pulmonary veins of small rodents and other mammals (Masani 1986). These cells are frequently the initiator of AF and are what we call PVCs. There is a general agreement that myocardial muscle fibers extend from the left atrium into all of the pulmonary veins at a length of 2 – 4 cm, independent of species (Calkins, 2008). Most of the previous studies have shed lights that PVCs cover almost all of the pulmonary vein ostium, however, the length and thickness of myocardial sleeves inside the pulmonary veins varied widely (Ho *et al.,* 2001, Mueller-Hoecker *et al*., 2008). The sleeves with PVCs are longer and thicker in the superior pulmonary veins compared to inferior pulmonary veins but with no difference in-between AF patients and healthy individuals (Ho *et al.,* 2001). The length of sleeves extends as far as the hilus of the lungs in rodents (Figure 1.2) but less so in humans where the lungs are usually devoid of PVCs (Ho *et al.,* 2001, Mueller-Hoecker *et al*., 2008).

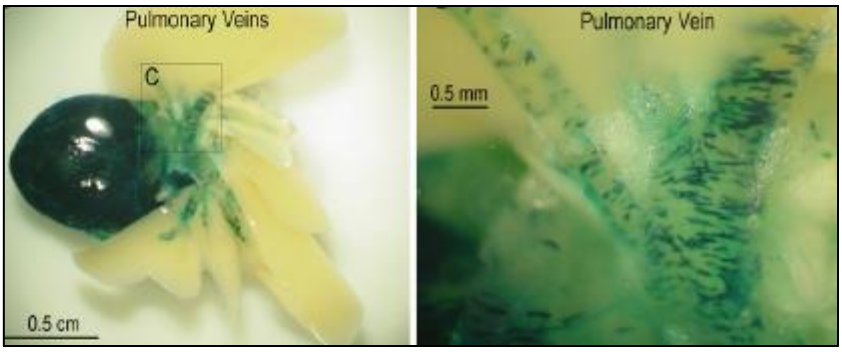

Figure 1.2. Abundant cardiac myocytes in the wall of pulmonary veins. A). Cardiac myocytes, identified by the lacZ expression targeted via a Troponin C promotor, are not only found in the heart but are also abundant in the pulmonary veins and reach inside the lungs. **B).** Cells expressing lacZ within the pulmonary veins demonstrating the location of PVCs (Kracklauer *et al.,* 2013).

The wall of pulmonary veins from rodent lungs includes a layer of endothelial cells, scant smooth muscle cells and a layer of striated cardiac muscle. The presence of PVCs inside the lungs of rodents enables us to study PVCs in lung slices (Rietdorf *et al.,* 2014, Rietdorf *et al.,* 2015). Light and electron microscopic (EM) studies have shown similarities between PVCs and atrial myocytes (Jones *et al.,* 1994, Townsley 2012). The alpha-myosin heavy chain gene expression pattern of PVCs appears to be similar to that of atrial myocytes (Jones *et al.,* 1994). Furthermore, both types of myocytes are connected by desmosomes and intercalated discs and, as a consequence, are in electrical continuity (Spach *et al.,* 1972, Tsai *et al.,* 2000). Previous studies have shown that ectopic activity in the form of spontaneously developing depolarisations of the membrane potential and calcium (Ca^{2+}) transients, leading to the occurrence of spontaneous action potentials (APs), can arise within the PVCs and travel back to the atria (Tsuneoka *et al.,* 2012). To date, the role of PVCs in pulmonary vein physiology is not completely understood. Interestingly, (Paes de Almeida *et al.,* 1975) suggested that contractions of the pulmonary veins caused by APs in PVCs in rodents might act like a “throttle valve” to prevent a backflow of blood into the lungs during systole, and therefore prevent a pulmonary oedema (Mueller-Hoecker *et al.*, 2008).

Several groups have reported evidence of conducting cells in pulmonary veins in both animals and humans. (Levin *et al.*, 2009) found melanocyte-like cells and (Perez-Lugones *et al.,* 2003) found pacemaker cells, transitional cells and Purkinje cells in human pulmonary veins from patients with a history of AF. Interestingly, these cells were not seen in pulmonary veins from humans without the history of AF. Furthermore, morphological studies in rats found conducting cells in pulmonary veins (Masani 1986) and more recently cardiac myocytes and interstitial Cajal-like cells (ICLC) have been found in pulmonary veins from both humans and rodents (Gherghiceanu *et al.,* 2008, Mueller-

Hoecker *et al.,* 2008). Although ICLC are involved in pace-making activity in the intestine, their role in the automaticity of the pulmonary vein is unclear as they have also been found in the normal atrium (Schotten *et al.,* 2011). The presence of conducting cells in PVCs makes it more likely that PVCs show spontaneous activity and may act as a pro-arrhythmic substrate.

1.4. Cardiac cycle

The cardiac cycle is the series of events that initiate the rhythmical beating of the heart. It constitutes of diastole and systole. During diastole, all four chambers are relaxed. During systole, an AP generated by the SA node leads to atrial and ventricular contraction. The SA node is the primary pacemaker centre of the heart and is located in the upper wall of the right atrium. The AP generated at the SA node travels to atrioventricular (AV) node and creates an electrical wave that sweeps over the atria and eventually causes the atria to contract and pump blood into the ventricles. Apart from the SA node, the atrioventricular (AV) node is the other major pacemaker and is located in the lower part of the right atrium. However, the AV node does not have a pacemaker role in normal heart. Nonetheless, on reaching the AV node, there is a brief pause in the conduction of the electrical signal (~0.1 s in humans) to allow the blood to be completely emptied from the atria into the ventricles before those start contracting. Additionally, the AV node acts as an insulator between the atria and ventricles. This property is very important in preventing the spreading of spontaneous electrical activities from the atria to the ventricles (Fearnley *et al.,* 2011). The electrical signal is then propagated down the bundle of His, which splits to the right and left, thereby activating both, the right and the left ventricle. Signal propagation continues down the Purkinje fibers, allowing the ventricles to contract simultaneously from the apex and upwardly, thus pushing the blood from the heart to the lungs through the pulmonary artery or to the rest of the body through the aorta. Backflow of blood into the atria is prevented by valves between the atria and the ventricles.

1.5. Excitation-contraction coupling

1.5.1. Coupling machinery

Just like other muscles, the cardiac muscle consists of bundles of myofibrils that contain myofilaments as illustrated in Figure 1.3. Each cardiac muscle cell (cardiac myocyte) is made up of sarcomeres (the distance between one Z-line to another) that contain thick and thin filaments. The Z-line is a region where thin actin filaments attach. The average distance between Z-lines is 1.8 µm in length in small rodents (Soeller and Cannell 1999). The thick filaments are composed of myosin and thin filaments are composed of actin (Figure 1.3). Shortening of the sarcomeres usually occurs when the actin filaments slide along the adjacent myosin filaments forming cross-bridges and bringing the Z-lines closer together, thus resulting in muscular contraction.

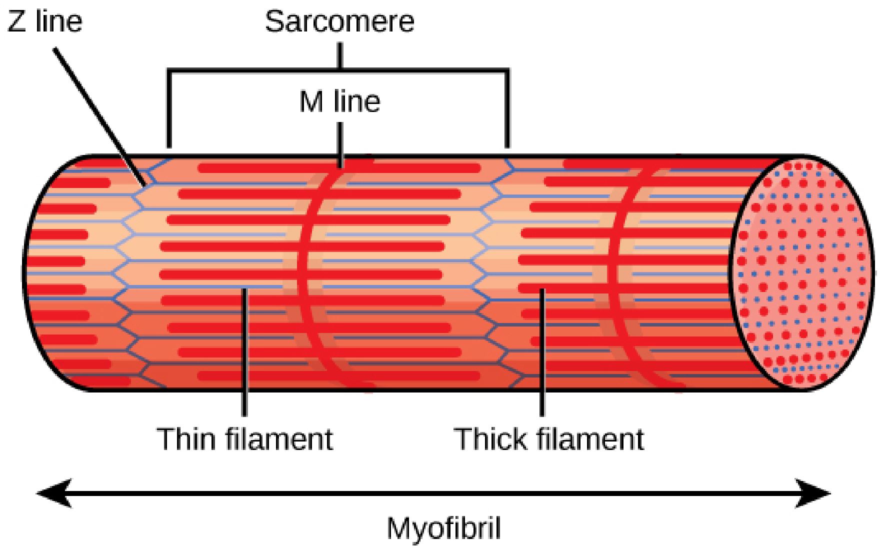

Figure 1.3. The basic structure of myofibril. An image showing the basic structure of a myofibril and the major proteins within a sarcomere (Figure from boudless.com).

1.5.2. Importance of Ca^{2+} for cardiac contraction

More than 130 years ago, The Journal of Physiology published the milestone discovery of Sidney Ringer (Sidney Ringer, 1883) that Ca^{2+} ions are an essential constituent in the extracellular fluids for normal cardiac contraction. Since then, the detailed steps linking changes in the intracellular Ca^{2+} concentration to the electrical depolarisation of cardiac myocytes and their contraction have been described / elucidated.

As described in 1.4, the SA node is the heart's main pacemaker. The APs generated at the SA node sweep across the heart cells, it opens voltage-operated Ca^{2+} channels (VOCCs) localised on the sarcolemma of cardiac myocytes. As the Ca^{2+} concentration outside the cell is ~1-2 mM, but it is only ~ 100 nm inside the cell, the opening of VOCCs leads to an influx of Ca^{2+} down its electrochemical gradient into the cell, more specifically into the dyadic cleft. The dyadic cleft is the ~10 – 12 nm wide space between the sarcolemma and Ryanodine receptors type 2 (RyR2) on the sarcoplasmic reticulum (SR) membrane (Ayettey and Navaratnam 1978). The opening of VOCCs causes an increase of Ca^{2+} within this micro-domain from ~ 100 nM to 10 µM. The elementary Ca^{2+} signal caused by the opening of VOCCs is known as a "Ca^{2+} sparklet" (Wongchaoren *et al.,* 2007; Fearnley *et al.,* 2011). This initial rise in cytosolic Ca^{2+} is not sufficient to elicit contraction, however, it allows the opening of RyR2s on the SR membrane, which to leads to an efflux of Ca^{2+} from the SR to the cytosol (Figure 1.4) in a process known as Ca^{2+}-induced Ca^{2+}release (CICR). The effect of CICR is to cause elementary Ca^{2+} release events in the dyadic cleft termed "Ca^{2+} sparks". It is estimated that ~10 - 100 RyR2s underlie a single Ca^{2+} spark, although this number can vary between different cell types (Fearnley *et al.,* 2011). The opening of RyRs increases the cytosolic Ca^{2+} concentration to over 100 µM in the dyadic cleft, which is high enough to elicit contraction of the cardiac myocyte. Diffusion of Ca^{2+} ions increases global Ca^{2+} concentration to ~ 500 nM - 1 µM (Fearnley *et al.,* 2011). At this cytosolic Ca^{2+}

level, Ca^{2+} binds to Troponin C (TnC). When Ca^{2+} binds to TnC, TnC binds more strongly to Troponin I (TnI) and pulls TnI away from its actin binding site, thus allowing the myosin heads to interact with actin, forming cross-bridges and eliciting contraction (Bers 2008).

Relaxation is initiated when the cytosolic Ca^{2+} concentration starts to fall again, owing to Ca^{2+} sequestration into the SR by the sarcoplasmic reticulum Ca^{2+} ATPase (SERCA) pump, by extrusion to the extracellular space by the Na^+/Ca^{2+} exchanger (NCX) and to a lesser extent by the plasma membrane Ca^{2+} ATPase (PMCA), as illustrated in Figure 1.4. The SERCA sub-type that is mostly expressed in cardiac cells is SERCA2a (Periasamy *et al.,* 2008; Park and Oh, 2013). In ventricular myocytes, the activity of SERCA2a is under the control of a protein that binds to the SR membrane known as phospholamban (PLN) whereas, in PVCs and atrial myocytes, sarcolipin (SLN) controls the SERCA2a activity. In their dephosphorylated states, both PLN and SLN inhibit SERCA2a; however, they release their inhibition when being phosphorylated, allowing more rapid pumping of Ca^{2+} back into the SR by SERCA2a and thus faster relaxation (Mattiazzi *et al.,* 2006, Bhupathy *et al.,* 2007, Smeazzetto*et al.,* 2011). In hearts of larger mammals like rabbits, dogs and humans, ~70 % of the decrease in the cytosolic Ca^{2+} concentration is accounted for by reuptake of Ca^{2+} into the SR, and only 30 % by elimination via NCX. In contrast, in mice and rats up to 90 % of the Ca^{2+} is sequestered into the SR (Bassani *et al.,* 1994, Pieske *et al.,* 1999, Bers 2008).

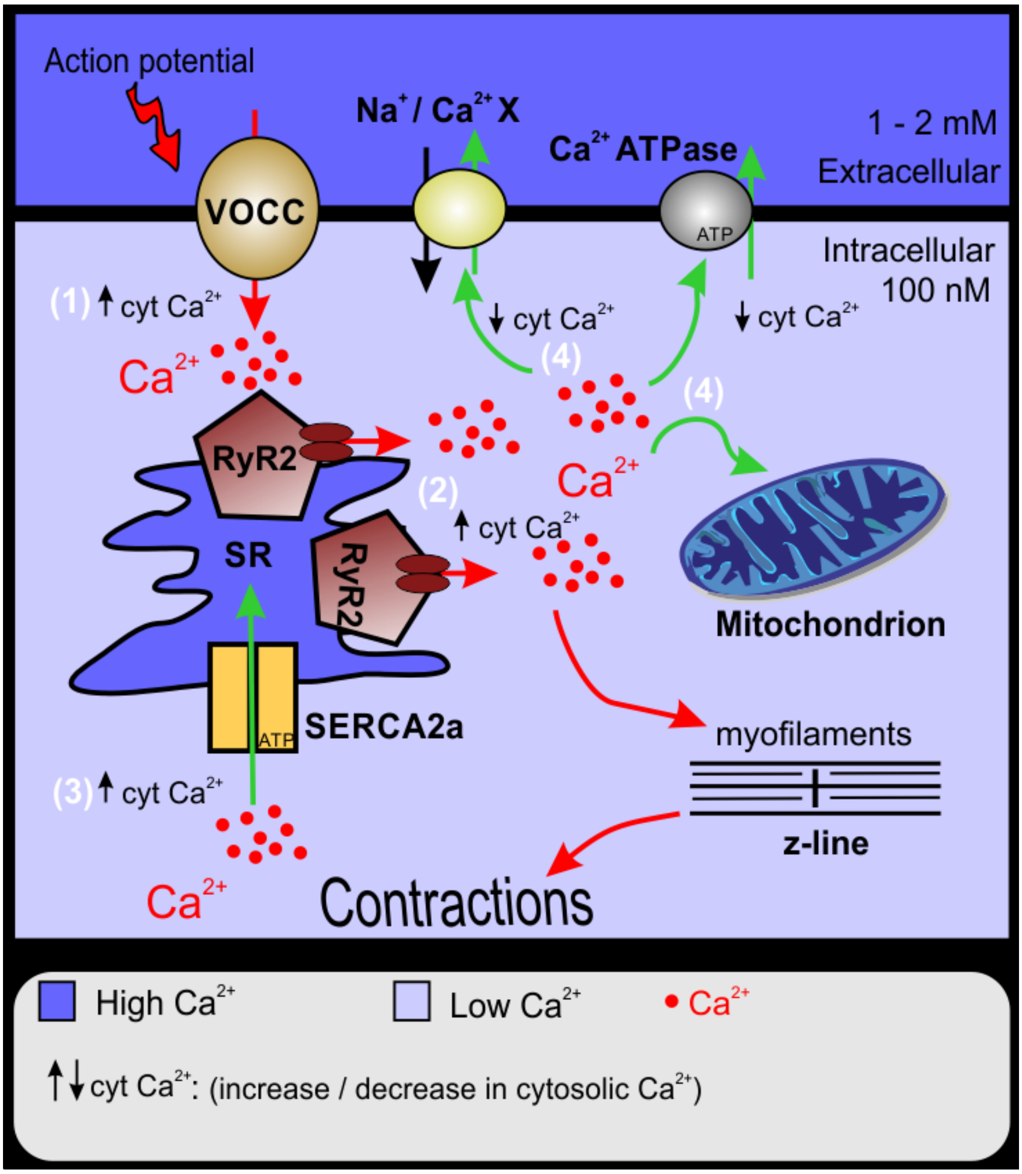

Figure 1.4. Scheme of events during excitation-contraction coupling in a cardiac myocytes. The AP opens VOCCs in the sarcolemma which allows an influx of Ca^{2+} down a concentration gradient (1) and activates RyR2s on the surface of the SR (2). This rise in the cytosolic Ca^{2+} generates a global Ca^{2+} transient and activates the contractile apparatus. Free cytosolic Ca^{2+} is then removed back into the SR by the SERCA2a pump (3) or out of the cell by PMCA, NCX and uptake into mitochondria (4).

1.5.3. Store operated Ca^{2+} entry

A rise in Ca^{2+} in the cytosol can arise from an influx of Ca^{2+} from the extracellular medium as described above, or through Ca^{2+} release from intracellular stores such as the SR. The depletion of Ca^{2+} from SR activates an influx of Ca^{2+} across the plasma membrane to refill the SR in a process known as store operated Ca^{2+} entry (SOCE), see Figure 1.5 (Hogan *et al.,* 2015). Despite the phenomenon of SOCE being a long established one, the molecular identities of the channel responsible for SOCE have only recently been identified. STIM1 and STIM2 function as Ca^{2+} sensors in the SR and can interact with plasma membrane channels Orai1, Orai2 and Orai3 to form a CRAC channel that allows Ca^{2+} into the cytosol, Figure 1.5 (Vig *et al.,* Feske *et al.,* 2005, Feske *et al.,* 2006).

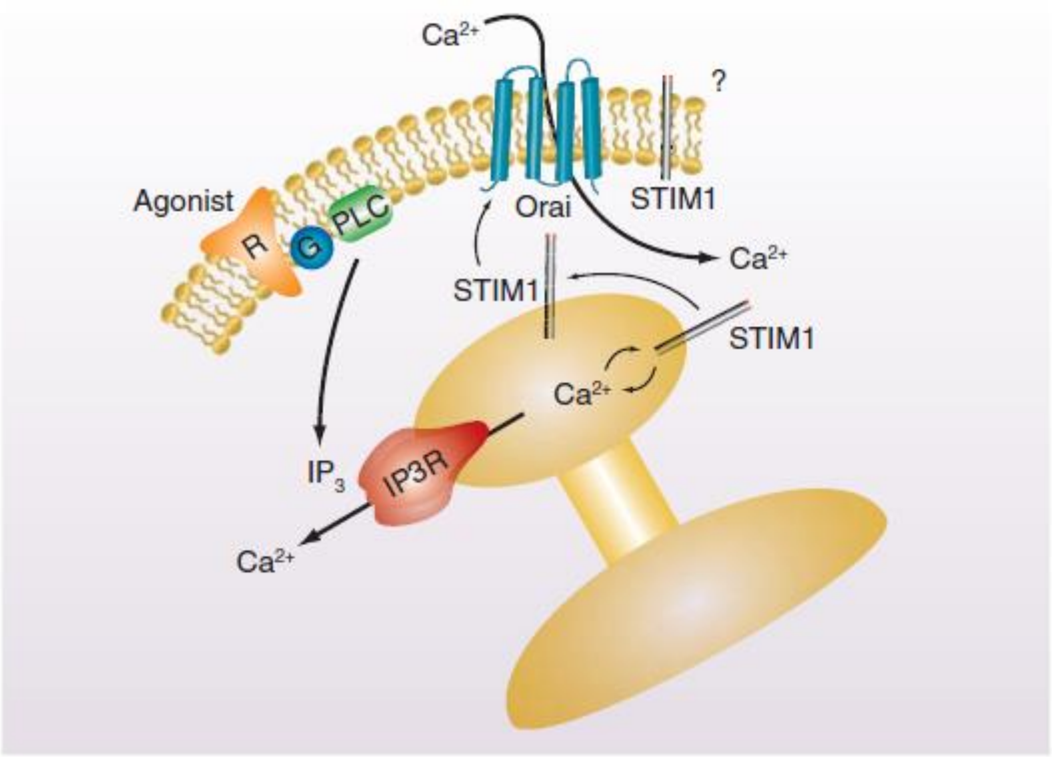

Figure 1.5. Mechanism of SOCE. An agonist activates a G-protein coupled receptor in the plasma membrane that leads to an increase in inositol 1, 4, 5-trisphosphate (IP_3) production that causes Ca^{2+} to be released from the ER. The reduction of Ca^{2+} in ER lumen assembles STIM1 to redistribute near the plasma membrane activating Orai channels and allows Ca^{2+} entry through a CRAC channel (From Putney 2010).

The main role of SOCE is to replenish SR Ca^{2+} and it helps maintaining the SR Ca^{2+} homeostasis. SOCE is best studied in non-excitable cells, where it is the key source of Ca^{2+} entry pathways (Mathews *et al.,* 1989; Hogan and Rao 2015). Recent studies have suggested that SOCE may also play a role in Ca^{2+} homeostasis in excitable cells (Touchberry *et al.,* 2011, Liu *et al.,* 2015); however, the role of SOCE in the heart is still unclear (Bootman and Rietdorf, 2017). Within the cardiovascular system, SOCE plays an important role in vascular contraction, for example, Ca^{2+} influx induced by intracellular stores depletion activated pulmonary artery and arterial smooth muscle contraction (Snetkov *et al.,* 2003, Bergdahl *et al.,* 2005). Additionally, SOCE is involved in maintaining the pace maker current in SA node cells (Liu *et al.,* 2015).

Having seen recently that SOCE also play a role in SA node cells which resemble PVCs in generating spontaneous APs (Liu *et al.,* 2015), and increased contractions and Ca^{2+} levels after a Ca^{2+} removal and addback protocol in PVCs (Rietdorf *et al.,* 2014), this thesis investigated if SOCE plays any role in PVCs. It is unclear whether SOCE plays any role in PVCs and whether they express CRAC channels. To investigate the role played by SOCE in PVCs, this thesis analysed the effects of BTP2 (an inhibitor of SOCE) on spontaneous Ca^{2+} transients (Chapter 4).

1.5.4. Molecular basis of excitation-contraction coupling

1.5.4.1. Voltage gated Ca^{2+}channels

Ca^{2+} channels are the main mode of Ca^{2+} entry into cells in excitable cells. In cardiac tissue, VOCCs can be classified as L-type (low threshold type) and T-type (transient type) Ca^{2+} channels based on their physical and pharmacological studies. L-type channels are found in all cardiac cell types whereas T-type channels are mainly found in pacemaker, atrial and Purkinje cells. PVCs have been reported to express both L-and T-type Ca^{2+} channels (Chen *et al.,* 2004, Logantha *et al.,* 2010). These channels may play a role in the release of spontaneous Ca^{2+} transients in PVCs. In PVCs, T-type Ca^{2+} channels are thought to be involved in their pacemaking and triggered activity (Chen *et al*., 2004), similar roles have also been suggested in SA node cells (Hüser *et al.,* 2000).

The basic structure of L-and T-type Ca^{2+} channels consists of 5 subunits – α_1, α_2, β, Y and δ which unite in different combinations to form a channel in its native state (see Figure 1.6). In mammals, 10 Ca_v subtypes have been identified and classified into three families Ca_v1, Ca_v2 and Ca_v3 on the basis of ion conducting α1 subunit (Van Petegem *et al.,* 2005). Among these, the Ca_v1 channels ($Ca_v1.1$ – 1.4) are L-type high voltage activated channels co-assemble with auxiliary subunits including the extracellular α2δ, the intracellular β and the transmembrane ϒ (Wu *et al.,* 2016). $Ca_v1.2$ is the cardiac specific subunit. The intracellular β subunit increases channel expression and accelerates the channel activation and inactivation kinetics (Cheng *et al.,* 2005). Structurally, Ca^{2+} channels have 4 homologous domains, each consisting of 6 membrane spanning segments which are shown in Figure 1.6 below.

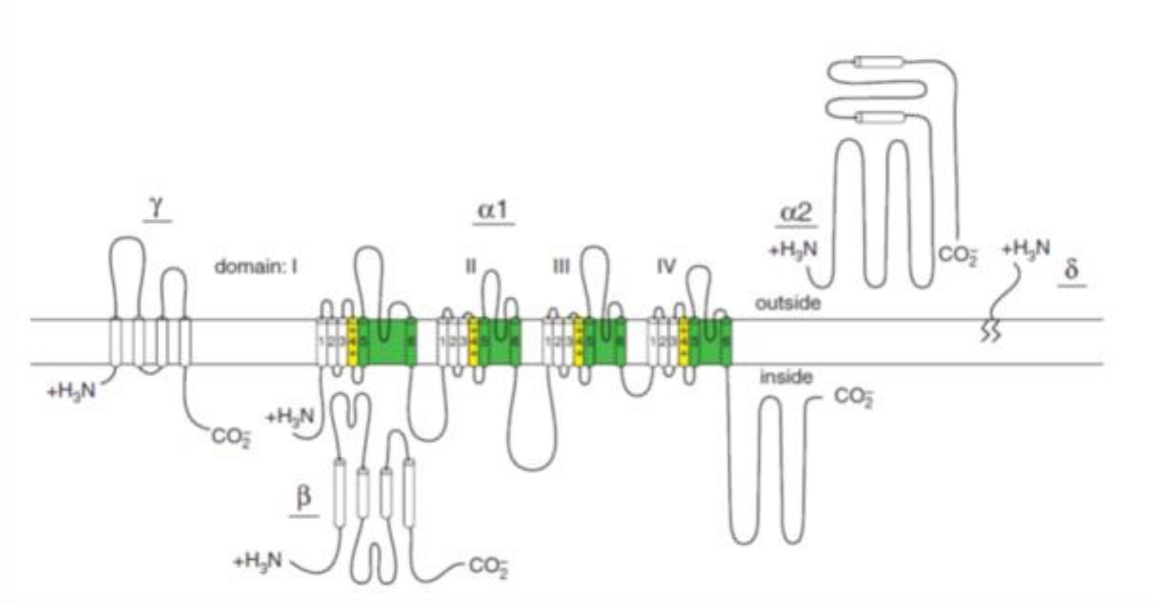

Figure 1.6. Basic structure of VOCCs. The Ca^{2+} channels consist of α1, α2, β, Y and δ. The predicted α helices are depicted as cylinders, the lengths of lines correlate the lengths of polypeptides and the zigzag line on the δ subunit demonstrates its phosphatidylinositol anchor. Adapted from (Catterall 2011).

Mutation studies on Ca^{2+} channels has led to proposal that the hairpin loop of the S5 / S6 regions of domain III bends back into the membrane lining the channel pore. The P-loop of each domain with the glutamate residues contribute to the pore structure (Catterall and Swanson 2015). The fourth transmembrane region which contains a lot of positively charged arginine / lysine (coloured in yellow in Figure 1.6) acts as a voltage sensor. Several molecular mechanisms contribute to inactivation of VOCCs. Membrane depolarization decreases the open probability of channels available for opening from 1 at – 45 mV to 0 at 0 mV (Grant 2009). Therefore, the open probability of VOCCs is lowest at hyperpolarised potentials and increases with depolarisation before decreasing again at potentials higher than – 45 mV. As mentioned before, in cardiac myocytes, the two Ca^{2+} channels which conduct current as they open are T-type and L-type. The T-type channels which are small conductance and rapidly inactivating. The L-type channels are activated with higher voltages producing a slowly, inactivating and longer lasting current. The carboxyl terminus of the Ca^{2+} channel has multiple Ca^{2+} binding sites and Ca^{2+} calmodulin (CaM) dependent kinase activity (Grant 2009). Alterations of Ca^{2+} levels around the channel can modulate opening and closing of the channels. Ca^{2+} in the immediate vicinity of the channel and phosphorylation of CaM has been shown to inactivate the channel (Zhou *et al.,* 1997, Qin *et al.,* 1999). Conversely, reduction of Ca^{2+} in the vicinity of VOCCs caused by the re-uptake of Ca^{2+} back to the SR could result in the recovery of the channel inactivation (Grant 2009). Changes in the regulation and electrical remodelling of VOCCs during ageing may result in AF as described later on in this chapter.

1.5.4.2. Ryanodine receptors

The RyR is a Ca^{2+} permeable non-selective cation channel that releases SR Ca^{2+} in excitable and non-excitable cells. In mammals, there are three genes encoding RyR1, RyR2 and RyR3 isoforms. RyR1 is expressed in skeletal muscle, particularly in fast twitch muscle; RyR2 is expressed in cardiac myocytes. RyR3 is constitutively expressed in brain, skeletal, smooth muscle cells and in non-excitable cells (Guerrero-Hernandez *et al.,* 2014). Both RyR1 and RyR2 play a central role in excitation contraction coupling but as RyR2 is the one that is highly expressed in cardiac cells, this thesis will mainly focus on RyR2.

The RyR2 is a tetramer with molecular mass of 565 kDa per subunit, making RyRs the largest known Ca^{2+} channel protein. Based on sequence analysis, RyRs proteins contain at least two functional domains: a large N-terminal cytosolic domain containing many regulatory / binding sites and a C-terminal domain containing several hydrophobic domains, these binding sites and hydrophobic domains are shown in Figure 1.7 below. Four of those are the transmembrane domains (M1 – M4) whilst one, located between M3 and M4, forms the channel pore (Capes *et al.,* 2011). Previous biochemical and cryo-

EM studies revealed that four subunits unite to form a functional channel (Sharma *et al.,* 1998, Benacquista *et al.,* 2000).

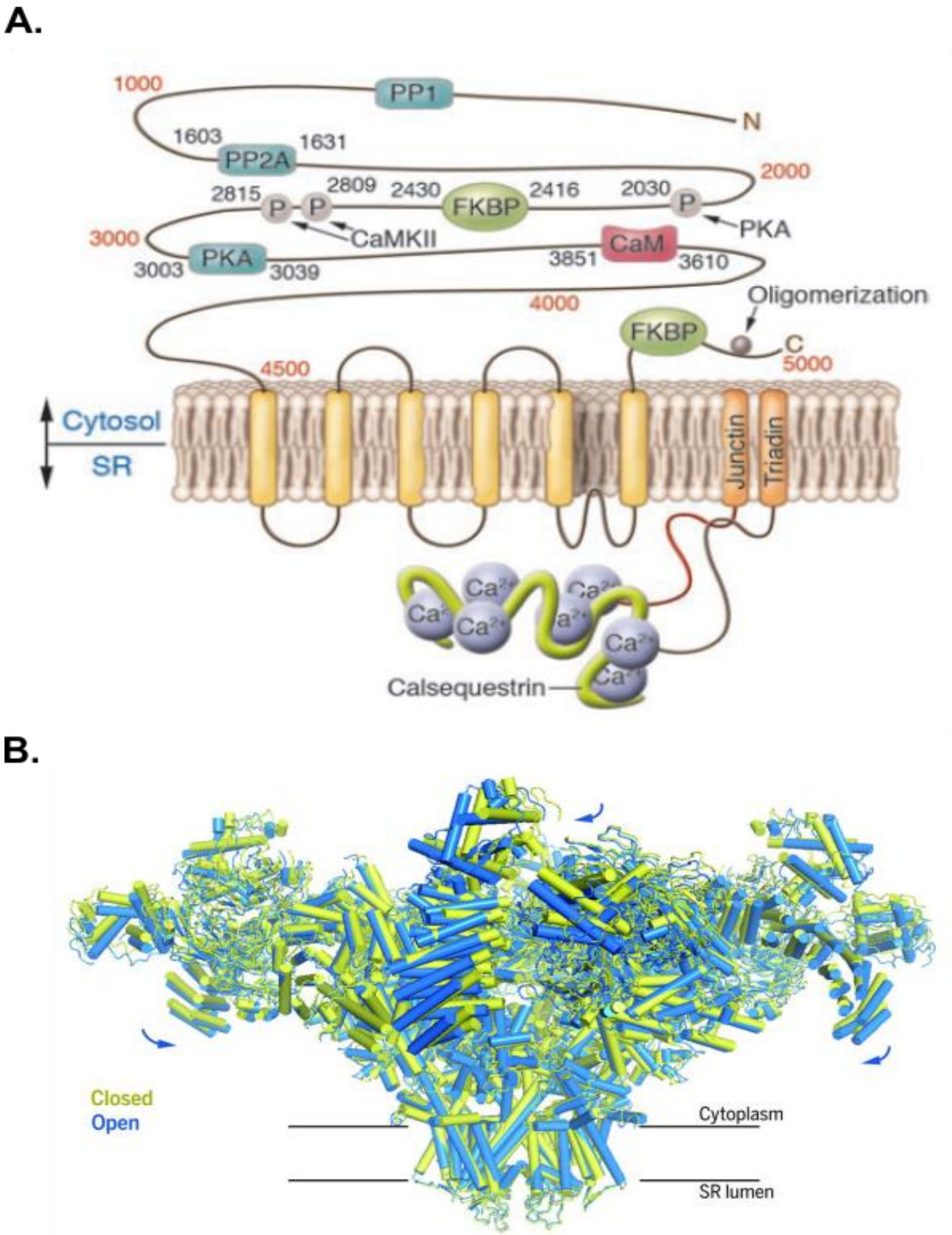

Figure 1.7. Structure of RyR2. (A) A predicted structure of RyR2 with ancillary proteins and phosphorylation sites. In the lumen side of the SR; triadin, junctin and calsequestrin can all interact with RyR2 in the SR. In the cytosolic side, several phosphorylation sites and Ca^{2+} binding proteins are located. **(B)** A cryogenic EM structures of RyR2 in both the closed and open states which are superimposed relative to the transmembrane domain. The blue arrows indicate the overall shifts of the cytoplasmic region from the closed state to the open state (Adapted from Priori and Napolitano, 2017).

Opening of VOCCs after arrival of an AP causes a localised increase in the intracellular Ca^{2+} concentration, which in turn stimulates the release of Ca^{2+} from the SR through RyRs. Ca^{2+} levels in the SR must be restored to pre-release state before the RyRs can release Ca^{2+} again at the arrival of the next AP. This is accomplished by the re-uptake of Ca^{2+} into the SR via SERCA2a. Thus, the amount of Ca^{2+} released by the SR must equal the amount of Ca^{2+} taken up the SR during steady-state (Eisner *et al.,* 2017). The open probability of RyRs is higher at a lower cytosolic Ca^{2+} concentration but is inhibited at higher Ca^{2+} concentration. Under steady conditions, Ca^{2+} concentrations in the range of 100 nM to approximately 10 µM activate all three RyRs (Bull and Marengo 1993). Complete Ca^{2+}-dependent inactivation in isolated RyR2 channels occurs at very high Ca^{2+} concentrations (>10 mM), so its physiological relevance is questionable (Bull and Marengo 1993, Chu *et al.,* 1993). This may reflect the existence of a low binding site that inhibits release, and a high binding site that stimulates the release (Capes *et al.,* 2011). The effects of agonists like adenosine triphosphate (ATP), and inhibitory effects of Mg^{2+} influence the kinetics of Ca^{2+}-dependent activation and inactivation (Suárez-Isla *et al.,* 1990, Valdivia *et al.,* 1995, Kasai and Ide 1996). However, the concentrations of these two ligands do not change substantially over a short period and therefore, they have been suggested to only play a significant role during a period of metabolic stress or intense muscle activity (Valdivia *et al.,* 1995, Capes *et al.,* 2011).

SR luminal Ca^{2+} is tightly regulated by a number of proteins such as calsequestrin 2 (CSQ2), junctin and triadin 1 (Györke and Györke 1998, Györke *et al.,* 2004, Blayney and Lai 2009). Although significant progress has been made in understanding the molecular basis of RyR regulation by cytosolic Ca^{2+}, less is known about the regulation via luminal Ca^{2+}. However, dysregulation of RyRs by luminal Ca^{2+} has been implicated in pathological states like arrhythmias, Ca^{2+} overload and heart failure (HF) (Pritchard and Kranias 2009).

Single channel experiments have confirmed that the greater the luminal Ca^{2+} concentration, the more responsive RyR2 becomes to Ca^{2+} in the presence of ATP (Györke and Györke 1998, Györke *et al.,* 2004). A specific Ca^{2+} sensitive luminal regulation site has been proposed on the receptor (Laver 2007). It has also been proposed that luminal RyR2 accessory proteins CSQ, triadin and junctin directly regulate the RyR2 channel's sensitivity to luminal Ca^{2+} (Blayney and Lai 2009). Cardiac CSQ is a major Ca^{2+} binding protein in the SR that can bind up to 40 Ca^{2+} ions and undergoes conformational change upon Ca^{2+} binding (Györke *et al.,* 2004, Blayney and Lai 2009). CSQ can interact with RyR either directly or via triadin and junctin. Since Ca^{2+} release rises steeply with an increased SR Ca^{2+} concentration, CSQ may play a role in Ca^{2+} buffering to regulate free luminal SR Ca^{2+} (Blayney and Lai 2009). Triadin and junctin, both of which have luminal and transmembrane regions, form a complex with CSQ that inhibits the open probability of RyRs when the luminal Ca^{2+} concentration is low and this inhibition is released with a rise in Ca^{2+} (Györke *et al.,* 2004). Previous studies in adult ventricular myocytes have shown that the amount of CSQ expressed affected the functional size of the SR Ca^{2+} load (Györke *et al.,* 2004, Blayney and Lai 2009, Pritchard and Kranias 2009). This regulation of the SR luminal Ca^{2+} by the CSQ-triadin-junctin complex remain the leading candidate for the mechanism of luminal Ca^{2+} regulation, however, it is still challenging to dissect out the possible contribution of each phenomena (Capes *et al.,* 2011).

1.5.4.3. RyR accessory proteins

The large cytoplasmic domain of the RyR represents the modulatory region of the receptor and contains several binding sites for nucleotides and FK506 binding proteins; 12-kDa FK506 binding protein (FKBP12) in RyR1, 12.6-kDa FK506 binding proteins (FKBP12.6) in RyR2 and both FKBP12 / FKBP12.6 in RyR3. Other characterised sites include a CaM binding site; high and low affinity Ca^{2+} binding sites and phosphorylation sites (Wagenknecht *et al.,* 1997, Sharma *et al.,* 1998).

FKBP binding proteins have been shown to be tightly associated with RyRs with up to 4 FKBP binding proteins per channel. Different studies have demonstrated previously that both FKBP12 and FKBP12.6 can regulate channel activity and decrease the opening probability of the channel and hence stabilise the channel (Timmerman *et al.,* 1993, Galfré *et al.*, 2012). Further insights about the role of FKBP12s on RyRs came with the development of knockout mice for FKBP12 and FKBP12.6 genes. FKBP12 knockout mice showed severe increased open probability and channel conductance in single channel recordings (Shou *et al.,* 1998). Although most previous studies suggest that FKBP12.6 binds to RyR2 to stabilise the channel, reducing the opening state of the channel and thus may offer a protective role (Wehrens *et al.,* 2003, Lehnart *et al.,* 2006, Shan *et al.,* 2012); others have found different results (Stange *et al.,* 2003, Xiao *et al.,* 2004, Zhang *et al.,* 2009), so this topic still remains controversial.

Another regulatory protein that interacts with RyRs is CaM, acting either directly or through Calmodulin kinase II (CaMKII). CaM is a Ca^{2+} binding protein containing four EF-hand type Ca^{2+} binding motifs in the N- and C-terminal regions. Previous studies have shown that RyR1, RyR2 and RyR3 each have at least 3 CaM binding sites; two in the central portion of the protein and a third one on the C-terminal region (Guerrini *et al.,* 1995). CaM tightly binds the RyRs in both its Ca^{2+}-bound (Ca^{2+}-CaM) and Ca^{2+}-free (apo-CaM) states. The stoichiometry of CaM binding is 1 molecule of CaM per RyR subunit (Huang *et al.,* 2012). Apo-CaM, the form of CaM that is not bound to Ca^{2+}, weakly activates RyR1 whereas Ca^{2+}-CaM inhibits it. In contrast, RyR2 is not activated by apo-CaM but is inhibited by Ca^{2+}-CaM at both low and high concentrations (Huang *et al.,* 2012). For RyR3, Ca^{2+}-CaM has been shown to potentiate the channel at low concentrations but inhibits the channel at higher Ca^{2+} concentrations (Yamaguchi *et al.,* 2005).

The RyR is a major channel involved in excitation contraction coupling whose opening and closing is tightly regulated involving a number of proteins which binds to the channel either directly or affect it through phosphorylation. As RyRs opening and closing affect the SR and cytosolic Ca^{2+} concentrations, dysregulation of the channel can result in arrhythmias and other cardiac diseases. This makes the RyR a major target for drugs that seek to establish sinus rhythm (Kumagai *et al.,* 2003, Vest *et al.,* 2005, Zhu *et al.,* 2005, Lehnart *et al.,* 2006).

1.5.4.4. Sarcoplasmic reticulum Ca^{2+} ATPase

SERCA is an intracellular protein that uses energy in the form of ATP to actively re-uptake Ca^{2+} from the cytosol onto the SR, therefore brings about muscle relaxation (Periasamy *et al.,* 2008). The three SERCA isoforms that have been described previously are SERCA1 (ATP2A1), SERCA2 (ATP2A2) and SERCA3 (ATP2A3). Alternative splicing of these isoforms can give rise to further variants, for example, SERCA1 can be spliced into SERCA1a sub-type which is expressed in adult skeletal muscles and SERCA1b that is in neonatal skeletal muscles, SERCA2a (in cardiac muscle) and SERCA2b (in all cell types) (Martin *et al.,* 2002). The sub-type that is the most relevant to this thesis is the cardiac isoform, SERCA2a (Periasamy *et al.,* 2008). Elevated Ca^{2+} levels in the cytosol are toxic to cardiac cells; therefore SERCA2a regulation is critical in maintaining normal physiology of the cardiac muscle. In fact, dysregulation of SERCA2a has been reported in several cardiac diseases like HF (Periasamy *et al.,* 2008; Lipskaia *et al.,* 2010, Park and Oh, 2013). The major regulator of SERCA2A in ventricular myocytes is PLN whereas in atrial myocytes and PVCs is SLN (Periasamy *et al.,* 2008, Park and Oh, 2013). In dephosphorylated states, both PLN and SLN act as inhibitors but release their inhibition when they get phosphorylated by Protein Kinase A (PKA) and CAMKII. As a consequence, Ca^{2+} transport increases. One of the effects of β adrenergic stimulation is through phosphorylation of PLN in ventricular myocytes or SLN in atrial myocytes or PVCs. SERCA2a is regulated not only through the phosphorylation states of PLN or SLN but also through their expression levels. Down-regulation of PLN and SERCA2a in HF has been correlated with diastolic and systolic dysfunction (Bhupathy *et al.,* 2007, Lipskaia *et al.,* 2010). Similarly, reduced SLN protein expressions have been reported previously in human AF that resulted in an enhanced SR Ca^{2+} uptake (Shanmugam *et al.,* 2011).

In summary, down-regulation of SERCA2a mRNA / protein levels and altered phosphorylation of the channel is often reported in cardiac diseases like HF (Bhupathy *et al.,* 2007, Lipskaia *et al.,* 2010, Shanmugam *et al.,* 2011). Hence, dysregulation of SERCA2a affects the SR Ca^{2+} handling and may lead to pathology. In this study, SERCA2a mRNA was quantified to elucidate whether the abnormal SR Ca^{2+} handling observed in HU-treated cells arose as a result of SERCA2a dysregulation (Chapter 5). Although the effects of SERCA2a deterioration / malfunction has been well documented in animal models, so far similar studies in humans are still infrequent and more studies are needed.

1.5.4.5. Na^+ / Ca^{2+} exchanger

NCX is one of the mechanisms for the extrusion of Ca^{2+} out of cardiac myocytes. In the hearts of larger mammals like rabbits, dogs and humans, ~ 30 % of cytosolic Ca^{2+} is eliminated via NCX. In contrast, in mice and rats, up to 10 % of the Ca^{2+} is removed by NCX (Bassani *et al.,* 1994, Pieske *et al.,* 1999, Bers 2008). In its forward electrogenic mode, NCX extrudes 1 Ca^{2+} in exchange of 3 Na^+, thus generating a net inward electrical current that depolarises membrane potential. Previously, the NCX has been shown to play a role in Ca^{2+} homeostasis in PVCs, which will be described in detail later (Patterson *et al.,* 2006, Namekata *et al.,* 2009, Okamoto *et al.,* 2012). NCX expression has been shown to be upregulated in AF, thus generating early afterdepolarizations (EADs) and delayed afterdepolarizations (DADs) and promoting arrhythmias (Patterson *et al.,* 2006, Venetucci *et al.,* 2007, Namekata *et al.,* 2009, Okamoto *et al.,* 2012) as described later in this thesis.

1.5.4.6. Plasma membrane Ca^{2+} ATPase

Another mechanism that is involved to the task of reducing elevated cytosolic Ca^{2+} levels to physiological basal Ca^{2+} levels in a cardiac myocyte is PMCA as briefly mentioned previously. The main role of PMCA is to remove cytosolic Ca^{2+} but in cardiac cells and most other cells; this role is quantitatively surpassed by other most powerful systems, i.e. SERCA and NCX (Bassani *et al.,* 1994, Pieske *et al.,* 1999, Bers *et al.,* 2008). The PMCA channel has four isoforms which are PMCA1 – PMCA4. The two isoforms (PMCA1 and PMCA4) operate in all tissues while the other two (PMCA2 and PMCA3) are expressed in specialized tissues, such as the muscle and the brain (Crouch and Schulte, 1996, Guerini *et al.,* 2005). Structurally, the channel contains 10 transmembrane domains and a cytosolic portion that contains A, N and P cytosolic domains. Unlike other Ca^{2+}-ATPases, the PMCA channels has a 40-residue-long domain responsible for the binding of activatory phospholipids and a long C terminal tail (120 residues) that contains a CaM binding site, PKA site and two PKC sites (Chakraborti and Dhalla, Chapter 1, 1st ed. 2016). Functionally, PMCA transfers one Ca^{2+} across the plasma membrane using energy from ATP hydrolysis (Guerini *et al.,* 2000). Under resting conditions, the C-terminal tail is proposed to interact with other cytosolic domain to maintain the channel in auto-inhibition mode. Upon CaM binding, the channel undergoes a conformational change and freeing the channel from auto-inhibition (Chakraborti and Dhalla, Chapter 2, 1st ed. 2016).

Therefore, the binding of CaM to the channel is one of the ways the opening and closing of the channel is regulated depending on Ca^{2+} levels. In addition to CaM binding, PMCA contains sites for phosphorylation and therefore PKC and PKA can also activate the channel, but the physiological relevance of this is still unclear (Chakraborti and Dhalla, Chapter 2, 1st ed. 2016).

1.5.4.7. The role of mitochondria in Ca^{2+} homeostasis

In cardiac myocytes, mitochondria occupy 30 % - 40 % of the total cell volume reflecting the huge demands of the contractile machinery and some pumps like SERCA2a and PMCA for ATP (Skepper and Navaratnam, 1995; Piquereau *et al.,* 2013; Yang *et al.,* 2013). It has been suggested previously that apart from providing ATP, cardiac mitochondria may also play an important role in maintaining normal Ca^{2+} homeostasis (Drago *et al.,* 2012, Liu *et al.,* 2013, Boyman *et al.,* 2014, Santulli *et al.,* 2015). Mitochondria are known to accumulate Ca^{2+} during a period of cytosolic Ca^{2+} elevations; however, their role during Ca^{2+} cycling and buffering still remains controversial (Dedkova and Blatter 2013). Some studies (Maack *et al.*, 2006, Drago *et al.,* 2012) showed that mitochondria significantly contributed to the systolic Ca^{2+} rises in a beat-to-beat, whereas others (Lu *et al.,* 2013, Boyman *et al.,* 2014) found no significant contribution in Ca^{2+} by the mitochondria. The large negative potential (~ - 180 mV) across the inner mitochondrial membrane (IMM), creates a huge driving force for Ca^{2+} into the mitochondrial matrix from the cytosol. Mitochondria possess an elegant system of Ca^{2+} uptake and extrusions that allows the regulation of the mitochondrial Ca^{2+}concentration. The best established method for mitochondrial Ca^{2+} uptake is through a selective channel called mitochondrial Ca^{2+} uniporter (MCU) down electrochemical gradient (Baughman *et al.,* 2011, De Stefani *et al.,* 2011). Depending on the experimental conditions, the open probability of the channel can range from as high as 0.9 to as low as 0.09 with a single channel conductance of ~ 6 -7 pS (Baughman *et al.,* 2011). It is estimated that there are ~ 200 MCU channels per mitochondrion in cardiac myocytes. Previous studies using a knockdown of the MCU showed an increase in the amplitude of cytosolic Ca^{2+} transients which may suggest a role of Ca^{2+} buffering by the mitochondria in cardiac myocytes (Drago *et al.,* 2012). The MCU is regulated by a number of activators and inhibitors which include divalent cations, adenine nucleotide, lanthanides and ruthenium compounds. RU360 is used experimentally to inhibit MCU. Apart from the MCU, other pathways of Ca^{2+} uptake have been proposed which are rapid mode of Ca^{2+} uptake (RaM), the mitochondrial ryanodine receptor type 1 (mRyR1) and the recently proposed leucine-zipper-EF-hand-containing transmembrane protein 1 (LETM 1). All the other pathways for Ca^{2+} uptake in the mitochondria still remain controversial and require further investigations see review (Dedkova and Blatter 2013).

Just like in the SR, the mitochondrial Ca^{2+} influx must be balanced with the mitochondrial Ca^{2+} efflux. Mitochondrial Ca^{2+} efflux is believed to depend on mitochondrial Na^{+} -Ca^{2+} exchanger (NCLX) and Na^{+}-proton exchanger (NHE). It has been suggested that NCLX extrude Ca^{2+} from the matrix as long as the Na^{+} that enters has a way to exit (Palty *et al.,* 2010). This is thought to be mediated by NHE. During Na^{+} overload, this balance can be compromised resulting in the production of reactive oxygen species (ROS) which is detrimental to the cell and will result in energy deficient (Nissim *et al.,* 2017). A number of drugs like benzodiazepines have been shown to inhibit NCLX (Czyż and Kiedrowski 2003, Ruiz *et al.,* 2014). The majority of the data supports that NCLX is electrogenic as it exchanges 3 Na^{+} for 1 Ca^{2+}. As an electrogenic, mitochondrial Ca^{2+} efflux will depolarise mitochondrial membrane potential by allowing Na^{+}, this should reduce mitochondrial Ca^{2+} influx (Lukyanenko *et al.,* 2009). The last of the system that is thought to be also involved in mitochondrial Ca^{2+} efflux is through an increase permeability of the IMM to ion and solutes with molecular weight of up to ~ 1.5 kDa, this increase in permeability is known as the opening of mitochondrial permeability transition pore (mPTP) (Izzo *et al.,* 2016, Giorgio *et al.,* 2017). The molecular identity of mPTP is still largely unknown, but it has been proposed to contain a voltage and Ca^{2+}-dependent channel, high conductance and cyclosporin A (CsA) sensitive. The channel has been proposed to contain adenine nucleotide translocator (ANT), cyclophilin D (Cyp D), VDAC, hexokinase, creatine kinase, mitochondrial peripheral benzodiazepine receptor, Bcl-2, glycogen synthase and cytochrome c (Zorov *et al.,* 2009). Some of these components of the mPTP that have been proposed are still controversial. The mPTP complex is activated by high matrix (Ca^{2+}), oxidative stress and depolarization but, what still remains controversial, is whether mPTP can serve as a pathway for mitochondrial Ca^{2+} efflux. It should also be mentioned that ageing is also a critical factor contributing to the ability of tissues to resist damaging stress. There is an age-related impairment of the ability of the heart to resist stress, such as during ischaemia / reperfusion injury (Juhaszova *et al.,* 2005, Wohlgemuth *et al.,* 2014, Tocchi *et al.,* 2015). The direct link between mPTP induction and oxidative stress-related cell death in cardiac myocytes reinforces the need for better understanding of the channel to prevent or limit the damage (Dedkova and Blatter 2013, Wohlgemuth *et al.,* 2014).

Additionally, an increase in ROS is due to mitochondrial dysfunction which deteriorates during ageing and stressful conditions such as diabetes (Xi *et al.,* 2005, Yang *et al.,* 2006). An increase in ROS production has been shown to affect Ca^{2+} homeostasis by modulating the opening of channels that are cysteine rich. The effects of ROS on Ca^{2+} homeostasis will be discussed in detail later on.

1.5.4.8. Mitochondrial size/structure and numbers: their relevance in the cardiac function

Cardiac mitochondria are the organelles responsible for energy in the heart in the form of ATP as mentioned above. Cardiac mitochondria are independent and distinct organelles that are highly organised between myofibres (intermyofibrillar mitochondria), near the nucleus (perinuclear mitochondria) and near the sarcolemma (sarcolemmal mitochondria) (Hoppel *et al.,* 2009). These three sub-types of cardiac mitochondria are labelled in Figure 3.3 in Chapter 3. In this study, only intermyofibrillar mitochondria were analysed. These reside between the myofibres. Alterations in cardiac mitochondrial morphology and dynamics have been documented previously in cardiac diseases as well as in ageing (Feldman and Navaratnam, 1981; Ausma *et al.,* 2001, Furuoka *et al.,* 2001, Hoppel *et al.,* 2009). The deteriorated mitochondria can be enlarged or decreased in size (Feldman and Navaratnam, 1981; Ausma *et al.,* 2001, Gupta *et al.,* 2010), increased / decreased in numbers (Feldman and Navaratnam, 1981, Terman *et al.,* 2003). Another feature of abnormal mitochondria involve changes in the cristae appearance. Cristae are folds of the inner mitochondrial membrane. Most previous studies have shown that disrupted mitochondria appeared to have swollen and misfolded cristae (Furuoka *et al.,* 2001). Therefore, if mitochondria are disorganised, the energy output could be diminished and may result in higher ROS levels and abnormal Ca^{2+} handling that may in turn cause diseases. Hence, to investigate whether mitochondrial numbers and/or size are altered in PVCs during ageing; this study analysed mitochondrial structure by focusing on mitochondrial numbers and sizes in PVCs from 3 month- and 24 month-old mice (Chapter 3).

1.5.5. Local and global Ca^{2+} transients

Ca^{2+} is an almost ubiquitous messenger that is able to regulate a myriad of physiological processes, ranging from fertilisation to cell death (Bootman *et al.,* 2006). This is achieved by the ability of cells to use different mechanisms to modulate the duration, amplitude, frequency and spatiotemporal properties (Berridge 1997, Berridge *et al.,* 1998, Bootman *et al.,* 2006). Because of the differences in Ca^{2+} channels, buffers, Ca^{2+} binding proteins and morphology in cardiac myocytes, a Ca^{2+} signal can arise to be local or global and may develop to an AP in excitable cells, as explained below.

PVCs, atrial and ventricular myocytes can generate local and global Ca^{2+} transients which arise either spontaneously or through a stimulus. Unlike atrial and ventricular myocytes, PVCs have a substantially higher frequency of spontaneous local and global Ca^{2+} transients (Rietdorf *et al.,* 2014, Rietdorf *et al.,* 2015). In an unstimulated cardiac myocyte, a local Ca^{2+} transient can spontaneously arise, lasting just 10 – 100 ms and be confined to an area of ~ 2 µm (Cheng *et al.,* 1993, Cheng and Lederer 2008). These spontaneous local Ca^{2+} events arise with local openings of RyRs from one cluster or different clusters of RyRs to form a Ca^{2+} releasing unit (CRU). CRU is a cluster of RyRs in the SR membrane (Cheng and Lederer, 2008). The kinetics of the local Ca^{2+} release events can be modulated by the opening of RyRs: the frequency of local Ca^{2+} release events increases with a higher opening probability of RyRs. The frequency of local Ca^{2+} release events can also be increased by the activity of VOCCs. Their opening allows an influx of Ca^{2+} from extracellular medium down electrochemical gradient. Interestingly, depolarisation on itself is not enough to evoke a local Ca^{2+} release. This is supported by studies where depolarisation failed to evoke local Ca^{2+} events when extracellular Ca^{2+} was removed or replaced with Ba^{2+}, showing that Ca^{2+} is needed to stimulate RyRs openings and initiate local Ca^{2+} release (Cheng and Lederer 2008, Maxwell and Blatter 2012, Sato *et al.,* 2014).

During ageing and in diseased states, local and global Ca^{2+} events are modulated and may results in arrhythmias or diminished cardiac output as discussed later (Blatter *et al.,* 2003, Cheng and Lederer 2008, Brochet *et al.,* 2012). PVCs studied in this thesis show local and global Ca^{2+} release events, which can change during ageing, repeated electrical field stimulation (EFS), pharmacological interventions and ROS levels as explained later in Chapters 4 and 5.

1.5.6. Differences in excitation-contraction coupling between PVCs, atrial and ventricular myocytes

The three types of cardiac myocytes vary in their ultrastructure, described below, resulting in different spatiotemporal patterns of Ca^{2+} signalling observed. One of the most obvious differences between PVCs, atrial and ventricular myocytes is the absence or presence of T-tubules. T-tubules are invaginations of the sarcolemma of cardiac myocytes that occur at each Z-line. T-tubules bring VOCCs in close proximity to RyR2s and mitochondria and therefore an AP on the cell surface can simultaneously propagated to non-junctional RyRs that results in a faster global response. The example of this scenario is shown below in Figure 1.8 where the presence of T-tubules in a ventricular myocyte resulted in a faster response as denoted by the orange curve. Most atrial myocytes lack T-tubules whereas ventricular myocytes contain an extensive T-tubules system, which can be revealed using membrane dyes such as di-8-ANNEPS (Lyon *et al.,* 2009, Dibb *et al.,* 2013). However, recent evidence shows that T-tubules are found in atrial myocytes from larger mammals and the extent of T-tubular network is thought to be correlated with cell width; (Richards *et al.,* 2011, Frisk *et al.,* 2014). As the cell width is found to be higher in larger mammals, more atrial myocytes have T-tubules to facilitate faster propagation (Richards *et al.,* 2011). Most atrial myocytes posses extensive “Z tubules” which are formed from internal SR membranes, but not the sarcolemma and therefore contains non-junctional RyRs which are not in close proximity with VOCCs (Bootman *et al.,* 2006).

Just like in ventricular myocytes, immunostaining for RyRs in atrial myocytes revealed that most of the RyRs are located around the Z-lines of the sarcomeres (Bootman *et al.,* 2006).

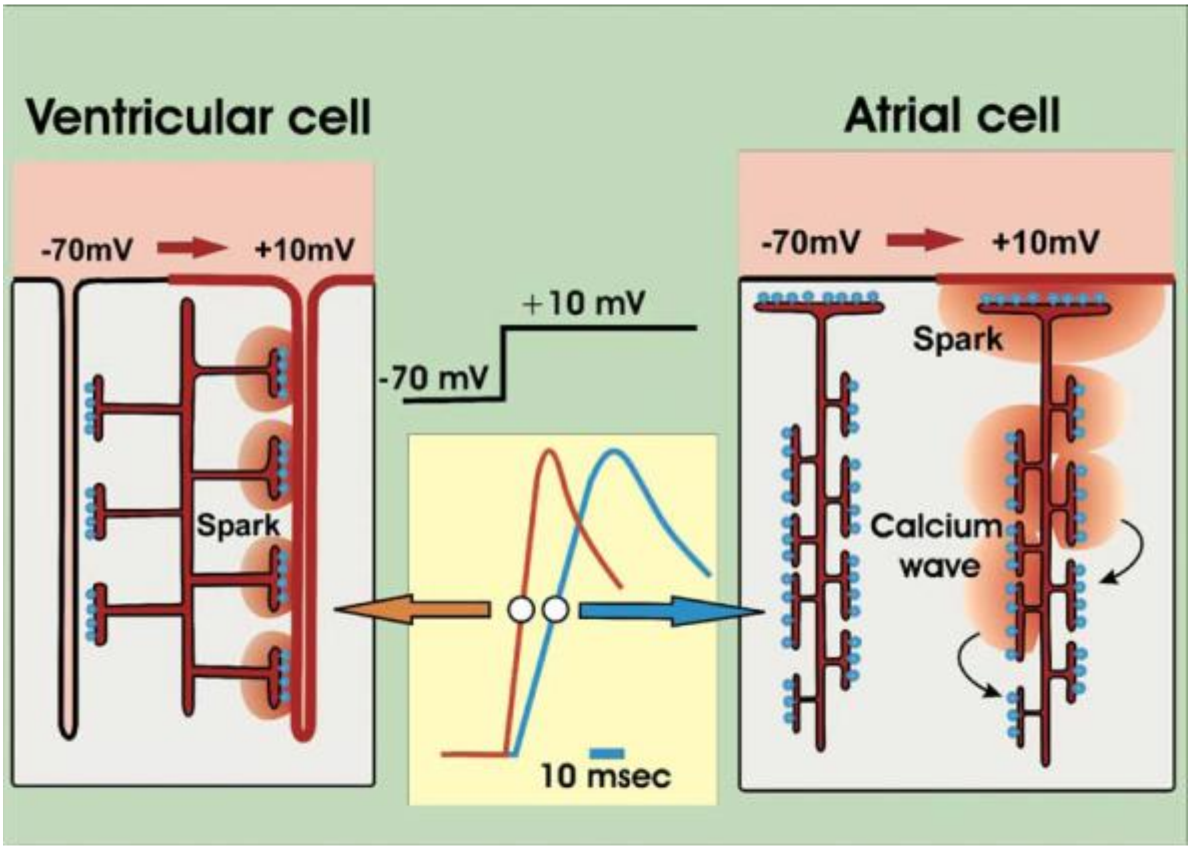

Figure 1.8. Different modes of Ca^{2+} signaling in cardiac myocytes. In ventricular myocytes, an AP is propagated down the T-tubules inside the cell to simultaneously activate Ca^{2+} sparks in all non-junctional zones, resulting in a faster efficient global Ca^{2+} transients orange curve). In atrial myocytes, the lack of T-tubules means the signals reside at the periphery and slowly propagate inside the cytosol via CICR, resulting in a slower response (blue curve). From (Berridge 2002).

In the absence of T-tubules, VOCCs are only localised at the cell's periphery in close apposition with junctional RyRs, but do not reach deep into the cytosol to contribute to a fast signal propagation. In contrast, the extensive T-tubular network in ventricular myocytes brings VOCCs in close proximity with non-junctional RyRs deep within the cytosol (Figure 1.8). T-tubules in ventricles allow local Ca^{2+} transients sites, which are deep within the cytosol, to be recruited during an AP, thus resulting in fast, synchronised global responses (Figure 1.8 and Table 1.1).

	PVCs	**Atrial myocytes**	**Ventricular myocytes**
T-tubules	Mostly lack T-tubules (Tsuneoka *et al.,* 2012, Rietdorf *et al.,* 2014).	Mostly lack T-tubules but are found in atrial myocytes from larger mammals (Clarke *et al.,* 2011, Frisk *et al.,* 2014).	Prominent T-tubular network (Lyon *et al.,* 2009, Frisk *et al.,* 2014).
Connexins	Express Cx40, Cx43 and Cx45 (Yamamoto *et al.,* 2006, Kugler *et al.,* 2017).	Express mainly Cx40 and to a lesser extent Cx43 (Sun *et al.,* 2008).	Express mainly Cx43 (Ou *et al.,* 2005; Tribulova *et al.*, 2005).
APs	Less negative resting membrane potential compared to atrial and ventricular myocytes (~ -65 mV) with no plateau (Chen *et al.,* 2002, Ehrlich *et al.,* 2003, Okamoto *et al.,* 2012). AP duration < 200 ms. Less negative resting membrane potential may potentiates extra APs that may result in arrhythmias.	Resting membrane potential is ~ - 75 mV, lacks a pronounced plateau (Chen *et al.,* 2002, Ehrlich *et al.,* 2003, Okamoto *et al.,* 2012). AP duration ~ 150 ms.	Resting membrane potential is ~ - 75 mV with a distinctive plateau (Chen *et al.,* 2002, Ehrlich *et al.,* 2003, Okamoto *et al.,* 2012). AP duration ~ 200 ms.
Excitation-contraction coupling	Higher frequency of spontaneous global activity compared to atrial and ventricular myocytes (Rietdorf *et al.,* 2014, Rietdorf, *et al.,* 2015). Higher spontaneous activity may facilitate arrhythmias.	Lower frequency of spontaneous global activity compared to PVCs (Berridge 2002).	Lower frequency of spontaneous global activity compared to PVCs (Berridge 2002).

Table 1.1. Comparison of the structural, electrical and Ca^{2+} homeostasis features in PVCs, atrial and ventricular myocytes.

Atrial myocyte Ca^{2+} signals initiate at the periphery immediately after depolarisation but are not propagated deep into the cytosol via T-Tubules. From this point on, factors like the SR Ca^{2+} content and the presence of agents that increase the force of contraction of the heart, determine whether the signal will propagate further in the cytosol (Bootman *et al.,* 2006).

PVCs have been proposed to operate the same excitation contraction coupling machinery as atrial and ventricular myocytes (Tsuneoka *et al.,* 2012, Rietdorf *et al.,* 2014). Structurally, just like atrial myocytes, most PVCs lack an extensive T-tubule system (Leem *et al.,* 2006, Rietdorf *et al.,* 2014). However, Ca^{2+} signaling in PVCs is thought to resemble that of ventricular myocytes rather than atrial myocytes; PVCs show global Ca^{2+} transients (i.e. ventricular-like) rather than peripheral Ca^{2+} signals (i.e. atrial-like) (Rietdorf *et al.,* 2014), these features are compared in Table 1.1 above. The underlying reasons why PVCs are structurally similar to atrial myocytes, but Ca^{2+} signals that are akin to those in ventricular myocytes are not yet completely understood.

1.6. Autophagy

Autophagy is a housekeeping process by which cells degrade dysfunctional organelles, long-lived proteins, non-protein targets like lipids and carbohydrates and produces ATP (Deter and De Duve 1967, Lilienbaum 2013, Wang and Wang 2015).

A basal level of autophagy occurs constitutively in cells and contributes to the cellular homeostasis in eukaryotic organisms (Deter and De Duve 1967). However, in response to stress like nutrient starvation, mitochondrial depolarisation, the presence of toxic protein aggregates or mechanical damage, autophagy can be upregulated (Graef and Nunnari, 2011, Komatsu *et al.,* 2005) and is generally considered to act as a pro-survival mechanism (Fulda, 2012). In contrast, during ageing (in the cardiac system) autophagy is generally downregulated (Kurz *et al.,* 2007; De Meyer *et al.,* 2010, La Rocca *et al.,* 2012).

Three different types of autophagy can be distinguished: macroautophagy, microautophagy and chaperone-mediated autophagy (Klionsky, 2005; Kurz *et al.,* 2007). Work in this thesis in Chapter 5 focussed on the process of macroautophagy, and the term 'autophagy' refers solely to macroautophagy.

The process of autophagy, and tools for studying it, are illustrated in Figure 1.9. During autophagy, molecules and organelles that are targeted for degradation become surrounded by a double membrane. Once this membrane is closed and forms a vesicle around the molecules / organelles, it is called autophagosome. Mature autophagosomes fuse with lysosomes. The resulting autolysosome has an acidic pH, and the actual digestion takes place by acidic hydrolases. Autolysosomes are degraded and release nutrients like amino acids and fatty acids for use by the cell.

As a result, the total number of autophagosomes present in a cell at any given time is determined by the rate of autophagosome formation and autophagosome degradation. This is described by term 'autophagic flux' and is a more accurate measure for the state of a cell than the level of basal autophagy.

Autophagy in cells can be induced by mammalian target of Rapamycin (mTOR) inhibitors like rapamycin or pp242, or by starvation. To measure autophagic flux, it is necessary to also provide evidence that formation and degradation of the novel autophagosomes is taking place. This can be done using the chemicals shown in Figure 1.9: autophagosome formation can be inhibited by 3-Methyladenine (3-MA) and the degradation can be blocked by bafilomycin A1 or chloroquine. Both drugs inhibit the autophagosome degradation by inhibiting the autophagosome-lysosome fusion (Klionsky *et al.,* 2016).

To measure the autophagic flux in living cells, four counts of the number of autophagosomes are necessary: in the basal state, in presence of PP242 / rapamycin alone (maximum induced level), PP242 / rapamycin + 3-MA (proving that de novo formation is taking place) and PP242 / rapamycin + bafilomycin/chloroquine (proving that degradation is taking place). The expected outcome of each drug application on the number of autophagosomes in a cell is indicated in Figure 1.9.

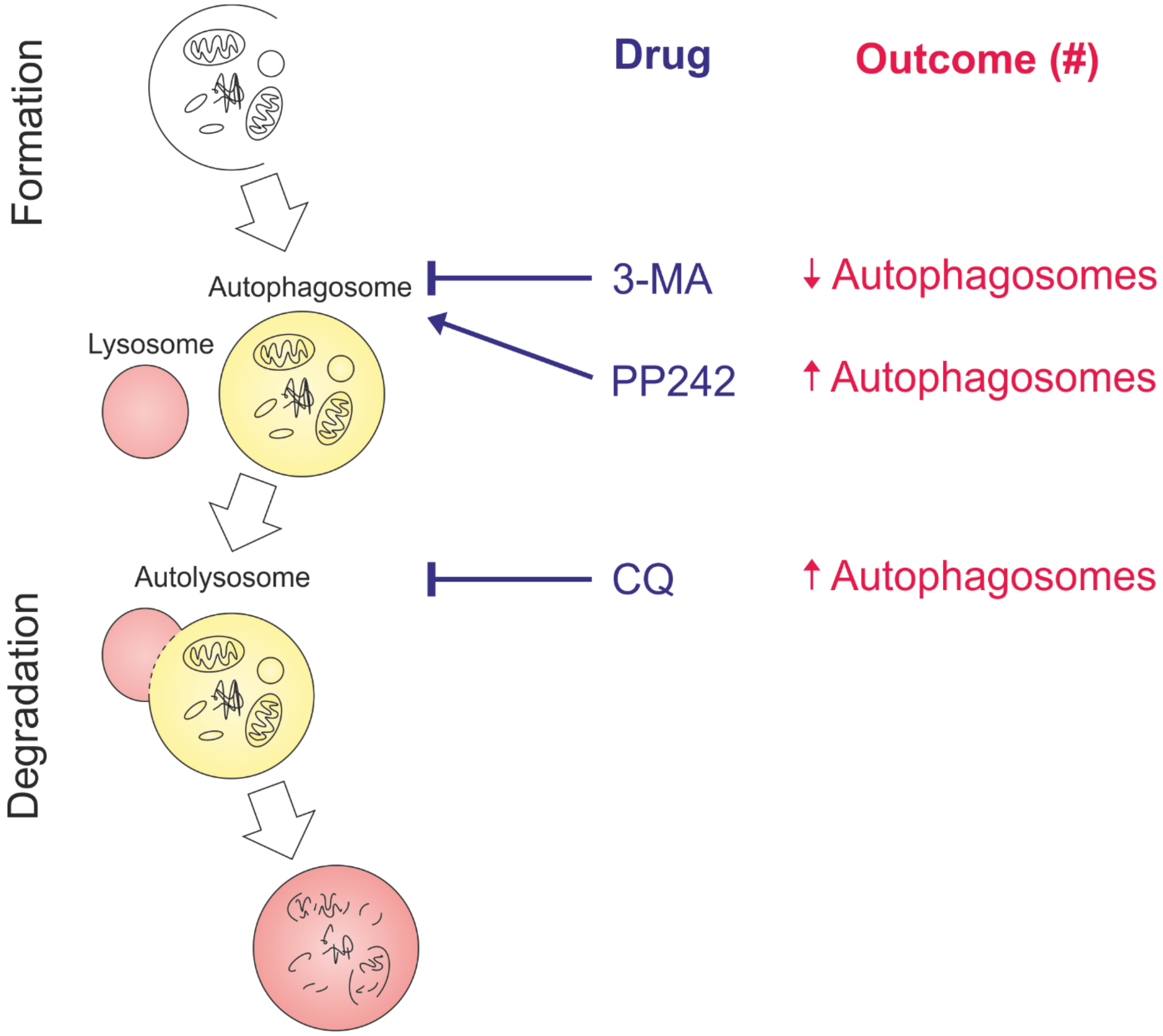

Figure 1.9. The process of autophagy and the tools for studying it. Organelles that are targeted for degradation are enclosed by a double membrane and forms autophagosomes. 3-Methyladenine (3-MA) inhibits the formation of autophagosomes whilst drugs like pp242 induce the formation of autophagosomes. Mature autophagosomes fuse with lysosomes to form autolysosomes before they are being degraded. This process can also be inhibited with drugs like chloroquine, i.e. increases the number of autophagosomes.

1.7. Changes in the heart with disease or age

1.7.1. Atrial fibrillation: general background

Atrial fibrillation (AF) is the most sustained form of a cardiac arrhythmia which is more common in elderly population (Kopecky *et al.,* 1987, Go *et al.,* 2001). AF is characterized by un-coordinated atrial activation with consequent deterioration of atrial mechanical function. It is well established now that ectopic electrical activity originating from pulmonary vein sleeve cells (PVCs) and (Haissaguerre *et al*., 1998, Sueda *et al.,* 2005) initiate AF. Prevalence of AF increases with age; only 0.1 % of AF cases occur in people aged 40 and above, 6 % in people over 65 years, 10 % in people over 80 years and above (Hayashi *et al.,* 2002, Nattel *et al.,* 2008). Prevalence of AF varies worldwide depending on the geographical location as shown below in Figure 1.10 (Schotten *et al.,* 2011, Chugh *et al.,* 2014, Shehab *et al.,* 2017).

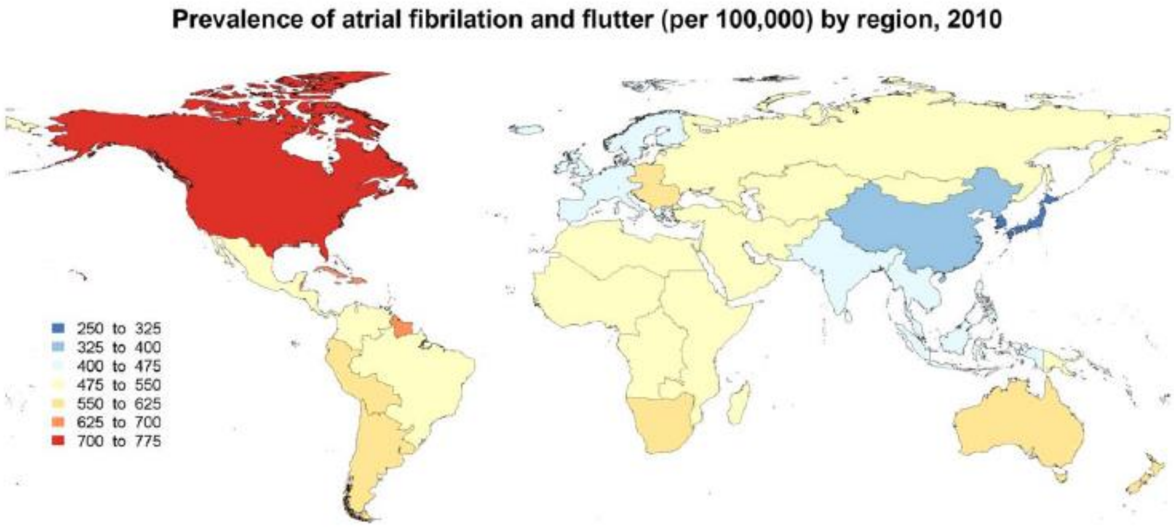
Prevalence of atrial fibrilation and flutter (per 100,000) by region, 2010

Figure 1.10. World map showing age-adjusted rates (per 100,000 populations) of AF. Adapted from (Chugh *et al.,* 2014).

In 2010, AF cases are reported to be the highest in North America. The AF incidence rates in North America for both men and women are 264.5 and 196.3 *per* 100000 respectively. The lowest cases are estimated in the Asia-Pacific region for both men (33.8 *per* 100000) and women (19.8 *per* 100000) as seen in Figure 1.9 above (Chugh *et al.,* 2014).

With our ever increasing ageing population, the prevalence of age-dependent cardiac diseases like AF will continue to rise in the future. In the USA, the prevalence of AF is estimated to escalate from 1.2 million cases in 2010 to 2.6 million cases in 2030 and to 5.6 million by 2050 (Colilla *et al.,* 2013). For unknown reasons, most studies find that AF is more common in men than women (Lloyd-Jones *et al.,* 2004, Heeringa *et al.,* 2006, Stefansdottir *et al.,* 2011, Chugh *et al.,* 2014).

Although AF is not life threatening in itself, it contributes significantly to morbidity and mortality. AF is associated with increased risk of deaths, thrombo-embolic events and HF. Often, AF patients suffered from reduced quality of life, reduced exercise capabilities and left ventricular dysfunction (Cai *et al.,* 2013). Over 70 % of AF patients have an underlying heart disease and nearly 20 -25 % of all strokes are caused by AF (Schotten *et al.,* 2011; Shehab *et al.,* 2017). A recent study looking at AF as cause of deaths in England between 1995 and 2010 showed that when AF is regarded as a contributing cause of deaths, the other common contributing causes of deaths were stroke, pneumonia and myocardial infarction (Duncan *et al.,* 2014). Additionally, AF is associated with a range of other health complications, for example, tachycardiomyopathy, hypertension obesity and diabetes mellitus (Schotten *et al.,* 2011).

Although mortality from other cardiovascular diseases have fallen considerably over the last 20 years or so, mortality from AF has increased steadily in both men and women as seen in Figure 1.11 below (Chugh *et al.,* 2014, Duncan *et al.,* 2014). This is partly because of our increasing ageing population as more people live longer to develop AF and highlight the need to better treatments.

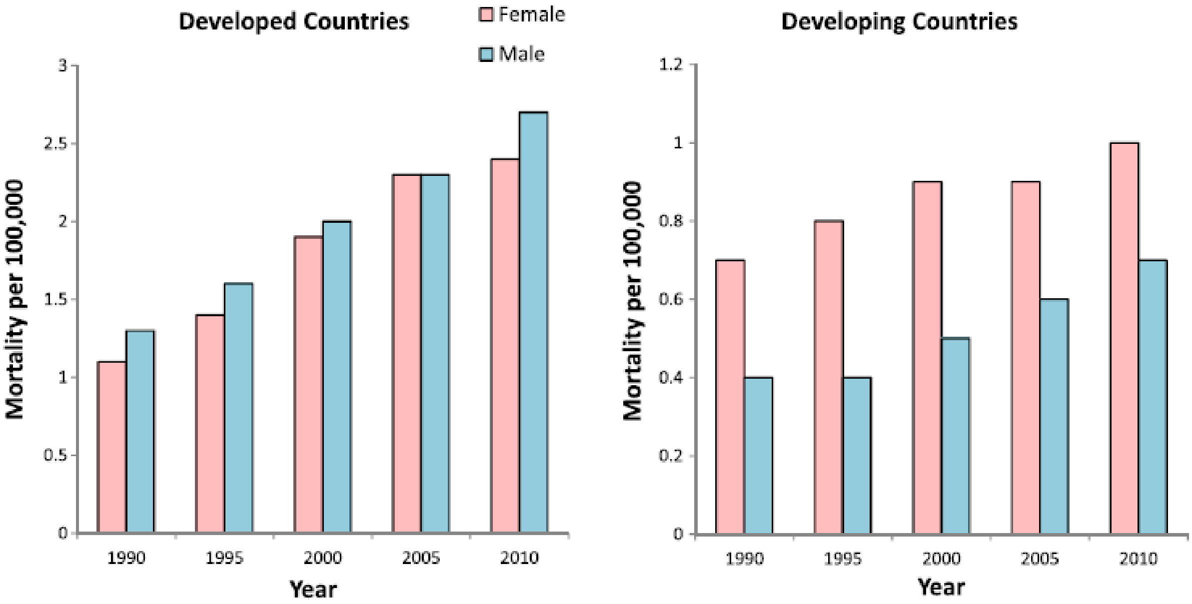

Figure 1.11. Mortality associated with AF in both sexes in developed *vs.* developing world over the last two decades. Mortality rate was higher in men than women in developed countries but higher mortality rates have been reported in women than men in developing countries. From (Chugh *et al.,* 2014).

AF diagnosis relies firstly on a physical examination and by performing an electrocardiogram (ECG). When AF episodes first occur, often they self-terminate and therefore might not be present when a doctor examines the patient and therefore complicates the diagnosis. If symptoms are present during when a doctor performs physical examination, often, irregular heart sounds or an irregular pulse can raise suspicion of AF. This, combined with clinical symptoms, helps the diagnosis. ECG traces from AF sufferers usually lack distinct P waves because of in-effective atrial contraction. Additionally, ECG traces from AF patients will often show irregular intervals, which lack repetitive patterns as shown in Figure 1.12 below:

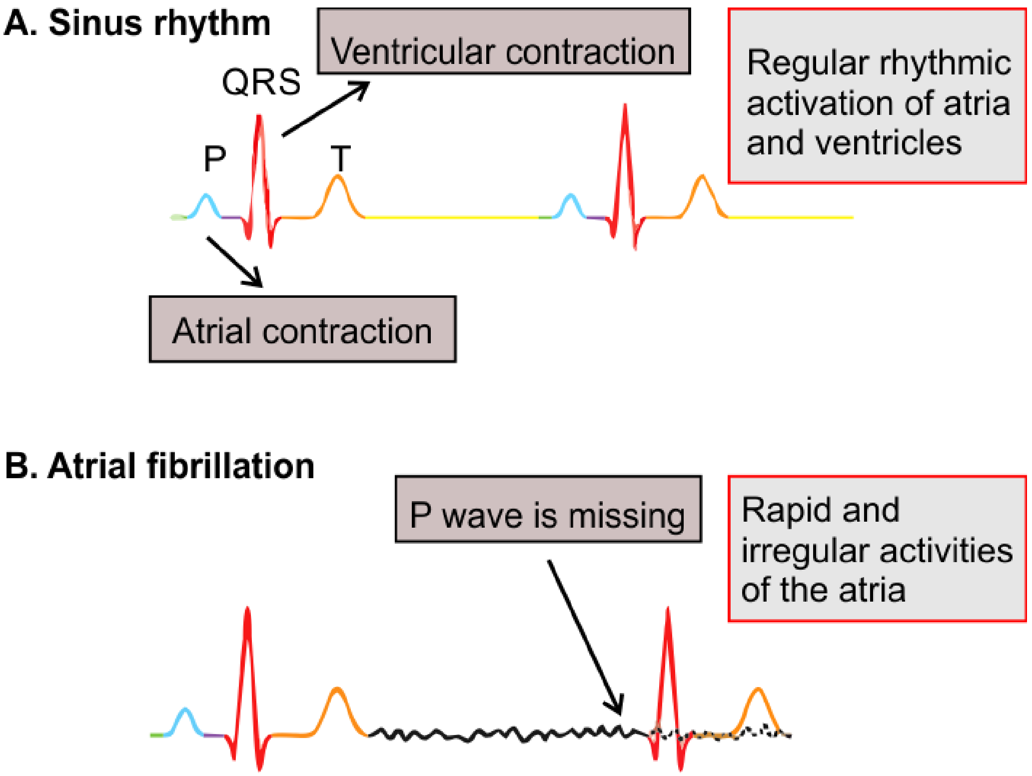

Figure 1.12. Traces illustrating ECG traces from a healthy individual (sinus rhythm) and an individual with AF. The top trace shows an ECG trace of a heart beating in sinus rhythm with a clear P wave, QRS complex and a T wave. In contrast, the bottom trace from an AF patient shows an ECG lacking a P wave because of irregular atrial contraction (modified from Wakili *et al.,* 2011).

Clinically, it is acceptable to distinguish 5 types of AF based on presentation and the duration of arrhythmia. These 5 types of AF are **first-diagnosed**, **paroxysmal**, **persistent**, **long-lasting persistent** and **permanent** (Camm *et al.,* 2010). Every patient who presents AF symptoms for the first time is considered having a **first-diagnosed AF** regardless of the symptoms and severity of arrhythmias. A patient is classified as having **paroxysmal AF** when AF episodes come and go and can last up to 7 days before self-terminating. Most of these episodes usually stop within 48 hours. **Persistent AF** refers to AF episodes that continue for longer than 7 days and can only be terminated by either a drug or direct current cardioversion (cardioversion means termination of AF by applying electrical shock to stop the arrhythmia and allow the normal pacemaker to resume function). **Long-**

standing persistent AF is when episode lasts longer than a year and a suitable control strategy is needed. **Permanent AF** is when episodes are present all the time and both a patient and a physician accept that sinus rhythm is no longer achievable and treatments to convert to sinus rhythm have failed (Camm *et al.,* 2010). Sinus rhythm is a term given to the normal rhythmical contraction of the heart where electrical stimuli are initiated at the SA node to evoke the cardiac cycle.

Management of AF is mainly aimed at relieving the symptoms and preventing complications of diseases associated with AF, like the risk of having a stroke. To prevent the formation of blood clots, daily intake of blood-thinning drugs like warfarin and aspirin are usually prescribed to AF patients. After anti-coagulation, anti-arrhythmic drugs like flecainide, carvedilol and verapamil are often used to prevent arrhythmias; however, administration of these drugs may vary depending on the underlying cardiovascular diseases of the patient (Camm *et al.,* 2010, Nottingham 2010). There are number of ways to classify anti-arrhythmic drugs but the most common way is the Vaughan Williams classification (1970) that categorises anti-arrhythmic drugs with respect to their mechanism of action (target), as shown in Table 1.2.

Class	**Mechanism of action**	**Rate *vs.* rhythm**	**Examples**	**Risks**
Class I (class IA, class IB, class IC)	Sodium-channel blockers	Rhythm control	Disopyramide, Quinidine (class 1a), Lidocaine, Mexiletine (class 1b), Flecainide, Propafenone (class 1c)	Hypotension, slowing of the ventricular rate, prolongation of the QT interval, worsening of heart failure, mortality
Class II	Beta-blockers	Rate control	Bisoprolol, Atenolol, Carvedilol, Propranolol	Slow heartbeat, weight gain, may trigger asthmatic attacks
Class III	Potassium channel blockers	Rhythm control	Amiodarone, Dronedarone, Sotalol	Systolic heart failure, hypokalaemia, moderate renal dysfunction, increased mortality
Class IV	Calcium channel blockers	Rate control	Diltiazem, verapamil	Slow heart rate, low blood pressure
Class V	Sodium-potassium ATPase blocker	Rate control	Digoxin	Effective at rest and not during exercise, may interact with other drugs

Table 1.2. Vaughan Williams classification of anti-arrhythmic drugs (1970).

Class IA (Quinidine and Disopyramide) are effective in AF but have fallen out of favour due to their adverse effects including worsening of HF and increased mortality as presented in Table 1.2 above (Shukla and Curtis 2014). Class IC drugs like Flecainide are recommended for AF patients without structural heart disease. Class III drugs like amiodarone and Sotalol have been shown to be effective on restoring sinus rhythm by prolonging the latencies between APs and preventing spontaneous electrical depolarisations that are pro-arrhythmic.

Anti-arrhythmic drugs have been used extensively to manage AF but one should consider carefully the type of AF and associated underlying diseases before choosing a drug. Although these drugs are effective, they have various adverse effects, listed in Table 1.2, which reinforce the need for better pharmacological means. A number of drugs are now in clinical trials which have been shown to be effective in restoring sinus rhythm. Vernakalant which has recently been approved in Europe as an effective and selective class III anti-arrhythmic drug inhibits potassium channels in the atria and has minimal effects on the ventricles, leading to less pro-arrhythmic risks (Tsuji and Dobrev 2013). Vernakalant has also been shown to reduce pro-arrhythmic events in PVCs. In efficacy studies, Vernakalant was also found to be more potent than the most widely prescribed class III anti-arrhythmic drug; amiodarone (Tsuji and Dobrev 2013). Another drug that is currently being tested is JTV-519 / K201 which was shown to attenuate inducible AF in animals by reducing RyR2-induced Ca^{2+} leak. It could potentially be used in the treatment of AF (Chen *et al.,* 2008, Dobrev *et al.,* 2012). JTV-519 has been tested in AF patients and was in phase II clinical trials but has had little success. Although JTV-519 affects mainly RyR2, it has been shown previously to have other targets and therefore further studies are needed (Kumagai *et al.,* 2003). Several other drugs are being tested to treat AF which are now at the stage of pre-clinical or in clinical trials with a range of actions from inhibiting RyR2 to modulating gap junctions (Dobrev *et al.,* 2012).

The major surgical treatment for AF is catheter ablation, which has been used to treat heart rhythm disorders for over two decades (Ames and Stevenson 2006). Catheter ablation involves inserting two long thin tubes (catheters) usually via the groin, which are then guided through the blood vessels into the heart. A mapping catheter is used to identify atrial regions that show ectopic activity (e.g. the development of spontaneous action potentials (AP)), which are then targeted for ablation as illustrated in Figure 1.13.

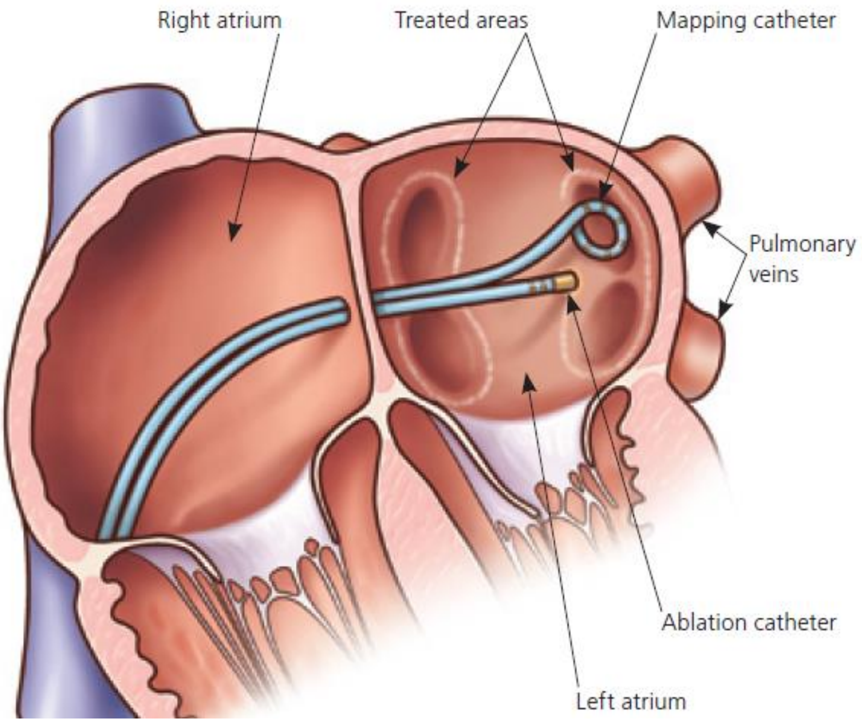

Figure 1.13. Catheter ablation treatment in AF. Two catheters are inserted from the groin and guided through blood vessels to the right atrium. They then need to puncture the atrial septum to enter the left atrium, in which the areas that trigger arrhythmias are usually found. Often those areas are in the pulmonary veins (labelled above as treated areas). The burning scars prevent ectopic activities arising from the PVCs to signal back into the atria, triggering AF (From Shapira *et al.,* 2009).

The catheters need to puncture the inter-atrial septum, which is one of causes of the side-effects and risks during the procedure. A radiofrequency electrical current is applied through the catheter to burn the targeted areas and electrically isolate the pulmonary veins from the left atrium (Figure 1.13). It has been reported that electrical ablation is successful in maintaining sinus rhythm for over a year in 90 % of AF patients, depending on the severity and the type of AF (Ames and Stevenson 2006). Unfortunately, the success rate is low for patients who have had the disease for many years, and for patients with underlying heart diseases (Ames and Stevenson 2006). Also, recurrences have been reported in 15 % - 45 % of the cases and could cause serious complications like pulmonary vein stenosis, (De Maat *et al.,* 2014, Nalliah *et al*., 2015). Repeated ablations are sometimes necessary to fully stop AF from re-occurring.

Our understanding of the pathophysiology of AF has improved substantially over the past years mainly through an increased awareness of atrial remodelling (the term used for phenotypic alteration of the atrial chambers during disease). The mechanisms thought to be involved in maintaining AF are electrical and structural remodelling together with abnormal Ca^{2+} handling in both PVCs and atrial myocytes (Hove-Madsen, *et al.,* 2004, Neef *et al.,* 2010). Surprisingly, little is known about age-dependent changes in structure and Ca^{2+} homeostasis in PVCs and atrial myocytes, both of which contribute to the maintenance of AF.

1.7.2. The cardiac action potential

The main focus of this thesis investigated changes in the ultrastructure and Ca^{2+} homeostasis in cardiac myocytes during ageing. However, in order to understand the arrhythmogeneic events which will be described later, it is necessary to look at the cardiac AP, the channels and currents that maintain it and the differences of the AP characteristics in-between cardiac cells. The cardiac AP, which is generated by the coordinated openings and closure of ion channels, is much more complex than the AP in nerves and skeletal muscles. In the heart, APs last several 100 milliseconds (ms) and consist of several phases. The resting membrane potential of atrial and ventricular myocytes is around -75 mV whereas PVCs have a less negative resting membrane potential of around – 65 mV (Chen *et al.,* 2002, Ehrlich *et al.,* 2003, Okamoto *et al.,* 2012).

Ventricular APs which are different to those in atrial myocytes; they are longer in durations. Ventricular APs are also similar to purkinje fiber AP except they are smaller and lack pacemaking activity. APs in the SA and AV node cells are similar to atrial APs but they lack a plateau and are much smaller. PVCs AP are thought to be similar to an atrial AP (see Figure 1.14). Ventricular APs include distinct 5 phases which include a large upstroke (phase 0), transient repolarization (phase 1), a plateau (phase 2), repolarization (phase 3) and resting level (phase 4). These 5 distinct phases and the contributing currents and channels are labelled in Figure 1.13. The rate of depolarisation (an initial upstroke phase during an AP) is determined by the rate at which Na^+ ions enter the cytosol and differes between the various cell types found in the heart. In cells whose APs relies on Na^+ channel openings, e.g. cardiac myocytes, skeletal muscles and neuronal cells, initial depolarizing currents are large, develop very fast but also show a quick inactivation.

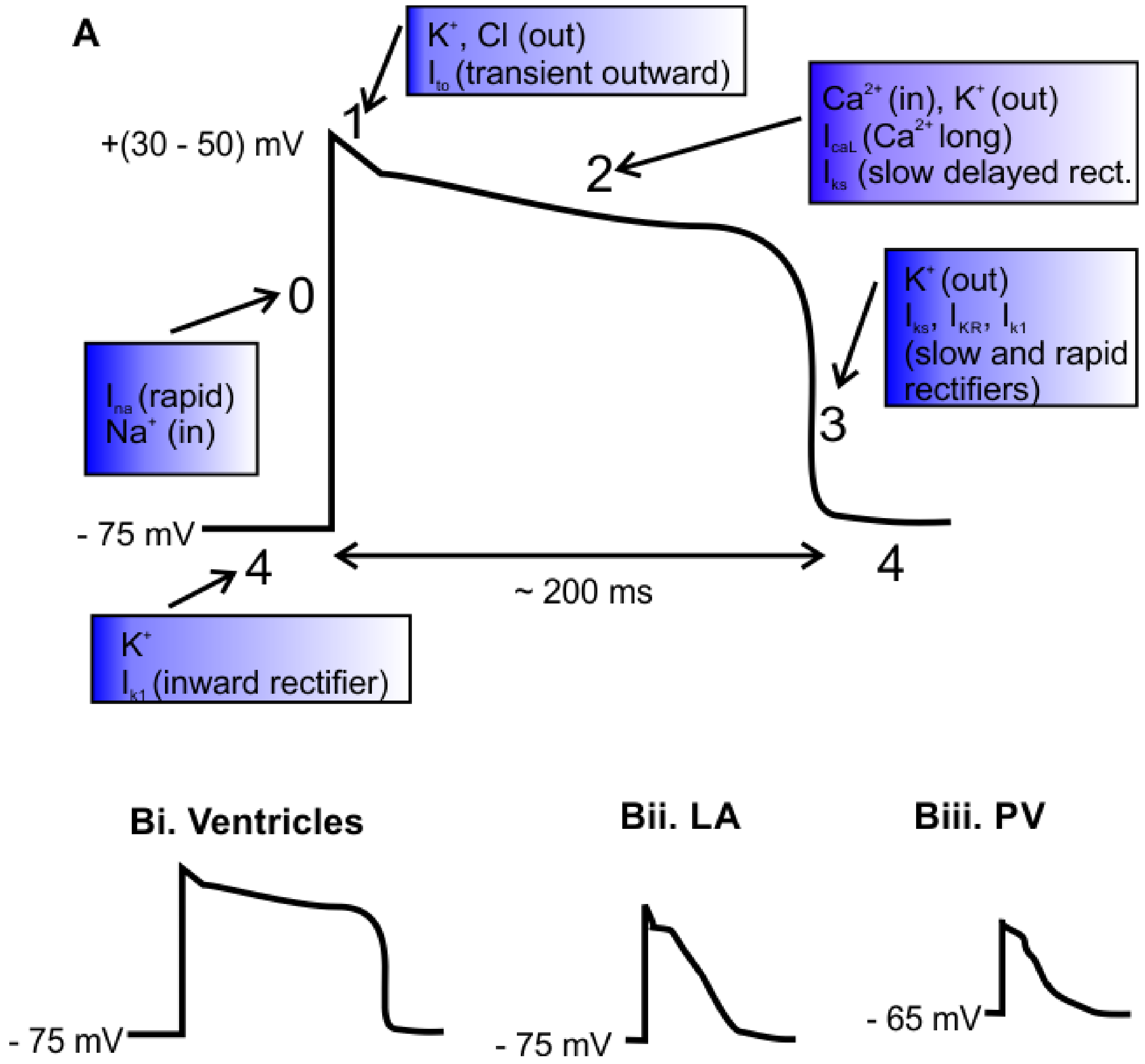

Figure 1.14. Phases of the ventricular myocytes AP. Panel **A,** ventricular AP has 5 distinct phases which are phase 0 (an upstroke), phase 1 (transient repolarisation), phase 2 (plateau), phase 3 (repolarisation) and phase 4 (resting membrane potential). Panel **Bi** (ventricular AP), panel **Bii** (atrial AP) and panel **Biii** (PV AP).

For these reasons, Na$^+$ currents are often referred to as *fast inward currents* (I_{Na}). In contrast, APs from SA and AV node cells rely on the openings of smaller (lower conductance) Ca^{2+} channels for the membrane depolarisation, resulting in a lower amplitude and slower upstroke during phase 0 of the AP.

Opening of Na$^+$ channels depolarises the cell to between +30 mV and +50 mV, at which point the channels inactivate. As the membrane potential depolarises, more and more

VOCCs are opening, including the T-type current which activates at -60 mV, and L-type VOCCs which activate between -40 and -30 mV. In the working cells of the atria, ventricles, purkinje and PVCs, L-type Ca^{2+} current *(I_{CaL})* contribute to the plateau phase of the AP (phase 2). This current also contributes to the depolarization of SA and AV nodes APs. At this point, various K^+ channels start to open but their activation is relatively slow. The plateau phase is maintained by the equilibrium of influx and eflux of Ca^{2+} and K^+ channels and eventually favouring repolarization and returs the membrane to resting potential (see Figure 1.14). The currents that repolarize cardiac myocytes (phase 3) as well as maintaining the resting pontential are carried out by several types of K^+ channels, some are labelled in Figure 1.14. These currents are known as *delayed rectifiers* because they open after the initial depolarization. The *inward rectifiers* which open during diastole helps to bring and maintain the resting membrane potential (Figure 1.14).

The Na^+ / Ca^{2+} exchanger generates both outward and inward membrane currents (I_{NCX}) when it exchanges 1 Ca^{2+} for 3 Na^+. Immediately after a myocyte depolarises, the exchanger generates an outward current which activates the reverse mode i.e. increases the efflux of Na^+. This outward current contributes to the initial / transient repolarisation phase (phase 1). Conversely, the forward mode which efflux Ca^{2+} released during excitation-contraction coupling contributes to the plateau and repolarisation phases of the cardiac AP. This current is usually maximal toward the end of the refractory period and is the main contributor of afterdepolarization, one of the pro-arrhythmic events that will be discussed later in this Chapter.

The description of the cardiac AP provided here is simplified, particularly with regards to the various K^+ currents. Having said that, especially since this is not an electrophysiological study investigating changes in individual currents, this brief description of the cardiac AP is sufficient in order to illustrate its importance for the arrhythmogenic events described in the following sections.

1.7.2.1. Cellular pro-arrhythmic mechanisms: Automaticity and triggered activity

Arrhythmias involve disturbances in the rhythm of excitation-contraction coupling events. Under pathological conditions like in AF and other cardiac diseases, arrhythmias can arise from a focal point at the cellular level to a tissue level and elicit remodelling (Narayan 2002, Koller *et al.,* 2005, Nassal *et al.,* 2015). Events that stimulate arrhythmias can be automatic (termed automaticity), triggered by a preceeding AP (termed triggered activity), re-entries and alternans.

1.7.2.2. Enhanced automaticity

This form of enhanced activity occurs when a myocyte with pacemaker activity, for example, PVCs, increase their spontaneous activity. This can be due to a lower threshold potential for the AP upstroke, or a less negative resting membrane potential like the one seen in PVCs (Chen *et al.,* 2002, Ehrlich *et al.,* 2003, Okamoto *et al.,* 2012).

1.7.2.3. Abnormal automaticity

Abnormal automaticity occurs when cardiac myocytes are depolarised, allowing them to reach a threshold potential needed for AP and thus showing spontaneous APs in-between the rhythmical heart beat. In many cases, this enhanced activity does not allow for a sufficient recovery of Na^+ channels before the next AP arrives. The depolarisation causing abnormal automaticity is often mediated by Ca^{2+} inward currents (Schotten *et al.,* 2011).

1.7.2.4. Triggered activity

One of the most common arrhythmogenic events is triggered activity which arises through oscillations of the membrane potential. Once the membrane potential reaches a threshold potential, APs are triggered. Depending on the timing of the membrane potential oscillations, these events can be classified as “early” or “delayed” afterdepolarizations as seen below in Figure 1.15.

EADs are membrane potential oscillations occuring during phase 2 or 3 of the AP (Hirose and Laurita 2007, Liu *et al.,* 2012). Several scenarios can explain the occurrence of EADs: (1) They may arise due to an increase in the AP duration which may provoke new APs and results in triggered activity (Figure 1.15 Ai). (2) β adrenergic stimulation, which elevates cytosolic Ca^{2+} and stimulates spontaneous SR Ca^{2+} release, can cause EADs. (3) A shortening of the AP duration (parasympathetic stimulation) whilst simultaneously the Ca^{2+} load of the cells is increased (sympathetic stimulation). In this situation, because of higher Ca^{2+} load, an AP generates a strong release of Ca^{2+} from the SR which lasts longer than AP duration and stimulates a strong inward rectifier I_{NCX} which may depolarise the membrane and may activate so called late-Phase 3 EADs (Figure 1.15 Bi). Late-Phase 3 EADs have been documented previously in AF animal models (Hirose and Laurita 2007). Most EADs occur in slower heart rate and DADs occur in a period of higher heart rate or rapid pacing (Song *et al.,* 2005).

DADs are oscillations of the membrane potential occuring after full repolarizations of the triggering APs. DADs are favoured by conditions that trigger Ca^{2+} overload like in ischaemia, β adrenergic stimulation, low extracellular K^+ concentration and in higher heart rate (Katra *et al.,* 2007). Ca^{2+} overload is an extremely pathological high SR Ca^{2+} content which increases the probability of RyRs opening, the frequency of local Ca^{2+} release events and the probability of global signal propagation (Song *et al.,* 2015). Excess Ca^{2+} released from the SR is removed from the cytosol to the extracellular fluid by the NCX which generates inward current I_{NCX} that depolarises the membrane and results in arrhythmias (Figure 1.15 Aii and Bii).

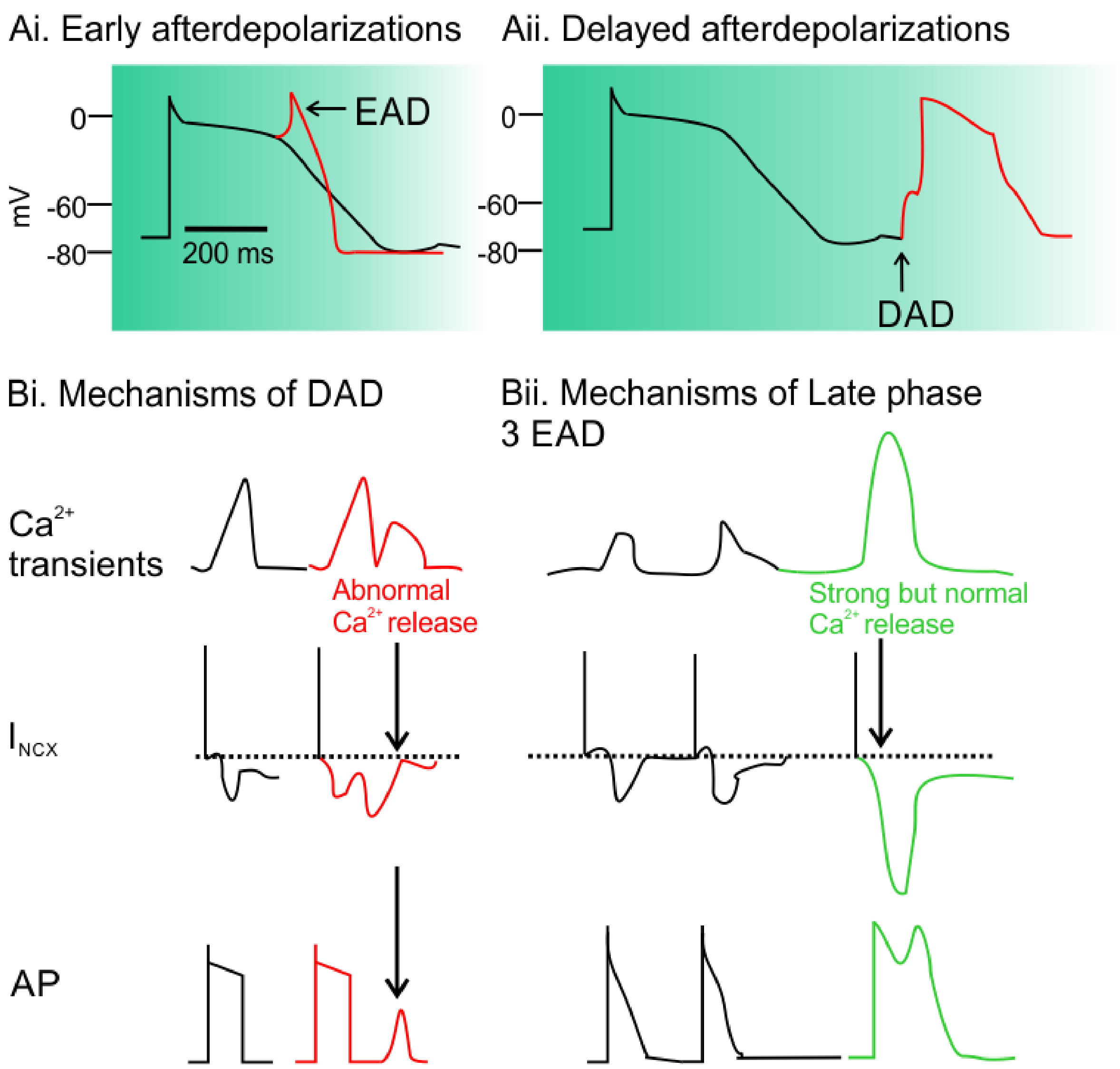

Figure 1.15. Cellular pro-arrhythmic events. Panel **A** shows schematic illustrations of EAD (Ai) and DAD (Aii). Panel **B** illustrates molecular events that leads to late phase 3 EAD (Bi) and DAD (Bii). SR Ca^{2+} release activates NCX current (I_{NCX}) which results in extra AP.

1.7.2.5. Re-entry

Re-entry occurs when an AP fails to extinguish itself and activates a region that has recovered from the previous stimulus and is ready to be re-activated. During the normal cardiac cycle, an electrical signal that is initiated at the SA node cells propagates over the entire heart, causing a simultanoeus contraction of the whole tissue. This electrical impulse diminishes when all regions have been activated and are in a state of refractoriness. However, when regions recover before the signal stops, they can serve as a link to re-activate previously depolarised regions that have already recovered from the initial depolarisation, resulting in re-entry, an example of this is illustrated in Figure 1.16 (Gaztañaga *et al*., 2012, Tse 2016).

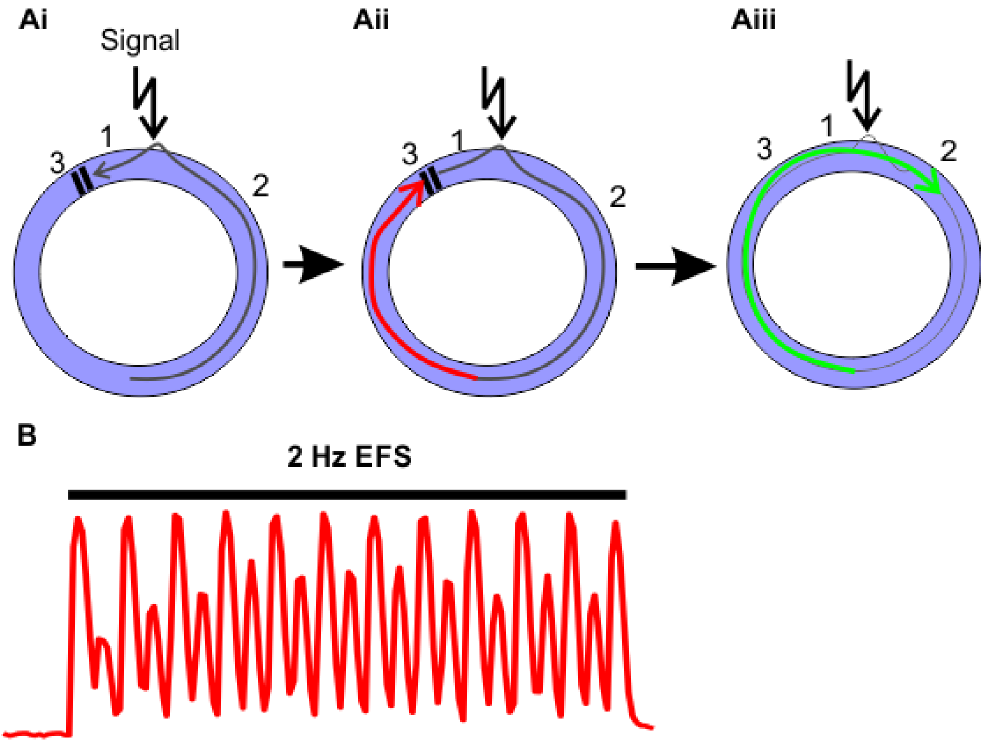

Figure 1.16. Re-entry and alternans. A re-entry is initiated when a signal that propagates through connected tissues travels through two different pathways, sites 1, 2 and 3 (panel **Ai**). However, when a signal reaches site 3 which is still in refractory, it causes a counduction block (panel **Aii**). When site 3 has recovered from a previous signal, this signal pathway then can then travel in one direction and activate sites 3, 1 and 2 and results in re-entry (panel **Aiii**). Panel **B** shows an example of alternating amplitudes of Ca^{2+} transients recorded during 2 Hz EFS, i.e. alternans.

There are many re-entry theories which can be divided into two main groups, these are either anatomical / classical or functional re-entry with different mechnisms. Since this study does not study re-entry mechanisms, the different theories will not be decsribed in detail. In PVCs, (Hassink *et al.,* 2003) conducted histology in patients with and without a history of AF and found that the pulmonary veins in patients with a history of AF were associated with fibrosis, hypertrophy and severe disorganisation in structure that may facilitate re-entries. Additionally, (Arora *et al.,* 2003) found a significant less conduction at the proximal pulmonary vein than in the rest of the left atrium. They also showed that these slow conduction regions within the pulmonary vein created a substrate for re-entry. Another study by (Hocini *et al.,* 2002) found zones of activation delays in canine pulmonary veins that may facilitate arrhythmias. Together, the differences in conduction velocities, delays, propagation, and the in increase in fibrosis in pulmonary veins may act as a substrate for re-entry that will facilitate arrhythmias.

1.7.2.6. Alternans

Alternans are cyclic, beat-to-beat alternations in contraction force, AP duration and intracellular Ca^{2+} release during a period of constant stimulation, e.g. manifestings as alternating large and small amplitude Ca^{2+} transients. Alternans are known to occur during a period of high frequency stimulation either intrinsic pacemakers or by extrinsic stimulations, this is illustrated in Figure 1.16 B (Narayan 2002, Narayan *et al.,* 2011). Cardiac alternans were initially described as mechanical and electrical alterations at the whole heart level and later at the cellular level. Cardiac alternans are now known to be pro-arrhythmic events that have been shown previously to precede the onset of AF episodes. Cardiac alternans have also been observed in ventricular arrhythmias and sudden cardiac deaths (Narayan 2002, Cutler *et al.,* 2009). The mechanisms underlying this event are still poorly understood but studies in isolated cardiac myocytes and in intact hearts have shed some light onto the subject. It is clear that at the cellular level, variations of AP duration result in alternans. These changes of the AP duration arise mainly because of dysregulated Ca^{2+} release. At resting heart rate, the SR Ca^{2+} release must be matched by the SR Ca^{2+} re-uptake that occurs primarily by the SERCA2a. One theory of alternans development links disturbances in SR Ca^{2+} re-uptake, especially during higher pacing rate, with diminished SR Ca^{2+} release and resulting alternans. Down-regulation of SERCA2a has been shown to result in alternans (Cutler *et al.,* 2009). In contrast, a previous study that used *in vivo* gene transfection to overexpress SERCA2a in myocytes showed the inhibition of alternans (Cutler *et al.,* 2009). However, another study on SERCA2a overexpression in atrial myocytes found no effects on alternans (Nassal *et al.,* 2015).

It is important to remember that the events underlying alternans may vary between atrial and ventricular myocytes because of the differences in structure, electrical characteristics and Ca^{2+} homeostasis. Most studies on alternans are done in ventricular myocytes, rather than in atrial myocytes. As mentioned above, over-expression of SERCA2a has been shown to inhibit alternans in ventricular myocytes whereas it failed to do so in atrial myocytes. One reason for this might be because of the lack of t-tubules and PLN in atrial myocytes (Kanaporis and Blatter 2017).

In summary, there are several mechanisms both electrically and structurally within the PVs that may facilitate arrhythmias. These pro-arrhythmic events include a lower threshold for AP upstroke, the occurrence of alternans, increases in conduction blocks and deterioration in structural organisations of the PVCs. These mechanisms are worsened during ageing or in AF as described later in this thesis. Hence, in this study, the presence of alternans were investigated in PVCs from 3 month- and 24 month-old mice (Chapter 4) and in NRVMs (Chapter 5) after EFS.

1.7.3. Structural remodelling in AF and during ageing

We have seen how cardiac myocytes are perfectly structured to allow an effective excitation contraction coupling. One example of this, described above, is the presence of T-tubules in greater abundance in ventricular myocytes than in atrial myocytes and PVCs. Hence, severe structural weakening that manifests either during ageing or in AF will diminish the cardiac output. Changes that have been documented in AF and during ageing will be discussed in detail below in sections 1.7.3.1 and 1.7.3.2.

1.7.3.1. Structural changes in AF

Clearly, structural alterations in the atria are not exclusively related to AF, but evidence of structural changes in the atria resulting from AF or they might have led to AF have been decribed. These changes include atrial fibrosis, atrial necrosis and changes in gap-junctions (Boldt *et al.,* 2006, Laky *et al*., 2011). Compelling evidence suggests that atrial fibrosis is one of structural remodelling in the development of AF. The molecular signaling changes underlying atrial fibrosis are not completely understood. Angiotensin II mediates fibrosis in a variety of cardiac diseases and studies on transgenic mice with cardiac-restricted Angiotensin converting enzyme overexpression show marked atrial dilation, fibrosis and AF (Nattel *et al.,* 2008). Angiotensin II works by activating Angiotensin type I and 2 receptors. Through downstream signaling pathways, they mediate fibroblast proliferation, cardiac hypertrophy and necrosis (Boldt *et al.,* 2004, Nattel *et al.,* 2008). Additionally, atrial fibrosis has been observed in patients with AF and other cardiac diseases (Schotten *et al*., 2011). In terms of PVCs, (Sun *et al.,* 2008) showed an increase in interstitial fibrosis in AF dogs models with mitral regurgitations compared to control dogs. Supporting these findings is the study (Boldt *et al.,* 2006) that showed that demostrated that Angiotensin converting enzyme inhibitors were able to attenuate structural remodelling in patients with chronic AF. In all of the previous studies, fibrosis was found to be increased in AF animal models as summarised in Table 1.3 below.

Another relevant factor for atrial remodelling is altered connexin expression. The main connexin sub-types expressed in cardiac myocytes are Cx40, Cx43 and Cx45 but the expression levels vary considerably depending on the cell type. Ventricular myocytes express mainly Cx43 whereas atrial myocytes highly express Cx40. PVCs have been shown to express Cx40, Cx43 and Cx45; however, the level of expression varies depending on the location of PVCs within the pulmonary vein (Chaldoupi *et al.,* 2009, Kugler *et al.,* 2017). A previous study has shown a reduction in Cx40 expression levels in atrial appendages from AF-induced goats (Van Der Velden *et al.,* 1998). In summary, previous results have shown that induction of AF in animal models resulted in altered distribution or a reduction of Cx40 whereas Cx43 mostly remained unchanged or increased (see Table 1.3 below) (Van Der Velden *et al.,* 1998, Ausma *et al.,* 2003, Yeh *et al.,* 2006). The effects of connexin and fibrosis remodelling have been suggested to facilitate electrical tissue non-homogeneity, slowed conduction and electrical uncoupling, all of which are pro-arrhythmic indicators.

In terms of the EM studies, previous studies have shown changes in atrial myocytes from AF-induced animals and in patients with AF. These changes include an increase in cell size, myolysis, perinuclear accummulation of glycogen and changes in mitochondrial size and number (Ausma *et al.,* 1997, Thijssen *et al.,* 2000, Ausma *et al.,* 2001, Ausma *et al.,* 2003). All of changes described are summarised in Table 1.3.

1.7.3.2. Structural changes during ageing

“Everyone is the age of their heart” is a Guatemalan proverb that emphasises the link between ageing and cardiovascular diseases like AF (Hatch *et al.*, 2011). Although the prevalence of AF strongly increases with ageing, it is difficult to study the effects of age in humans due to the long time span of senescence and lack of human PV tissue in healthy young individuals. Therefore, most ageing studies have been done in animals. Here, some examples of the changes that are seen previously in atrial myocytes during ageing will be decribed.

Structurally, age-dependent changes have been documented in atrial and ventricular myocytes from animals. In dogs, (Koura *et al.,* 2002) showed an age-dependent increase in interstitial fibrosis and fatty infiltrates. Also, Cx43 becomes increasingly concentrated at end to end junctions between myocytes. Similarly, another study found an age-dependent upregulation of apoptotic bodies which could hinder conduction (Boyle *et al.,* 2013).

Most of the previous ageing studies in cardiac myocytes that focused on the structural changes analysed mitochondrial changes, myofilaments and the presence of dense bodies (lipofuscin). (Feldman and Navaratnam 1981) found an age-dependent increase in mitochondrial size in the aged atria. They found mitochondria to be swollen, combined with an increased presence of lipofuscin granules and an increased disorganisation of the myofilaments. Similarly, other studies have found a significant degeneration of the ultrastructure with swollen mitochondria and disrupted cristae, disorganised myofilaments and disruption of the nuclear membrane as summarised above in Table 1.3 (Gupta *et al.,* 2010). To the best of our knowledge, there are no studies that have been done in PVCs describing the effects of ageing on the ultrastructure. Therefore, this thesis will characterise structural remodelling in PVCs from mice during ageing (Chapter 3) and how these alterations affect the function (Chapter 4) and promotes arrhythmias.

	Ageing or AF	Component and direction of change	Species	References
Fibrosis	AF	Fibrosis ↑	Humans	(Boldt *et al.,* 2004, Boldt *et al.,* 2006)
	AF	Fibrosis ↑	Humans	Laky *et al.,* 2011
	AF	Fibrosis ↑	Goats	(Ausma *et al.,* 2001)
	AF	Fibrosis ↑	Goats	(Verheule *et al.,* 2010)
	AF	Fibrosis ↑	Dogs	(Sun *et al.,* 2008)
	Ageing	Fibrosis ↑	Dogs	(Koura *et al.,* 2002)
Connexins	AF	Cx40 ↓ Cx43 ↓	Dogs	(Sun *et al.,* 2008)
	AF	Cx40 ↓ Cx43 →	Goats	(Van Der Velden *et al.,* 1998)
	AF	Cx40 ↓ Cx43 →	Goats	(Ausma *et al.,* 2003)
	AF	Cx40 ↓ Cx43 ↑	Dogs	(Yeh *et al.,* 2006)
	Ageing	Cx43 distribution changed	Dogs	(Koura *et al.,* 2002)
Mitochondria	AF	MN ? MS ↓↑	Goats	(Ausma *et al.,* 1997)
	AF	MN ? MS ↓	Goats	(Ausma *et al.,* 2001)
				Laky *et al.,* 2011
	AF	MN ? MS ↑	Dogs	
	Ageing	MN ? MS ↑	Mice	(Gupta *et al.,* 2010)
	Ageing	MN ? MS ↑	Rats	(Feldman and Navaratnam 1981)

Table 1.3. Summary of the structural changes during ageing and AF.

MN = mitochondrial number   MS = mitochondrial size.

1.7.4. Changes in Ca^{2+} homeostasis in AF and during ageing

As stated before, altered Ca^{2+} homeostasis in atrial myocytes and PVCs in AF and during ageing is one of the factors that facilitates AF. There has been an extensive research that focused on Ca^{2+} homeostasis remodelling during AF mostly in atrial myocytes and to a lesser extent in PVCs. Similarly, there are a lot of studies that have been conducted to investigate the effects of ageing on Ca^{2+} homeostasis in cardiac myocytes. Interestingly, to the best of my knowledge, there are studies that have been done to investigate the changes in Ca^{2+} homeostasis during ageing in PVCs. The findings so far that were seen in atrial myocytes and PVCs in AF and during ageing are presented below.

1.7.4.1. Altered Ca^{2+} homeostasis in atrial myocytes and PVCs in AF

Changes in the intracellular Ca^{2+} concentration are involved in a range of physiological processes including the beating of the heart and hence, any disruption in Ca^{2+} homeostasis could result in arrhythmias and AF. Ca^{2+} homeostasis in cardiac myocytes is a complex subject that involves a number of channels, Ca^{2+} binding proteins, kinases / phosphatases and organelles, all linking to several intracellular signalling pathways, as described in section 1.5. In AF, changes in VOCCs, RyR2s, SERCA2a, NXC, ROS and mitochondrial dysfunction have all been documented and will be outlined below.

A number of studies have reported a decrease in the reduction of Ica_L current, together with reduced mRNA levels and a lower epression of VOCCs in cardiac myocytes from AF (Lai *et al.,* 1999, Mestre Prates *et al.,* 2002, Klein *et al.,* 2003, Schotten *et al.,* 2003, Gaborit *et al.,* 2005). These changes are likely to interfere with the morphology of APs, and it has been suggested that they may contribute to an increase in AP duration, thus inhibiting Ca^{2+} influx and that they could promote re-entry (Nattel and Harada 2014).

Antother important channel for cardiac Ca^{2+} signalling is the RyR. In AF, previous studies have suggested either no change in the expression levels or a significant reduction (Brundel *et al.,* 1999, Lai *et al.,* 1999, Neef *et al.,* 2010). Even with unaltered expression levels, changes in the open propability of the RyR could affect their function in the cell. Several studied reported an increase in the opening probability of the channel which result in an increased SR Ca^{2+} leak, increased frequency of local and global Ca^{2+} events and hyperactivity that leads to arrhythmias (Vest *et al.,* 2005, Neef *et al.,* 2010, Voigt *et al.,* 2012).

As the Ca^{2+} leak from the SR increases in AF patients and animal models (Vest *et al.,* 2005, Neef *et al.,* 2010, Voigt *et al.,* 2012), one would expect SERCA2a function to increase as well. This was the case in one study that found an increase in SERCA2a function in atrial myocytes from AF patients (Shanmugam *et al.,* 2011). However, this increase in SERCA2a function could be caused by the reduction in sarcolipin; an inhibitory protein of SERCA2a that is exclusively expressed in atrial myocytes (Shanmugam *et al.,* 2011). The changes in SERCA2a function however are not conclusive. In contrast to the former study, (Voigt *et al.,* 2012) reported a decrease in SERCA2a mediated Ca^{2+} removal even with an increase in SR Ca^{2+} leak. Therefore, results regarding the remodelling of SERCA2a in AF are inconsistent and require further investigations (Greiser *et al.,* 2009, Greiser and Schotten 2013).

The most consistent feature in Ca^{2+} homeostasis remodelling in AF patients and in animal models is the upregulation of the NCX. NCX is the dominant mechanisms for the extrusion of Ca^{2+} out of the cardiac myocytes. In its forward electrogenic mode, the NCX extrudes 1 Ca^{2+} in exchange of 3 Na^{+} and is thus generating a net inward electrical current that depolarises membrane potential. NCX expression has been shown to be upregulated in

AF, contributing to the generation of EADs and DADs and promoting arrhythmia (Patterson *et al.,* 2006, Venetucci *et al.,* 2007, Okamoto *et al.,* 2012).

Another important factor for modulating cardiac Ca^{2+} signalling is ROS levels that have been shown to be increased in AF animal models (Guo *et al.,* 2014; Huang *et al.,* 2017). An increase in ROS production by mitochondria has been shown to affect Ca^{2+} homeostasis by modulating the opening of channels that are cysteine rich through redox modifications (Cooper *et al.,* 2013). (Cooper *et al.,* 2013) showed that ageing significantly increased the SR Ca^{2+} leak through RyR2 via post-translational thiol oxidation of the receptor caused by mitochondrial ROS production.

1.7.4.2. Changes in Ca^{2+} homeostasis in atrial myocytes during ageing

As we saw with the structural changes, ageing is associated with a progressive deterioration in the cardiac output due to alterations in the structure of cardiac myocytes (Ausma *et al*., 2001, Ausma *et al.,* 2003). Age-dependent remodelling results in a disturbed electrical and Ca^{2+} homeostasis that may in turn affects the contractions. These changes become more apparent during a period of higher energy demand, for example during exercise. The alterations that come with age vary between men and women (Feridooni *et al.,* 2015); this supports the prevalence of data that shows AF to be more common in men than women. Nevertheless, Ca^{2+} homeostasis changes during ageing are similar to those found in AF (downregulation of I_{caL} and increased opening probability of RyRs due to either hyperphosphorylation or in direct effects of increased ROS). All these changes have also been reported in cardiac myocytes from aged animals (Zhu *et al.,* 2005, Hatch *et al.,* 2011). In addition to this, Wongcharoen *et al.,* 2007 demonstrated a larger amplitude of DADs and longer AP duration in PV tissues from aged rabbits. Ageing also depolarised the resting membrane potential of PV tissues from aged rabbits and showed higher propensity for AP alternans as well as contractile alternans (Wongcharoen *et al.,* 2007). Just like in AF animal models, RyR protein levels do not change with age (Zhu *et al.,* 2005, Rueckschloss *et al.,* 2010). Most ageing studies in atrial myocytes have demonstrated a down regulation of SERCA2a in male animals but not in females. It has been suggested that this decrease contributes to a prolonged transient duration in myocytes from aged male animals (Feridooni *et al.,* 2015, Herraiz-Martinez *et al.,* 2015). Additionally, whilst the NCX inward current is found to be upregulated during ageing, most studies found no change in the NCX protein expression levels during ageing (Li *et al.,* 2007, Hatch *et al*., 2011, Feridooni *et al.,* 2015). As a result of these changes, studies have reported an increase in the frequency of local and global Ca^{2+} transients, a reduced ability to follow electrical pacing, an increased presence of alternans, an increase in transient duration and a lower amplitude of the global Ca^{2+} transients (Hatch *et al.,* 2011, Feridooni *et al.,* 2015, Herraiz-Martinez *et al.,* 2015). For further details about all of the changes in Ca^{2+} homeostasis during ageing and all of the differences between male and female AF animal models, please refer to review by (Feridooni *et al.,* 2015).

In summary, previous studies have shown that changes in the structure and Ca^{2+} homeostasis facilitate AF in atrial myocytes. Interestingly, similar studies in PVCs during ageing are still lacking. This thesis characterises changes in the structure and links them with changes in Ca^{2+} handling during ageing to elucidate how they might facilitate the occurrence of arrhythmias i.e. AF.

1.8. Cellular ageing model with hydroxyurea

Ageing can be defined as a progressive decline of the body to performs physiological functions and and a loss of repair mechanisms that may lead to a loss of function and an elevated risk of death (Dong *et al.,* 2014, Zhai *et al.,* 2017). Ageing research has attracted a lot of interests over recent years to understand the molecular alterations that manifest during ageing. A review by (Lopez-Otin *et al.,* 2013) highlighted nine hallmarks of ageing that may contribute to the ageing process. These hallmarks are genomic instability, loss of proteostasis, telomere attrition, epigenetic alterations, deregulated nutrient-sensing, mitochondrial dysfunction, stem cell exhaustion, cellular senescence and altered intercellular communication. This thesis will mainly focus on cellular senescence and mitochondrial dysfunction by attempting to induce ageing chemically with hydroxyurea (HU) in Chapter 5. To understand the mechanisms underlying the cellular ageing process, most studies use cellular senescence as an ageing model (Park *et al.,* 2000, Yeo *et al.,* 2000, Zhai *et al.,* 2017). Cellular senescence can be characterised as a loss of repair mechanisms that lead to cellular DNA damage (Chen *et al.,* 2007; Lopez-Otin *et al.,* 2013). HU is widely used as a tumour therapeutic agent that has been suggested to exert its effects by inhibiting ribonucleotide reductase and prevents the reduction of ribonucleotides to deoxyribonucleotides and hence inhibits DNA synthesis (Krakoff *et al.,* 1968). HU incubation in cells effectively inhibits DNA repair mechanisms, induces DNA damage and senescent like phenotypes (Park *et al.,* 2000, Yeo *et al.,* 2000, Dong *et al.,* 2014; Zhai *et al.,* 2017). Previous studies where they used HU to induce senescence in cells found an increased expression of p16, p21 and p53 which are found to be increased during ageing (Ressler *et al.,* 2006). Similarly, HU treatment in neuronal, human diploid fibroblasts and cancer cells increased senescence, growth arrest and ROS levels, but no induction of apoptosis (Park *et al.,* 2000; Yeo *et al.,* 2000; Cooper *et al.,* 2013; Dong *et al.,* 2014; Guo *et al.,* 2014; Huang *et al.,* 2017). To date, similar studies in cardiac myocytes are still lacking. Therefore, this study will try to establish a cellular ageing model with HU treatment in NRVMs. Traditionally, most ageing studies are done by analysing the changes in cells and tissues from young and old animals. However, these analysis are time-consuming, costly and require animal sacrifices. Therefore, using an ageing model may prove an easier and a quicker way to study ageing. The benefits and limitations of studying ageing using either a traditional way (young *vs.* old animals), or an ageing model by inducing senescence chemically are summarised below in Table 1.4.

Factors	**Young *vs.* old model**	**An ageing model with HU**
Time	Very time consuming, longer waits are needed for the animals to age naturally. For this study, (3-and 24 month-old mice were used. Other studies, 2-and 32 month-old rats (Feldman and Navaratnam, 1981).	It is relatively quick. For this model, HU was incubated for a maximum of 7 days. Other studies; Hu incubated for upto 9 days (Park *et al.,* 2000); ≤ 28 days (Yeo *et al.,* 2000), ≤ 3 days (Zhai *et al.,* 2017).
Cost	Expensive as it involves buying and maintaining the animals.	Cheaper and easier to maintain as cell lines can be used to induce senescence.
Home Office license	Required. This can also lead to the delay of experiments.	Not necessary.
Cell-to-cell communication	Better as it mimicks the physiological environments. For example, in this study, PVCs within a pulmonary vein in lung slices.	Poor can be achieved. For this study, NRVMs had a good cell-to-cell comunication because of gap-junctions.
Reliability	More reliable because changes analysed are from "natural ageing".	Less reliable. Although the changes are similar to those observed in naturally aged cells/tissues, as described before ageing involves alterations in different hallmarks and HU may ust be inducing senescence and not necessarily ageing.
Scope of experiments	Limited. Primary cells deteriorate very quickly and hence they need to be used for experiments quickly. This limits the range of experiments that can be performed.	More experiments can be performed because cells can be viable for longer.

Table 1.4. Comparisons of the advantages and disadvantages between naturally ageing models and chemically induced ageing models.

1.9. Aims

The main aims of this study are:

1. To compare and analyse the structure of PVCs, atrial and ventricular myocytes during ageing and how these age-dependent changes might facilitate the occurrence of arrhythmias like in AF.

2. To provide a comprehensive description of Ca^{2+} homeostasis in PVCs.

3. To analyse the changes in Ca^{2+} homeostasis and response to drugs in PVCs during ageing.

4. An attempt to establish an ageing model chemically using Hydroxyurea (HU) in neonatal rat ventricular myocytes (NRVMs).

5. To compare and analyse the changes in naturally aged PVCs and in chemically induced NRVMs to gain further understanding of the potential future treatments for the treatment of cardiac arrhythmias like AF.

Chapter 2: Materials and Methods

2.1. Cell preparations

2.1.1. Solutions and compounds in cell preparations

2.1.1.1. Lung slice experiments

sHBSS contained KCl 5.3 mM; KH_2PO_4 0.4 mM, NaCl 137.9 mM, NaH_2PO_4 0.3 mM, $NaHCO_3$ 4.2 mM, D-Glucose 5.6 mM, $MgCl_2$ 0.5 mM, $MgSO_4$ 0.4 mM, $CaCl_2$ 1.3 mM, HEPES 20 mM and the pH was adjusted to 7.4 using NaOH.

PBS was diluted from ready-mixed powder (Sigma-Aldrich, St. Louis) and contained 138 mM NaCl and 2.7 mM KCl. The pH was adjusted to 7.4 using NaOH.

4 % PFA: Dissolve 0.4 g in 50 ml distilled water and 50 ml 0.2 M phosphate buffer inside a fume hood. The pH was adjusted using NaOH on a heated stirrer.

2.1.1.2. Neonatal rat ventricular myocyte experiments

Neonatal buffer contained NaCl 100 mM, KCl 5.4 mM, $MgSO_4$ 0.8 mM, D-glucose 1%, $NaH_2PO_{4.}H_20$ 0.8 mM, HEPES 20 mM. The pH was adjusted to 7.35 using NaOH.

Plating medium contained 4 parts DMEM with 4.5 g / l D-glucose (Gibco, product number 15235697), and 1 part M199 (Sigma-Aldrich, St. Louis), supplemented with 10% Donor horse serum (Gibco), 5% fetal calf serum (Gibco), 1 mM sodium pyruvate (Gibco), 1 mM MEM non-essential amino acids (Gibco), 1% antibiotic / antimycotic (Gibco) and 3 µM cytosine β-D-arafuranoside (ara-C, Sigma-Aldrich, St. Louis).

Digestion buffer contained Pancreatin 0.2 mg / ml (Sigma-Aldrich, St. Louis), DNase 0.015 mg / ml, activity ≥ 1500 units per mg (USBiological), and Collagenase type II (0.25 mg / ml, activity ≥ 125 units per mg. (Sigma-Aldrich, St. Louis).

2.1.2. Preparation of lung slices

The C57/bl/6j mice aged 3 and 24 month-old were euthanised by Schedule 1, under the Animals Scientific Procedure Act (ASPA) 1986 as approved by the Institutional Animal Care and Use Committee of The Open University, UK. After opening the chest cavity, the lungs were inflated with ~ 1 ml of 37°C, 1.8 % low melting point agarose (Life Technologies, Carlsbad, CA) in Hank's buffered salt solution (HBSS, composition given in Section 2.1.1.1) (Life Technologies, Carlsbad, CA) that was pH buffered to 7.4 using HEPES (sHBSS). The trachea was cannulated and the agarose was injected to inflate the lungs. Care was taken not to inflate the lungs to a volume above that of the rib cage. Immediately following the inflation, the lungs were covered with tissue paper wetted with ice cold sHBSS and the mouse was put in the fridge for few minutes to solidify the agarose inside the lungs. Solidified lungs were cut into 180 µm thick slices using a VF-300 microtome (Precisionary Instruments Inc., Greenville, NC). Lung slices were collected into sHBSS and inspected for the presence of PVCs using a light microscope with low magnification. PVs were generally distinguishable from arteries by these criteria: the vein is not next to an airway and or / striated cells can be observed in the cells surrounding the vein. For EM and immunofluorescence studies the slices were fixed with 4 % paraformaldehyde for 24 hours in the fridge. After 24 hours they were washed twice in HBSS, and kept in HBSS in the fridge until used. Or, for functional studies, slices were put in Dulbecco's Medium Eagle Medium (DMEM) supplemented with antibiotics / antimycotics and 10 % foetal bovine serum and kept in a humidified tissue culture incubator at 37°C with 5 % CO_2. Slices were used within 48 hours of preparation.

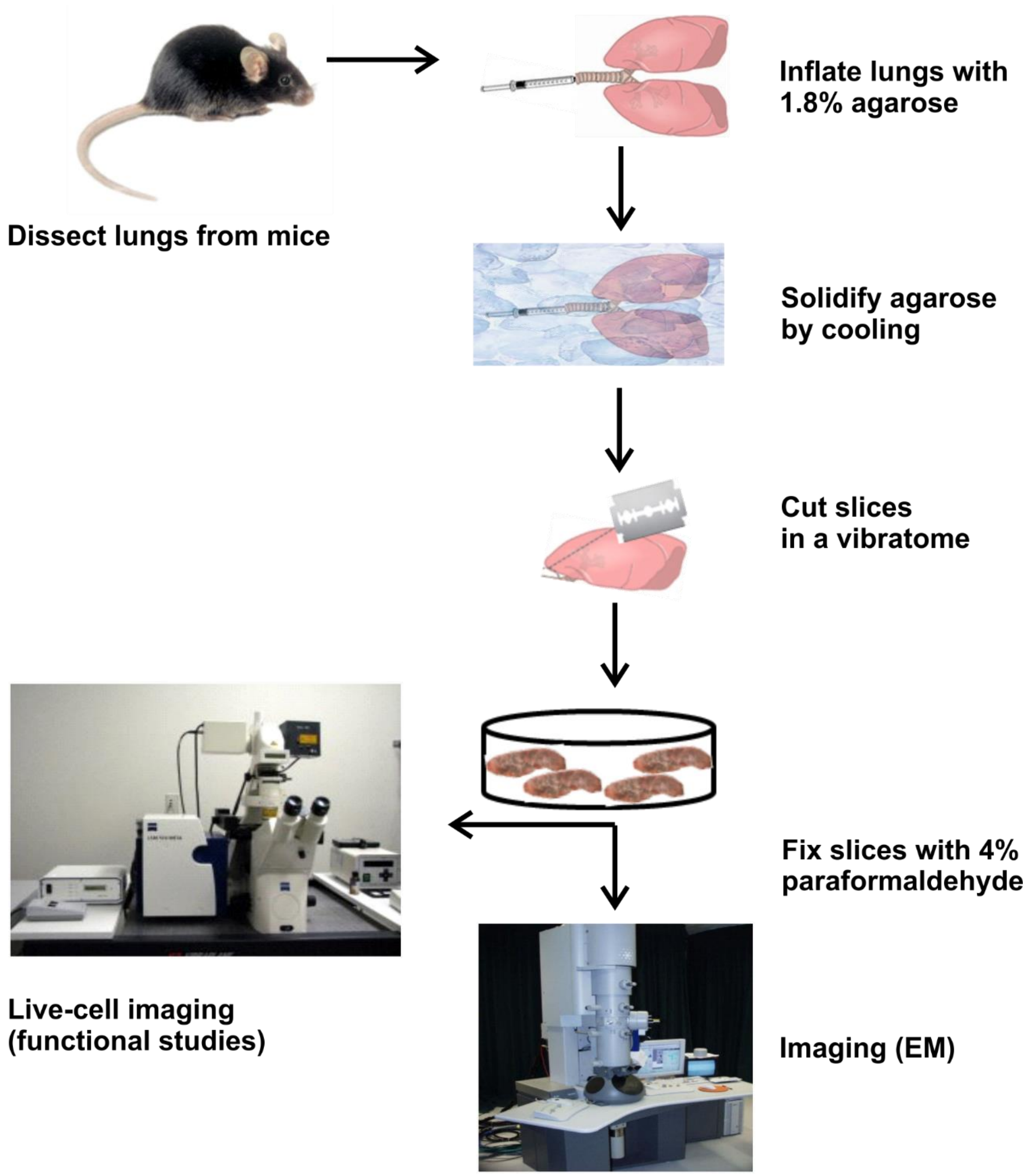

Figure 2.1. Lung slices preparation and use. Steps of the lung slices preparation are shown. The slices were either fixed with 4 % paraformaldehyde to preserve the ultrastructure and used for structural studies or kept in DMEM culture medium for up to 48 hours and loaded with fluorescent indicators for live-cell studies.

2.1.3. Preparation of neonatal rat ventricular myocytes

Rat pups aged 2 – 5 days were sacrificed according to Schedule 1 by cervical dislocation followed by destruction of the brain under the Animals Scientific Procedure Act (ASPA) 1986 as approved by the Institutional Animal Care and Use Committee of the Open University, UK. After opening the chest cavity, the pup's hearts were removed with scissors and placed in ice-cold 1X neonatal buffer (composition given in Section 2.1.1.2) before being minced into ~ $1mm^3$ cubes using a razor blade. The neonatal buffer was removed and 5 ml digestion buffer containing collagenase type II (Worthington, UK), pancreatin (Sigma-Aldrich, St. Louise) and DNase I (USBiological) (composition given in Section 2.1.1.2) was added to the minced hearts. They were transferred into one 50 ml falcon tube using a sterile cut-off 3 ml plastic Pasteur pipette and incubated at 30°C for 10 minutes with gentle stirring (190 rpm). After 10 minutes, minced hearts were gently triturated, allowed to settle and the supernatant was removed and discarded. 5 ml of fresh digestion buffer was added and the minced hearts were incubated for 20 minutes at 30°C with gentle stirring (190 rpm). The minced hearts were then triturated and the supernatant containing isolated cells was placed in a Falcon tube containing 30 ml plating medium (composition given in Section 2.1.1.2) and incubated at 37°C in a humidified cell culture incubator. Another 5 ml digestion buffer was added to the minced hearts and they were again incubated at 30°C for 20 minutes with gentle agitation. After 20 minutes, the minced hearts were triturated and supernatant added in a tube containing plating medium which will now fill up to ~ 40 ml and should contain ~ 10 ml of cell suspension in digestion buffer. The contents of this tube were filtered through a 100 µm cell strainer (Corning^{TM}) to separate the heart chunks from the isolated cells. The filter was rinsed with 10 ml fresh plating medium to collect all the isolated cells and the cells were centrifuged at 1200 rpm for 5 minutes. The resulting pellet was resuspended in a falcon tube with 10 ml plating medium and incubated at 37°C; this will be tube 1. Meanwhile, the above mentioned steps resulting in collecting the isolated myocytes in tube 1 are repeated to collect tubes 2 and 3. The resuspended cell pellets from tube 1-3 were combined and pre-plated in a T175 flask (Greiner Bio-one, UK) and pre-plated for an hour at 37°C to allow fibroblasts, which adhere to cell-culture surfaces much more readily than cardiac myocytes, to adhere and reduce their number in the cell suspension. Cells not stuck down are collected in the medium, centrifuged at 1200 rpm for 5 mins. This pellet, containing the cardiac myocytes, is resuspended in a 15 ml plating medium in a falcon tube. Cells were counted and seeded at a density 9.0 x 10^4 cells / ml on either 1 % gelatin-coated (Sigma-Aldrich, St. Louis) six well plates or 25 µM / ml laminin (Sigma-Aldrich, St. Louis) coated 16 mm coverslips (VWR International Ltd) and placed at 37°C, 5 % CO_2 in a humidified incubator. After 24 hours, the plating medium was exchanged to remove any debris on top of cells. When indicated, hydroxyurea (HU) (Sigma-Aldrich, St. Louis) was added on day 2 after the preparation, once the cells were beating synchronously.

2.2. Immunofluorescence

2.2.1. Solutions and compounds used in immunofluorescence

Permeabilisation buffer: 0.2 % Triton (Sigma-Aldrich, St. Louis) in PBS.

Blocking buffer: 0.1 % Triton in PBS supplemented with 10 % bovine serum albumin (BSA) (Sigma-Aldrich, St. Louis).

Washing buffer: 0.1 % Triton in PBS.

Antibody	Concentration	Source
RyR2	1:50	A kind gift from Prof. Vincenzo Sorrentino
Cx40	1:100	St. John's lab, UK
Cx43	1:100	Abcam, UK
Alexa Fluor 488 goat anti rabbit 2°Ab	1:500	Life Technologies, Carlsbad, CA
Alexa Fluor 568 goat anti rabbit 2°Ab	1:500	Life Technologies, Carlsbad, CA
Phalloidin iFluor (488)	1:250	Stratech, UK

Table 2.1. Indicators and antibodies used for immunofluorescence.

2.2.2. Immunofluorescence in lung slices

Immunostaining was performed on lung slices that were previously fixed with 4 % PFA. Lung slices were permeabilised in permeabilisation buffer for 2 hours to allow the entry of the antibodies from the extracellular medium into the cytoplasm. To block unspecific binding of proteins, lung slices were incubated in blocking buffer for further 2 hours. After that, slices were incubated with RyR2 primary antibodies (1:50 dilution), Cx43 antibodies (1:100 dilution) or Cx40 antibodies (1:100 dilution) in 1 % BSA / 0.1 % Triton overnight at 4°C. After being washed six times with washing buffer (5 minutes for each wash) to wash off any unspecifically bound antibodies, slices were incubated for an hour with an Alexa-Fluor 568 goat anti rabbit secondary antibody (1:500 dilution) in 1 % BSA / 0.1 % Triton (Life Technologies, Carlsbad, CA) at RT. All steps following the addition of secondary antibodies were performed in the dark to protect the slices from light which will cause photo bleaching of the fluorescent dye conjugated to the secondary antibody. Slices were washed again with washing buffer four times and twice with PBS to remove any Triton before mounting the samples. Slices were then stained with 488 Phalloidin-iFluor

(Stratech, UK), diluted 1:200, for 2 hours to stain the myofilaments. Finally, the stained slices were mounted on slides with Prolong Gold Mounting Medium (Life Technologies, Carlsbad, CA) overnight at RT. Afterwards, slices were stored at 4°C until use.

2.2.3. Microscope settings for immunofluorescence

Immunofluorescence images were taken on a Zeiss 510 META Laser Scanning Microscopy (LSM) confocal microscope (Carl Zeiss, Germany). All images were taken using the following settings: x, y planes, 12-bit images, 1024 x 1024 pixels, unidirectional scan and 63X magnification. The specimens were excited with an Argon/2 laser (wavelength 488 nm) and HeNe1 (wavelength 561 nm). The optical slice thickness was set at 2.0 µm.

2.2.4. Immunofluorescence image analysis

Image analysis was performed using ImageJ (National Institutes of Health, Bethesda, Maryland). Opening the images using the LSM toolbox ensured the correct scale bar settings.

2.2.4.1. Analysis of RyR localisation

ImageJ was used to measure the distance between striations. The distance between 5 striations was measured using the line hand tool, and the measured value was divided by 5, giving the average distance between striations. This measurement was performed in 3 regions per PV per slice for each age group.

2.2.4.2. Analysis of Connexin localisation

For Cx40 and Cx43 analysis, connexin and phalloidin intensities were measured in ImageJ using the particle analysis tool. First, the threshold in the phalloidin image was adjusted so only the cytoplasm was visible. Using the particle analysis tool, this value was used to measure the area of the image filled by cells. Secondly, the threshold in the connexin images was adjusted to overlay the areas with positive staining. Using the particle analysis tool the number of positive particles and their average size were extracted. The number of particles was then normalised to the cell area in the image. The average values in 3 regions per PV (slice) of 3 animals per group were plotted using Prism 6.0.

2.3. Electron microscopy

2.3.1. Solutions and compounds in electron microscopy

0.2 M phosphate buffer contained 36 mM $NaH_2PO_4.H_2O$ (VWR International Ltd, Australia) and 164 mM Na_2HPO_4 (Fisher Scientific Ltd, UK).

0.1 M phosphate buffer contained 18 mM $NaH_2PO_4.H_2O$ (Sigma-Aldrich, St. Louis) and 82 mM Na_2HPO_4 (Sigma-Aldrich, St. Louis).

2 % PFA (Sigma-Aldrich, St. Louis) contained 666.67 mM PFA in 50 ml distilled water and 50 ml 0.2 M phosphate buffer.

Storage solution contained: 124.05 mM ethylene glycol (Sigma-Aldrich, St. Louis), 725.5 mM sucrose (Fischer Scientific Ltd, UK) and ~ 350 ml 0.1 M phosphate buffer.

Epon medium resin was prepared by mixing 20 ml of Agar 100 resin, 16 ml of dodecenyl succinic anhydride (DDSA), 8 ml of benzyl dimethylamine (BDMA) and 1.3 ml of methyl nadic anhydride (MNA). All of the compounds used to prepare Epon were purchased from Agar Scientific Ltd, Essex, UK.

2.3.2. Processing of lung slices and NRVMs for electron microscopy

For EM studies, it is important to preserve the ultrastructure as close to the *in vivo* situation as possible. In this thesis, the ultrastructure in PVCs (lung slices), atria, ventricles and NRVMs was studied. Atria and ventricles were cut into small strips before fixation. NRVMs were gently scraped off the surface, pelleted by centrifugation and the pellet was fixed. Lung slices, atria and ventricles were fixed with 4 % PFA overnight whereas NRVMs were fixed with 4 % PFA for 15 minutes. Lung slices and NRVMs were then washed twice in PBS and kept in the fridge until use. After primary fixation, slices, atria and ventricles were post-fixed with 1 % osmium tetroxide for 1 – 2 hours and 30 minutes for NRVMs. All cells were then washed three times with 0.1 M phosphate buffer before undergoing ascending dehydration with acetone. The Table 2.2 below lists the AnalaR reagents and dehydration times used:

AnalaR reagent	**Dehydration time**	
	Lung slice and NRVMs	Atria and Ventricles
30 % acetone	5 min	10 min
50 % acetone	5 min	10 min
70 % acetone	5 min	10 min
90 % acetone	5 min	10 min
100 % acetone	10 min	20 min
100 % acetone over a molecular sieve	10 min	20 min

Table 2.2. List of AnalaR reagents and dehydration times.

Lung slices, atria, ventricles and NRVMs were then incubated in 50:50 epoxy resins: acetone and left overnight on a rotating mixer. The following day, the tissues were incubated in a freshly prepared epoxy resin for 2 - 4 hours on a rotating mixer without caps to allow excess acetone to evaporate. Soon after, lung slices were removed from the epoxy resin and laid flat between clean aclar sheets. Weights were put on top of the aclar sheets whilst-polymerising them at 60°C for 24 - 48 hours. Simultaneously, capsules with unique identification codes were filled with epoxy resin and polymerised for 24 - 48 hours at 60°C. Once they are polymerised, each capsule with a unique code was stuck on top of aclar layer with a lung slice and left to polymerise at 60°C for 24 hours before sectioning.

Atria, ventricles and NRVMs were put in moulding wells containing epoxy resin and were polymerised at 60°C for 24 - 48 hours. For atria and ventricles, unique codes were stuck to the bottom of each moulding wells to identify the tissues. For NRVMs, codes were stuck to the bottom of Eppendorf tubes.

After dehydration and embedding, the tissues were sectioned using a Leica ultracut microtome (UCT; Leica Microsystems Ltd). For lung slices, a trapezoid shape is made around the pulmonary vein using a razor blade whereas for the atria and ventricles, a trapezoid shape can be made anywhere in the tissue. Semithin sections are cut ~ 0.5 µm in thickness on an ultramicrotome using glass knives and collected on plastic boats. A sable paint brush was used to transfer each semi-thin section to a microscope slide, dried on a hot plate and stained with 1 % toluidine blue for ~ 3 minutes until a gold rim is visible around the drop of stain. Once they are stained, toluidine blue was washed off with distilled water and the section was examined on a light microscope. Using a diamond knife, ultra-thin sections were cut ~70 nm in thickness and collected on copper grids (2 x 1 mm – Agar Scientific Ltd, UK) and left to dry in petri dishes with filter paper. After drying, ultrathin sections were counter-stained with 4 % uranyl acetate for 30 minutes and lead citrate for 10 minutes with three washes with deionised water in between. Imaging was done using a JEOL 1400 TEM (JEOL, Japan).

2.3.3. Transmission electron microscope settings

A JEOL 1400 Transmission electron microscope was used for taking electron microscope images. An 80 kV electron beam gun was used for excitation and images were taken with a XR60 camera (Advance microscopy techniques (AMT), Woburn, MA, USA). The spot size was set at 2 µm. The software used for taking images was AMTV600 (AMT, Woburn, MA, USA).

2.3.4. Electron microscopy image analysis

Electron micrographs were analysed using ImageJ by setting the scale using the scale bar from the EM images. Images that showed post mortem changes (i.e. severe loss of myofibrils, myofibrils appearing stretched and the presence of extracellular spaces) were excluded from the analysis. Low magnification images (<1000X) were also excluded from the quantifications as it was difficult to see the outline of organelles like mitochondria.

2.3.4.1. Analysis of mitochondrial number and size

Mitochondria were outlined manually in ImageJ to measure their area. In addition, the number of mitochondria per image was counted. Counting of mitochondria was done manually by visual inspection of the images and converted to the number of mitochondria per 50 μm^2. For both lung slices and NRVMs studies, only intermyofibrillar mitochondria were analysed because of the lack of sufficient images to analyse number and size of perinuclear and sarcolemmal mitochondria. Three images from three animals per age group were analysed for each, PVCs, atrial and ventricular myocytes. Overall, ~ 90 mitochondria were analysed from 3 animals per age group. In NRVMs images, 22 images from 2 litters per group were analysed. For the statistical analysis, the average mitochondrial size per image or the absolute number of mitochondria per 50 µm² were compared. As dehydration can shrink the tissue, we used the distance between sarcomeres as an indicator for possible shrinkage. The average distance between sarcomeres in cardiomyocytes and PVCs is 1.8 µm, a fact that we confirmed using immunofluorescence staining in lung slices that underwent less processing (Chapter 3). This distance can be used as a molecular ruler (Soeller and Cannell, 1999). The 'shrinkage factor' for each image was calculated by dividing the expected sarcomere length (1.8 µm) with the actual sarcomere length. The 'shrinkage factor' was applied for calculating the mitochondrial area. Table and graphs were plotted using Microsoft Excel and GraphPad Prism 6.0.

2.3.4.2. Analysis of the organisation of myofibres

The organisation of myofibres and width of sarcomeres was analysed in ImageJ as described in detail in Chapter 3, section 3. 6.1.1.

2.4. Ca^{2+} imaging

2.4.1. Solutions and compounds for Ca^{2+} imaging

sHBSS see Section 2.1.1.1.

Calcium-sensitive fluorescent indicator: Cal-520™ AM (Stratech, UK).

Drugs were purchased from various suppliers: BTP2 / YM - 58433 (Tocris, UK), carvedilol (Enzo Life Sciences, USA), dantrolene (Tocris, UK), Isoproterenol (Sigma-Aldrich, St. Louis), JTV – 519 (Sigma-Aldrich, St. Louis), Propranolol (Sigma-Aldrich, St. Louis), Norepinephrine

(Sigma-Aldrich, St. Louis), SN-6 (Tocris, UK), trolox (Sigma-Aldrich, St. Louis) and verapamil (Sigma-Aldrich, St. Louis).

2.4.2. Indicator loading and microscope setting for imaging lung slices

For imaging experiments, lung slices were mounted on custom built chambers sealed with silicon grease. A fine nylon mesh was placed on top of the slices to allow solution changes without moving the slice (see Figure 2.2 below).

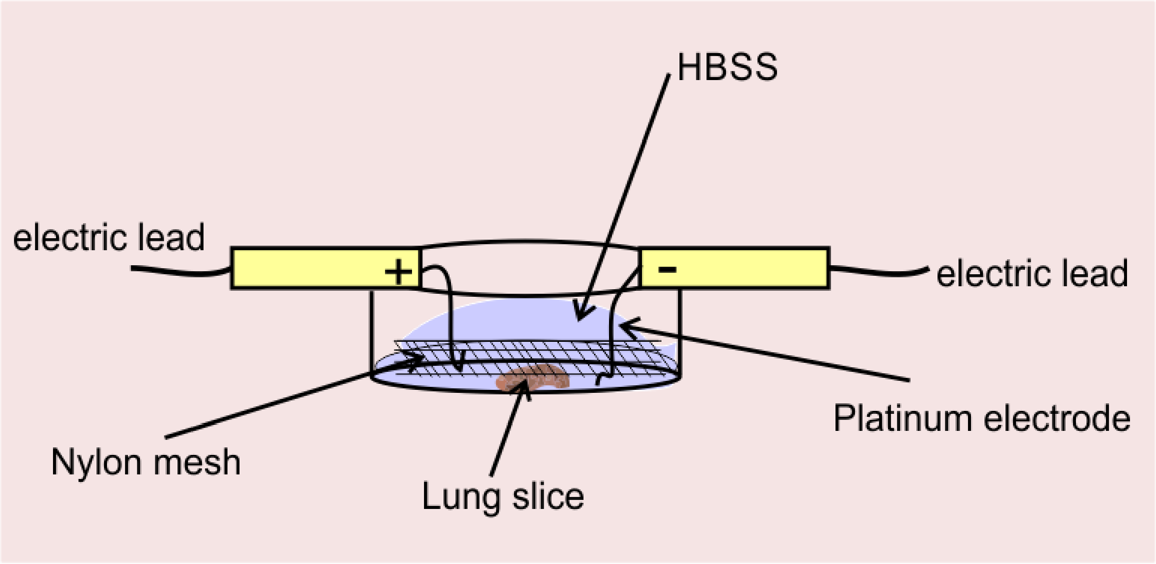

Figure 2.2. Imaging chamber and components needed to measure changes of Ca^{2+} in PVCs within a lung slice. An example of a set-up of an imaging chamber used to measure changes in Ca^{2+} in slices. The chamber contains a nylon mesh to stop a slice moving whilst changing solutions and platinum electrodes which were connected to a Grass instrument simulator SD9.

The Ca^{2+} indicator was used in its AM-ester form to allow good loading into the cells. The AM-ester group mask the charged groups of the indicator, which enables the charged indicator molecule to cross the plasma membrane by diffusion. Once inside the cell, the ester groups are cleaved off the indicator by endogenous cytoplasmic esterases to generate the active Ca^{2+} -sensitive indicator. This process is called de–esterification. Upon Ca^{2+} binding, the emission intensity of the dye alters. In case of Cal-520, it increases. These changes in fluorescence can be detected, calibrated and interpreted as fluctuations in the intracellular Ca^{2+}concentration.

For these experiments, lung slices were loaded with 10 µM Cal-520^{TM} AM (AAT Bioquest, USA) in sHBSS for 1 hour at room temperature in the dark. The loading solution also contained 0.1 % Pluronic F127 (Life Technologies) to aid the indicator transfer over the cell membrane and 200 µM sulfobromophthalein (Sigma), to prevent dye leakage from the cells. The loading was then followed by a de-esterification period of at least 30 minutes in the presence of sulfobromophthalein. Imaging was performed on the Zeiss 510 META Laser Scanning Microscope (LSM) (Carl Zeiss, Germany).

Cal-520^{TM} AM was excited at 488 nm and the emitted fluorescence was collected with a bandpass filter at wavelengths above 505 nm. The numerical aperture was set at 2.0 µm.

Videos were collected at 10 Hz (10 frames per second), 120 x 120 pixels and imaged with a 63X oil immersion objective. Line scans were performed at ~ 333 Hz (333 frames per second).

All images were taken using the following settings: x, y planes, 12-bit images, 1024 x 1024 pixels, unidirectional scan and 63X magnification on an oil immersion objective. The specimens were excited with an Argon/2 laser (wavelength 488 nm) and HeNe1 (wavelength 561 nm). Image analysis was performed using ImageJ (National Institutes of Health, Bethesda, Maryland).

For EFS, pulses of sine wave current of ~ 4.2 - 8 mAmps, 60 V and 10 ms duration were applied using a Grass Instruments SD9 simulator and platinum electrodes placed at each end of the slice (Figure 2.2 above). The stimulation frequency was set at 1 Hz, 3 Hz or 5 Hz.

2.4.3. Indicator loading and microscope setting for imaging NRVMs

NRVMs grown on laminin coated glass coverslips were mounted on custom built imaging chambers sealed with silicon grease (Corning). No nylon mesh was necessary to keep the cells in place as these adhered to the laminin-coated glass coverslips.

NRVMs were loaded with 10 µM Cal-520^{TM} AM (AAT Bioquest, USA) in presence of 0.1 % Pluronic F127 (Life Technologies, UK) for 30 minutes in the dark at RT, followed by a 30 minutes de – esterification period. Imaging was performed at the Leica widefield epifluorescence imaging system, using a 20X air objective (numerical aperture 0.4) (Leica, UK).

Cal-520^{TM} AM was excited at 488 nm and the emitted fluorescence was collected at wavelengths above 505 nm, the K_d for Ca^{2+} affinity is 320 nM.

For EFS, NRVMs were stimulated with 60 V, 10 ms duration pulses generated by a Grass Instruments SD9 simulator set to 2 Hz. Platinum electrodes were placed at the opposing sides of the imaging chamber.

Videos were collected at a frequency of 12 – 20 frames per second using 4 x 4 binning. The intensity was set at 5, the gain at 10, the exposure time at 50 ms.

2.4.4. Ca^{2+} imaging analysis

2.4.4.1. Analysis of the spontaneous activity and pacing in lung slices

To assess the frequency of the spontaneous activity and the ability of PVCs to follow EFS, line scans were collected for 18 seconds on the confocal microscope. The experiments were performed as follows:

1. Slices were paced with 1, 3 and 5 Hz for 12 second.

2 6 seconds recording without any EFS.

Phase 1 allowed to see whether the slices can respond to EFS pulses with regular responses and to analyse whether EFS suppressed the frequency of the spontaneous activity. Phase 2 showed whether the EFS affects the frequency of spontaneous activity following after cessation of the pulses in PVCs from 3 and 24 month-old mice, and to see if any APs occur after the end of the EFS.

ImageJ was used to open LSM files and the experiments were analysed as illustrated in Figure 2.3. Regions of interests (ROIs) were placed inside the cells and in the background (Figure 2.3B) and the changes in fluorescence over time in the ROIs were extracted. Fluorescence profiles, similar to the traces in Figure 2.3, were plotted in GraphPad Prism 6.0, and the changes in fluorescence at any given time (F) was normalised to the minimum fluorescence (F_0) and then expressed as F/F_0 (Figure 2.3D). To assess the frequency of Ca^{2+} waves (Figure 2.3C-E) these were counted over time, calculated as transients per second and expressed in Hz. To assess the percentage of PVCs following pacing, 3 different regions along the PV were imaged per slice. Successful pacing was defined as PVCs responding to all EFS pulses in a continuous train of pulses. Whether a

Ca^{2+} transient was a response to an EFS pulse was judged by the appearance of vertical lines in line scan images or the rate of rise of the Ca^{2+} transients as described in Table 4.1. For quantification of the average percentage of PVCs following pacing per slice was analysed. To compare the level of activity and the pattern of responses to EFS in slices from 3 and 24 month-old mice, the number of slices showing an activity below or above 0.5 Hz was counted. To compare pattern of responses to EFS, the number of slices showing regular responses, alternans or irregular responses (defined in Chapter 4, Section 4.5 was counted.

To calculate the amplitude of the Ca^{2+} transients, the changes in F/F_0 were calculated as follows: maximum amplitude of the transient – minimum amplitude of the transient. These were called $\Delta F/F_0$. The calculation was done manually in GraphPad Prism 6.0 by measuring amplitudes of the Ca^{2+} transients (Figure 2.3E). To avoid bias, for cells with a frequency of > 0.6 Hz (> 10 transients / 18 seconds imaging period) and variable amplitudes of global Ca^{2+} transients, $\Delta F/F_0$ was calculated for a minimum of 10 global Ca^{2+} transients to measure an accurate average amplitude. For PVCs with a frequency of < 0.6 Hz, all of the Ca^{2+} transients were measured to calculate the average $\Delta F/F_0$. The transient amplitude contributed to the classification into local Ca^{2+} transients or Ca^{2+} wave as explained in detail in Figure 4.2 and Table 4.1.

The transient durations (TD_{50}) was calculated as the time it takes for Ca^{2+} transients to reach half maximal amplitude. It was calculated by measuring the time differences (T1 – T2) for $\Delta F/F_0$ to reach the half maximal value (Figure 2.3E).

All data were presented as means ± S.E.M. of the activity per slice. Details of the statistical analysis were given with the Figures.

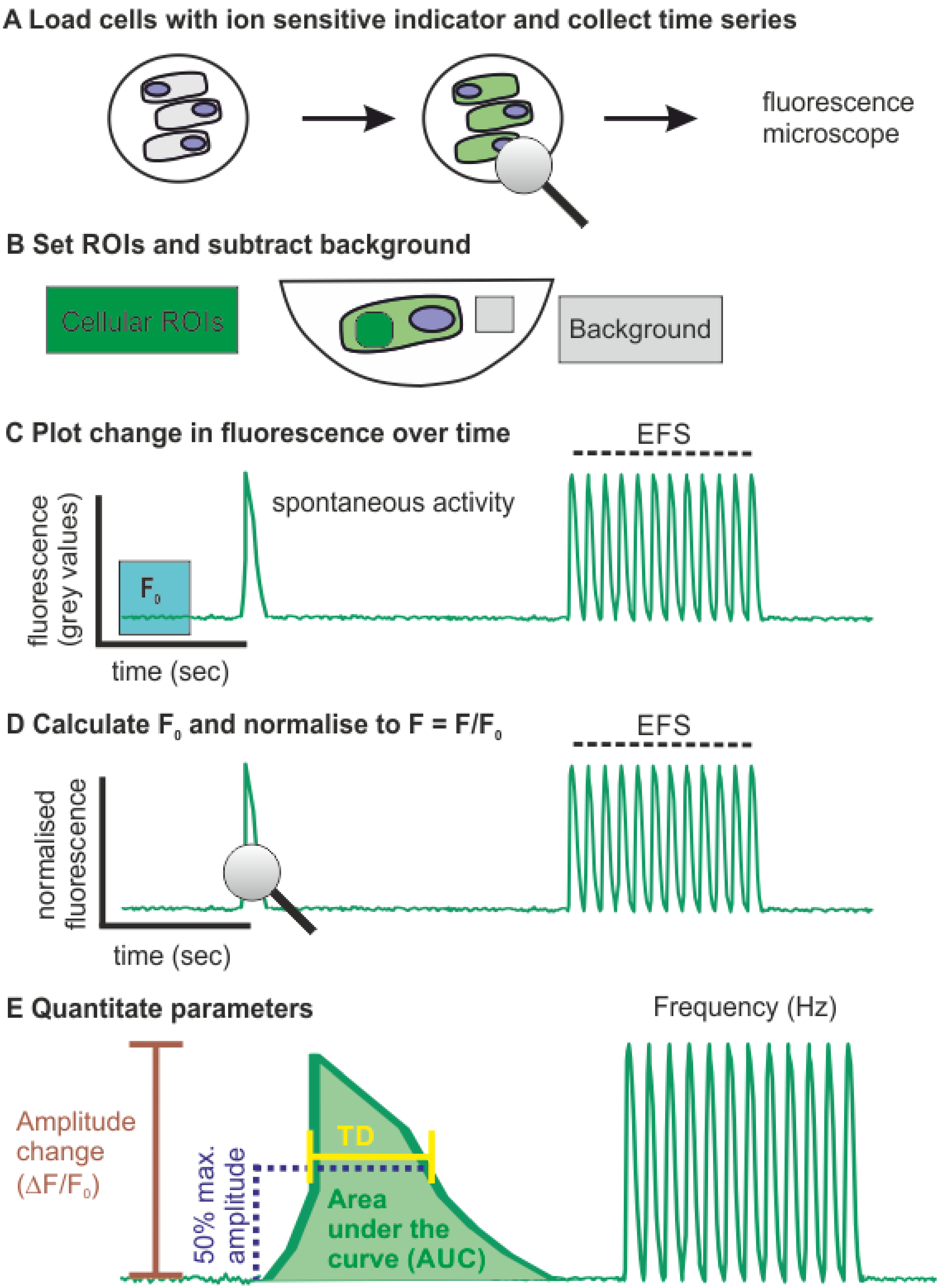

Figure 2.3. Ca^{2+} imaging analysis. Panel **A** illustrates loading of the cells with fluorescent Ca^{2+} indicators, **B** the setting or regions of interest (ROI), **C** the Ca^{2+} traces as change in absolute fluorescence over time, which will be normalised to the minimum fluorescence (F_0) found in the same cell, shown in **D**. **E** illustrates the various parameters of the Ca^{2+} transients that were quantified.

2.4.4.2. Analysis of the spontaneous activity and pacing in NRVMs

A minute before imaging, NRVMs were paced at 2 Hz for 10 seconds to balance possible differences in the SR Ca^{2+}-content between control and HU-treated cells. NRVMs were imaged as follows:

1. 10 seconds *pre* EFS.
2. 10 seconds with 2 Hz EFS.
3. 10 – 30 seconds *post* EFS.

This protocol allowed to quantify the frequency of the spontaneous Ca^{2+} transients before applying pacing (phase 1), the ability of NRVMs to follow electrical pacing (phase 2) and the frequency of the spontaneous Ca^{2+} transients after 2 Hz EFS (phase 3). For analysis, 2 – 3 regions per coverslip were imaged as described above on 3 coverslips per condition from 3 separate litters. ImageJ was used for opening LSM files. Ca^{2+} traces were plotted using GraphPad Prism 6.0 and data were presented as means ± S.E.M. of the activity per coverslip.

2.4.4.3. Analysis of drug effects in lung slices

For analysing the effects of various drugs, mentioned in Chapter 4.4, videos were collected on the confocal microscope to analyse the spontaneous activity before and after drug treatments as follows. The line-scans were 18 seconds long and taken at a rate of 333 frames per second.

Run 1 (before drug treatment):

1. 18 seconds where no stimulus was applied to the cells (in this period only spontaneous Ca^{2+} signals occurred).
2. 18 seconds long, 12 seconds with application of 1 Hz EFS and 6 seconds where no stimulus was applied.

Following Run 1, the lung slices were superfused with a drug on stage and left for a 10 minutes period before starting Run 2.

Run 2 (after drug treatment):

1. 18 seconds where no stimulus was applied to the cells (in this period only spontaneous Ca^{2+} signals occurred).
2. 18 seconds long, 12 seconds with application of 1 Hz EFS and 6 seconds where no stimulus was applied.

ImageJ was used to open the files and ROIs were selected to measure the changes in cytosolic Ca^{2+} on the same cells over time for Run 1 and Run 2. For the analysis, 3 - 5 slices per animal were analysed in 4 - 5 animals per age group. Data were presented as means ± S.E.M. for the activity per slice.

2.4.4.4. Analysis of drug effects in NRVMs

To analyse the effects for various drugs in NRVMs, listed in Chapter 4.4, videos were taken to compare the spontaneous Ca^{2+} transients *pre* and *post* 2 Hz EFS, and the ability of cells to follow 2 Hz EFS. The recording in NRVMs lasted 50 seconds with an image acquisition frequency of 12 frames per second as follows:

Run 1 (before drug treatment):

1. 10 seconds where no stimulus was applied to the cells (in this period only spontaneous Ca^{2+} signals occurred).
2. 10 seconds with application of 2 Hz EFS.
3. 30 seconds where no stimulus was applied to the cells.

Following Run 1, the lung slices were superfused with a drug on stage and left for a 10 minute period before starting Run 2.

Run 2 (after drug treatment):

4. 10 seconds where no stimulus was applied to the cells (in this period only spontaneous Ca^{2+} signals occurred).
5. 10 seconds with application of 2 Hz EFS.
6. 30 seconds where no stimulus was applied to the cells.

For quantification, 6 coverslips were imaged per condition from 2 litters. Data were presented as means ± S.E.M. of the activity per coverslip.

2.5. Assessing mitochondrial membrane potential in NRVMs

2.5.1. Solutions and compounds for measuring the mitochondrial membrane potential

JC-10 (AAT Bioquest, USA).

MitoTracker (579 nm / 599 nm; excitation / emission) (Life Technologies, USA).

Anti-, Oligomycin (Sigma-Aldrich, St. Louis).

2.5.2. Microscope settings for assessing the mitochondrial membrane Potential

To measure the mitochondrial membrane potential, the cells were stained with 50 µM JC-10 (AAT Bioquest, USA) for 30 minutes. To avoid artefacts in the results caused by different loading, the loading conditions were kept similar and to the exact timings. Following the staining period, NRVMs were briefly washed with HBSS before being imaged on the Leica imaging system. JC-10 was excited at 450-490 nm (green images)/ 590-650 nm (red images) and emission was measured above 650 nm to visualise healthy and depolarised mitochondria. Additionally, NRVMs were also stained with 100 nM MitoTracker (579 nm / 599 nm; excitation / emission) (Life Technologies, USA) for 30 minutes to stain all mitochondria regardless of the state of their membrane potential. Antimycin and Oligomycin (5 µM) were added on stage to depolarise mitochondria.

2.5.3. Analysis assessing the mitochondrial membrane potential

Image analysis was done in ImageJ. Regions of interest were placed inside cells. The change in fluorescence over time were measured and plotted in GraphPad Prism 6.0. For analysis, 5 – 10 images were taken pe*r* coverslip from 3 coverslips on 3 separate days for each condition. Data were presented as means ± S.E.M. of the fluorescence (arbitrary units) values per cell.

2.6. ROS Measurements

2.6.1. Solutions and compounds for measuring ROS levels

ROS Brite ™ (AAT Bioquest, USA).

Antimycin (Sigma-Aldrich).

2.6.2. Measuring Basal ROS levels in lung slices

2.6.2.1. Microscope settings for measuring basal ROS levels in lung slices

To investigate the basal levels of ROS in PVCs from 3 and 24 month-old mice, slices were incubated with 50 µM ROS Brite ™ (AAT Bioquest, USA) for 30 minutes before being imaged on the Zeiss 510 META laser scanning microscope. ROS Brite was excited with 488 nm and emission was measured above 515 nm.

2.6.2.2. Analysis of measuring basal ROS levels in lung slices

The LSM files were opened with ImageJ. PVCs were outlined and the average fluorescence intensity was measured in the whole cells from 3 and 24 month-old mice. For the basal fluorescence, the average of the background subtracted first 10 images was calculated. 3 slices per animal were analysed and a total of 3 animals per group were examined. Data were presented as means ± S.E.M. of fluorescence per slice.

2.6.3. Measuring basal and inducible ROS levels in NRVMs

2.6.3.1. Microscope settings for measuring basal and inducible ROS levels in NRVMs

Control and HU treated NRVMs were incubated with 50 µM ROS Brite ™ (AAT Bioquest, USA) for 30 minutes and imaged with a Leica widefield imaging system. ROS Brite ™ was excited at 488 nm and emission was measured above 515 nm. NRVMs were imaged for

120 seconds at a frequency of 25 frames per second with a 20X objective, numerical aperture 0.4.

2.6.3.2. Analysis of measuring basal and inducible ROS levels in NRVMs

For the basal fluorescence, the average of the background subtracted first 10 images was calculated. The inducible fluorescence was measured by normalising the background subtracted fluorescence at any given time (F) to the minimum fluorescence (observed at the beginning of the experiment) (F_0) and expressed as F/F_0. ROS production was induced by addition of 10 µM antimycin 10 seconds after starting the imaging experiment. ImageJ was used to open LIF files. The cells were outlined and used as ROIs, and changes in their fluorescence were analysed. Data were presented as means ± S.E.M. of fluorescence per coverslip.

2.7. Autophagy assay in NRVMs

2.7.1. Solutions and compounds for the autophagy assay

CYTO-ID kit (Enzo).

Loading buffer plating medium (see Section 2.1.1.2), supplemented with 1 mM non-essential amino acids (Gibco) and 1 mM sodium pyruvate (Gibco).

Nutrient rich medium contains the assay buffer (Enzo) supplemented with 1 mM non-essential amino acids (Gibco) and 5% FBS.

2.7.2. Microscope settings for the autophagy assay

Autophagy was measured in control and HU treated NRVMs by using a CYTO-ID autophagy detection kit (Enzo Life Sciences) and followed the protocol as per manufacturer’s instructions. The cells were removed from the incubator and placed into loading buffer before staining with the autophagy kit for 30 minutes according to the manufacturer's instructions. For the measurement of basal autophagy, cells were stained immediately after removing them from the incubator and placing them into loading buffer. In order to see whether autophagy can be induced, and to what extent, NRVMs were treated with 5 µM pp242 (Tocris, UK) for 2 hours in nutrient rich medium, before staining with the autophagy kit for 30 minutes / for the last 30 minutes the autophagy stain was added to the PP242 containing medium. Cells were then imaged with a 63X objective (numerical aperture 1.40) on the Leica widefield imaging system. The green detection dye was excited with 488 nm and emitted fluorescence was collected at wavelengths above 505 nm.

2.7.3. Analysis of the autophagy assays

For quantification, 5 - 6 coverslips per condition (control or HU-treated) from 3 litters were imaged on day 1, 4 and 7 after HU addition. ImageJ was used to open LIF files. Autophagosomes were counted using the particle analysis and nucleus counter plugins in ImageJ. Data were presented as means ± S.E.M. of the number of autophagosomes per region.

2.8. Western blotting

2.8.1. Solutions and Compounds for western blotting

Lysis buffer: (Tris – HCl 20 mM, 1% Triton x-100, NaCl (Sigma-Aldrich, St. Louis) 150 mM, Na_3VO_4 (Sigma-Aldrich, St. Louis) 2µM, leupeptin (Sigma-Aldrich, St. Louis) 2µg / ml, protease inhibitors cocktail concentration 2 µM (Sigma-Aldrich, St. Louis), pH 7.6.

Tris Buffered Saline (TBS): 10 mM Tris-HCL and 150 mM NaCl, pH 7.6.

TBS-T: 0.1% Tween-20 and TBS.

Transfer buffer: (1X transfer buffer contains 5 % 20X transfer buffer solution (Novex, Life Technologies, Carlsbad, CA) with 20 % methanol and distilled water).

Blocking buffer: TBS – 0.1 % Tween + 5 % Marvel milk powder.

2.8.2. Cell lysis and protein quantification

NRVMs grown in T175 flasks were dislodged gently using a cell scraper (Fisher Scientific UK Ltd) and resuspended in ice-cold PBS. Cells were centrifuged at 2500 rpm for 5 minutes at 4°C and pellets were stored at - 80°C. For protein measurement, pellets were resuspended in lysis buffer and lysed for 30 minutes on ice at a rotating platform. Protein concentrations were determined using a Bradford assay (BIO-RAD, UK) according to the manufacturer’s instructions. 2 µl of the undiluted samples were quantified. The BSA standard curve contained absorbance values with different concentrations of BSA. Absorbance was measured at 595 nm using a plate reader (FLUOstar OPTIMA, BMG LABTECH). The standard curve was plotted in GraphPad Prism 6.0.

2.8.3. SDS polyacrylamide gel electrophoresis (SDS PAGE)

10 % SDS PAGE gels were made a few days prior to use by pouring separating gel solution into an empty cassette, 1.0 mm thickness (BIO-RAD, UK) and allowed to solidify for 1 hour. Drops of 70 % Ethanol were added on top to remove any bubbles that forms on top of the separating gel solution. Once the separating gel solution had solidified, stacking gel solution was then poured on top and comb inserted to generate 12 wells and left to solidify. The gels were wrapped in tissue paper moisturised with running buffer to prevent the gels from drying out and stored at 4°C until use. The separating and stacking mixes used to make a single 10 % SDS gel were:

8 ml of 10 % separating gel	5 ml of 6 % stacking gel
3.8 ml ddH$_2$0	2.9 ml ddH$_2$0
2 ml 40 % Acrylamide (BIO-RAD)	0.75 ml 40 % Acrylamide (BIO-RAD)
2 ml 1.5 M Tris pH 8.8	1.25 ml 0.5 M Tris pH 6.8
80 µl 10 % SDS	50 µl 10 % SDS
80 µl 10 % APS	50 µl 10 % APS
8 µl TEMED (BIO-RAD)	5 µl TEMED (BIO-RAD)

Just prior to running the SDS-PAGE gel, the frozen protein samples were thawed and diluted in denaturing solution to achieve an equal loading of 14.6 µg of protein per well. 4X sample buffer (NuPage LDS sample buffer 4X, Invitrogen^{TM}, UK) was added to the samples. The samples were heated at 90°C for 5 minutes to denature the proteins before being loaded into wells. For a molecular marker lane, 5 µl of molecular marker (Invitrogen^{TM}, UK). The electrophoresis tank was set-up and filled to 2/3 depth with running buffer and samples were electrophoresed for 45 – 60 minutes at 150 V.

2.8.4. Semi-dry transfer procedure

The gel cassette was removed from the electrophoresis tank. The SDS gel with proteins was taken out of the cassette and put in Tris Buffered Saline (TBS) whilst the PVDF membrane (Amersham Pharmacia Biotech, UK) was prepared. The PVDF membrane was activated by immersion in methanol for 15 seconds, and then kept for 2 minutes in water before placing it into transfer buffer. Proteins were transferred from the gel to the PVDF membrane by sandwiching a gel with the PVDF membrane in-between transfer buffer-soaked Whatman filter papers and sponges. The sandwich was then soaked in transfer buffer and the transfer was performed by a semi-dry procedure using a POWERPAC 1000 (Bio-Rad, UK) set at 20 V for 2 hours.

2.8.5. Immunostaining (western blotting)

Following the transfer, the PVDF membrane was removed from the transfer system and exposed to PonceauS Red (Boehringer Mannheim, Germany) to check for protein transfer. The positions of the molecular weight markers were labelled on the PVDF membrane. Blotting membrane was then incubated in blocking buffer for an hour at RT.

The blotting membrane was subsequently exposed to primary antibodies diluted in 5 % marvel skimmed milk in TBS-T at 4°C overnight. Table 2.3 below lists the primary antibodies used in this study.

Antibody and isoform	***Concentration***	***Source***	***Catalogue number***
Troponin T, polyclonal rabbit	1:200	CUSABIO	CSB-PA10047A0Rb
SERCA2a, polyclonal rabbit	1:200	CUSABIO	CSB-CL002333DO
PARP1, polyclonal rabbit	1:200	Abcam	Ab151794
Advanced glycation end products, polyclonal rabbit	1:100	CUSABIO	CSB-PA14209A0Rb
p53, polyclonal rabbit	1:200	St. John's laboratory	STJ94890

Table 2.3. List of the antibody used.

The primary antibodies were removed and membrane washed (6 x 5 minutes) with TBS – T. The membrane was incubated for 1 hour with HRP-conjugated secondary goat anti rabbit antibodies, diluted 1:5000 in 5 % marvel in TBS – T. The blots were then washed again with TBS – T (6 x 5 minutes) before being treated with super signal chemiluminescent substrate (Thermo Scientific) for 5 minutes. Images were taken on a GelDoc system (Syngene, Cambridge UK).

2.8.6. Western blotting analysis

Western blots were repeated 3 times for all antibodies tested. Images from the GelDoc system were open with ImageJ and bands were measured and normalised against the intensity of Troponin T in the same lane. Graphs were plotted on GraphPad Prism 6.0 and data were presented as means ± S.E.M.

2.9. Summary of the statistical analysis used in this study

Student's unpaired t-test: This test was performed whilst analysing two different variables. In this study, EM data on mitochondrial numbers and sizes in PVCs from 3 and 24 month-old mice were analysed using unpaired *t*-tests. It was also used for the Ca^{2+} imaging analysis (young *vs.* old), ROS (young *vs.* old) and immunofluorescence (young *vs.* old) experiments.

Paired t-test: This test was performed when analysing the effects of pharmacological tools on the frequency of Ca^{2+} transients in PVCs from both age groups. As the effects of pharmacological inhibitors were tested at different time-points on the same cells i.e. PVCs in young and old animals or in NRVMs whilst testing pharmacological drugs, paired analysis was conducted.

One way ANOVA: This test is performed when we analysed three different variables as in Chapter 5. Those variables were control, 50 µM HU and 500 µM HU treatment. Ca^{2+}

imaging, autophagy and mitochondrial membrane potential experiments in control, 50 µM HU and 500 µM HU treated cells were analysed usning a One way ANOVA.

Fisher's Test: EFS-induced pacing in PVCs during ageing was measured as categorical date (yes/no), and was therefore analysed using a Fisher's test.

For PVCs data, each lung slice was used as an experimental unit. For experiments on NRVMs, each coverslip was used as an experimental unit. For ANP granules / mitochondrial data, lung slices (PVCs) and heart sections (atrial and ventricular myocytes) were used as an experimental unit. All data are expressed as means ± S.E.M.

Chapter 3: A comparative study of the structure of rat pulmonary vein sleeve cells, atrial and ventricular myocytes during ageing

3.1. Introduction

Alterations in the structure of cardiac myocytes have been suggested to occur during ageing and the development of cardiac dysfunction. It is likely that changes in atrial myocytes and PVCs contribute to the susceptibility to arrhythmias such as AF, which increases in both incidence and severity with ageing. Despite evidence for morphological alterations of atrial and ventricular cardiac myoctes occuring during ageing and disease, as described in Chapter 1, structural studies of PVCs during AF or ageing are still limited, and to our knowledge no systematic study comparing atrial, ventricular and PVC cardiac myocyte structures has been performed.

The work presented in this Chapter describes the structure of PVCs *in situ* within murine lung slices. The structure of PVCs is compared with those of atrial and ventricular cardiac myocytes. Electron microscopy (EM), light microscopy and confocal immunofluorescence were used to characterise specific structural and morphological aspects of these cell types, and to examine the expression of key proteins involved in cardiac excitation-contraction coupling. These analyses were performed using 3 month- and 24 month-old mice for each of the cells types, in order to explore putative changes within the cells that may underlie an ageing-related decline in cardiac function.

3.2. Aims of this Chapter

This work described in this Chapter had three main aims:

(1) To undertake a detailed structural characterisation of PVCs using light microscopy, EM, and confocal imaging.

(2) To investigate differences in excitation-contraction coupling and the Ca^{2+} signalsome of PVCs from young and old mice.

(3) To provide a side-by-side comparison of the structure of atrial, ventricular and PVC cardiac myocytes, and to explore putative structural and functional changes occurring in each of the cell types during natural ageing.

3.3. The morphology of murine lung slices, and identifying PVCs within a lung slice

Murine lung slices are an established model that allow PVCs to be studied whilst retaining features such as viability, position, orientation and connections relative to surrounding cells within the pulmonary veins (Rietdorf *et al.*, 2014) (described in Chapter 2, section 2.1.1). A low magnification bright-field image of a lung slice is shown in Figure 3.1A, depicting many of the typical structures seen within a lung slice; pulmonary vein(s), airways, alveolar tissue and pulmonary arteries.

Pulmonary veins are usually readily distinguishable from pulmonary arteries and airways because they are surrounded by an obvious layer of muscle cells. This muscle layer is the sheath of PVCs. However, the correct identification of PVCs was essential for this project, and a number of obvious morphological and positional differences were used to determine the presence of PVCs around a pulmonary vein. For example, PVCs are striated, and depending on the cutting angle used to make the lung slice, the striated pattern of PVCs was visible under a light microscope with sufficient magnification (Figure 3.1B and C). Striated cells are absent from the pulmonary arteries and airways.

Furthermore, the striated PVCs typically displayed spontaneous contractions. Additionally, pulmonary arteries are closely associated with an airway and tend to be collapsed in lung slices; a feature that is not seen with pulmonary veins (Figure 3.1A). Airways can clearly be identified as having a lining of epithelial cells with beating cilia.

The lung slice image presented in Figure 3.1A shows transverse sections through two pulmonary veins, with both veins having obvious PVCs around their outer circumferences. In common with many pulmonary vein slices, the thickness of the PVC layer is not the same around the whole circumference of either vein (Figure 3.1A). Previous studies have established that the PVC layer can vary in thickness and coverage around a pulmonary vein (Ho *et al.,* 2001, Mueller-Hoecker *et al*., 2008). A further reason for the difference in thickness of the PVC layer is that the cut used to make the slice was not fully transverse to the long axis of the pulmonary vein vessel, but rather at an angle. Based on the position and diameter of the veins shown in Figure 3.1A, it is possible to determine that this slice was from a site close to the hilus region, shortly after the main pulmonary vein has branched into two. Whilst it was possible to generally ascribe the position of the lungs / pulmonary vein from which a slice originated, this study did not examine differences between PVCs along the longitudinal section of the vein (e.g., hilus *versus* periphery). Rather, this study was focussed on whether the PVC sleeves were uniform or heterogeneous around the circumference of a vein. For this, slices were chosen for analysis in which the pulmonary veins were obviously transversely cut, such as that shown in Figure 3.1.

Similar to other veins, pulmonary veins have endothelial cells facing the vein lumen, and a thin layer of smooth muscle cells underneath the endothelial cells. The endothelial cells can be seen under the light microscope following toluidine blue staining, as shown in

Figure 3.1B and C. In contrast to the PVCs, the smooth muscle cells are poorly visible under a light microscope without staining, but can clearly be identified in EM images.

Although PVCs were often highly evident in lung slices, this study used a combination of the following criteria to formally identify cells as PVCs: (1) PVCs were associated with (usually surrounding) a blood vessel, (2) PVCs displayed spontaneous contractions, (3) PVCs were not located next to an airway, and (4) PVCs were striated (normally evident in both light and electron microscopy). It should be noted that the presence of striations depended on the angle at which the slice was cut, as discussed below.

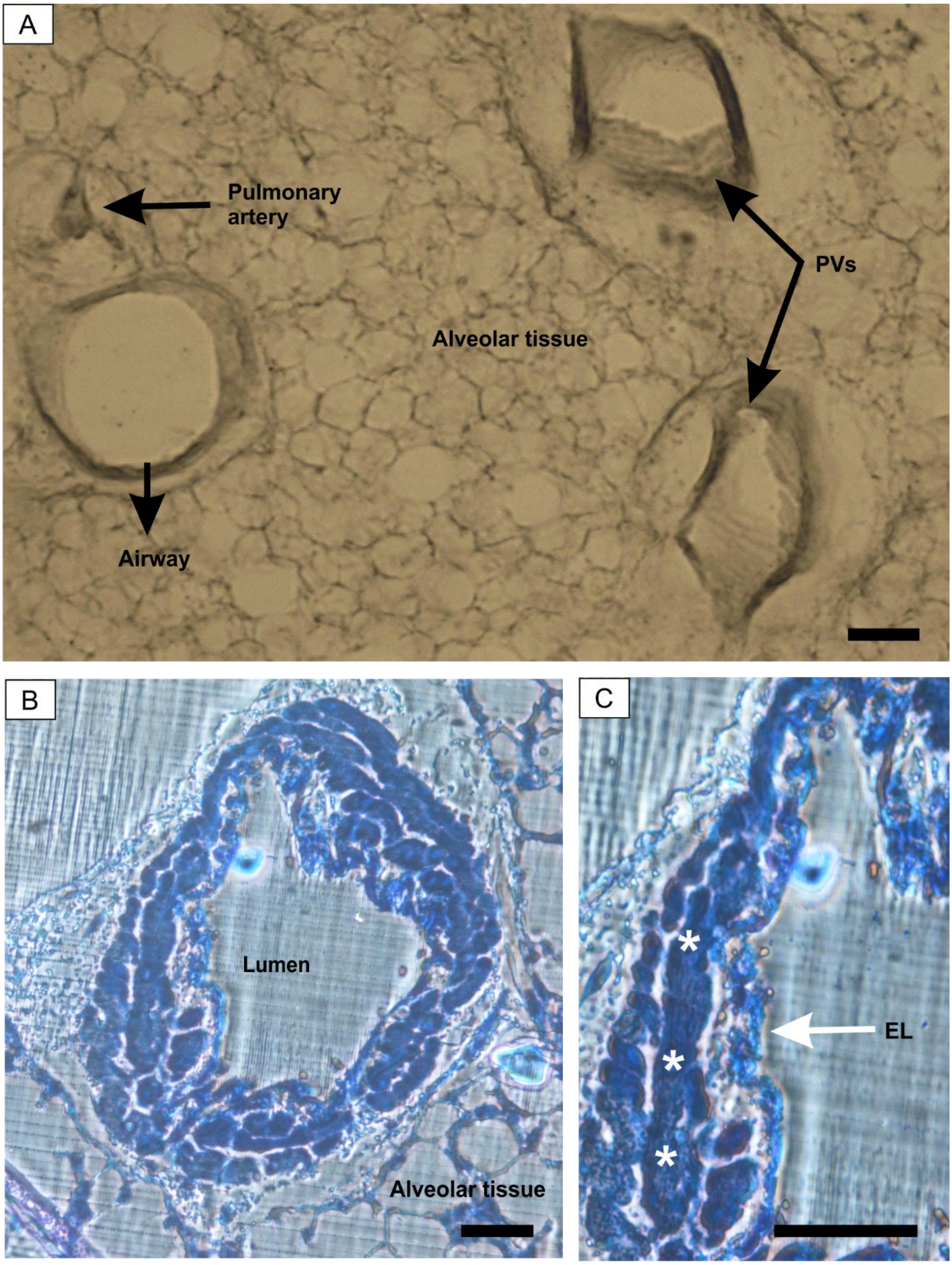

Figure 3.1. Light microscopic images of a lung slice. Panel **A** shows a representative low magnification image of a lung slice, containing two pulmonary veins (PVs), an airway, a pulmonary artery and alveolar tissue. Panel **B** shows a semi-thin lung slice section of a pulmonary vein and the surrounding alveolar tissue. Panel **C** shows a higher magnification of a semi-thin section of the same pulmonary vein as in B. The endothelial layer (EL) and the PVCs (asterisks) are clearly visible. The semi-thin sections were stained with 1.5% toluidine blue for 2 minutes. Scale bar in all panels represent 100 µm.

3.4. Organisation, orientation and structure of PVCs

Each mouse lung slice preparation yielded tens of different slices to examine, and it was possible to obtain slices in which pulmonary veins had been cut at various angles relative to the microtome. The representative low magnification transmission electron microscope (TEM) image shown in Figure 3.2A depicts a pulmonary vein with PVCs located around the outer circumference of the vessel lumen (the areas of PVCs are indicated using red and blue lines). Regions of PVCs from Figure 3.2A are shown at a higher magnification in Figures 3.2B and C.

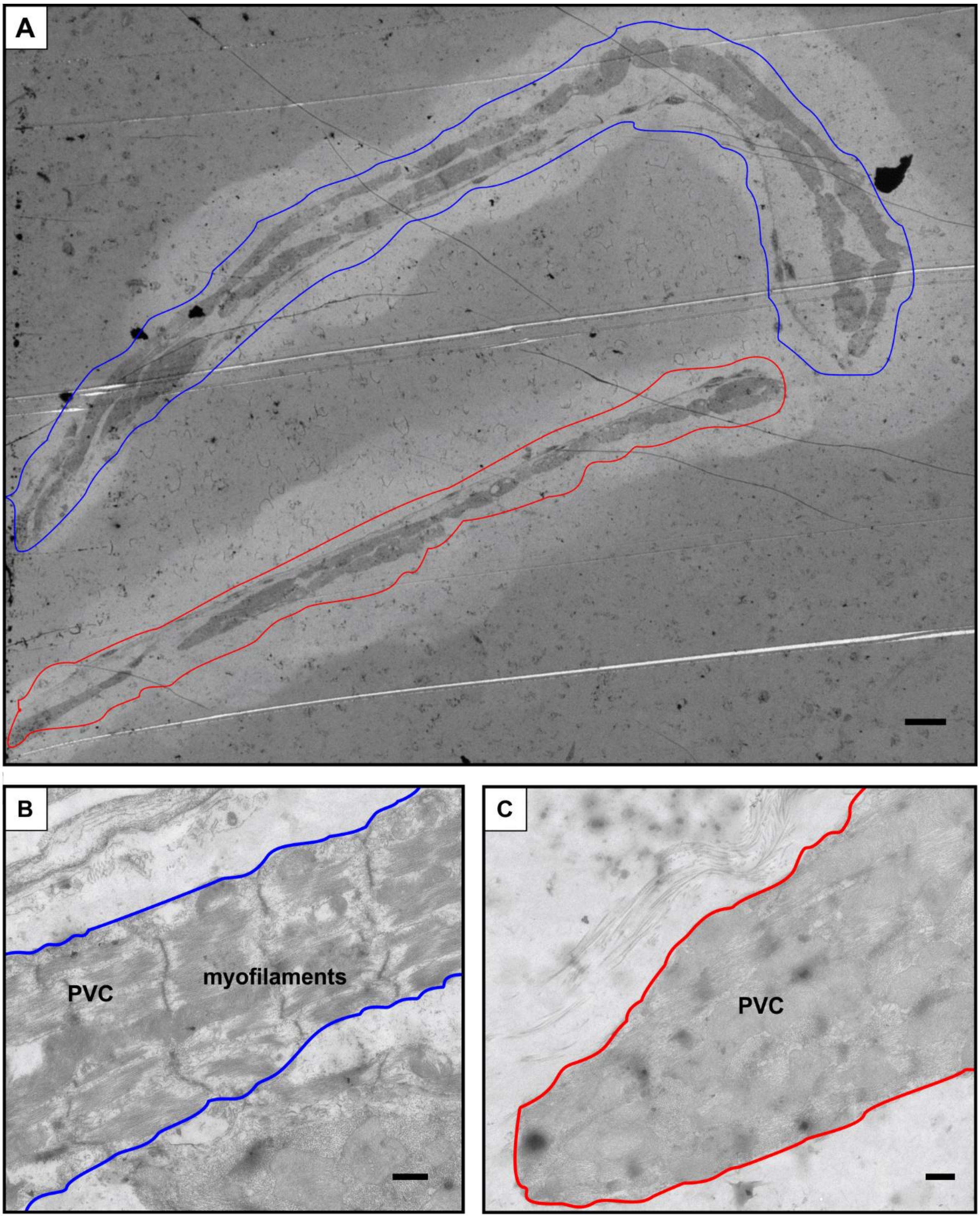

Figure 3.2. The general structure of PVCs. Panel **A** is a low magnification electron micrograph of a pulmonary vein. The scale bar represents 10 µm. Panel **B** a higher magnification image of PVCs containing myofibres with clearly visible Z-lines, imaged from the area outlined in blue in Panel A. Panel **C** is a higher magnification image of PVCs containing myofibres without obvious Z-lines, due to cutting the the slice at an angle in which the z-lines were not evident. The image is taken from the region outlined in red in Panel A. The scale bars in Panels B and C represent 500 nm.

At the lower magnification, shown in Figure 3.2A, both regions of PVCs appear quite similar in terms of cell thickness and contrast. However, the higher magnification images presented in Figures 3.2B and C illustrate a feature of PVCs that was frequently observed in this study; the orientation of the PVCs was not the same around the circumference of a vessel. The image shown in Figure 3.2B depicts PVCs containing myofibres with clear Z-lines. In contrast, the image shown in Figure 3.2C presents PVCs in which Z-lines were not clearly visible. The images in Figures 3.2B and C are of PVCs surrounding the same pulmonary vein, cut at the same angle and treated similarly in every way. The reason for the different appearance of the PVCs is that they had a different orientation relative to the vessel and the cut. The region of PVCs outlined in blue Figures 3.2A and B displays obvious Z-lines because the cells were oriented with their long axis perpendicular to the long axis of the vein. In contrast, the cells outlined in red in Figure 3.2A and C were oriented so their long axis was parallel to the long axis of the vein, and consequently, no Z-lines (or longitudinal myofibres) are visible.

A more detailed view of PVCs within a slice, and their surrounding cells, is shown in Figure 3.3. The portion of a pulmonary vein captured in Figure 3.3A depicts the different layers of cells in the wall of a pulmonary vein; a layer of endothelial cells is facing the vein lumen, followed by a layer of smooth muscle cells between the endothelial cells and the PVCs. The cytoplasm of PVCs is densely filled with myofilaments, which are important for contractile activity. However, of the three PVCs visible in Figure 3.3A, only one of them (outlined in blue) shows myofibres with clear Z-lines. Similar to the situation described for Figure 3.2 above, the PVC outlined in yellow was cut at an angle perpendicular to the direction of the myofilaments. Such a perpendicular cut of the myofilaments is evident on closer inspection of the EM images. For example, the region of the PVC bounded by the dashed yellow box in Panel 3.3A shows two circular bundles of myofilaments end-on. The third PVC (outlined in red) appears to be orientated at an angle that is intermediate between the other two PVCs. This is evident from the appearance of slight Z-lines that are faint and discontinuous. The images presented in Figures 3.2 and 3.3 typify the heterogeneous alignment of the PVCs around a pulmonary vein vessel. Moreover, the heterogeneous alignment was not only evident around different parts of the pulmonary vein, as illustrated in Figure 3.2, but was visible in adjacent PVCs (Figure 3.3). These observations are consistent with other reports suggesting that the alignment of PVCs along a pulmonary vein is heterogeneous (Hocini *et al.,* 2002, Mueller-Hoecker *et al*., 2008).

During the course of this study, through examining numerous EM images, it became evident that PVCs contain three distinct sub-populations of mitochondria, which can be seen in Figure 3.3B. Perinuclear mitochondria (outlined in orange) were localised near the nucleus, and tended to be smaller and more rounded in shape compared to other mitochondria. In contrast, the inter-myofibrillar mitochondria (outlined in blue) were found between the myofibril bundles, and were mostly oval in shape. The inter-myofibrillar mitochondria were the most abundant sub-population of mitochondria found in PVCs. The third sub-population of mitochondria were found in the sub-sarcolemmal region, underneath the sarcolemma (outlined in red). In higher magnification EM images, glycogen granules could be seen in the cytoplasm of PVCs (groups of them are outlined in green in Figure 3.3C). As in atrial and ventricular cardiac myocytes, intercalated discs were found at the junctions between neighbouring PVCs (Figure 3.3D). Intercalated disks are thought to be sites where intercellular communication occurs via gap junctions, thereby allowing individual cardiac myocytes to work as a single functional unit or a syncytium (Ou *et al.,* 2005; Tribulova *et al.,* 2005). Intercalated discs can easily be identified within EM images by the ‘zig-zag’ appearance of the non-electron-dense junctions as shown in Figure 3.3D.

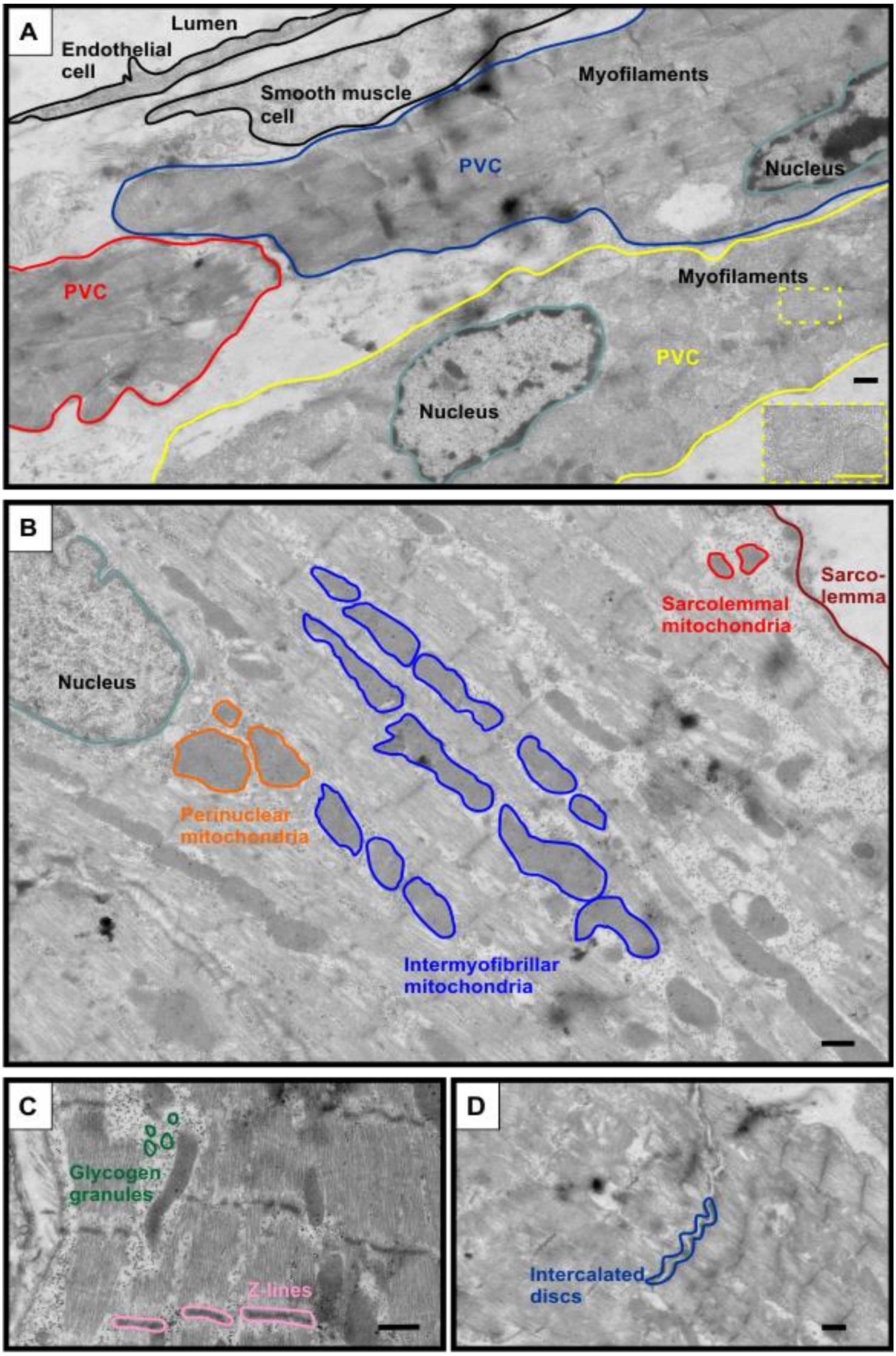

Figure 3.3. Ultrastructural aspects of PVCs. Panel **A** is a representative TEM image showing the endothelial cell layer facing the vein lumen, followed by a layer of smooth muscle cells and then layers of PVCs. Panel **B** illustrates different sub-populations of mitochondria within a PVC. Panel **C** shows examples of Z-lines and glycogen granules within a PVC. Panel **D** illustrates that PVCs are connected via intercalated discs. The scale bars in all panels represent 500 nm.

3.5. Expression and localisation analysis of RyRs and connexins in PVCs

3.5.1. Expression and localisation of RyR2 in PVCs from 3 month- and 24 month-old mice

In atrial and ventricular cardiac myocytes the distance between Z-lines has a consistent spacing of 1.8 µm (Soeller and Cannell, 1999). It has been shown previously that is also true for PVCs from young mice (Rietdorf *et al.,* 2014), but it is unknown if RyR expression or SR structure changes within the PVCs of ageing animals. To examine putative alterations in RyR2 localisation or expression, the distance between Z-lines (i.e., sarcomere length) in PVCs from 3 month- and 24 month-old mice was quantified (Figure 3.5). PVCs were stained with phalloidin (an F-actin stain) and immunolabelled using anti-RyR2 antibodies in conjunction with fluorescently-labelled secondary antibodies (described in detail in Chapter 2, section 2.3). Examples of phalloidin- and RyR2-labelled PVCs are shown in Figure 3.4A and B. It is evident that the RyR immunofluorescence labelling had a regular striated appearance in PVCs from both the young and old animals (Figure 3.4Aii and Bii). RyR2 expression is greatest at the Z-lines in cardiac myocytes, so the bright immunolabelled RyR striations indicate the positions of the Z-lines and underlying SR (Bootman *et al.,* 2006). Merging the phalloidin- and RyR2-labelled images revealed that the Z-lines occurred within gaps in the F-actin staining (Figure 3.4Aiii and Biii). PVCs therefore have a similar structure to atrial and ventricular cardiac myocytes; Z-lines where RyR2 are densely clustered, which signify the edge of sarcomeres, and dense F-actin within the areas between the Z-lines where the contractile filaments are located.

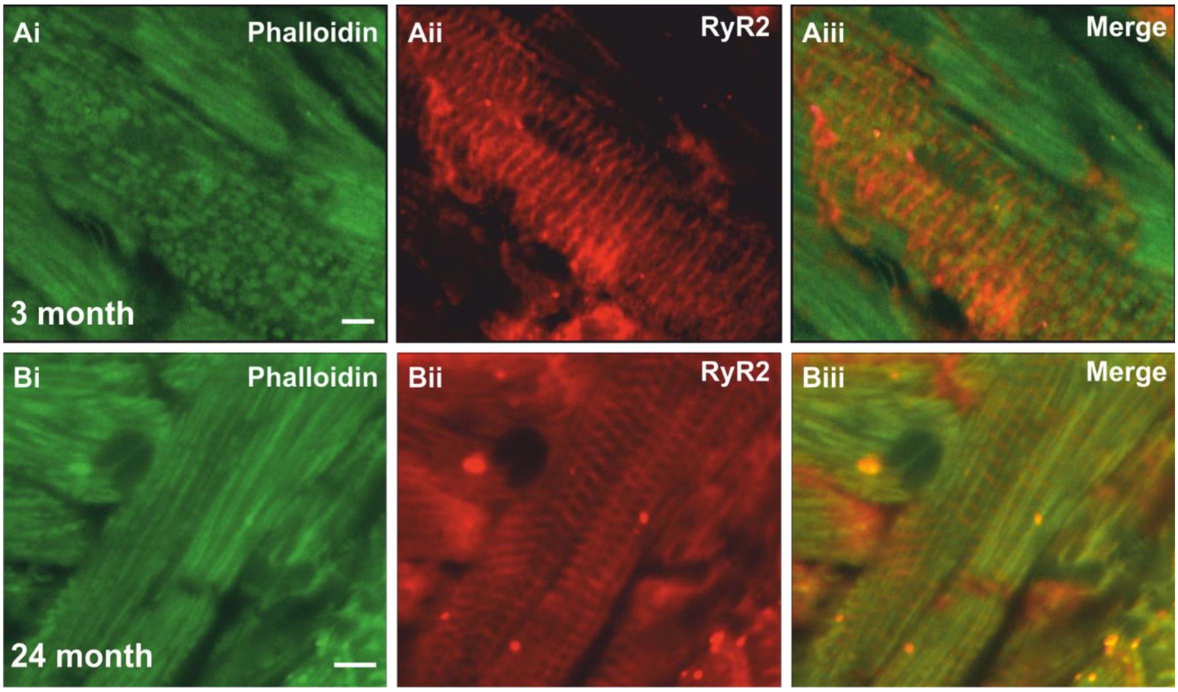

Figure 3.4. Regular striated RyR2 expression in PVCs from both,3 month- and 24 month-old mice. The panels show representative images of cells stained with phalloidin (F-actin) and immunolabelled using an antibody that recognises RyR2 (red). Panels **Ai - iii** represent PVCs from 3 month-old mice, and Panels **Bi - iii** represent PVCs from 24 month-old mice. The scale bars in Panels Ai and Bi represent 5 µm.

Specific labelling of RyR2 provided a means to measure the spacing between Z-lines (sarcomere length), as depicted in Figure 3.5A – B. In brief, the distance between the peak of RyR2 immunolabelled from one Z-line to the next (e.g., arrow in Figure 3.5 Aii) was measured using ImageJ (described in detail in Chapter 2, section 2.3.2). The average distance between Z-lines in 3 month- and 24 month-old mice was 1.74 ± 0.1 and 1.79 ± 0.1 µm, respectively (Figure 3.5C), indicating that there were no significant changes in the spacing between Z-lines or the length of sarcomeres.

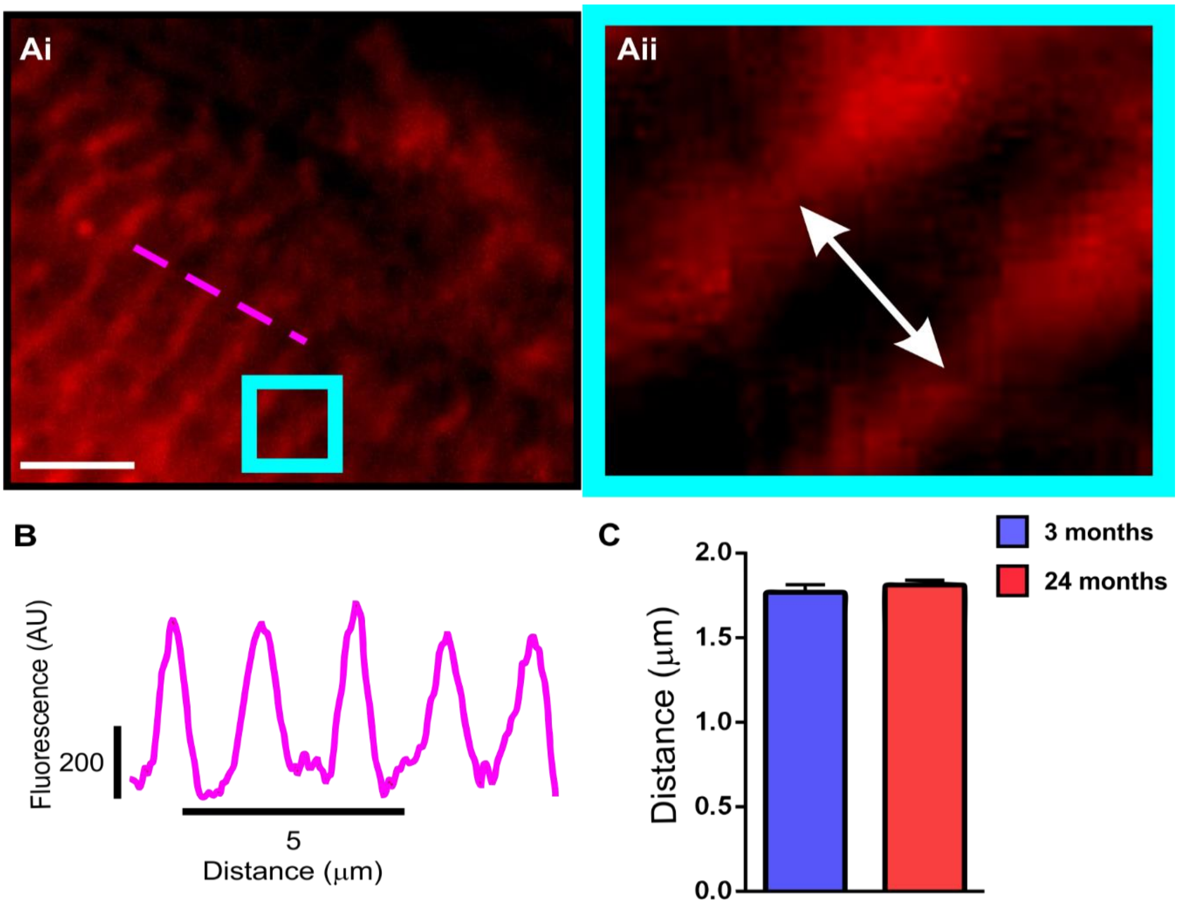

Figure 3.5. Measuring the distance between Z-lines in PVCs from 3 month- and 24 month-old mice. Panel Ai is a representative image of a PVC that was immunolabelled with anti-RyR2 antibodies, and shows that RyR2 was expressed in a striated manner in PVCs. **Panel Aii** is an enlargement of region bounded by the turquoise box shown in Panel Ai. The distance between two adjacent Z-lines is indicated by the white double headed arrow. **Panel B** shows the RyRs immunofluorescence intensity profile along the cell region denoted by the pink dotted line in **Panel Ai**. The peaks represent the Z-lines (striations seen in light microscope images and EM images), where RyR2 are most abundant. **Panel C** is a quantitative representation of the average distance between Z-lines in PVCs from 3 month- and 24 month-old mice, calculated as the average distance over 5 sarcomeres per analysed cell. The data represent the mean ± S.E.M. P = 0.44, calculated using an unpaired Student's *t*-test, *n* = 7 slices from 3 animals for both 3 month- and 24 month-old groups (i.e., 21 slices in total for each age group).

3.5.2. Cx43 and Cx40 localisation in PVCs from 3 month- and 24 month-old mice

A number of studies have shown that cardiac diseases can be associated with a change in the expression of connexins (e.g., Cx43 and Cx40), which are crucial for intercellular communication and electrical continuity between cardiac myocytes (Ou *et al.,* 2005; Tribulova *et al.,* 2005). Altered connexin expression has been associated with an increased predisposition for arrhythmias. Previous studies have shown that PVCs express Cx43, Cx40 and Cx45 (Yeh *et al.,* 2003, Xiao *et al.,* 2016, Kugler *et al.,* 2017), and as for other cardiac myocytes they likely to be responsible for intercellular propagation of messengers and electrical impulses. As described in Chapter 1, the triggering of AF by PVCs requires electrical signals originating in the pulmonary veins outside the heart to propagate into the left atrial chamber. Given that connexins underlie the spreading of electrical signals between cells, and that PVCs trigger more AF during ageing, the expression of connexins was examined in 3 month- and 24 month-old mice (Figures 3.6 and 3.7).

The PVCs within mouse lung slices obtained from the young and old animals were stained with phalloidin to provide a marker for sarcomeres, cell borders and junctions between cells (Figures 3.6Ai - Di), and immunolabelled using antibodies specific for Cx43 and Cx40 (Figures 3.6Aii – Dii). By merging the phalloidin staining and connexin immunolabelling (Figure 3.6Aiii – Diii), it was evident that Cx43 was localised at the cell-cell junctions, and was also present on the sarcolemma along the lateral sides of the PVCs with cells from both 3 month- and 24 month-old animals (Figures 3.6A and B). The number of distinct spots showing Cx43-immunolabelled pixels, and their average area of the immunolabelled spots, were quantified using ImageJ. There was no statistically significant difference for either of the parameters when comparing the PVCs from the young and old mice (Figure 3.7A).

Cx40 showed a weaker expression in PVCs compared to Cx43 (Figure 3.6C and D). Moreover, Cx40 immunolabelling was found mostly along at cell-cell junctions, with relatively little evidence of Cx40 on the lateral parts of the sarcolemma. In contrast to Cx43, there was a difference in the Cx40 immunolabelling of PVCs from the young and old mice: the number of Cx40-immunolabelled spots was significantly reduced in PVCs from 24 month-old animals compared to PVCs from 3 month-old animals (Figure 3.6C and D and Figure 3.7Bi). In fact, Cx40 immunolabelling was not always detectable in slices when using the same image acquisition parameters as for Cx43-immunolabelled cells. The average area of Cx40-immunolabelled spots tended to be smaller in PVCs from 24 month-old cells compared to cells from 3 month-old animals, but this was not statistically significant (Figure 3.7Bii).

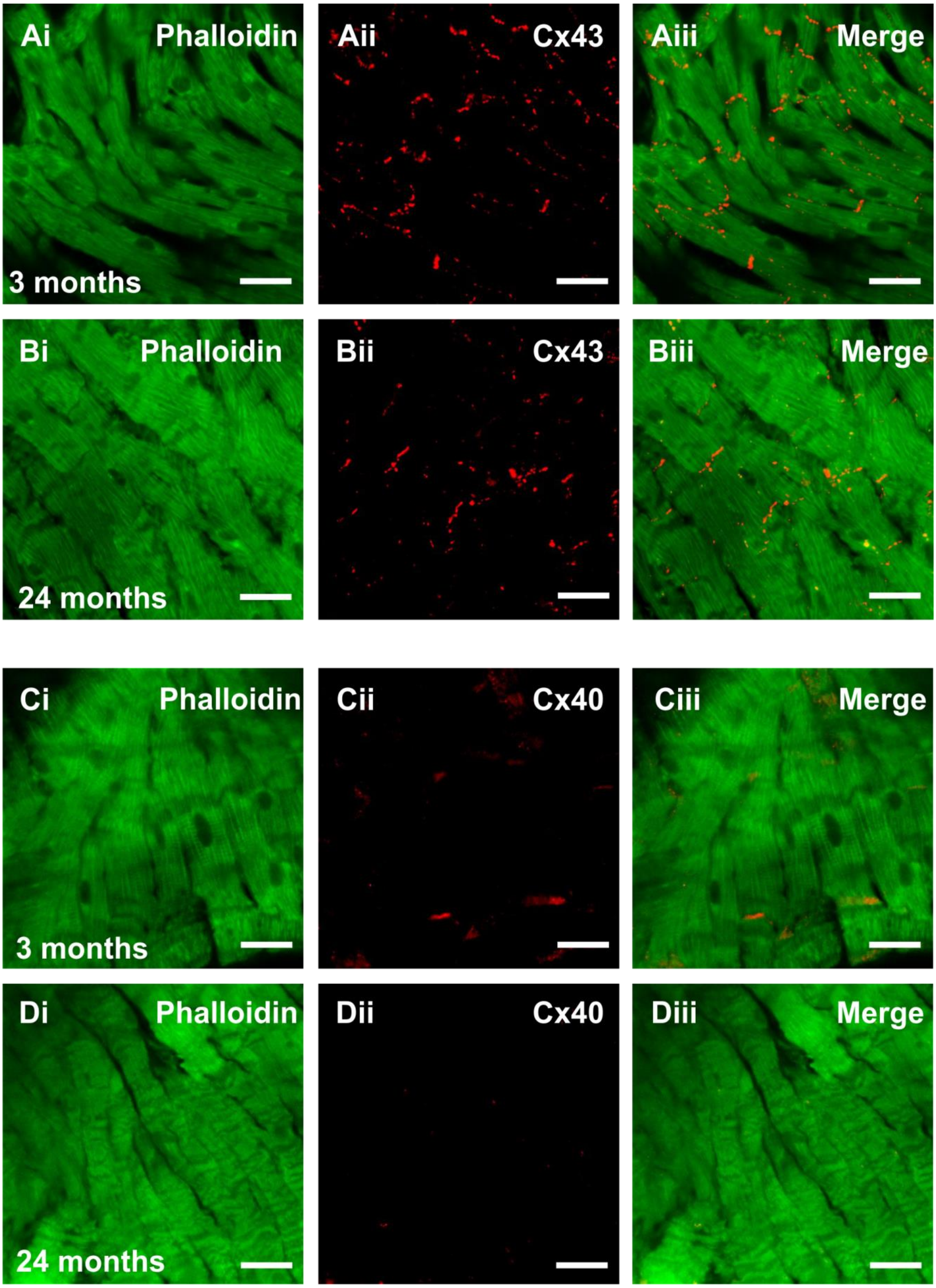

Figure 3.6. Cx43 and Cx40 expression in PVCs from 3 month- and 24 month-old mice. Panels **A** and **B** show representative images of phalloidin-stained and Cx-43 immunolabelled PVCs from 3 month- (Panel **A**) and 24 month-old mice (Panel **B**). Panels **C** and **D** show representative images of Cx40 staining in 3 month- (Panel **C**) and 24 month-old mice (Panel **D**). The scale bars represent 20 µm.

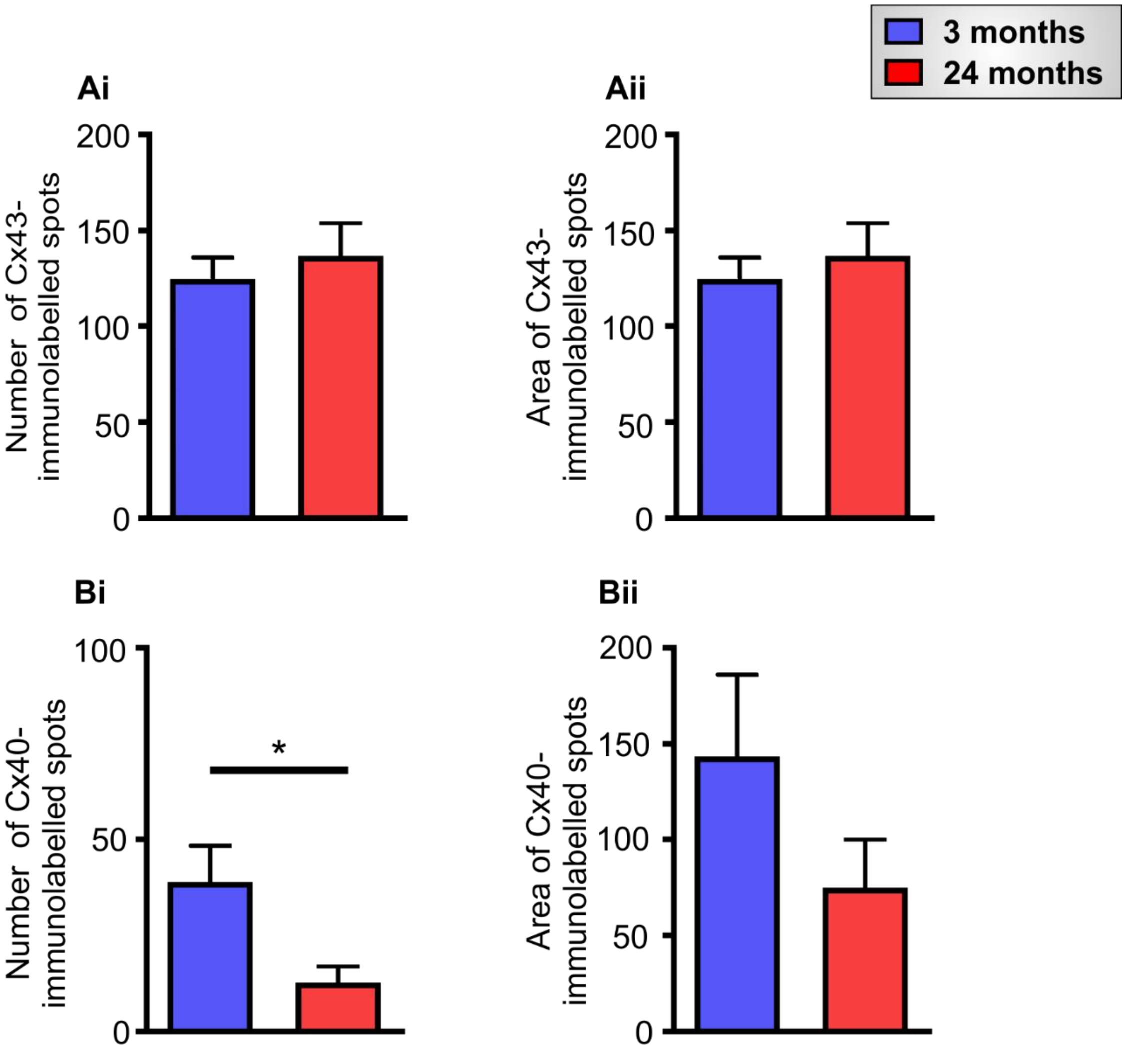

Figure 3.7. Quantification of Cx43 and Cx40 expression in PVCs from 3 month- and 24 month-old animals. Panel **A** shows quantitation of the number of Cx43-immunolabelled spots (i), and average area of the Cx43-immunolabelled spots (ii) in young and old animals. Panel **B** shows quantitation of the number of Cx40-immunolabelled spots (i), and average area of the Cx40-immunolabelled spots (ii) in young and old animals. The data are presented as mean ± S.E.M. Statistical significance was calculated using an unpaired Student's *t*-test, * denotes $P < 0.05$. For Cx43, *n* = 27 - 29 slices from 4 animals for both 3 month- and 24 month-old groups. For Cx40, *n* = 7- 8 slices from 2 - 3 animals for both 3 month- and 24 month-old groups.

3.6. Ultrastructural changes in cardiac myocytes during ageing

3.6.1. Ultrastructure of PVCs from 3 month- and 24 month-old mice

3.6.1.1. Myofibre structure

The structure of myofibres within PVCs from young and old mice was examined using high magnification TEM of fixed cells. The EM images of PVCs were quantitated using a number of parameters to provide an objective measure of myofibre content and organisation, as illustrated in Figure 3.8. Specifically, the following parameters were measured:

1. Sarcomere width, which was measured as the distance across myofibre bundles (denoted by blue arrows in Figure 3.8Ai - Aii).
2. The offset between Z-lines in neighbouring sarcomeres, which could indicate displacement of myofibres (denoted by red arrows in Figure 3.8Bi - Bii)
3. The angle between neighbouring Z-lines, which could indicate misalignment of myofibres (denoted by dark red arrows in Figure 3.8Ci - Cii).
4. The percentage of Z-lines disorganisation (Index of disorganisation) was calculated by using the following formula:

   Index of disorganisation = (Z-line offset/sarcomere width) x 100 (Figure 3.8D)

Figure 3.8. The parameters used to analyse the organisation of myofibres in PVCs from 3 month- and 24 month-old mice. Sarcomere width is indicated by the blue lines with double arrowheads, and was measured as the distance across myofibre bundles (Panels **Ai** and **Aii**). The offset was measured as the lateral distance between the Z-lines of adjacent myofibre bundles, as indicated by red arrows (Panel **Bi** and **Bii**). The black dotted extrapolated line was used to indicate the point at which the neighbouring Z-line is located. The angle between neighbouring Z-lines was measured by as indicated by dark red labelling (Panels **Ci** and **Cii**). Panels **Di** and **Dii** illustrate how percentage of Z-lines disorganisation was calculated. The scale bars represent 500 nm.

Ai. Sarcomere width

Sarcomere width was calculated by measuring the transverse edge-to-edge distance across myofibre bundles. Examples of typical measurements are indicated by the blue lines with double arrowheads in Aii.

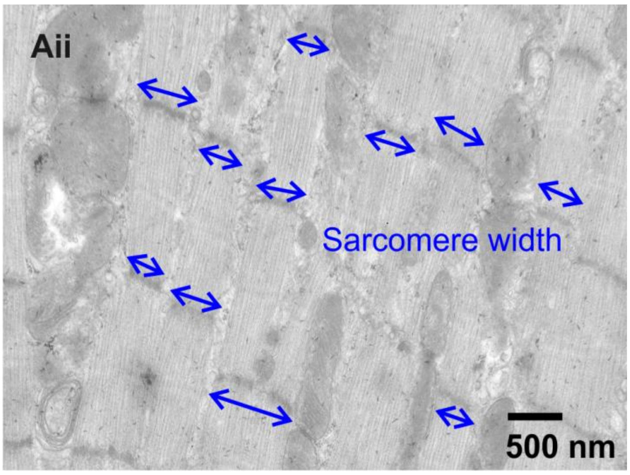

Bi. Offsets between Z-lines

The offset between Z-lines was calculated by extrapolating a line from the Z-line of one myofibre bundle into an adjacent bundle, and then measuring the lateral displacement of the Z-lines. Examples of typical measurements are indicated by the black and red lines in Bii.

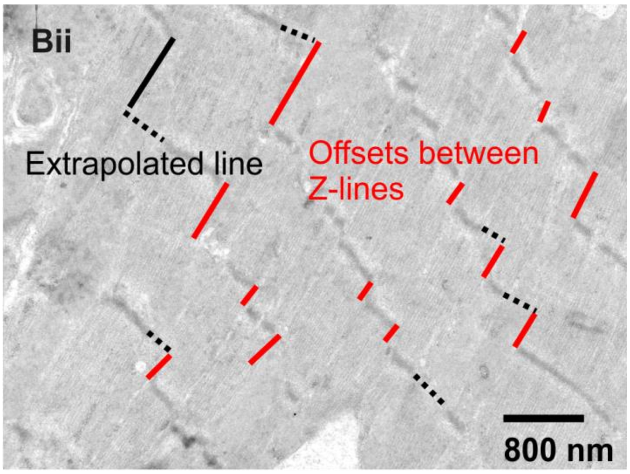

Ci. Angles between Z-lines

This measurement was made by extrapolating lines from the Z-lines of adjacent bundles, and then measuring the angle between the extrapolated lines. Examples of typical measurements are indicated by the red lines in Cii..

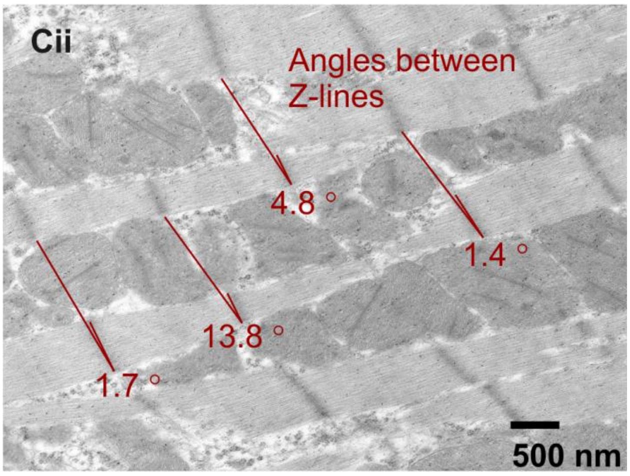

Di. Index of disorganisation

This measurement was performed to provide an indicator of changes in sarcomere structure, and was calculated using the following formula:.

$$\text{IoD} = \frac{\text{Z-line offset}}{\text{Sarcomere width}} \times 100$$

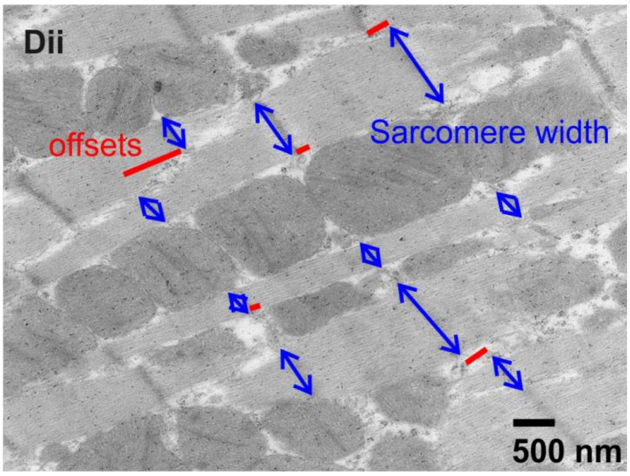

The results of the analysis of myofibre structure in PVCs from 3 month- and 24 month-old animals are presented in Figure 3.9. It is evident that there was a significant difference in sarcomere width in PVCs from 3 month- and 24 month-old mice (Figure 3.9A). However, there were no changes in any of the criteria used to characterise the organisation of myofilaments: neither the offset (Figure 3.9B), the angle between the Z-lines (Figure 3.9 C), nor the percentage of disorganised Z-line (Figure 3.9D) were significantly different between 3 month- and 24 month-old mice.

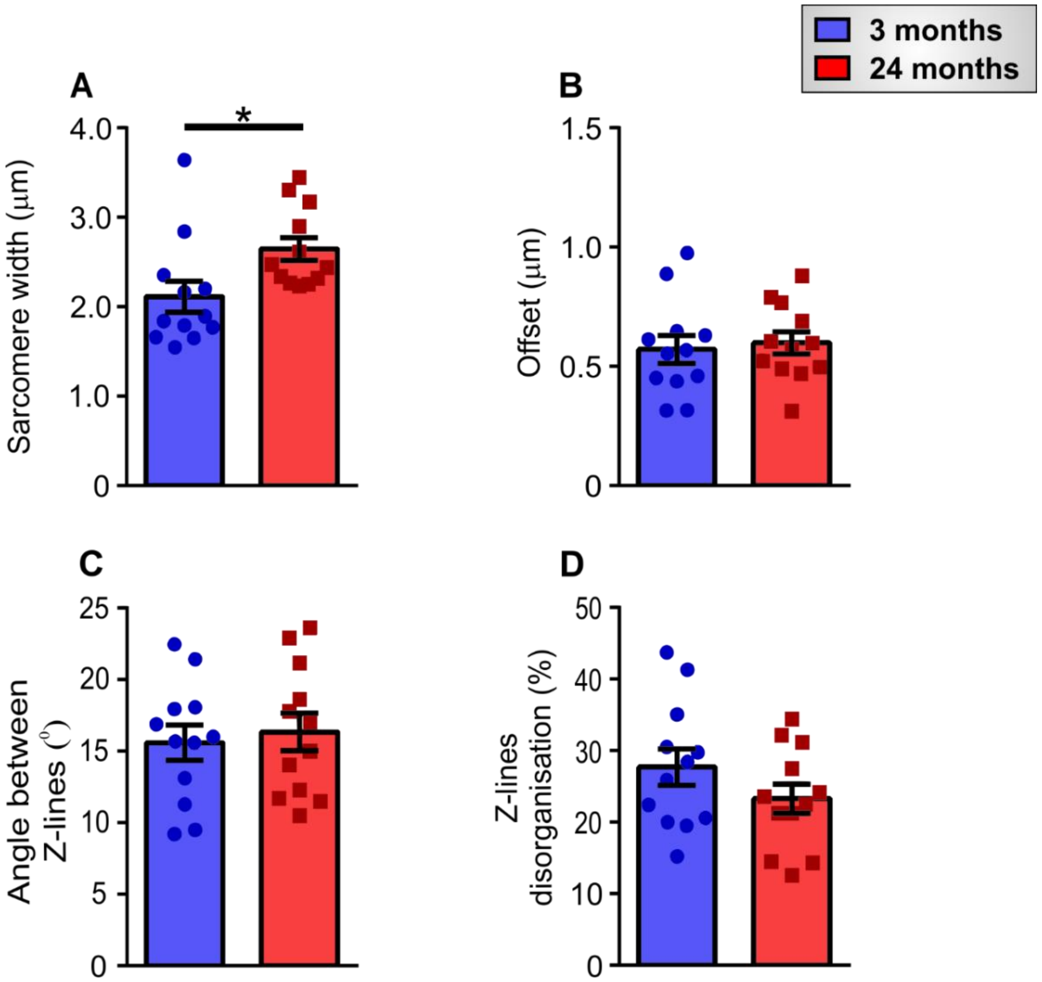

Figure 3.8. Quantitation of myofibre structure in PVCs from 3 month- and 24 month-old mice. Panels **A - D** present quantitative analysis of myofibre structure and organisation in TEM images obtained using PVCs from 3 month- and 24 month-old mice. The data are presented as mean ± S.E.M. Statistical significance was calculated using an unpaired Student's *t*-test, * denotes P < 0.05. *n* = 4 slices from 4 animals for both 3 month- and 24 month-old groups.

3.6.1.2. Mitochondria

A striking difference in PVCs structure and organisation between the 3 month- and 24 month-old groups concerned mitochondria. TEM images of PVCs from 3 month- and 24 month-old mice in which mitochondria have been outlined are presented in Figures 3.10 and 3.11. It is evident that at both ages mitochondria were highly abundant between myofibres within the PVCs. To avoid bias, all inter-myofibrillar mitochondria within an image were analysed, however, only few were outlined in oranges in Figures 3.10 and 3.11 for presentational purposes. Quantitation of mitochondria number and the average area of individual mitochondria revealed that the organelles were more abundant and larger in PVCs from the older animals (Figures 3.11 and 3.12). A qualitative difference that was evident in the TEM images what that the mitochondria in PVCs from 3 month-old animals tended to be oblong or ovoid shaped organelles that were present in linear arrangements (Figures 3.10 A and 3.11 A). In contrast, the mitochondria in PVCs from 24 month-old animals were sometimes less evidently in linear arrangements, and tended to be more circular and tightly packed together (Figures 3.10 and 3.11B).

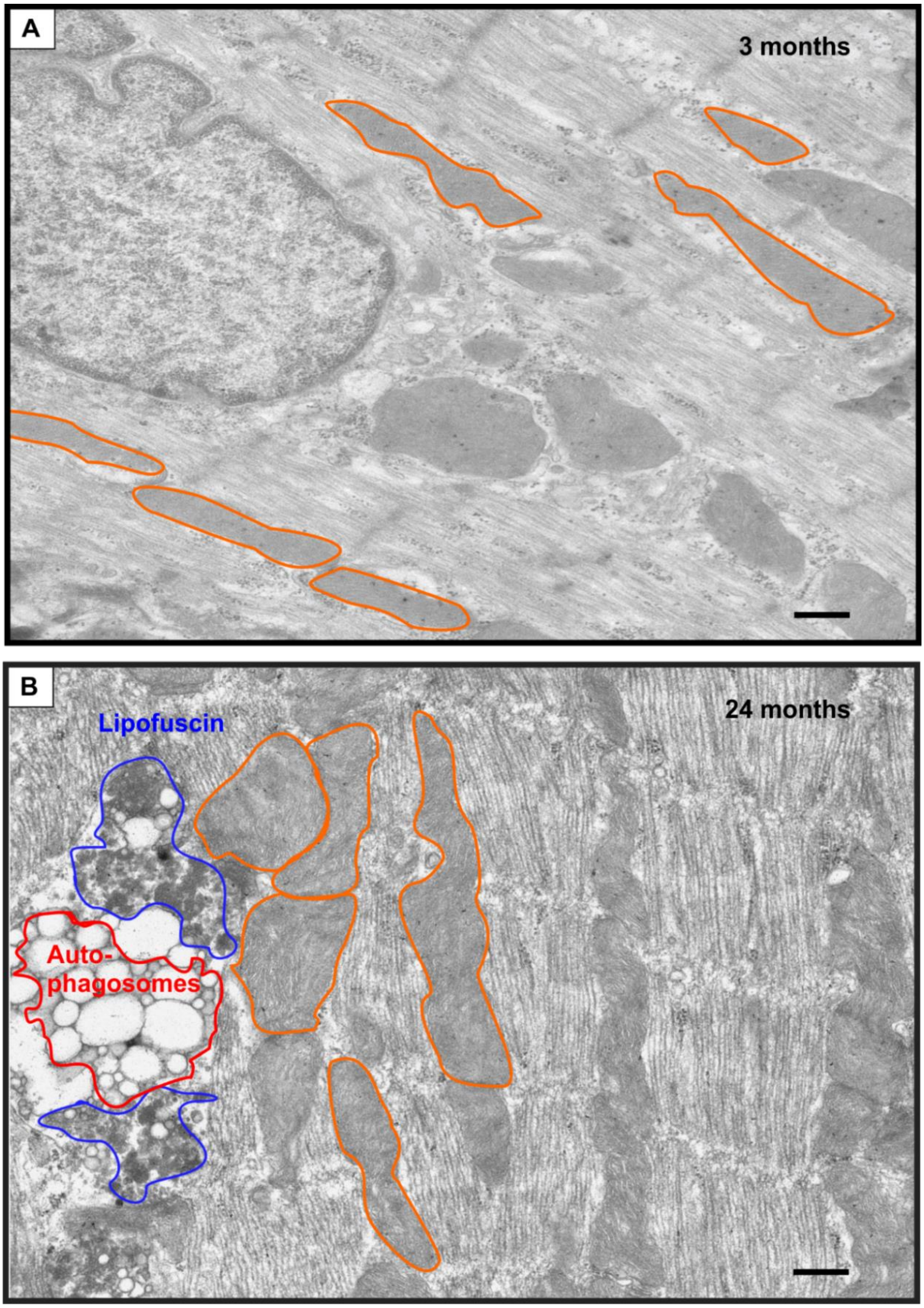

Figure 3.9. Mitochondria, and the absence or presence of lipofuscin and autophagosomes, within PVCs from 3 month- and 24 month-old mice. Panel **A** shows a representative TEM image of a PVC from a 3 month-old mouse showing well aligned and regularly-shaped mitochondria (outlined in orange) between the myofilaments. Panel **B** is a representative TEM image of a PVC from a 24 month-old mouse illustrating mitochondria (outlined in orange), lipofuscin (outlined in blue) and autophagosomes (outlined in red). The scale bars represent 500 nm.

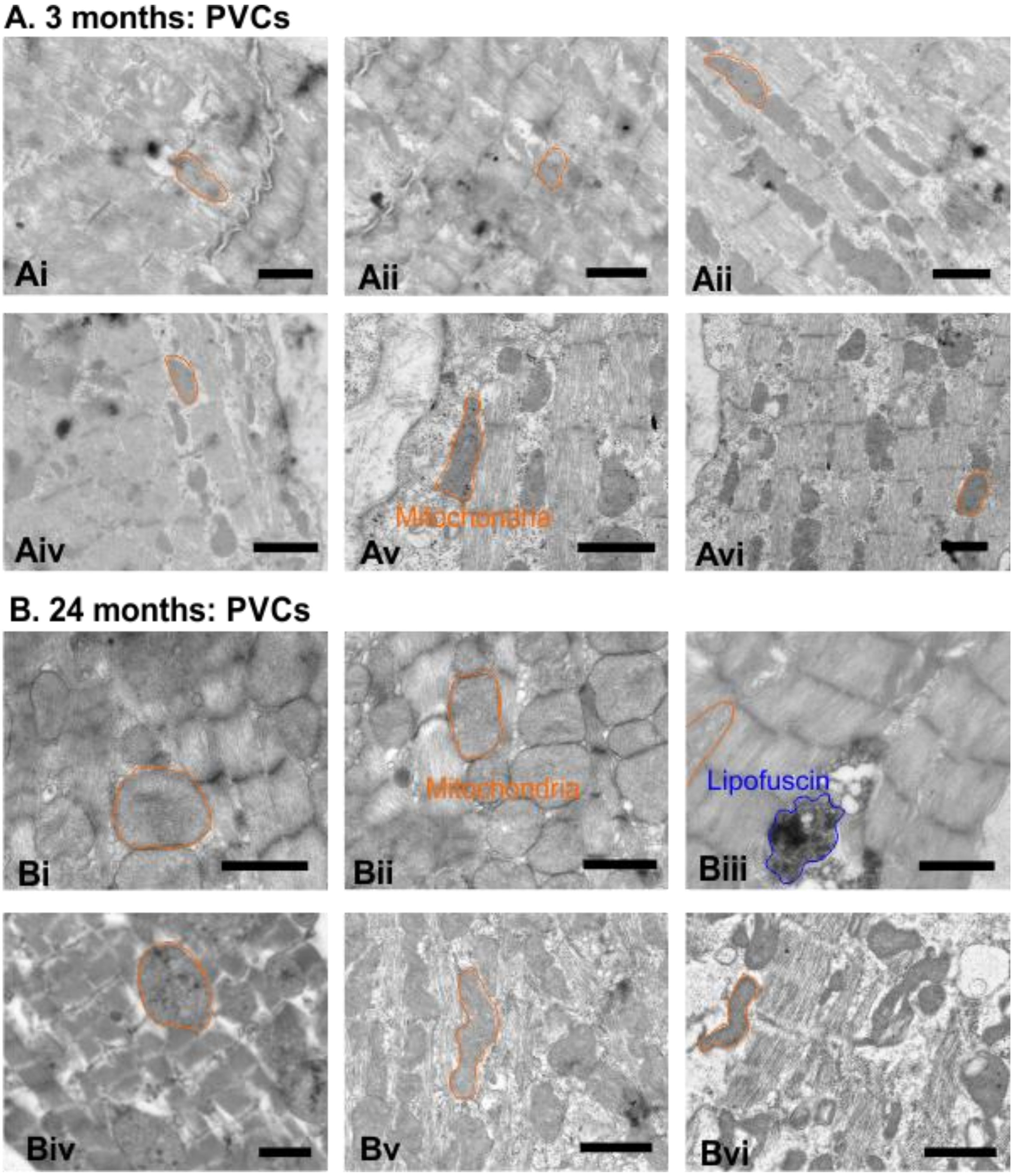

Figure 3.10. TEM images of PVCs from 3 month- and 24 month-old mice. Panels **Ai – Avi** are representative TEM images of PVCs from 3 month-old mice. Panels **Bi – Bvi** are representative TEM images of PVCs from 24 month-old mice. The PVCs from 24 month-old animals showed an increase in mitochondrial area (outlined in orange) (**Bi**, **Bii** and **Biv**), and an increased presence of lipofuscin granules (outlined in blue) (**Biii**). The scale bars in all panels represent 1 µm. For quantification, all inter-myofibrillar mitochondria were analysed and not just those outlined here.

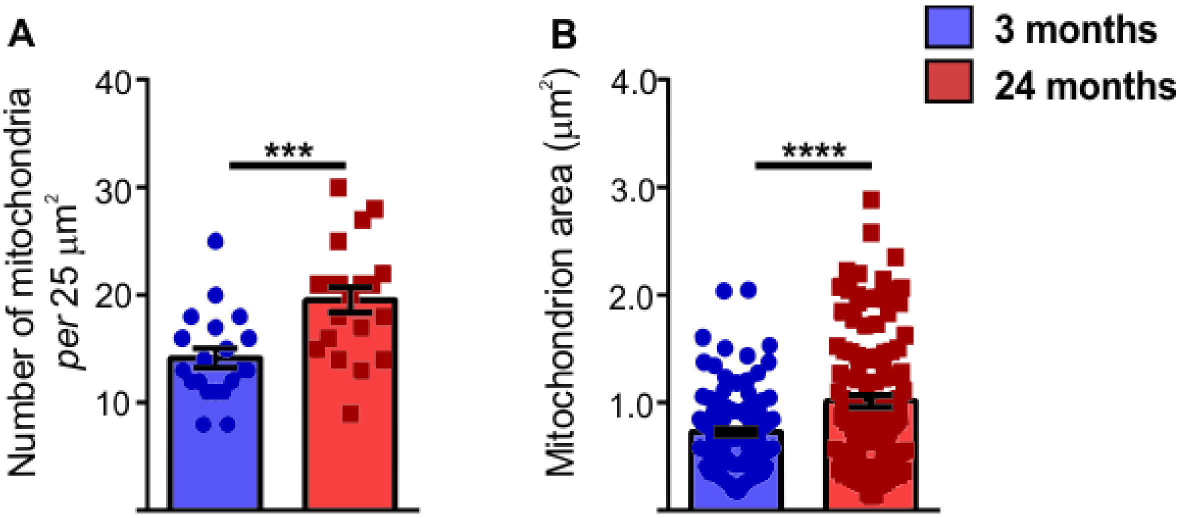

Figure 3.11. Quantification of mitochondrial number and area in PVCs from 3 month- and 24 month-old mice. Panel **A** indicates the number of mitochondria within PVCs, whilst Panel **B** shows the average mitochondrial area. The data are presented as mean ± S.E.M. Statistical significance was calculated using an unpaired Student's *t*-test, *** denotes $P < 0.001$, **** $P < 0.0001$ $n = 4$ slices from 4 animals for both 3 month- and 24 month-old groups.

3.6.1.3. Lipofuscin

In addition to the greater mitochondrial number and augmented mitochondrial area, there was an increased appearance of lipofuscin granules in PVCs from 24 month-old mice. The electron dense lipofuscin granules are obvious in Figure 3.10B (outlined in blue), and were only observed in the PVCs from 24 month-old animals. None of the 52 TEM images of PVCs from 3 month-old animals that were analysed in this study contained any evidence lipofuscin. Whilst, 10 out of 52 TEM images (19.2 %) of PVCs from 24 month-old mice showed at least one area containing lipofuscin granules. The average area occupied by lipofuscin granules in the 24 month-old animals was 0.3 ± 0.1 μm^2 (Figure 3.13).

The results obtained from the analyses of the PVC TEM images for 3 month- and 24 month-old animals are collated in Table 3.1.

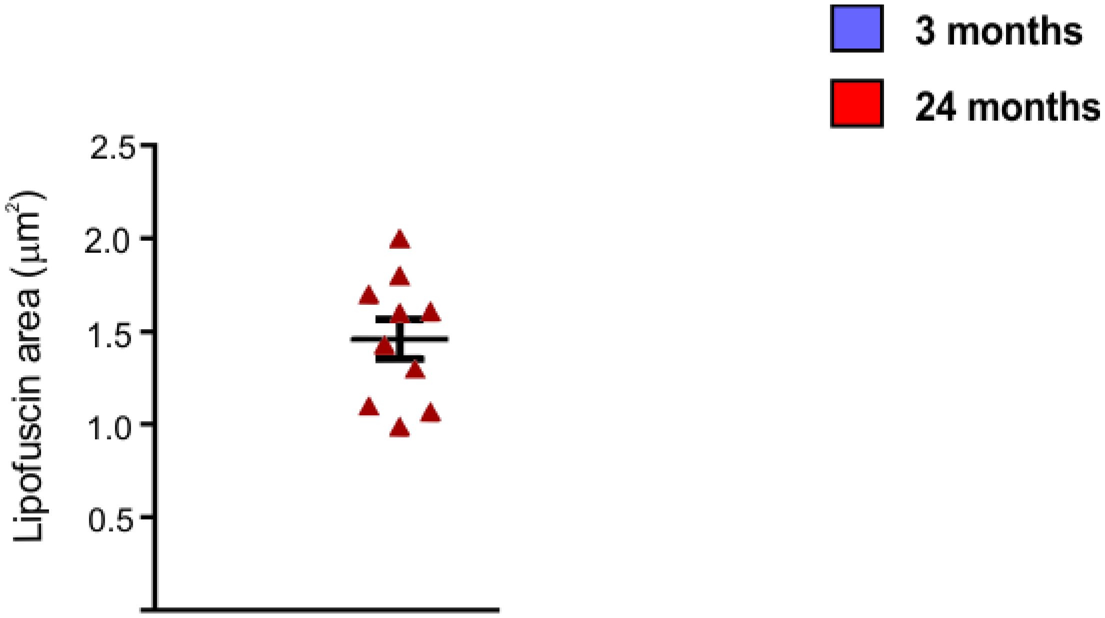

Figure 3.12. Average area of lipofuscin granules in PVCs from 24 month-old mice. The data are presented as mean ± S.E.M. *n* = 4 slices from 4 animals.

Parameter	**PVCs from 3 month-old mice**	**PVCs from 24 month-old mice**	**Change**	**Statistical significance**
Sarcomere width	2.1 ± 0.2 µm	2.7 ± 0.1 µm	Increase	(p = 0.02) N = 4 slices from 4 animals
Offset between Z-lines	0.6 ± 0.1 µm	0.5 ± 0.1 µm	n.s.	(p = 0.71) N = 4 slices from 4 animals
Angle between Z-lines	15.6 ± 1.2 °	16.3 ± 1.3 °	n.s.	(p = 0.68) N = 4 slices from 4 animals
Z-lines showing disorganisation	27.7 ± 2.6 %	23.3 ± 2.1 %	n.s.	(p = 0.19) N = 4 slices from 4 animals
Mitochondrial number	14.2 ± 0.9	19.6 ± 1.2	Increase	(p = 0.001) N = 4 slices from 4 animals
Mitochondrial area	0.7 ± 0.03 µm^2	1.0 ± 0.1 µm^2	Increase	(p = 0.0001) N = 4 slices from 4 animals
Lipofuscin granules	N/A	0.3 ± 0.1 µm^2	N/A	N/A N = 4 slices from 4 animals

Table 3.1. Comparison of ultrastructural parameters measured in PVCs from 3 month- and 24 month-old mice. This table shows a side by side comparison of the PVC ultrastructural parameters presented in Figures 3.9 – 3.12.

3.6.2. Ultrastructure of atrial myocytes in 3 month- and 24 month-old mice

Atrial cardiac myocytes are similar in structure to PVCs in that they have myofibre bundles interspersed with mitochondria. TEM images of atrial cardiac myocytes from 3 month- and 24 month-old animals are shown in Figures 3.14 and 3.15. A characteristic feature of atrial cardiac myocytes is that they contain atrial natriuretic peptide (ANP)-containing vesicles (sometimes called ‘atrial specific granules’) that can be released in response to atrial pressure and other stimuli (Berkenfeld *et al.,* 2005; 2012) to reduce blood pressure. ANP granules were visible in TEM images of atrial myocytes as circular electron dense granules (Figures 3.14 and 3.15). Neither the number of ANP granules, nor their area, was different in atrial myocytes from 3 month- and 24 month-old mice (Figure 3.16).

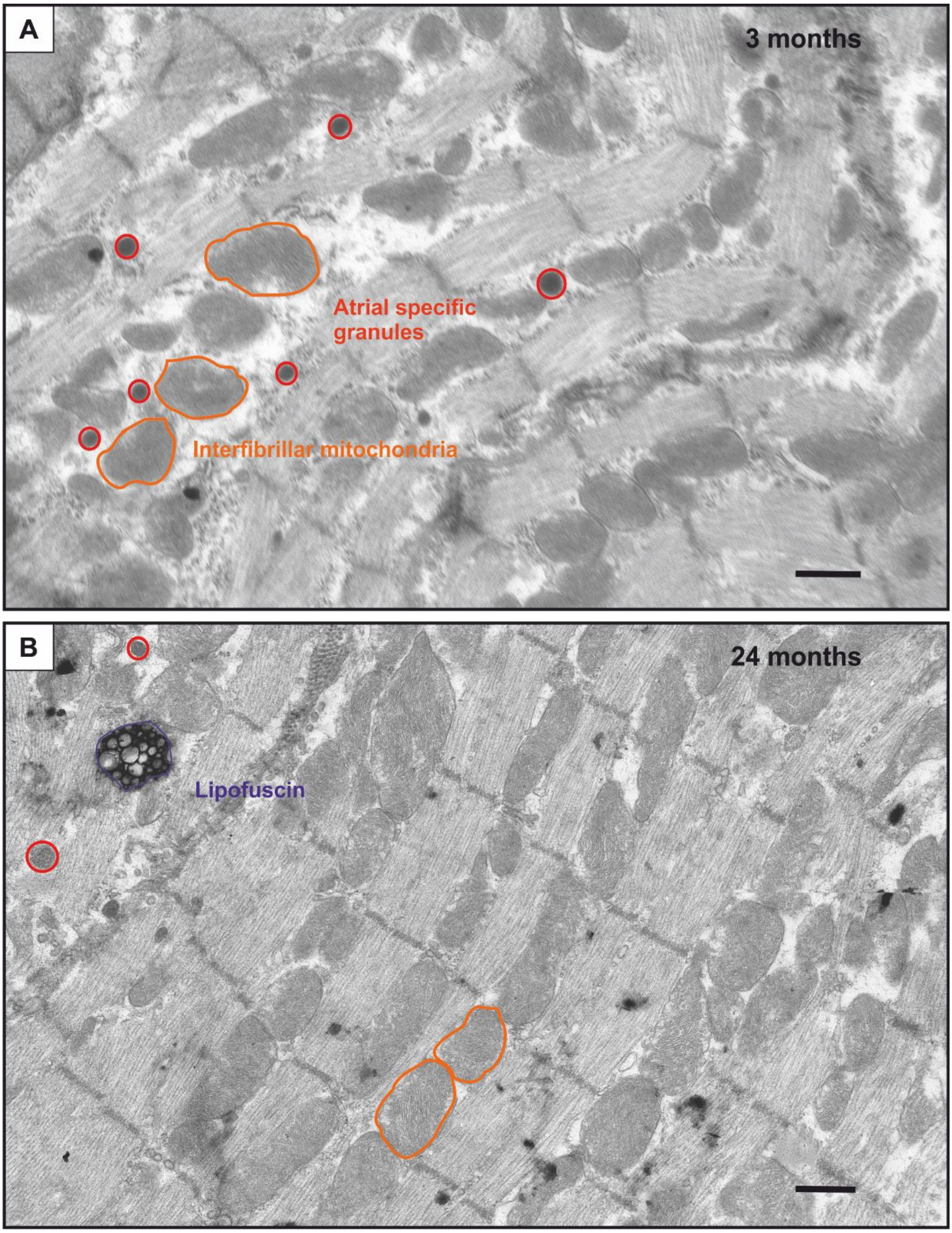

Figure 3.13. Ultrastructure of atrial myocytes from 3 month- and 24 month-old mice. Panel **A** is a representative TEM image of an atrial myocyte from a 3 month-old mouse, which demonstrates the presence of ANP granules (outlined in red). Panel **B** is a representative TEM image of an atrial myocyte from a 24 month-old mouse, which demonstrates the presence of lipofuscin granules in addition to ANP granules. Lipofuscin granules were rarely observed in TEM images of atrial myocytes from 3 month-old mice. Both Panels show an abundance of inter-myofibrillar mitochondria, outlined in orange. The scale bars represent 500 nm.

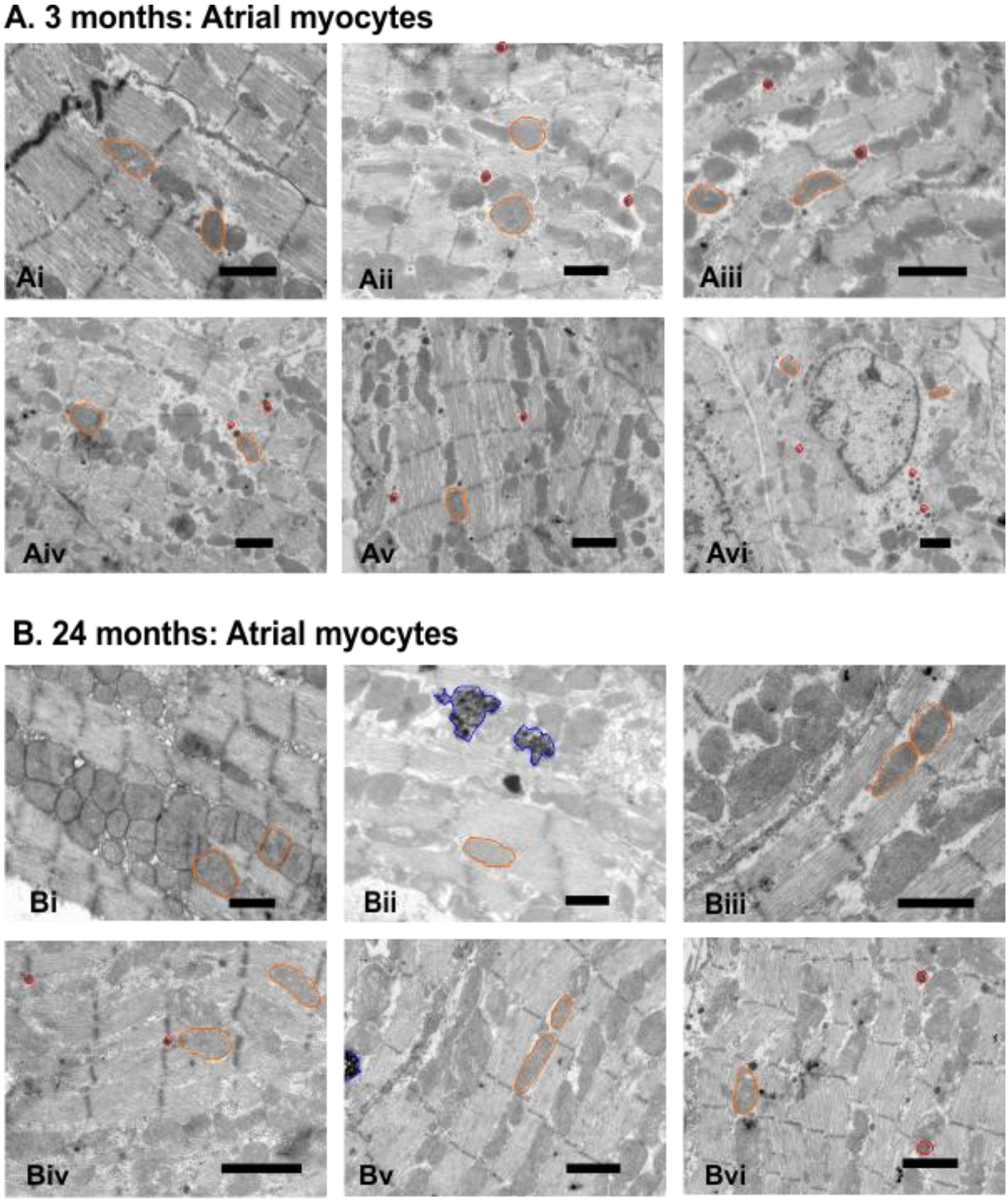

Figure 3.14. TEM images of atrial myocytes from 3 month- and 24 month-old mice. Panels **Ai – Avi** show examples of TEM images of atrial myocytes from 3 month-old mice. Panels **Bi – Bvi** show examples of TEM images of atrial myocytes from 24 month-old mice. Mitochondria are outlined in orange, ANP granules are outlined in red, and lipofuscin granules are outlined in blue. The scale bars in all panels represent 1 µm.

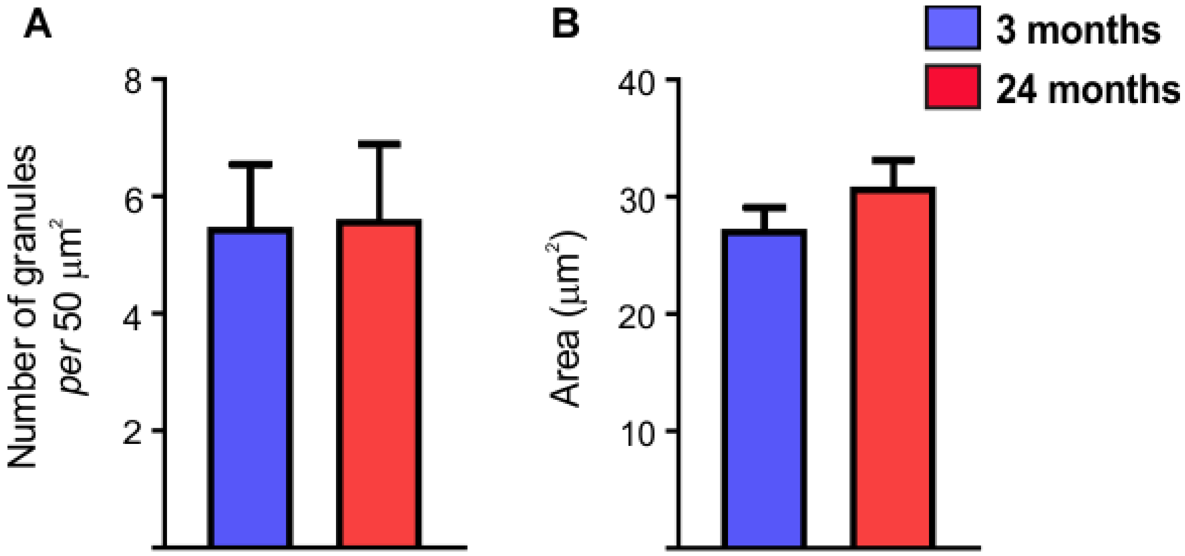

Figure 3.15. Quantification of the number and area of ANP granules in atrial cardiac myocytes from 3 month- and 24 month-old mice. Panel **A** shows the number of granules within a TEM image normalised against cell area. Panel **B** shows the area of ANP granules in atrial myocytes from 3 month- and 24 month-old mice. The data are presented as mean ± S.E.M. Statistical significance was calculated using an unpaired Student's *t*-test. *n* = 4 slices from 4 animals for both 3 month- and 24 month-old groups.

3.6.2.1. Myofibre structure

To examine the effect of ageing on atrial cardiac myocyte structure, TEM images of atrial cells from 3 month- and 24 month-old mice were characterised in a similar manner to that used for PVCs (see Section 3.6.1.1). In contrast, the results obtained from PVCs (Figure 3.9 and Table 3.1); there was no significant difference in the sarcomere width in atrial cardiac myocytes from 3 month- and 24 month-old mice (Figure 3.17A). Furthermore, there were no significant alterations of the offset between Z-lines, angle between Z-lines or proportion of Z-lines showing disorganisation in atrial myocytes from 3 month- and 24 month-old mice.

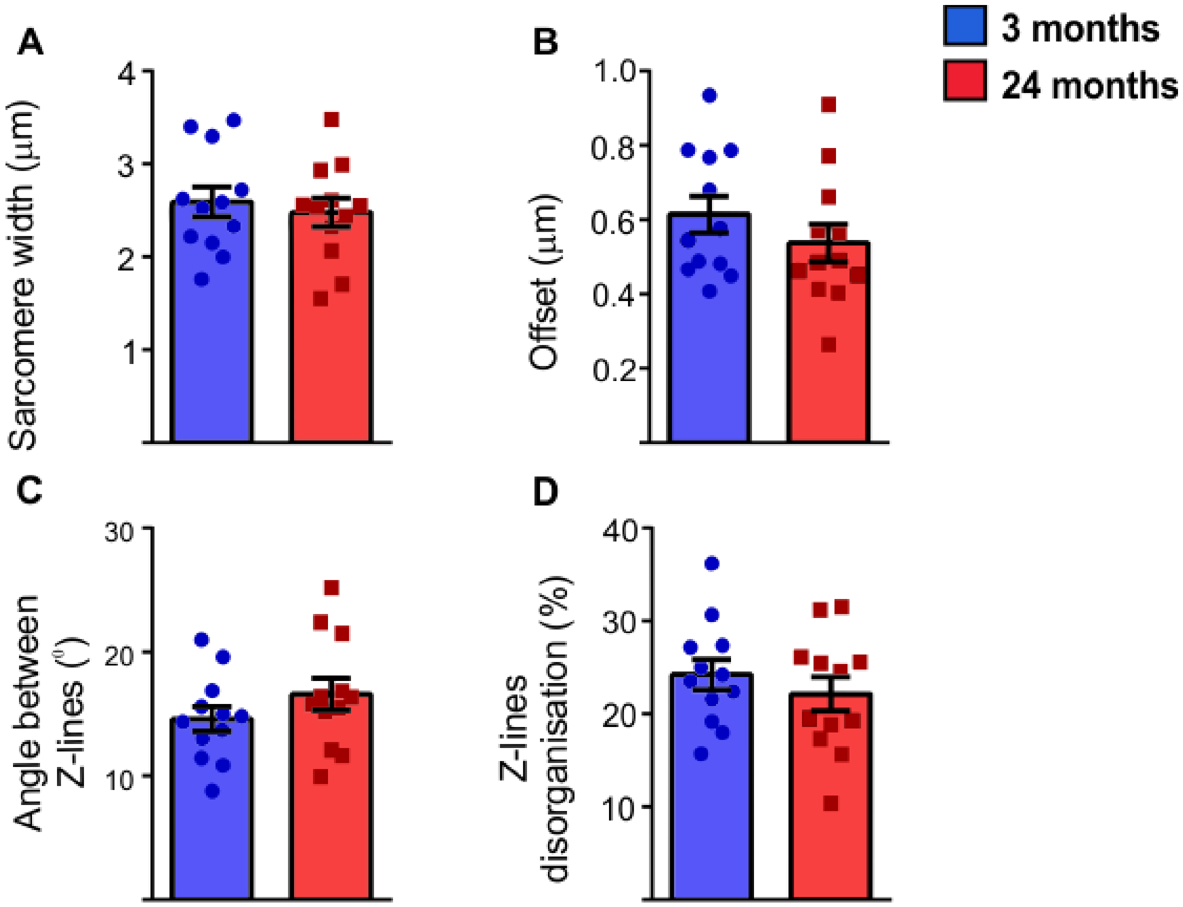

Figure 3.16. Quantitation of myofibre structure in atrial cardiac myocytes from 3 month- and 24 month-old mice. Panels **A - D** present quantitative analysis of myofibre structure and organisation in TEM images obtained using atrial cells from 3 month- and 24 month-old mice. The data are presented as mean ± S.E.M. Statistical significance was calculated using an unpaired Student's *t*-test, * denotes $P < 0.05$. $n = 4$ slices from 4 animals for both 3 month- and 24 month-old groups.

3.6.2.2. Mitochondria

In contrast to the analyses of PVCs, where the number of inter-myofibrillar mitochondria were increased in 24 month-old mice (Table 3.1 and Figure 3.12), there was no change in the number of inter-myofibrillar mitochondria in atrial cardiac myocytes between the 3 month- and 24 month-old mice (Figure 3.18A). However, similar to the results obtained with PVCs (Table 3.1 and Figure 3.12), the area of inter-myofibrillar mitochondria in atrial cardiac myocytes significantly increased in 24 month-old animals (Figure 3.18B).

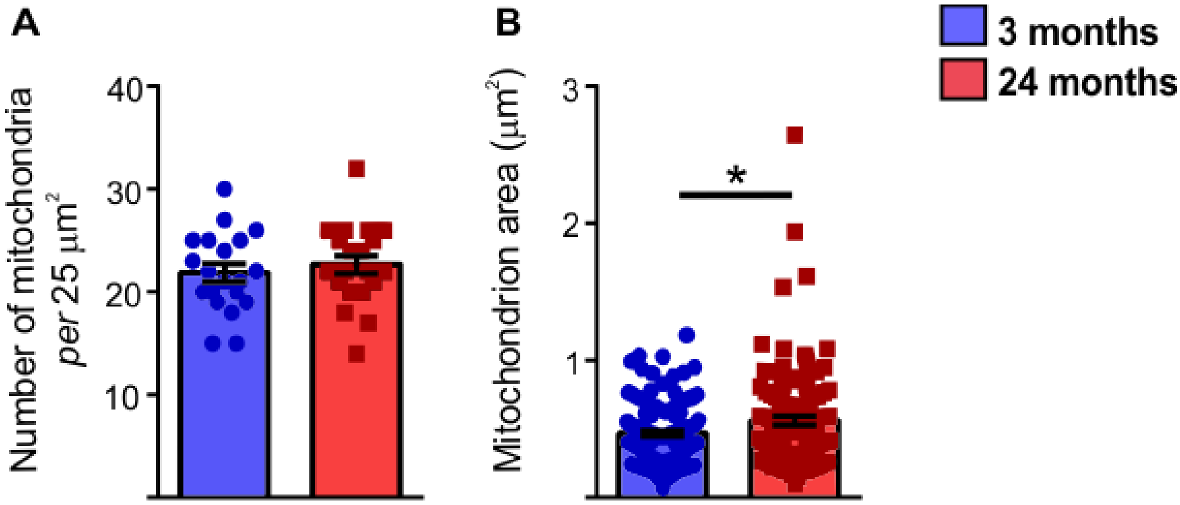

Figure 3.17. Quantification of mitochondrial number and area in atrial cardiac myocytes from 3 month- and 24 month-old mice. Panel **A** indicates the number of mitochondria within atrial myocytes, whilst Panel **B** shows the average mitochondrial area. The data are presented as mean ± S.E.M. Statistical significance was calculated using an unpaired Student's *t*-test, * denotes $P < 0.05$. $n = 4$ slices from 4 animals for both 3 month- and 24 month-old groups.

3.6.2.3. Lipofuscin

Whereas PVCs from 3 month-old mice showed no lipofuscin granules, there were evident lipofuscin granules in a small proportion of atrial cardiac myocytes from 3 month-old animals. Lipofuscin granules were present in 4 out of 46 TEM images (8.7 %; present in 2 out of 4 slices analysed) from 3 month-old animals. The number of lipofuscin granules increased to 15 out of 46 images (32.6 %, present in 4 out of 4 slices analysed) for 24 month-old animals. When calculating the total area lipofuscin granules in all of the TEM images, there was no significant difference between the two age groups (Figure 3.19). The results obtained from the analyses of the atrial cardiac myocyte TEM images for 3 month- and 24 month-old animals are collated in Table 3.2.

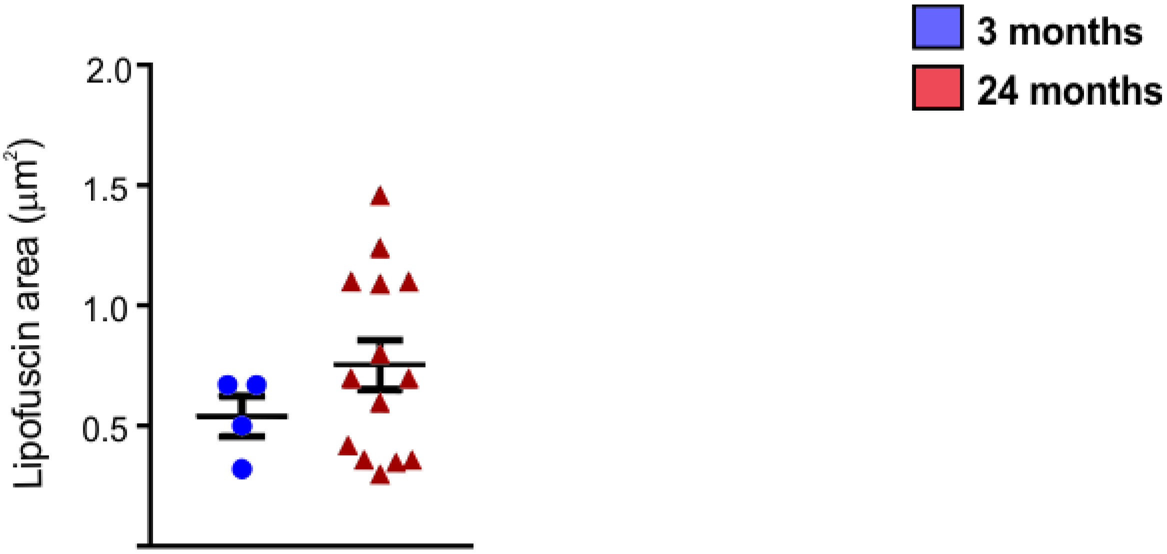

Figure 3.18. Average area of lipofuscin granules in atrial cardiac myocytes from 3 month- and 24 month-old mice. The data are presented as mean ± S.E.M. Statistical significance was calculated using an unpaired Student’s *t*-test. *n* = 4 slices from 4 animals for both 3 month- and 24 month-old groups.

Parameter	**Atrial myocytes from 3 month-old mice**	**Atrial myocytes from 24 month-old mice**	**Change**	**Statistical significance (p value)**
Sarcomere width	2.6 ± 0.2 µm	2.5 ± 0.2 µm	n.s.	p = 0.62 N = 4 slices from 4 animals
Offset between Z-lines	0.6 ± 0.1 µm	0.5 ± 0.1 µm	n.s.	p = 0.29 N = 4 slices from 4 animals
Angle between Z-lines	14.6 ± 1.0 °	16.6 ± 1.3 °	n.s.	p = 0.24 N = 4 slices from 4 animals
Z-lines disorganisation	22.2 ± 21.6 %	22.1 ± 1.8 %	n.s.	p = 0.4 N = 4 slices from 4 animals
Mitochondrial number	21.9 ± 0.9	22.7 ± 0.9	n.s.	p = 0.52 N = 4 slices from 4 animals
Mitochondrial area	0.5 ± 0.02 μm^2	0.6 ± 0.03 μm^2	Increase	p = 0.02 N = 4 slices from 4 animals
Lipofuscin granules	0.54 ± 0.08 μm^2	0.76 ± 1.0 μm^2	n.s.	P = 0.13 N = 4 slices from 4 animals

Table 3.2. Comparison of ultrastructural parameters measured in atrial myocytes from 3 month- and 24 month-old mice. This table shows a side by side comparison of the atrial myocytes ultrastructural parameters presented in Figures 3.14 – 3.19.

3.6.3. Ultrastructure of ventricular myocytes in 3 month- and 24 month-old mice

Similar analyses to those undertaken for PVCs and atrial cardiac myocytes were also performed for TEM images of ventricular cardiac myocytes from 3 month- and 24 month-old animals. Examples of ventricular cardiac myocyte TEMs from young and old animals are shown in Figures 3.20 and 3.21. Similar to the other cell types, ventricular myocytes have bundles of myofibres interspersed with linearly arranged mitochondria.

3.6.3.1. Myofibre structure

To examine the effect of ageing on ventricular cardiac myocyte structure, TEM images of ventricular cells from 3 month- and 24 month-old mice were characterised in a similar manner to that used for PVCs (see Section 3.6.1.1). In contrast the results obtained from PVCs (Figure 3.9 and Table 3.1), and similar to the data obtained with atrial cardiac myocytes (Figure 3.17 and Table 3.2), there was no significant difference in the sarcomere width in ventricular cardiac myocytes from 3 month- and 24 month-old mice (Figure 3.22A). However, there were significant alterations of the offset between Z-lines, angle between Z-lines, or proportion of Z-lines showing disorganisation in ventricular myocytes from 3 month- and 24 month-old mice (Figure 3.22B – D).

An interesting finding with ventricular myocytes was that they appeared to be the most regular structure in 3 month-old animals, but also showed the highest degree of change in 24 month-old animals. For example, in 3 month-old animals 16.4 ± 1.4 % of the Z-lines that showed disorganisation, which is lower than any of the other types of myocytes at either age. The proportion of disorganised Z-lines in ventricular myocytes increased significantly in the 24 month-old animals to 28.1 ± 3.2 %, which is the highest degree of disorganisation in any cell type at either age (Figure 3.22D).

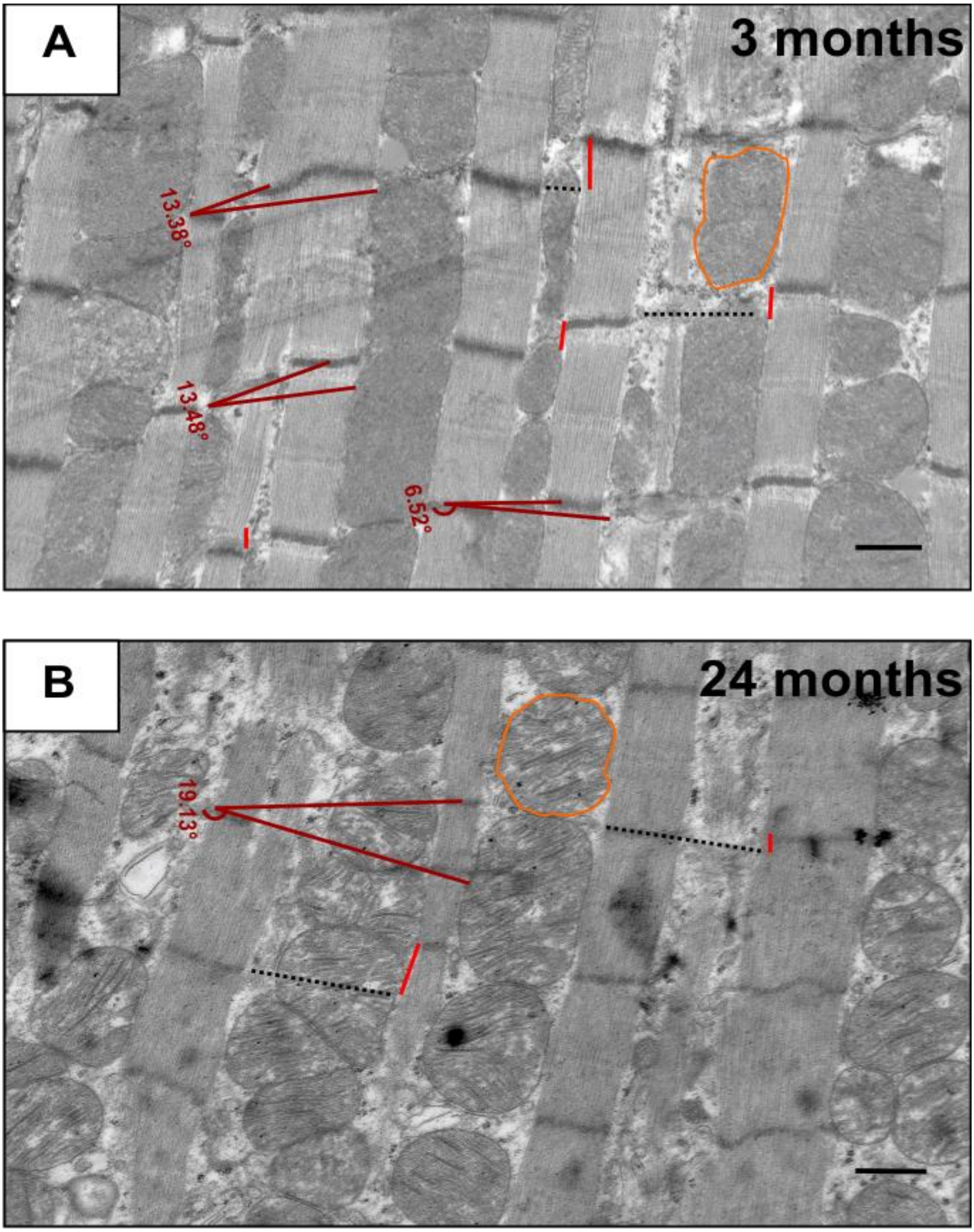

Figure 3.19. Ultrastructure of ventricular cardiac myocytes from 3 month- and 24 month-old mice. Panels **A** and **B** show representative TEM images of ventricular myocytes from 3 month- and 24 month-old mice respectively. Both Panels show an abundance of inter-myofibrillar mitochondria (outlined in orange), and shows how Z-line offsets and angles between Z-lines were measured. The scale bars represent 500 nm.

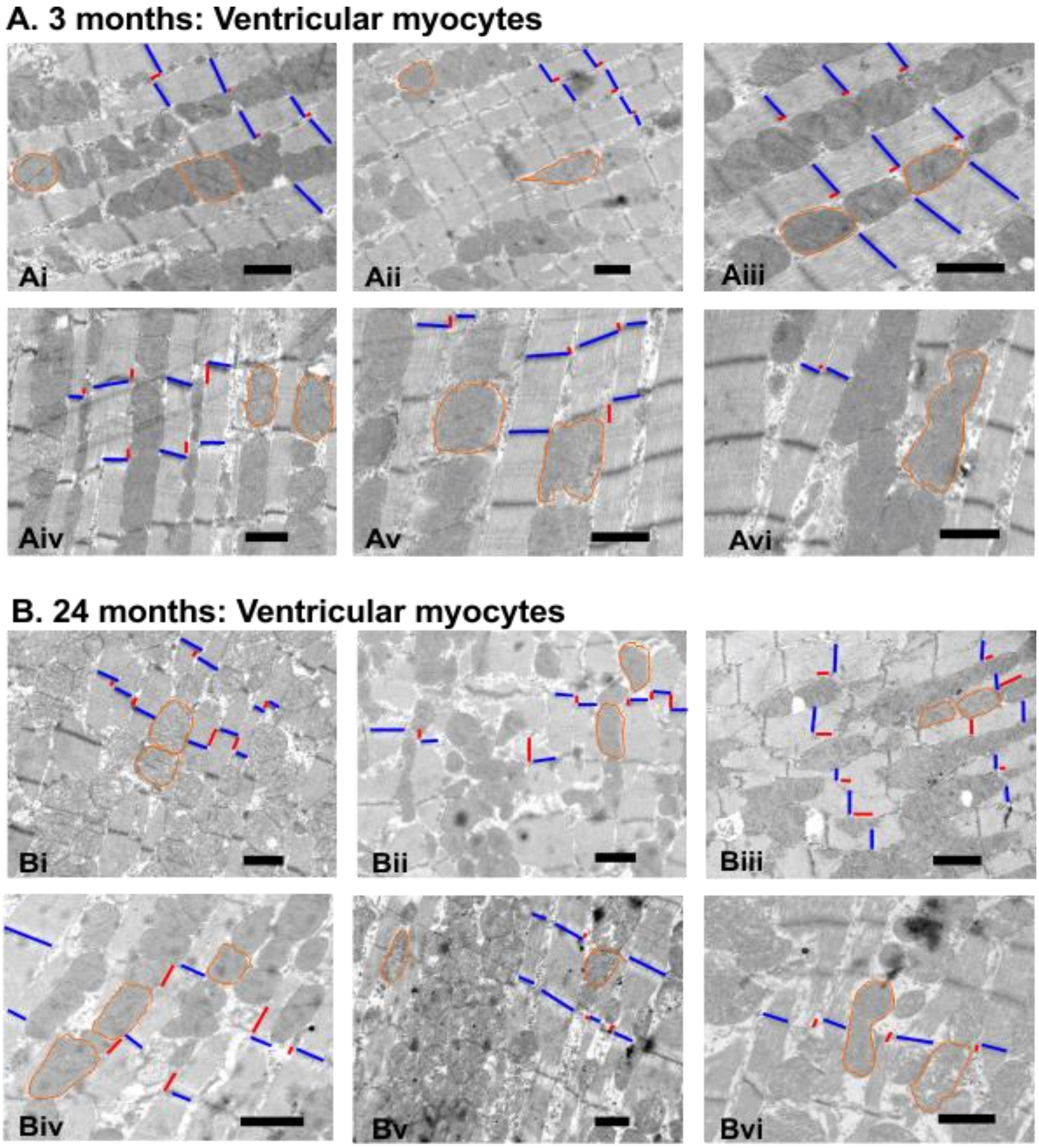

Figure 3.20. TEM images of ventricular myocytes from 3 month- and 24 month-old mice.

Panels **Ai** – **Avi** are examples of TEM images of ventricular myocytes from 3 month-old mice. Panels **Bi** – **Bvi** are examples of ventricular myocytes TEM images from 24 month-old mice. Mitochondria are outlined in orange; locations, where sarcomere width and Z-line offsets were measured, are indicated by blue and red lines. The scale bars in all panels represent 1 µm.

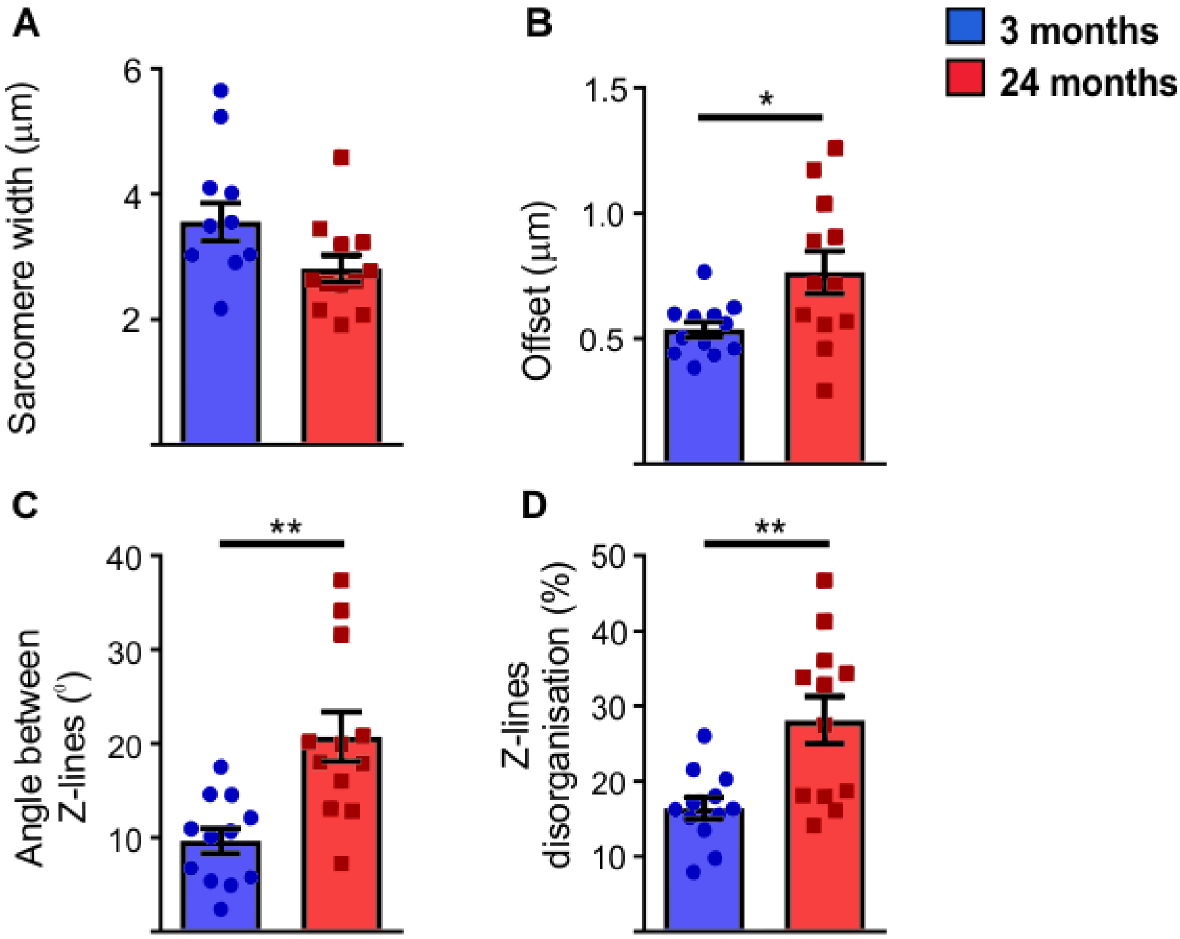

Figure 3.21. Quantitation of myofibre structure in ventricular cardiac myocytes from 3 month- and 24 month-old mice. Panels **A - D** present quantitative analysis of myofibre structure and organisation in TEM images obtained using ventricular cells from 3 month- and 24 month-old mice. The data are presented as mean ± S.E.M. Statistical significance was calculated using an unpaired Student's *t*-test, * and ** denote $P < 0.05$ and $P < 0.01$, respectively. *n* = 4 slices from 4 animals for both 3 month- and 24 month-old groups.

3.6.3.2. Mitochondria

In contrast to the results obtained from PVCs (Figure 3.12 and Table 3.1) and atrial myocytes (Figure 3.18 and Table 3.2), there were no differences in either the mitochondrial parameters measured from 3 month- and 24 month-old mice in ventricular myocytes (Figure 3.23).

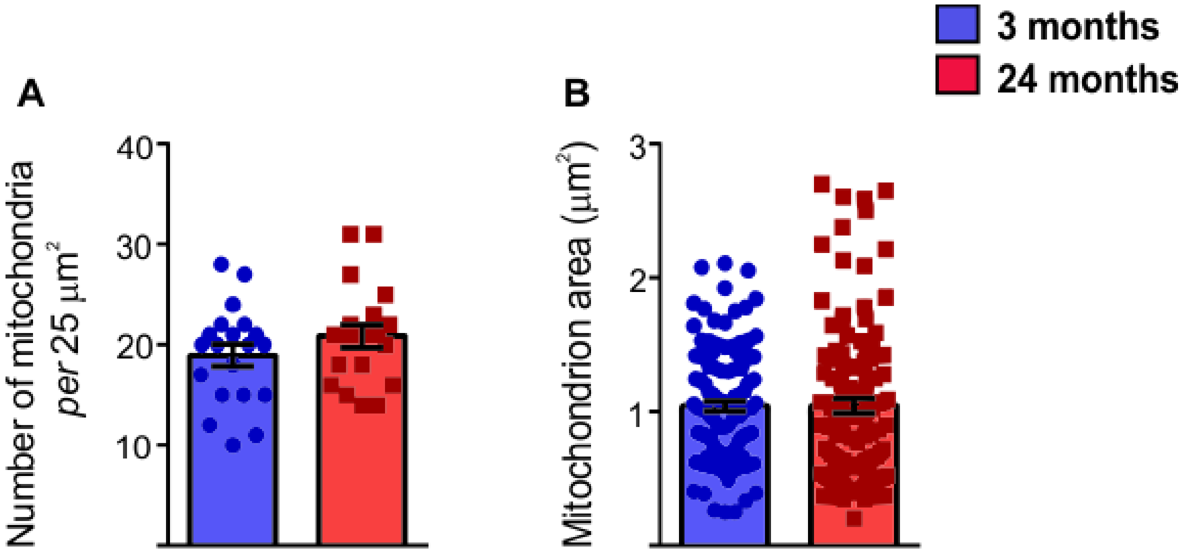

Figure 3.22. Quantification of mitochondrial number and area in ventricular cardiac myocytes from 3 month- and 24 month-old mice. Panel **A** indicates the number of mitochondria within ventricular myocytes, whilst Panel **B** shows the average mitochondrial area. The data are presented as mean ± S.E.M. Statistical significance was calculated using an unpaired Student’s *t*-test. *n* = 4 slices from 4 animals for both 3 month- and 24 month-old groups.

3.6.3.3. Lipofuscin

Similar to the observations described above for PVCs (Figure 3.13) and atrial myocytes (Figure 3.19), ventricular myocytes from 3 month-old mice had fewer lipofuscin deposits than 24 month-old animals. Of 40 ventricular TEM images examined from 3 month-old mice, only 1 cell showed evidence of lipofuscin (lipofuscin was evident in 1 out of 40 electron micrographs analysed from 4 animals). In contrast, 6 out of 40 TEM images from ventricular myocytes of 24 month-old animals showed lipofuscin granules (lipofuscin was evident in 3 out of 4 animals). The size of the lipofuscin granules in ventricular myocytes from 24 month-old animals is shown in (Figure 3.24), and was similar to those observed in PVCs (Figure 3.13) and atrial myocytes (Figure 3.19).

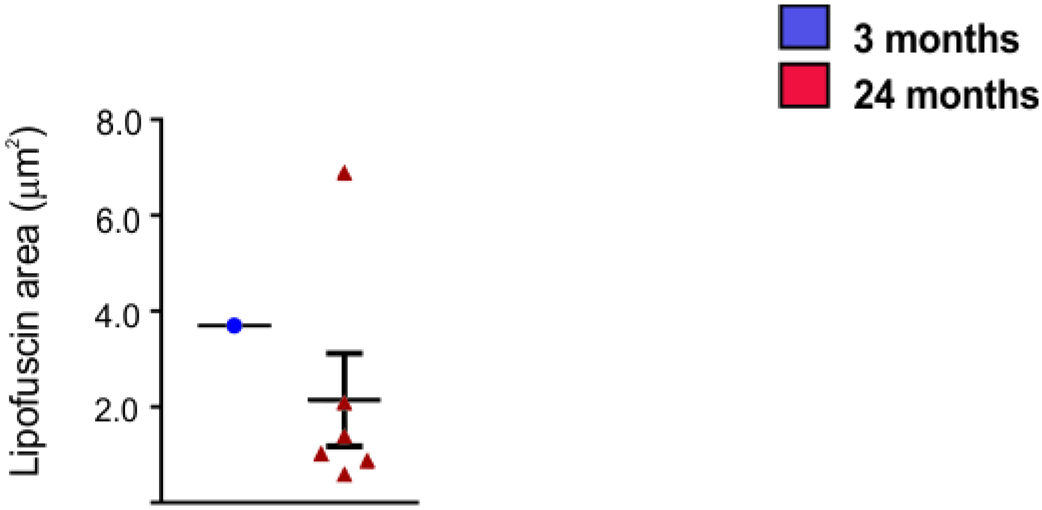

Figure 3.23. Average area of lipofuscin granules in ventricular cardiac myocytes from 3 month- and 24 month-old mice. The data are presented as mean ± S.E.M. *n* = 4 slices from 4 animals for both 3 month- and 24 month-old groups.

Parameter	**Ventricular myocytes from 3 month-old mice**	**Ventricular myocytes from 24 month-old mice**	**Change**	**Statistical significance (p value)**
Sarcomere width	3.6 ± 0.3 µm	2.8 ± 0.2 µm	n.s.	p = 0.22 N = 4 slices from 4 animals
Offsets between Z-lines	0.5 ± 0.03 µm	0.8 ± 0.1 µm	Increase	p = 0.02 N = 4 slices from 4 animals
Angles between Z-lines	9.7 ± 1.3 °	20.8 ± 2.6 °	Increase	p = 0.002 N = 4 slices from 4 animals
Percentage of Z-lines disorganisation	16.4 ± 1.4 %	28.1 ± 3.2 %	Increase	p = 0.04 N = 4 slices from 4 animals
Mitochondrial number	19.0 ± 1.1	20.9 ± 1.1	n.s.	p = 0.22 N = 4 slices from 4 animals
Mitochondrial size	1.0 ± 0.04 µm^2	1.0 ± 0.05 µm^2	n.s.	p = 0.98 N = 4 slices from 4 animals
Lipofuscin granules	3.27 µm^2	2.15 ± 1.0 µm^2	N/A	N/A, one value for PVCs from young mice. N = 4 slices from 4 animals

Table 3.3. Comparison of ultrastructural parameters measured in ventricular myocytes from 3 month- and 24 month-old mice. This table shows a side by side comparison of the ventricular myocytes ultrastructural parameters presented in Figures 3.20 – 3.24.

3.7. Comparison of the structure of cardiac myocytes from 3 and 24 month-old mice

3.7.1. Comparison of the myofibre organisation from PVCs, atrial and ventricular myocytes from 3 and 24 month-old mice

Comparative data, showing the angle between Z-lines for PVCs, atrial and ventricular myocytes from 3 month- and 24 month-old mice is presented in Figure 3.25. It is evident that ventricular myocytes from 3 month-old mice displayed the smallest angle between neighbouring Z-lines. The Z-line angle did not significantly change in atrial myocytes or PVCs from 24 month-old mice. However, the Z-line angle in ventricular myocytes from 24 month-old mice was significantly increased (Figure 3.25).

The values for the ‘offset between Z-lines’ and the percentage of ‘Z-lines showing disorganisation’ were lower for ventricular cardiac myocytes from 3 month-old mice, compared to their PVC and atrial cardiac myocyte counterparts (c.f. Tables 3.1, 3.2 and 3.3). These data indicate that of the three cell types investigated ventricular cardiac myocytes from young animals had the highest level of alignment between myofibres. However, ventricular cardiac myocytes also show the strongest deterioration of myofibre alignment with ageing. The myofibres within PVCs and atrial myocytes are not as well organised as in ventricular cardiac myocytes in young animals, but their organisation does not significantly deteriorate.

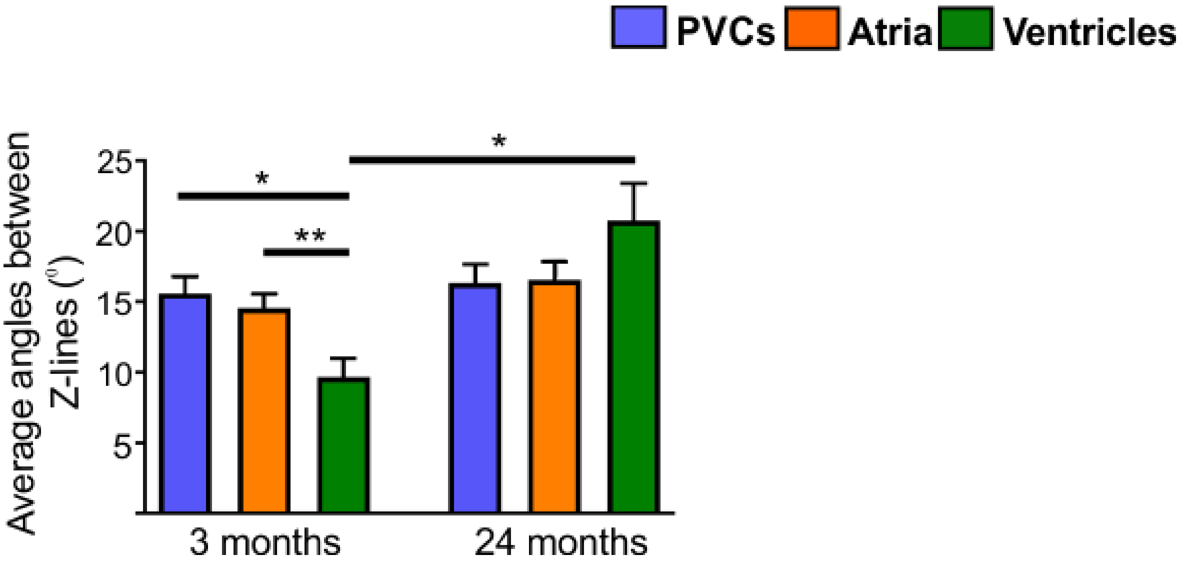

Figure 3.24. Organisation of myofilaments in PVCs, atrial and ventricular myocytes in 3 month- and 24 month-old animals. The average angles between Z-lines in PVCs, atrial and ventricular myocytes from 3 month- and 24 month-old mice. The data presented as mean ± S.E.M., and were analysed using one-way ANOVA. *n* = 4 slices from 4 animals per age group. * indicates P < 0.05, and ** indicates P < 0.01.

3.7.2. Comparison of the mitochondria from PVCs, atrial and ventricular myocytes from 3 and 24 month-old mice

Comparative data, showing the number of mitochondria and mitochondrial area for PVCs, atrial and ventricular cardiac myocytes from 3 month- and 24 month-old mice is presented in Figure 3.26. A similar number of mitochondria was found in atrial and ventricular cardiac myocytes from both 3 month- and 24 month-old animals. However, PVCs from 3 month-old animals contained significantly less mitochondria than atrial and ventricular cardiac myocytes from the same age group (Figure 3.26A). Evidently, the number of mitochondria in PVCs increased significantly during ageing (Figure 3.26A).

Atrial myocytes had the smallest mitochondria in both 3 month- and 24 month-old animals, whereas ventricular myocytes had the biggest mitochondria in both age groups (Figure 3.26B). However, only the mitochondria within PVCs showed a significant change in size between 3 month- and 24-month old animals (Figure 3.26B). These data suggest that the mitochondria within PVCs become both more numerous and larger during ageing.

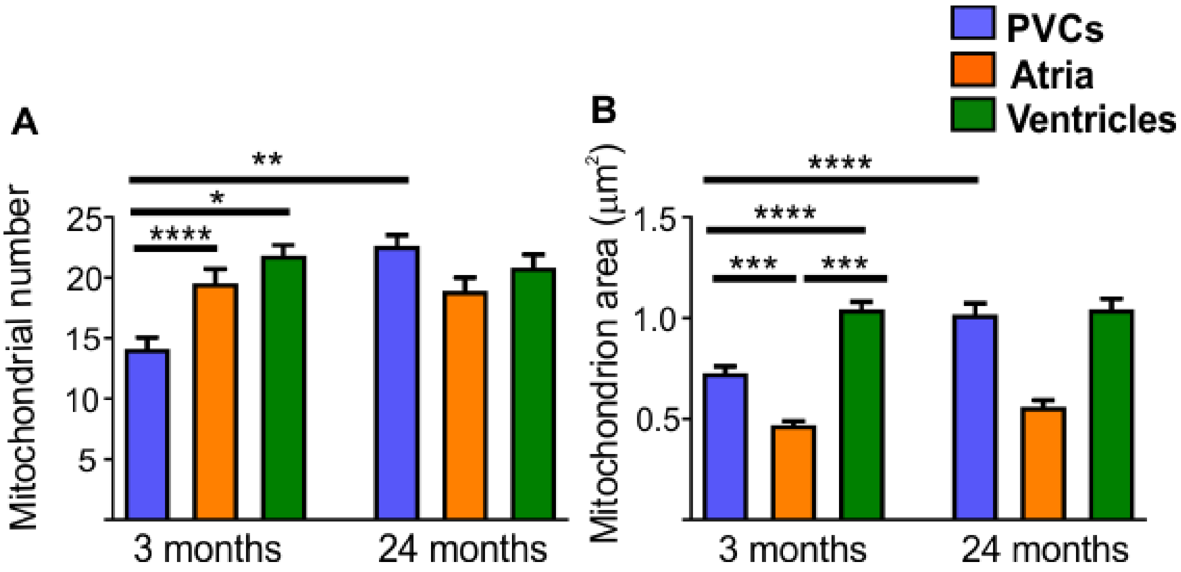

Figure 3.25. Comparison of mitochondrial number and area in PVCs, atrial and ventricular cardiac myocytes in 3 month- and 24 month-old mice. Panel **A** shows mitochondrial number in PVCs, atrial and ventricular myocytes. Panel **B** shows mitochondrial area in PVCs, atrial and ventricular myocytes. The data are presented as mean ± S.E.M. Statistical significance was calculated using one-way ANOVA, *, **, and *** denote P < 0.05, P < 0.01, P < 0.001, respectively. *n* = 4 slices from 4 animals for both 3 month- and 24 month-old animals.

3.8. Summary

1. Criteria were developed for identifying PVCs within mouse lung slices. In particular, PVCs are the only striated, spontaneously contractile cells associated with blood vessels running through the lung slices (section 3.3).

2. The blood vessels around which PVCs were found had an inner layer of endothelial cells that were surrounded by smooth muscle cells. The PVCs were located outside the smooth muscle cells. The thickness of a PVC layer, and the extent to which it ran around the circumference of a vessel, varied substantially from slice to slice (section 3.3).

3. Due to variation in the orientation of PVCs, Z-lines were not always evident. In fact, neighbouring PVCs within a slice could have different orientations relative to each other (section 3.4).

4. PVCs have different sub-populations of mitochondria. Specifically, perinuclear, inter-myofibrillar and sub-sarcolemmal mitochondrial populations were distinguished on the basis of spatial separation within PVCs. Mitochondria were more abundant and larger in PVCs from 24 month-old mice, compared to cells from 3 month-old animals (sections 3.4 and 3.6.1).

5. At the level of the light microscope, there were no differences in RyR2 expression, or localisation, in PVCs from 3 month- or 24 month-old animals (section 3.5.1).

6. PVCs express connexins, and have typical intercalated disk structures, which likely underlie cell-cell communication and spread of electrical signals. Cx43 expression was the same in PVCs from 3 month- or 24 month-old mice, but Cx40 expression decreased in the older animals (section 3.5.2).

7. Several different parameters were analysed to compare the sarcomeric structure of PVCs, atrial and ventricular myocytes from 3 month- and 24 month-old mice. All three cell types had a similar sarcomeric organisation, and only ventricular myocytes showed increased sarcomeric disorganisation in the older animals. Of the three cell types studied, ventricular cardiac myocytes were the most organised cells in the 3 month-old mice, but were the most disorganised in the 24 month-old animals (section 3.7.1).

8. Lipofuscin was more evident in PVCs, atrial and ventricular cardiac myocytes from 24 month-old mice, compared to cells from 3 month-old animals (sections 3.6.1.3, 3.6.2.3 and 3.6.3.3).

3.9. Discussion

3.9.1. Using mouse lung slices for studying PVC structure

The work described in this Chapter sought to undertake a comparative characterisation of the structure of PVCs, atrial and ventricular cardiac myocyte in young and old mice. The rationale for this investigation was the established clinical link between ageing, cardiac myocyte remodelling and arrhythmias (Hayashi *et al*., 2002; Nattel *et al*., 2008). The principal cell type under investigation in this study was PVCs, which are known to participate in the genesis of AF (Haissaguerre *et al.,* 1998; Sueda *et al.,* 2005). It has been demonstrated that pro-arrhythmic electrical signals can originate from the PVCs in the pulmonary vein sleeves, but the mechanism(s) causing these electrical signals to arise is unclear. Moreover, the structural and functional changes that occur within ageing PVCs to make them more prominently trigger AF in older people are unknown. Critical factors that are believed to be involved in the genesis and maintenance of AF within atrial cardiac myocytes are electrical remodelling, structural remodelling and changes in Ca^{2+} homeostasis (Ausma *et al.,* 2001, Chen *et al.,* 2002, Hocini *et al.,* 2002, Shanmugam *et al.,* 2011, Nattel *et al.,* 2013), and it is plausible that the same factors underlie the propensity of PVCs to be pro-arrhythmic. Previous studies have examined the structures of PVCs and atrial myocytes from human AF patients (Boldt *et al.,* 2004; Boldt *et al.,* 2004, Laky *et al.,* 2011) and animal models of AF (Ausma *et al.,* 1997, Thijssen *et al.,* 2000, Ausma *et al.,* 2001, Ausma *et al.,* 2003), but not during ageing. Given the impact of aberrant electrical signalling on atrial function, there is a clear need to understand PVCs from structural and functional perspectives.

To analyse the effects of structural changes during ageing in PVCs, lung slices from 3 month- and 24 month-old mice were analysed. In this study, C57/BL/6J mice were used as an ageing model. Using mice rather than humans in ageing research has a number of benefits including a shorter life span, similar genetic backgrounds, controlled nurturing environments and the ability to do experiments using cells from animals of a specific age (Vanhooren *et al.,* 2013; Nkuipou-kenfack *et al.,* 2017). Additionally, longitudinally studies are easier to conduct in mice than humans. Mice are known to reach the age of 30 – 32 months and anything ≥ 24 months is interpreted as advancing age, whilst 3 - 4 months is considered as young (Fahlström *et al.,* 2011). C57/BL/6 aged mice have been shown previously to be susceptible to age-dependent hearing loss, changes in cognitive function, altered sensorimotor-dependent behaviours and weight loss, but not cardiac function (Fahlström *et al.,* 2011). In mice, the sleeves of PVCs continue into the lungs, and hence lung slices were used in this study (Ho *et al.,* 2001, Mueller-Hoecker *et al.,* 2008). Lung slices contain pulmonary veins with PVCs, smooth muscle cells and endothelial cells, in addition to pulmonary arteries and airways. A significant advantage of lung slices is that they preserve cellular niches where PVCs are viable and do not deteriorate. Moreover, the slices maintain cell-cell contacts and cellular orientations that resemble *in situ* physiological positions (Rietdorf *et al.,* 2014). This study used a combination of the following criteria to formally identify cells as PVCs: (1) PVCs were associated with (usually surrounding) a blood vessel, (2) PVCs displayed spontaneous contractions, (3) PVCs were not located next to an airway, and (4) PVCs were striated (normally evident in both light and EM) (Figure 3.1). These criteria provided a reliable method for correctly identifying PVCs. Addition confirmation of the identification of PVCs came from immunohistochemical studies where staining of PVCs with phalloidin also presented striated expression (Figures 3.4 and 3.6).

3.9.2. Expression of RyR2 in PVCs from 3 month- and 24 month-old mice

The expression and localisation of RyR2 within 3 month- and 24 month-old PVCs was investigated using immunofluorescence and confocal imaging. The data presented in this Chapter indicates that neither the sarcomere arrangement nor RyR2 localisation was different when comparing PVCs from 3 month- and 24 month-old mice (c.f. Figures 3.4 and 3.5). Whilst immunofluorescence, as performed in this study is not strictly quantitative, by using the same immunostaining protocol, antibody dilutions and image acquisition parameters, it is possible to assess immunostaining intensity between samples. There was no evident difference in the levels of fluorescence, suggesting that not only the localisation, but also the RyR2 expression levels are unaltered between the age groups. These data support the results of several studies performed using atrial and ventricular myocytes from rodents that examined RyR2 changes with age. Most of these studies found no change in the levels of RyR2 expression with age (Rueckschloss *et al*., 2010, Turdi *et al*., 2010).

3.9.3. Expression of connexins in PVCs from 3 month- and 24 month-old mice

The expression and localisation of connexins within 3 month- and 24 month-old PVCs was investigated using immunofluorescence and confocal imaging. PVCs in our study expressed both, Cx40 and Cx43. Of these connexins, Cx43 gave a stronger staining (both, regarding the intensity and the number of positive slices) than Cx40 (Figure 3.6). This study found a significant reduction in Cx40 staining in PVCs during ageing, but no change in Cx43 staining between young and old mice (Figure 3.7). A reduction in Cx40 may result in altered electrical conduction that could promote arrhythmias. Previous results have shown that induction of AF with electrical pacing in animal models resulted in altered distribution or a reduction of Cx40, whereas Cx43 remained unchanged or increased (Elvan *et al*., 1997, Velden *et al.,* 1999, Van der Velden *et al.,* 2000, Ausma *et al.,* 2003, Yeh *et al.*, 2006). These studies, together with our study, suggest that connexin expression is remodelled during ageing or in AF.

3.9.4. Comparison of PVCs with atrial and ventricular myocytes

A number of previous studies have been conducted using atrial myocytes to investigate the effects of ageing in facilitating AF (Boldt *et al.*, 2004a; 2005b, Laky *et al.,* 2011). Similar studies are limited in PVCs and there has been no side-by-side comparison of the ultrastructure of PVCs with atrial and ventricular myocytes. Therefore comparisons of the structure of PVCs, atrial and ventricular myocytes were undertaken using 3 month- and 24 month-old mice. Similar to atrial and ventricular myocytes, PVCs express RyR2 in a striated, sarcomeric pattern with myofilament bundles between the Z-lines. Additionally, they also have three sub-populations of mitochondria which are perinuclear, inter-myofibrillar and sub-sarcolemmal (Figure 3.3). The EM study demonstrated that PVCs within a pulmonary vein can be oriented at different angles relative to each other (Figure 3.2), which could plausibly impact on the propagation of action potentials. Similar to atrial myocytes in rodents, PVCs mostly lack T-tubules (Tsuneoka *et al.,* 2012, Rietdorf *et al.,* 2014). PVCs are different to atrial and ventricular myocytes in that they show a higher frequency of spontaneous Ca^{2+}/ electrical signals and have been reported to have a less negative resting membrane potential (Chen *et al.,* 2002, Ehrlich *et al.,* 2003, Okamoto *et al.,* 2012). The increase in the spontaneous activity, less negative resting membrane potential and PVCs orientation are some of the factors that may lead to arrhythmias.

3.9.5. Changes in myofibres in PVCs, atrial and ventricular myocytes from 3 month- and 24 month-old mice

Putative structural changes of myofibres within cardiac myocytes from young and old mice were examined using high magnification TEM of fixed cells. Previous studies have demonstrated an increase in spacing between myofibres or loss of myofibres (myolysis) in atrial myocytes from AF animal models (Ausma *et al.,* 1997, 2001). The loss of myofibres observed in AF might facilitate the occurrence of arrhythmias as it may hinder electrical conduction and alter Ca^{2+} homeostasis. Thus, in this thesis, changes in myofibres during ageing in PVCs, atrial and ventricular myocytes during ageing were analysed. The EM images of cardiac myocytes were quantitated using a number of parameters to provide an objective measure of myofibre content and organisation (Figure 3.8). The criteria used for this study were sarcomere width, offset between Z-lines, angle between Z-lines and percentage of disorganisation (illustrated in Figure 3.8). By analysing these parameters, it was possible to quantitate possible changes in myofibre structure during ageing. There was a significant difference in sarcomere width in PVCs from 3 month- and 24 month-old mice (Figure 3.9A). However, there were no changes in any of the other criteria used to characterise the organisation of myofilaments (Figure 3.9). In atrial myocytes, there was no significant difference in any of the parameters measured in cells from 3 month- and 24 month-old mice (Figure 3.17). In ventricular myocytes, there was no significant difference in the sarcomere width from 3 month- and 24 month-old mice (Figure 3.22A), but there were significant alterations of the offset between Z-lines, angle between Z-lines, or proportion of Z-lines showing disorganisation in ventricular myocytes from 3 month- and 24 month-old mice (Figure 3.22B – D). Comparison of the three cell types indicated that ventricular cardiac myocytes from young animals had the highest level of alignment between myofibres. However, ventricular cardiac myocytes also showed the strongest deterioration of myofibre alignment with ageing. The myofibres within PVCs and atrial myocytes were not as well organised as in ventricular cardiac myocytes in young animals, but their organisation did not significantly deteriorate during ageing (Figure 3.25).

3.9.6. Changes in mitochondria in PVCs, atrial and ventricular myocytes from 3 month- and 24 month-old mice

To analyse putative mitochondrial changes during ageing of PVCs, TEM images of PVCs from 3 month- and 24 month-old mice were examined (Figures 3.10 and 3.11). At both ages mitochondria were highly abundant between myofibres within the PVCs. Quantitation of mitochondrial number and the average area of individual mitochondria revealed that the organelles were more abundant and larger in PVCs from the older animals (Figures 3.11 and 3.12). Unlike the situation in PVCs, mitochondria in atrial myocytes were enlarged but did not increase in number during ageing (Figure 3.26). There were no significant mitochondrial changes in ventricular myocytes from young and old mice (Figure 3.23). In the three cardiac myocytes studied, PVCs showed the biggest changes in mitochondrial number / morphology. Similar to our findings, previous studies in AF animal models have demonstrated either an increase or a drecrease of mitochondrial size in atrial myocytes. For example, in a canine AF model mitochondrial size increased (Morillo *et al*., 1995), whereas a goat AF model was associated with an increase in mitochondrial number and a decrease in mitochondrial size (Ausma *et al*., 1997). An age-dependent increase in atrial myocyte mitochondrial size has been reported in rats (Feldman and Navaratnam 1981). These data, together with ours, suggest that mitochondria may remodel during ageing.

3.9.6.1. Limitations to 2D mitochondrial analysis

Although 2D mitochondrial analysis conducted here suggested changes in mitochondria during ageing, particularly in PVCs, these results need to be confirmed further by doing a 3D analysis. The analysis performed in this study measured mitochondrial area in TEM images using ImageJ, however, mitochondrial volume was not calculated. As mitochondria are organised in the myocyte at different angles relative to the imaging plane, deriving areas from 2D TEM images is problematic and conducting 3D mitochondrial analysis should be of great interest to strengthen the results.

3.9.7. Changes in lipofuscin in PVCs, atrial and ventricular myocytes from 3 month- and 24 month-old mice

The TEM analysis of PVCs, atrial and ventricular myocytes indicated an increase in the appearance of lipofuscin granules in cardiac myocytes from aged mice. In PVCs none of the TEM images from 3 month-old mice showed any lipofuscin granules whereas 10 out of the 52 TEM images had lipofuscin deposits in PVCs from 24 month-old mice (Figure 3.13). Similar results were also found using atrial and ventricular myocytes, where more lipofuscin granules were found in TEM images obtained from 24 month-old mice (Figures 3.19 and 3.24). It has been suggested that lipofuscin interferes with normal cellular functioning, most importantly autophagic clearance of damaged organelles and cell products. Increased amounts of lipofuscin have been linked to various pathological conditions such as lysosomal storage diseases, tumours and malnutrition (Terman *et al.,* 2004b; Jung *et al.,* 2007). The increased lipofuscin seen in cardiac myocytes from old mice in this study would suggest an age-related decrease in lysosomal degradation and/or defective autophagy in cells from old mice as it is described in the reviews by (Terman *et al.,* 2004a; Terman *et al.,* 2005).

In summary, the main alteration in PVCs during ageing were increased sarcomere width, reduced Cx40 expression, more mitochondria, which were also enlarged, and the presence of lipofuscin. Of the three cardiac myocytes analysed, PVCs appeared to show the most mitochondrial alterations during ageing, whereas ventricular myocytes presented the most disruption to the alignment of myofibres between young and old animals. The changes in mitochondria seen in PVCs, coupled with the observations of an increased presence of lipofuscin granules, are consistent with a hypothesis in which PVCs from older animals have deteriorating homeostasis. It is plausible that these structural and biochemical changes contribute to the mechanisms whereby PVCs become more profoundly pro-arrhythmic during ageing. However, further studies are required to characterise the impact of these changes on the physiological functions within PVCs.

Chapter 4: Characterisation of Ca^{2+} signalling in PVCs

4.1. Introduction

As outlined in Chapter 1, ageing- and AF- induced changes in Ca^{2+} signalling in atrial myocytes, as well as structural and functional remodelling, have been extensively studied (Brundel *et al.,* 1999, Lai *et al.,* 1999, Mestre Prates *et al.,* 2002, Vest *et al.,* 2005, Neef *et al.,* 2010, Voigt *et al.,* 2012). Despite the importance of PVCs for onset and maintenance of AF, relatively little research has been focussed on the events occurring in PVCs that lead to AF. Ca^{2+} signalling is an intriguing aspect of PVC function, as a number of studies have demonstrated their propensity to display spontaneous Ca^{2+} signals (Logantha *et al.,* 2010, Rietdorf *et al.,* 2014, Rietdorf *et al.,* 2015, Xiao *et al.,* 2016) that may disrupt responses to rhythmic action potentials and contribute to ectopic electrical activity (Haissaguerre *et al*., 1998, Sueda *et al.,* 2005, Tsuneoka *et al.,* 2012). The reasons why PVCs show such profound spontaneous Ca^{2+} signalling are unclear, but it is plausible that aberrant Ca^{2+} signals contribute to pro-arrhythmic activity. Moreover, an increase in spontaneous Ca^{2+} signalling with ageing, coupled with a concomitant reduction in the fidelity of electrical signalling, could underlie the increased PVC-dependent AF observed in older individuals. The work in this Chapter therefore sought to probe mechanisms responsible for causing spontaneous Ca^{2+} signals within PVCs from 3 month- and 24 month-old mice, with the intention of highlighting ways in which the fidelity of PVC electrical signalling could be improved. To date, an investigation into ageing-induced changes in Ca^{2+} signalling in PVCs has not been undertaken.

The structural studies described in Chapter 3 (section 3.6.1) indicated that PVCs from 24 month-old mice had changes in morphology and organisation that may allude to altered cellular function. For example, 24 month-old mice had an increase in both number and size of mitochondria in comparison to PVCs from 3 month-old mice. However, whilst EM images are suitable for analysing the characteristics of cells and organelles, it is not possible to determine whether there are functional differences. Previous studies have established that aspects of mitochondrial function do deteriorate during ageing in rat hearts (Petrosillo *et al.,* 2009; Duicu *et al.,* 2013) and in ventricular myocytes and tissues (Jian *et al.,* 2011, Barton *et al.,* 2017). For example, there is an increased production of ROS (Cooper *et al.,* 2013, Guo *et al.,* 2014, Huang *et al.,* 2017). As described in the Chapter 1, mitochondria have important roles in cardiac myocyte energy production and Ca^{2+} homeostasis (Drago *et al.,* 2012, Liu *et al.,* 2013, Boyman *et al.,* 2014, Santulli *et al.,* 2015), so alteration in mitochondrial function or number could plausibly impact on spontaneous Ca^{2+} signalling and lead to pro-arrhythmic effects. The studies presented in this Chapter therefore also sought to determine if there were detectable changes in mitochondrial function and ROS production within PVCs during ageing.

4.2. Aims of this Chapter

The work presented in this Chapter compared Ca^{2+} signalling, mitochondrial function and ROS production in PVCs from 3 month- and 24 month-old mice. The specific aims were:

(1) Characterise Ca^{2+} signalling in PVCs from 3 month- and 24 month-old mice. In particular, the following aspects were investigated:

- Spontaneous Ca^{2+} signalling.
- The ability of PVCs to following electrical pacing.
- The role of components of the PVC Ca^{2+} signalsome (e.g. VOCC, NCX, SOCE and RyR) in Ca^{2+} signalling and homeostasis.

(2) Examine the involvement of mitochondria in Ca^{2+} signalling within PVCs from 3 month- and 24 month-old mice.

(3) Investigate the production of ROS and its consequences for EC-coupling, in PVCs from 3 month- and 24 month-old mice.

4.3. Analysis of spontaneous and EFS-induced Ca^{2+} transients in PVCs

4.3.1. Measuring Ca^{2+} signals in PVCs

A key aim in this study was to compare Ca^{2+} signalling within PVCs from 3 month- and 24 month-old mice in order to highlight ageing-induced changes in cell behaviour that might explain why PVCs have a greater propensity to trigger AF in older individuals. The single-wavelength fluorescent Ca^{2+} indicator Cal-520 was used to visualise Ca^{2+} signals in PVCs within lung slices. This indicator was found to give a consistent loading within the PVCs, and preliminary studies carried out in the laboratory indicated that Cal-520 was the most resistant of the currently available single wavelength indicators with respect to organelle compartmentation, leakage and bleaching (Rietdorf *et al.,* 2014). Moreover, fluorescence from Cal-520 was visible in cells with a resting Ca^{2+} concentration (thus making the cells sufficiently visible to focus on), and had an appropriate dynamic range to enable detection of Ca^{2+} signals of variable amplitudes with good temporal resolution and signal to noise (Figure 4.1).

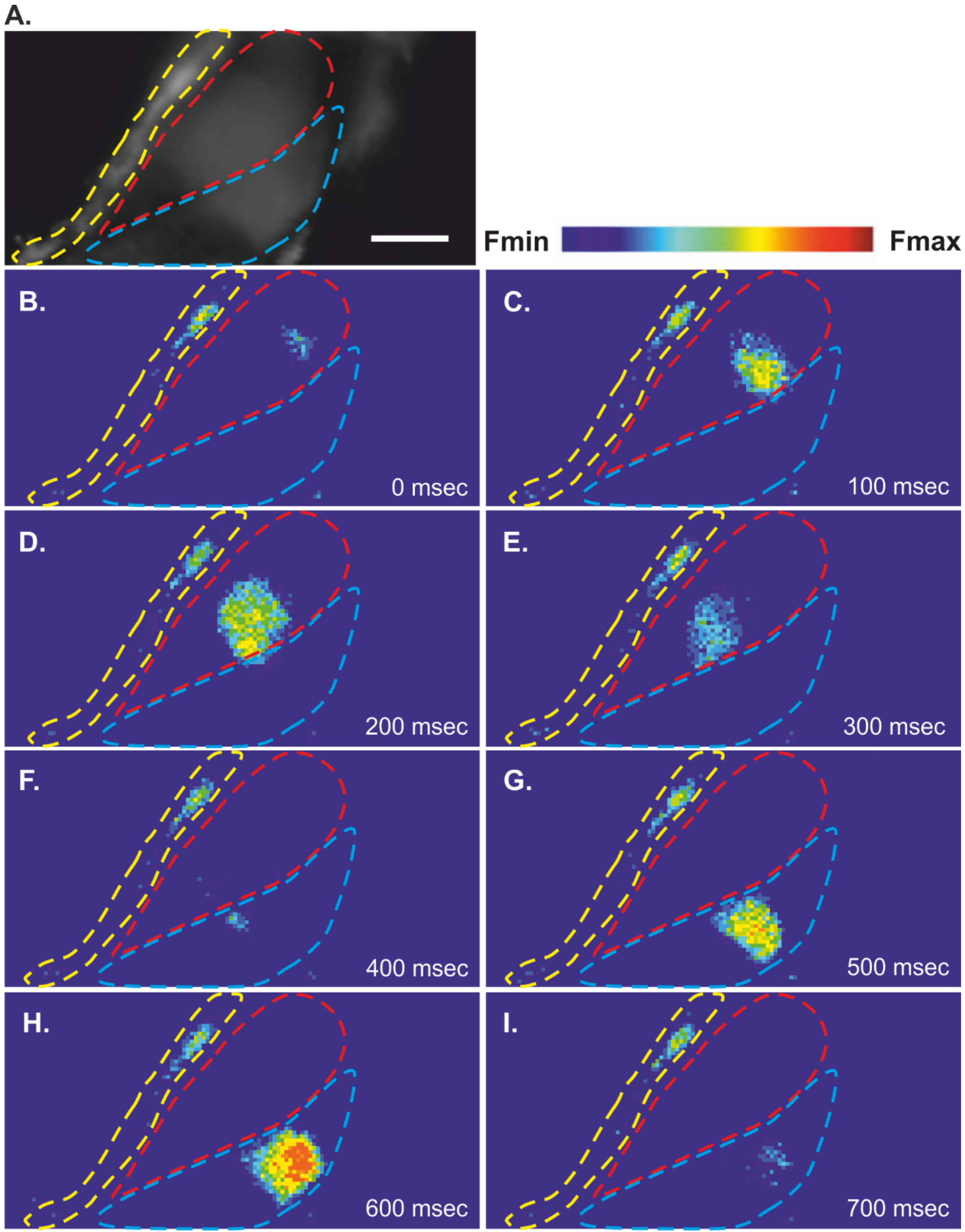

Figure 4.1. Visualisation of Ca^{2+} signals within PVCs using Cal-520. Panels **A** shows an image of Cal-520-loaded PVCs (outlined in red and blue) within a pulmonary vein next to an endothelial layer (outlined in yellow). The cells were loaded with Cal-520 using the protocol described in Chapter 2. The PVCs sequestered Cal-520 (or any Ca^{2+} indicator) more readily than their neighbouring smooth muscle cells, which aided in their identification in imaging experiments. The montage of images in panels **B-I** was captured sequentially at 0.1 second intervals, and illustrate the typical visualisation of a Ca^{2+} wave propagating through the top PVC (outlined in red, panels **B-E**). In panel **F**, the wave moves into the bottom cell (outlined in blue) at 400 msec, and moves into the opposite direction (panels **F-I**). The scale bar denotes 20 µm.

To capture and visualise the Ca^{2+} signals occurring within PVCs, different imaging techniques and forms of representation have been used. Confocal video microscopy of whole fields of PVCs provided 2-dimensional (2D) recordings of Ca^{2+} signals over time in the form of sequentially-captured images (Figure 4.1). An advantage of video microscopy is that the whole area of many PVCs can be visualised simultaneously so that any discrete, localised Ca^{2+} signals are not missed. However, due to the number of pixels being scanned to form the 2D images, the rate of image acquisition was relatively slow (typically 10 Hz in this study). Moreover, it is cumbersome to display montages of images to illustrate Ca^{2+} signals that occurred.

An alternative to video microscopy is line-scanning, where a line is drawn across a field of view and is repeatedly scanned. The consecutive lines are stacked in a temporal sequence so that Ca^{2+} signals can be seen over time. A line-scan provides a 2D result, but with one spatial dimension (usually vertical) and one time dimension (usually horizontal). Examples of line-scans are shown below. The key advantage of line-scanning is speed (typically 333 Hz in this study), which is particularly useful for fast Ca^{2+} signals, such as those occurring within PVCs. The drawback of line-scanning is that the scanned line is preselected before an experiment is initiated, and it is possible to miss Ca^{2+} signals if they occur outside the line of pixels being scanned. It is conceivable to derive pseudo-line-scans from 2D video microscopy image sequences by using post-analysis tools to sample an area/line within the captured field over successive frames. Preliminary experiments in this study showed that the propagation speed and frequency of Ca^{2+} signals in PVCs were sufficiently rapid to warrant the need for line-scanning in most situations. A description of how experiments involving video microscopy or line-scanning of PVCs were set up is presented in Chapter 2.

4.3.1.1. Identifying different types of Ca^{2+} signals in line scans

At the inception of the imaging experiments in this study, it became obvious that PVCs often displayed complex mixtures of Ca^{2+} signals with different spatial and temporal characteristics (Figure 4.2). Since a key aim of this study was to understand mechanisms that may cause PVCs to trigger arrhythmic activity, it was critical to be able to distinguish spontaneous Ca^{2+} signals and EFS-triggered Ca^{2+} signals, and thereby examine the influence of spontaneous Ca^{2+} signals on the fidelity of electrical pacing.

Figure 4.2. Distinguishing different types of Ca^{2+} signals in PVCs. The cartoon of cells in Panel **A** illustrates how the line to be repeatedly scanned would be typically placed across adjacent cells (the scanned line is denoted by the vertical dashed black line). A typical line-scan plot is shown in Panel **A**, with the spatial dimension through the cells being vertical, and the time dimension running horizontally from left to right. The horizontal dashed white lines indicate the boundary between the cells. All of the Ca^{2+} signals evident in the line-scan plot were due to spontaneous activity (as no EFS was applied). The traces below the line-scan show how the cytosolic Ca^{2+} concentration changed over the duration of the recording. The traces were derived by averaging pixel intensities along the line-scan plot at the regions indicated by the arrows, and are presented as the change in fluorescence intensity (F/F_0) over time. Local Ca^{2+} transients are indicated by orange squares behind the traces. Whereas, Ca^{2+} waves are identified by blue squares behind the traces. Panel **B** shows a cartoon of cells with the typical placement of a line for scanning, a representative line-scan, and corresponding Ca^{2+} traces. In this case, the PVCs displayed synchronous EFS-induced Ca^{2+} transients. The timing of EFS pulses (1 Hz) is indicated by the series of black arrows above the line-scans. Panels **C** and **D** show a quantitative summary of the properties of local Ca^{2+} transients, Ca^{2+} waves, and EFS-induced Ca^{2+} transients that were observed in the series of experiment that yielded the data shown in Panels **A** and **B**. The scale bar represents 20 µm.

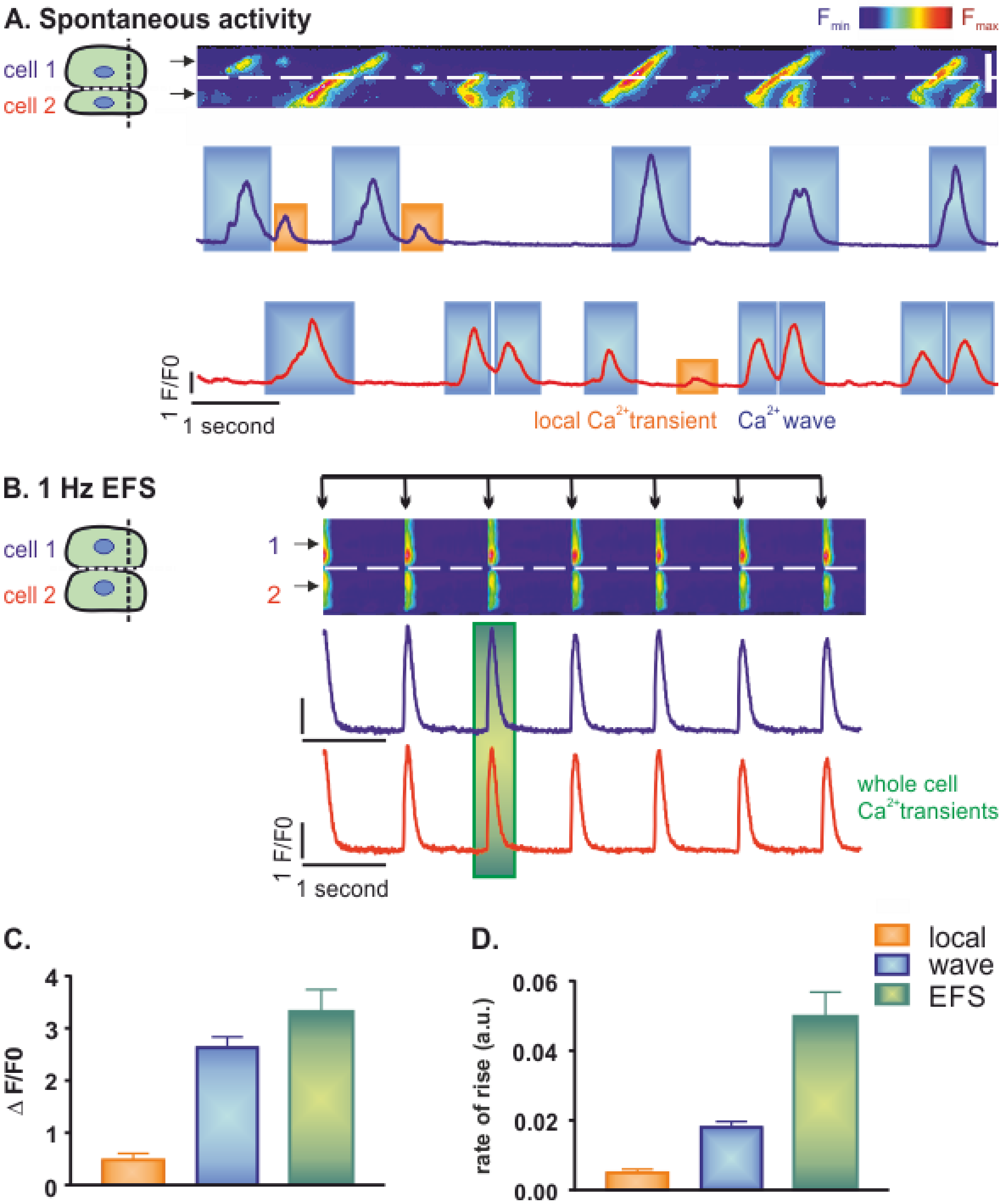
A. Spontaneous activity
Fmin
Fmax
cell 1
cell 2
1 F/F0
1 second
local Ca2+ transient
Ca2+ wave
B. 1 Hz EFS
cell 1
cell 2
1
2
1 F/F0
1 second
whole cell
Ca2+ transients
C.
Δ F/F0
0
1
2
3
4
D.
rate of rise (a.u.)
0.00
0.02
0.04
0.06
local
wave
EFS

Characteristic Ca^{2+} signals are illustrated by the line-scans presented in Figure 4.2. For the purposes of this study, Ca^{2+} signals were classified into three types to allow qualitative and quantitative analysis:

(1) **Local Ca^{2+} transients**. These brief Ca^{2+} signals are most likely the PVC equivalent of Ca^{2+} sparks that have been identified in atrial and ventricular myocytes (Cheng *et al.,* 1993, Bootman *et al.,* 2006, Cheng and Lederer 2008, Herrai-Martinez *et al.*, 2015). However, they were not identified as Ca^{2+} sparks using formal criteria in this study, and are therefore referred to as local Ca^{2+} transients. In a line–scan plot, local Ca^{2+} transients were evident as discrete circular/comet-shaped changes in Cal-520 fluorescence intensity, which remained spatially limited and did not propagate through a cell (Figure 4.2A). Local Ca^{2+} transients occurred in different regions of a cell at various times, although not all PVCs displayed local Ca^{2+} transients. Another distinguishing factor of local Ca^{2+} transients was their amplitude and rate of rise, which were lower than that of Ca^{2+} waves or EFS-induced Ca^{2+} transients (described below) in the same cell (Figure 4.2C and D). Due to their lesser amplitude, local Ca^{2+} transients typically have a light blue/turquoise appearance in line-scans, as per the calibration spectrum shown in Figure 4.2A.

(2) **Ca^{2+} waves**. In contrast to local Ca^{2+} transients, Ca^{2+} waves did propagate away from their initiation site, and were therefore typically visible in line-scans as changes in Cal-520 fluorescence intensity with '/', '\' or '<' shapes (Figure 4.2A). The initiation site for Ca^{2+} waves was the first point along the temporal axis at which the fluorescence intensity increased (i.e. a change from deep blue colour towards a warmer colour in the line-scan plots).

Ca^{2+} waves were heterogeneous even within a single PVC. Ca^{2+} waves could propagate either entirely, or partially, through a PVC. This is illustrated by the line-scan in Figure 4.2A (upper cell); four '/'-shaped Ca^{2+} waves that travelled through the cell from bottom to top are evident, along with a Ca^{2+} wave that started to spread but halted near the middle of the line-scan. Successive Ca^{2+} waves could originate at different initiation sites within a PVC (Figure 4.3), and propagate from end to end, or from the middle of the cell to each end (Figures 4.4). If Ca^{2+} waves collided they annihilated each other (Figure 4.4). Analysis of Ca^{2+} waves within PVCs from 3 month-old animals indicated that 48.1 ± 13% of cells displayed a single initiation point for all Ca^{2+} waves. Whereas, in 51.9 ± 13% of the PVCs multiple Ca^{2+} wave initiation points were observed (*n* = 10 slices from 4 animals). The majority of Ca^{2+} transients (77.4 ± 9.9%; *n* = 10 slices from 4 animals) initiated at only one site, which was typically close the end of a cell, and propagated through the cell in one direction only. The average propagation velocity of Ca^{2+} waves was 77 ± 7 μms^{-1} (*n* = 10 slices from 4 animals), although the speed of Ca^{2+} waves varied between PVCs. Despite PVCs expressing connexins (Chapter 3 section 3.5.2: Cx43 and Cx40 localisation in PVCs from 3 month- and 24 month-old mice) and being electrically coupled (Yeh *et al.,* 2003; Xiao *et al.,* 2016; Kugler *et al.,* 2017), Ca^{2+} waves tended to stop at cell boundaries. However, in some cases, the arrival of a Ca^{2+} wave at the sarcolemma of a PVC would trigger a Ca^{2+} wave in an adjacent cell.

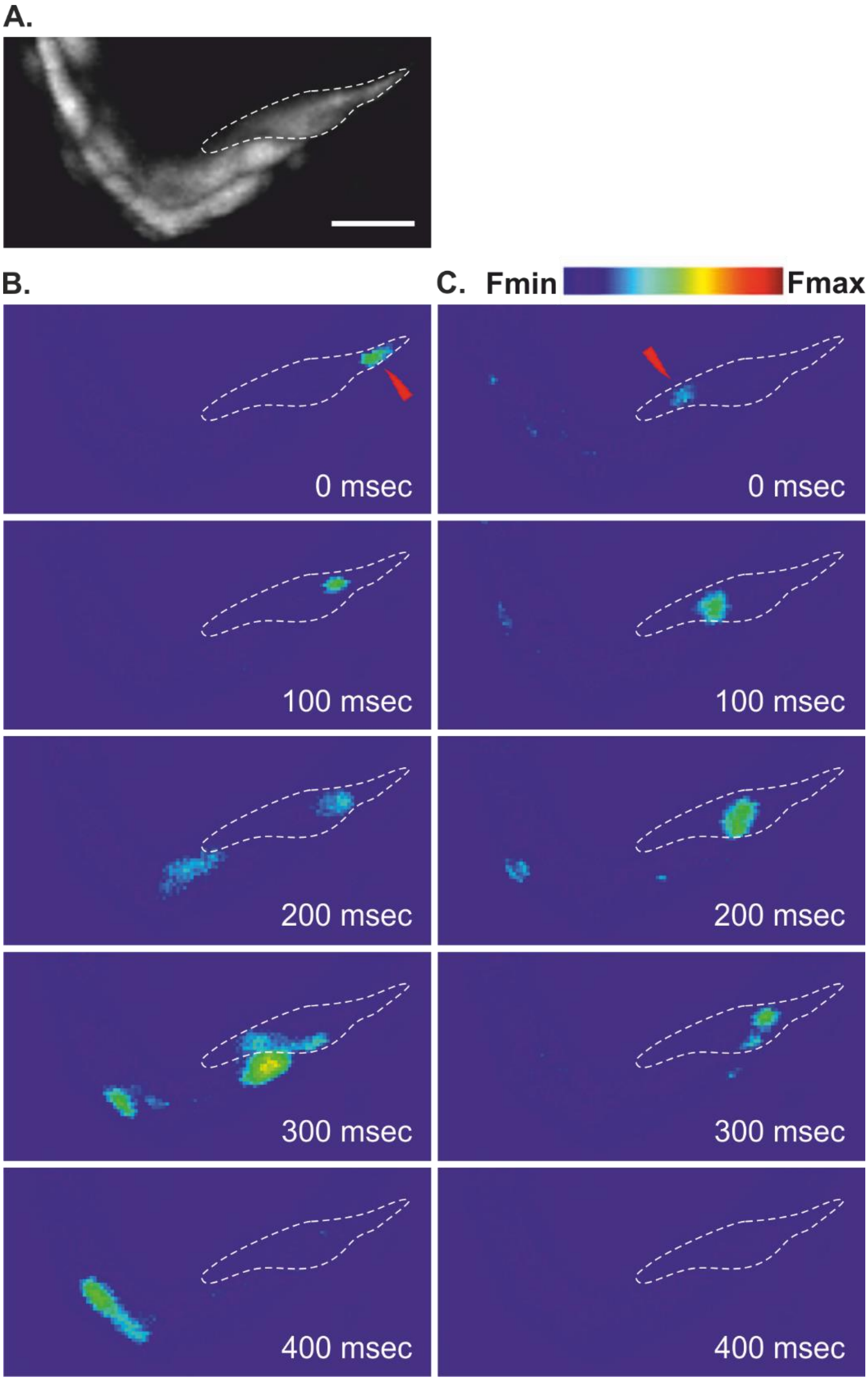

Figure 4.3. Ca^{2+} waves initiating at different sites within a PVC. Panel **A** shows PVCs in a lung slice loaded with Cal-520. The montages of images in Panels **B** and **C** show successive Ca^{2+} waves travelling through the same PVC, outlined with a white dashed line in panels **A-C**. The Ca^{2+} waves had different initiation points (red arrowheads in the top row of both Panels). Some activity in other cells is visible in the montage. The scale bar represents 20 µm.

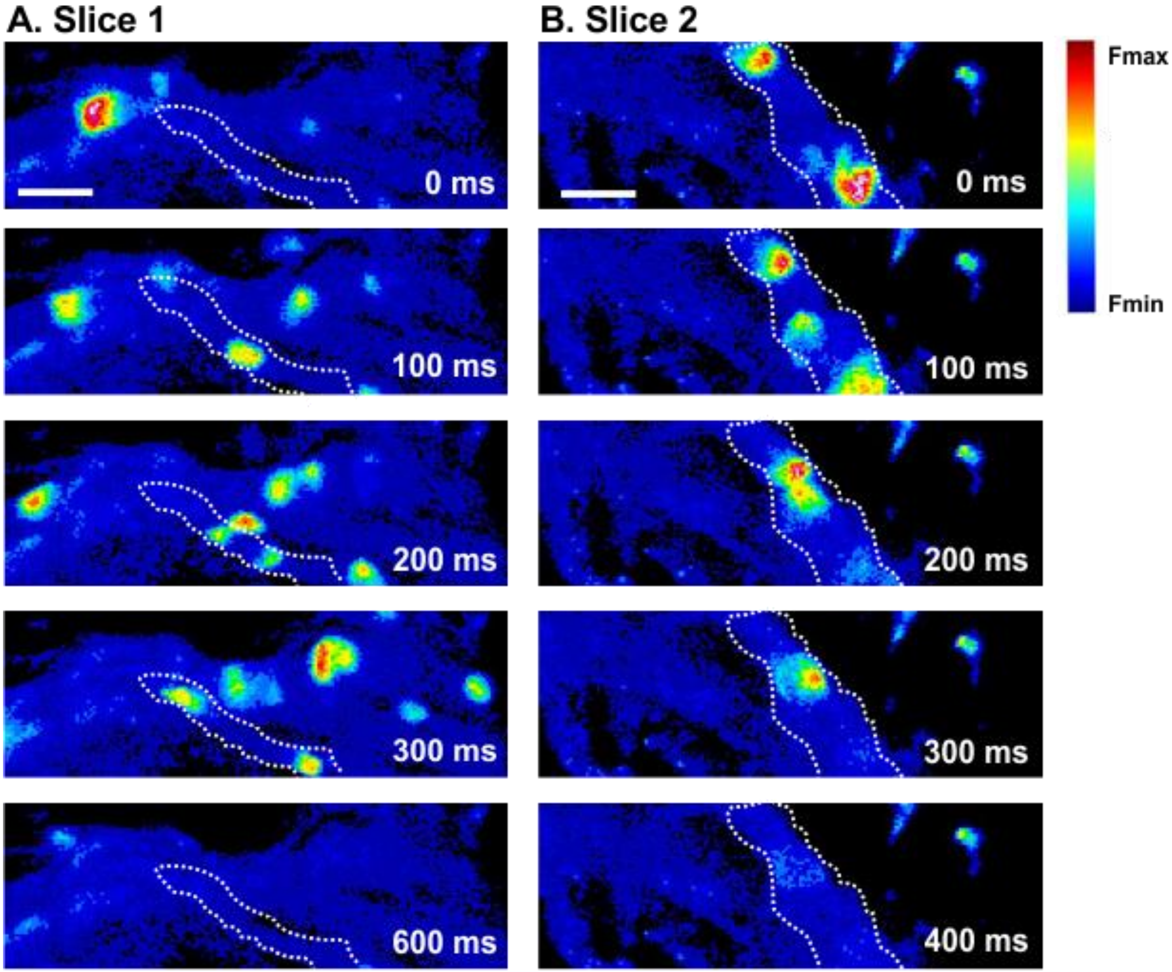

Figure 4.4. Ca^{2+} waves propagating in different directions within PVC. The montages of images in Panels **A** and **B** show Ca^{2+} waves propagating through PVCs. The Ca^{2+} wave in Panel **A** originated near the centre of the cell, and then split into two Ca^{2+} waves that travelled to either end of the cell simultaneously. In contrast, Panel **B** illustrates a cell with multiple Ca^{2+} wave initiation sites. The Ca^{2+} waves travelled towards each other, and collided at ~300 ms before annihilating each other. The cell boundaries are indicated with a white dotted line. The scale bar represents 20 µm.

(3) **EFS-induced Ca^{2+} transients**. The third type of Ca^{2+} signal discussed in this study is Ca^{2+} transients induced by depolarisation of PVCs using EFS (Figure 4.2B). EFS-induced Ca^{2+} transients are evident in line-scan plots as a rapid, step-like increase in Cal-520 fluorescence intensity. In Ca^{2+} traces, EFS-induced Ca^{2+} transients had a faster rate of rise than a Ca^{2+} wave, and had a larger amplitude than a local Ca^{2+} transient (Figure 4.2C and D). EFS-induced Ca^{2+} transients were often whole cell responses, where the fluorescence increased simultaneously across all the regions of the cell. However, as discussed later, the ability of a PVC to respond to EFS depended on the occurrence of spontaneous Ca^{2+} signals.

4.3.1.2 Identifying three types of Ca^{2+} signals in Ca^{2+} traces

The Ca^{2+} traces presented in this study only display those Ca^{2+} signals that occurred within the cellular region that was both sampled during the experimental line-scanning and was analysed post-experiment. Since the majority of Ca^{2+} waves propagated within cells to a considerable extent, they were likely to be visible both within a line-scan and the Ca^{2+} trace that is subsequently derived. However, due to the limited spatial spreading of local Ca^{2+} transients, they tended to be undersampled. An example of this is shown in Figure 4.2A, where more local Ca^{2+} transients are visible in the line scan than in the corresponding Ca^{2+} trace.

As noted earlier, the three types of Ca^{2+} signals that were observed in PVCs have specific characteristics that allow them to be identified within line-scans. The three types of Ca^{2+} signals can also be distinguished in Ca^{2+} traces based on rate of rise of the Ca^{2+} signal and Ca^{2+} signal amplitude (Figure 4.2C and D). In this study, different Ca^{2+} signals were discriminated by using a combination of line-scan plots to establish their spatial properties, as well as Ca^{2+} traces to show their kinetic and amplitude characteristics. A summary of the properties of local Ca^{2+} transients, Ca^{2+} waves and EFS-induced Ca^{2+} transients, and their discriminating characteristics, are presented in Table 4.1.

	Properties of Ca^{2+} signal in a line-scan	**Properties of Ca^{2+} signal in a Ca^{2+} trace**	**Amplitude ($\Delta F/F_0$)**	**Rate of rise ($\Delta F/F_0$ per s)**
Local Ca^{2+} transient	Spatially restricted increase in Cal-520 fluorescence that was circular or comet-shaped.	The lowest amplitude Ca^{2+} signal recorded in the PVCs. Typically, <20% of the maximal amplitude change of a Ca^{2+} wave in the same cell.	0.5 ± 0.1 ** vs. Ca^{2+} wave *** vs. EFS-induced Ca^{2+} transient	0.005 ± 0.0009 n.s. vs. Ca^{2+} wave **** vs. EFS-induced Ca^{2+} transient
Ca^{2+} wave	Propagating increase in Cal-520 fluorescence with /, \ or < shapes.	Variable amplitude, slower in onset than an EFS-induced Ca^{2+} transient.	2.7 ± 0.2 ** vs. Local Ca^{2+} transient n.s. vs. EFS-induced Ca^{2+} transient	0.02 ± 0.002 n.s. vs. Local Ca^{2+} transient **** vs. EFS-induced Ca^{2+} transient
Whole cell Ca^{2+} transient	Rapid, step-like increase in Cal-520 fluorescence. The increase in Cal-520 could be whole-cell, or a portion of the cell depending on spontaneous Ca^{2+} signalling.	Fastest rate of rise and highest amplitude of any Ca^{2+} signal recorded in the PVCs.	3.3 ± 0.4 ** vs. Local Ca^{2+} transient n.s. vs. Ca^{2+} wave	0.05 ± 0.007 **** vs. Local Ca^{2+} transient **** vs. Ca^{2+} wave

Table 4.1. Summary of the criteria used to distinguish different Ca^{2+} signals in line-scans plots and Ca^{2+} traces. *, **, *** and **** indicate P values of < 0.05, < 0.01, < 0.001 and < 0.0001, respectively.

4.3.2. Complex spontaneous Ca^{2+} signals and EFS-induced Ca^{2+} transients in PVCs

The local Ca^{2+} transients and Ca^{2+} waves described above are examples of spontaneous Ca^{2+} signalling in the PVCs. During the imaging experiments undertaken in this study, with recordings typically lasting for 10 - 35 seconds, the majority of PVCs from 3 month-old animals (70 ± 13.6%; *n* = 28 cells, 10 slices from 4 animals) showed local Ca^{2+} transients. Whereas, all PVCs from 3 month-old animals showed Ca^{2+} waves (*n* = 10 slices from 4 animals).

The frequency of spontaneous Ca^{2+} signals within the PVCs differed considerably. This was true on different levels: between animals, between slices prepared from one animal and also between adjacent PVCs within one lung slice. The average frequency for spontaneous activity (local Ca^{2+} transients and Ca^{2+} waves) was 0.4 ± 0.04 Hz (*n* = 62 slices from 11 animals), and ranged from ~0.1 Hz to ~1.7 Hz.

The three types of Ca^{2+} signals introduced above could occur within the same cell (if EFS was applied) and interacted in the sense that the occurrence of one type of Ca^{2+} signal could affect the triggering of another. This is exemplified by the line-scans and Ca^{2+} traces in Figure 4.5. This figure shows the spontaneous activity within three PVCs prior to application of EFS, and then during stimulation with EFS at 1, 3 and 5 Hz. It is evident that the pattern of spontaneous Ca^{2+} signalling changed with application of EFS, and also that pacing of the cells with EFS was not always consistent. The three cells that were subjected to line-scanning all showed local Ca^{2+} transients and Ca^{2+} waves, but varied in their patterns of spontaneous Ca^{2+} signals (Figure 4.5B). The frequencies of spontaneous Ca^{2+} signals in these cells were 0.4, 0.7 and 0.3 Hz for cells 1 to 3, respectively.

Application of EFS at 1 Hz triggered whole-cell EFS-induced Ca^{2+} transients in cell 1 and eradicated spontaneous Ca^{2+} signals. Whereas, cells 2 and 3 did not respond to 1 Hz EFS, and continued to show spontaneous Ca^{2+} signals (Figure 4.5C). Increasing the EFS frequency to 3 Hz also caused evoked EFS-induced Ca^{2+} transients in cell 1, but with the appearance of alternans (Figure 4.5D). Cell 2 responded to 3 Hz EFS, albeit weakly, with relatively low-amplitude EFS-induced Ca^{2+} transients, and still some on-going spontaneous Ca^{2+} signals. Cell 3 continued to be non-paced and solely displayed spontaneous Ca^{2+} transients. Elevating the EFS frequency to 5 Hz led to a complex pattern of response in cell 1 with alternating EFS-induced Ca^{2+} transients, Ca^{2+} waves and missed responses to EFS (Figure 4.5E). Cell 2 showed a similar activity to cell 1, and cell 3 remained unaffected the EFS pulses. The cells were imaged for a period after the EFS was turned off, and they typically re-set back to the pattern of spontaneous activity observed before EFS was applied, although there could be some lasting consequences, such as the increased entrainment of Ca^{2+} waves between cells (see the periods of spontaneous activity post EFS in Figure 4.5C – E).

The complex patterns of response shown in Figure 4.5 demonstrate the heterogeneity and complexity of Ca^{2+} signalling within PVCs. Such complex patterns of Ca^{2+} signalling are not desirable in a cell type that is required to faithfully follow action potentials emanating from the sinoatrial node. Indeed, the spontaneous Ca^{2+} signals arising in PVCs have been shown to prevent PVCs from being regularly paced (Rietdorf *et al.,* 2014, Rietdorf *et al.,* 2015). The observations presented above highlight one of the major aims of trying to understand Ca^{2+} signalling within PVCs; is it possible to abrogate spontaneous Ca^{2+} signals and ensure faithful electrical pacing?

Figure 4.5. Spontaneous Ca^{2+} signals and EFS-induced Ca^{2+} transients in PVCs. The cartoon of cells in Panel A illustrates the line that was repeatedly scanned placed across three adjacent cells (the scanned line is denoted by the dashed black line). Panel B shows a line-scan plot illustrating the spontaneous Ca^{2+} signals observed within the PVCs. The Ca^{2+} traces below the line-scans were derived from regions within the line-scans. The white dashed lines in the line-scans indicate the boundaries between the cells. Panels C – E show representative line-scans and corresponding Ca^{2+} traces obtained whilst applying EFS at 1 Hz (C), 3 Hz (D) and 5 Hz (E), followed by a period of with no EFS. The timing of EFS pulses is indicated by the series of black downward arrows above the line-scans. The scale bar represents 20 µm.

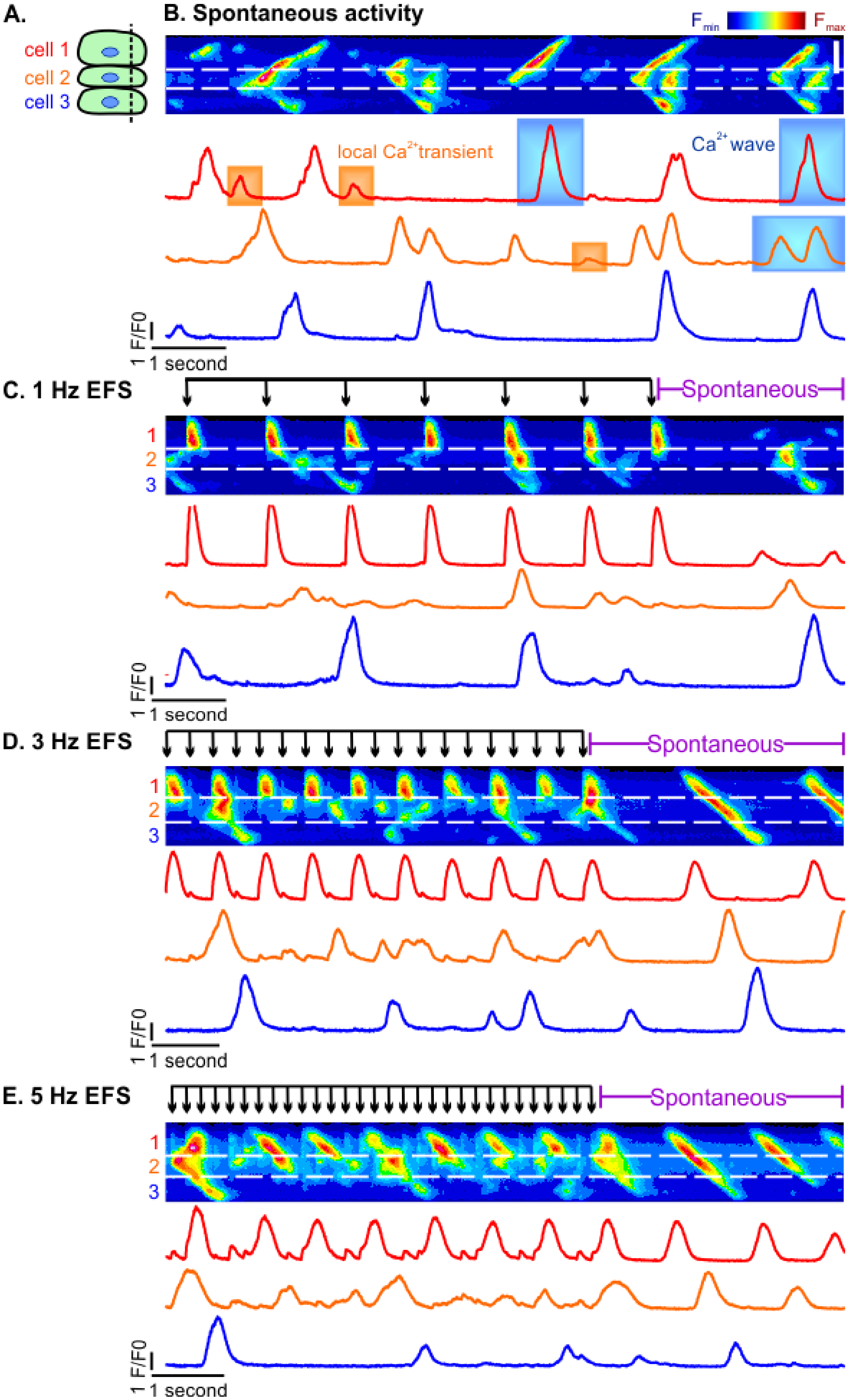
A.
cell 1
cell 2
cell 3
B. Spontaneous activity
Fmin
Fmax
local Ca2+ transient
Ca2+ wave
1 F/F0
1 second
C. 1 Hz EFS
Spontaneous
1
2
3
1 F/F0
1 second
D. 3 Hz EFS
Spontaneous
1
2
3
1 F/F0
1 second
E. 5 Hz EFS
Spontaneous
1
2
3
1 F/F0
1 second

4.4. Testing the role of different Ca^{2+} sources for spontaneous Ca^{2+} signalling in cardiac myocytes

4.4.1. Testing the role of different Ca^{2+} sources for spontaneous Ca^{2+} signals and EFS-induced Ca^{2+} transients in NRVMs

To understand the mechanisms underlying spontaneous Ca^{2+} signals within PVCs, and their impact on EFS-induced Ca^{2+} transients, experiments were designed in which pharmacological reagents would be used to inhibit putative components of the PVC Ca^{2+} signalsome. However, before these experiments were undertaken, as series of adjunct experiments were performed involving NRVMs, as described below.

The reason for these adjunct experiments was to establish that the compounds were active prior to their use on lung slices. Whilst tissues slices, such as those used here, are advantageous in maintaining PVCs' orientations and connections, it is more difficult to perfuse cells with external reagents. The lung slices used in this study are ~180 µm thick, and access to cells deep within a slice would be through a tortuous pathway of extracellular spaces. To avoid false negative observations, it was necessary to firmly establish that reagents were working within the laboratory.

NRVMs were loaded with Cal-520 and imaged using a wide-field fluorescence microscope, since confocal imaging was not needed to record Ca^{2+} signals in monolayers of these cells. The experimental protocol used for these experiments is illustrated in Figure 4.6Ai and ii. To test the effect of the compounds, a field of NRVMs was imaged twice; once before addition of compound (Run 1) and once following addition of a compound (Run 2). Both imaging experiments lasted 35 seconds, and were comprised as follows:

Run 1:

3. **10 seconds where no stimulus was applied to the cells (in this period only spontaneous Ca^{2+} signals occurred).**
4. **10 seconds with application of 2 Hz EFS.**
5. **30 seconds where no stimulus was applied to the cells.**

Following Run 1, a reagent (or HBSS as a control) was superfused over the cells whilst they were maintained on the microscope stage. Following a 5-minute incubation period, Run 2 was initiated.

Run 2:

1. **10 seconds where no stimulus was applied to the cells (in this period only spontaneous Ca^{2+} signals occurred).**
2. **10 seconds with application of 2 Hz EFS.**
3. **30 seconds where no stimulus was applied to the cells.**

Run 1 was used to assess the spontaneous activity of the NRVMs, and their responsiveness to EFS. Whilst Run 2 was used to assess the influence of the reagent on spontaneous Ca^{2+} signals and EFS-induced responses. The frequency and amplitude of spontaneous Ca^{2+} signals (largely Ca^{2+} waves in the NRVMs), and the ability of the cells to follow EFS pacing were analysed by comparing the respective responses before and after the reagent addition in a paired manner. Similar experiments were carried out using HBSS, JTV-519, carvedilol, dantrolene, SN-6 and BTP2 (Figure 4.6). The rationale for choosing these reagents was that they are reported to inhibit different Ca^{2+} transport pathways, as described in Chapter 1, section 5.3. PVCs were considered to be 'successful paced' if they responded to all the EFS pulses in continuous train of pulses, and with consistent Ca^{2+} signal amplitudes (+/- ≤ 10% of $\Delta F/F_0$ Ca^{2+} signal amplitudes).

Representative Ca^{2+} traces obtained from individual cells recorded during these experiments are shown in Figure 4.6. Similar to PVCs, the NRVMs displayed spontaneous Ca^{2+} signals and whole-cell Ca^{2+} responses to EFS, although the frequency of spontaneous activity in the NRVMs was lower than typically seen in PVCs (NRVMs 0.18 ± 0.09 Hz *vs.* PVCs 0.38 ± 0.04 Hz (n = 40 cells from 3 litters for NRVMs and 24 slices from 11 animals for PVCs, respectively). The effects of the various reagents on the frequency and amplitude of displayed spontaneous Ca^{2+} signals are presented quantitatively in Figures 4.7 and 4.8., whilst the effect of the reagents on the ability of the NRVMs to respond to EFS pulses is shown quantitatively in Figure 4.9. The control experiments, using HBSS superfusion, established that Run 1 and Run 2 evoked similar responses (Figures 4.6A, 4.7A, 4.8A and 4.9A). Any changes in either spontaneous Ca^{2+} signals or ability to respond to EFS pulses between Run 1 and Run 2 would therefore be a consequence of superperfusion with the reagents. A summary of the effect of each of the reagents is given below.

JTV-519

JTV-519 is a RyR inhibitor that has been shown to reduce RyR2 activation by increasing the binding of FK506-binding proteins (FKBPs) to RyR2 (Shou *et al.,* 1998; Vest *et al.,* 2005; Dobrev *et al.,* 2012). JTV-519 is currently being tested in clinical trials and reduces RyR2 openings, thus reducing SR Ca^{2+} leak and prevents spontaneous firing rate and may prevent arrhythmias (Kumagai *et al.,* 2003; Chen *et al.,* 2008). Therefore, in this study, 100 µM JTV-519 was used to inhibit the frequency of spontaneous Ca^{2+} signals in NRVMs here and PVCs later (section 4.6). Unfortunately, apart from inhibiting RyR2, JTV-519 has been demonstrated to affect other additional off targets (Kumagai *et al.,* 2003, Chen *et al.,* 2008, Elliot *et al.,* 2011). JTV-519 has been shown to inhibit L-type Ca^{2+} currents and inward and delayed rectifier K^+ currents. In addition to this, JTV-519 has also been shown to prolong the AP duration in atrial myocytes (Kimura *et al.,* 1999, Kumagai *et al.,* 2003, Chen *et al.,* 2008, Elliot *et al.,* 2011). Therefore, although JTV-519 inhibits RyR2 by facilitating the closed state of the channel, one should consider the unspecific effects of the drug and it should be used with caution.

In this study, a significant effect of JTV-519 was to reduce the occurrence spontaneous Ca^{2+} signals, both before and after EFS application (Figures 4.6B and 4.7B), but it did not alter the amplitude of spontaneous Ca^{2+} signals when they did arise (Figure 4.8B). JTV-519 also reduced the ability of NRVMs to respond to EFS pulses (Figure 4.9B). Stimulation of NRVMs with EFS in the presence of JTV-519 caused the occurrence of Ca^{2+} signal alternans in 83.3 % of the cells (Figure 4.6B).

Carvedilol

Carvedilol is a β blocker that inhibits both α and β adrenoceptors and is used extensively in treating HF (Reiken *et al.,* 2003, Zhou *et al.,* 2011). For this study, 100 µM carvedilol was used to reduce the spontaneous Ca^{2+} in NRVMs and PVCs. Carvedilol was tested to investigate whether the changes observed after drug incubation were either from RyR2 inhibition or from suppressing α/β adrenoceptors. It should be noted however, previously, carvedilol has also been shown to inhibit RyR2 openings (Reiken *et al.,* 2003, Zhou *et al.,* 2011).

Carvedilol had a similar effect to JTV-519 on the NRVMs; it reduced the incidence of spontaneous Ca^{2+} signals, both before and after EFS application (Figures 4.6C and 4.7C), but it did not alter the amplitude of spontaneous Ca^{2+} signals when they occurred (Figure 4.8C). Carvedilol also reduced the ability of NRVMs to respond to EFS pulses (Figure 4.9C).

In the presence of carvedilol, the responses to EFS were irregular in 66.7 % of the cells, and the amplitude of the Ca^{2+} transients gradually decreased with successive EFS pulses.

Dantrolene

Dantrolene is muscle relaxant that is highly used as a treatment for malignant hyperthermia (Fruen *et al.,* 1997). It functions by inhibiting RyR1 opening, thereby reducing the SR Ca^{2+} leak. Although dantrolene is traditionally used to facilitate RyR1 closure, it has also been reported to inhibit RyR2 (Jung *et al.,* 2012). Hence, 100 µM dantrolene was tested in this thesis to investigate its effects on RyR2 in NRVMs and PVCs.

Unlike JTV-519 and carvedilol, dantrolene had no effect on the occurrence of spontaneous Ca^{2+} signals, either before or after EFS application (Figures 4.6D and 4.7D), and it did not alter the amplitude of spontaneous Ca^{2+} signals when they occurred (Figure 4.8D). Dantrolene had no effect on the ability of NRVMs to respond to EFS pulses (Figure 4.9D).

SN-6

In this project, 10 µM SN-6 was tested to elucidate the role played by NCX in generating spontaneous Ca^{2+} signals. SN-6 inhibits the forward mode of NCX channel and therefore is used to inhibit NCX-mediated Ca^{2+} transport out of the cell. SN-6 has been demonstrated previously to be cardioprotective in ischaemia-reperfusion injury by inhibiting NCX (Inoue *et al.,* 2004). Sadly, similar with other drugs, the effects of SN-6 are not fully specific to NCX. Previously, SN-6 has also been shown to inhibit L-type VOCCs (Gandhi *et al.,* 2013).

In contrast to the other reagents used, SN-6 reduced the amplitude of the spontaneous Ca^{2+} transients (Figure 4.8E). However, SN-6 had no effect on the occurrence of spontaneous Ca^{2+} signals, either before or after EFS application (Figures 4.6E and 4.7E).

There was a tendency for cells to be less responsive to EFS pulses in the presence of SN-6, but it was not statistically significant (Figure 4.9E).

BTP2

BTP2 is an antagonist of SOCE and has been shown to block an influx of Ca^{2+} without affecting K^+ transport or VOCCs (Zitt *et al.,* 2004, He *et al.,* 2005). Previously, BTP2 has been shown to inhibit the firing rate in SA node cells (Liu *et al.,* 2015). Therefore, to explore if SOCE plays any role in cardiac myocytes, the effects of 100 µM BTP2 were analysed.

BTP2 had the most dramatic effects of all the reagents used; it significantly reduced the occurrence and amplitude of spontaneous Ca^{2+} transients (Figures 4.7F and 4.8F), and it completely abrogated any cellular Ca^{2+} signals in 32% of the cells (Figure 4.6F). BTP2 reduced the ability of NRVMs to respond to EFS pulses (Figure 4.9D).

The test experiments using NRVMs indicated that the reagents could have complex effects and may affect different activities. Of the reagents used, JTV-519, carvedilol and BTP2 had significant effects on the occurrence of spontaneous Ca^{2+} transients (Figure 4.7). Of these reagents, JTV-519 gave a strong suppressive effect on spontaneous Ca^{2+} transients. Not only was the frequency of the spontaneous Ca^{2+} transients reduced by JTV-519, but the percentage of NRVMs showing any spontaneous Ca^{2+} transients was reduced from 99 ± 0.2% to 26.7 ± 16% (P = 0.006, analysed using a paired *t*-test, *n* = 6 coverslips from 2 litters). The fact that BTP2 could completely abrogate all Ca^{2+} signals within NRVMs suggests that it may have more targets than just SOCE, and should be used with caution. The reverse-mode NCX inhibitor SN-6 was seemingly only active in reducing the amplitude of spontaneous Ca^{2+} transients (Figure 4.8). Dantrolene did not affect the occurrence or amplitude of spontaneous Ca^{2+} transients in NRVMs (Figure 4.7), indicating that under the conditions, or concentration, used in this study it did not block RyRs sufficiently to inhibit Ca^{2+} signalling.

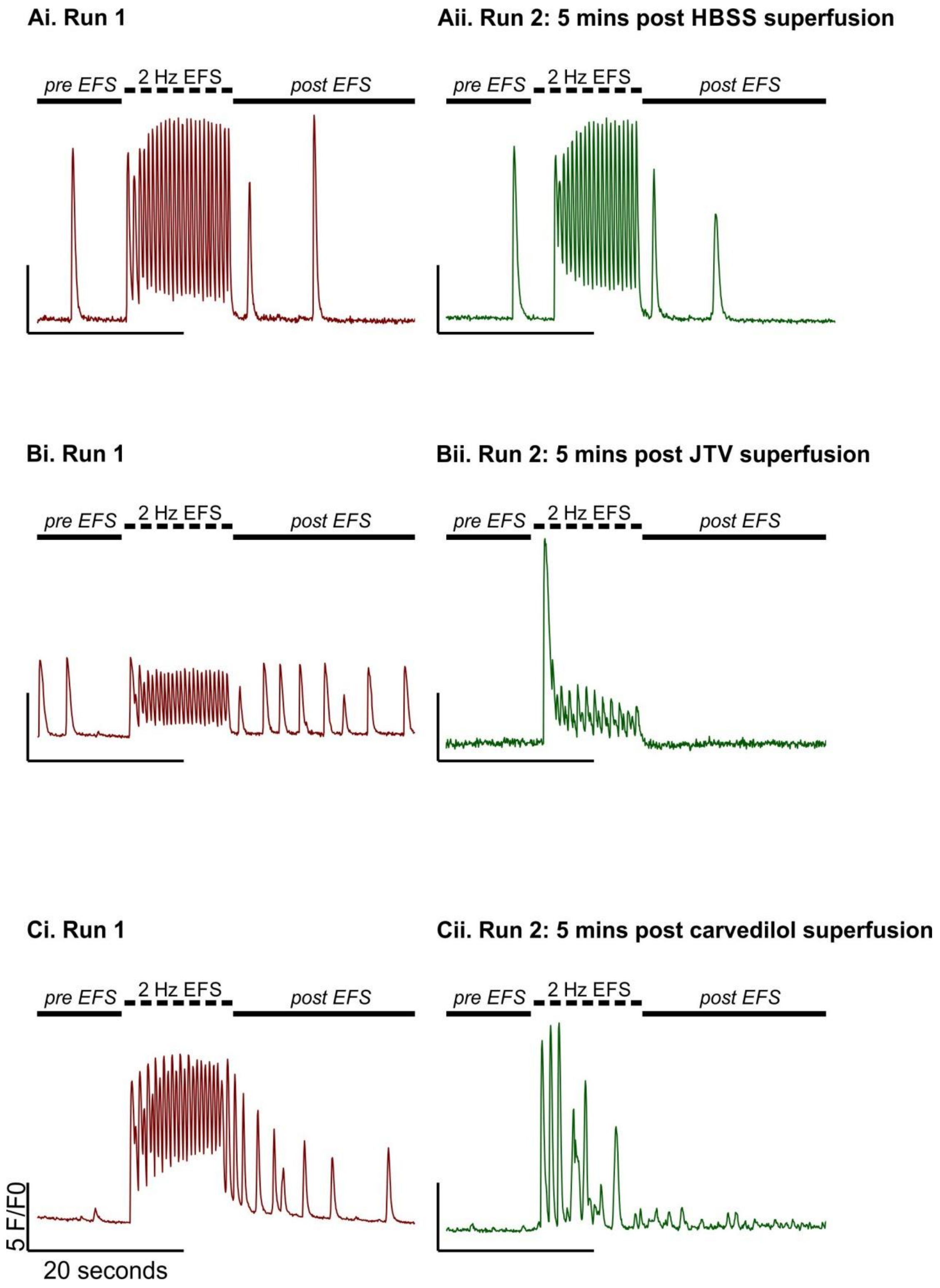

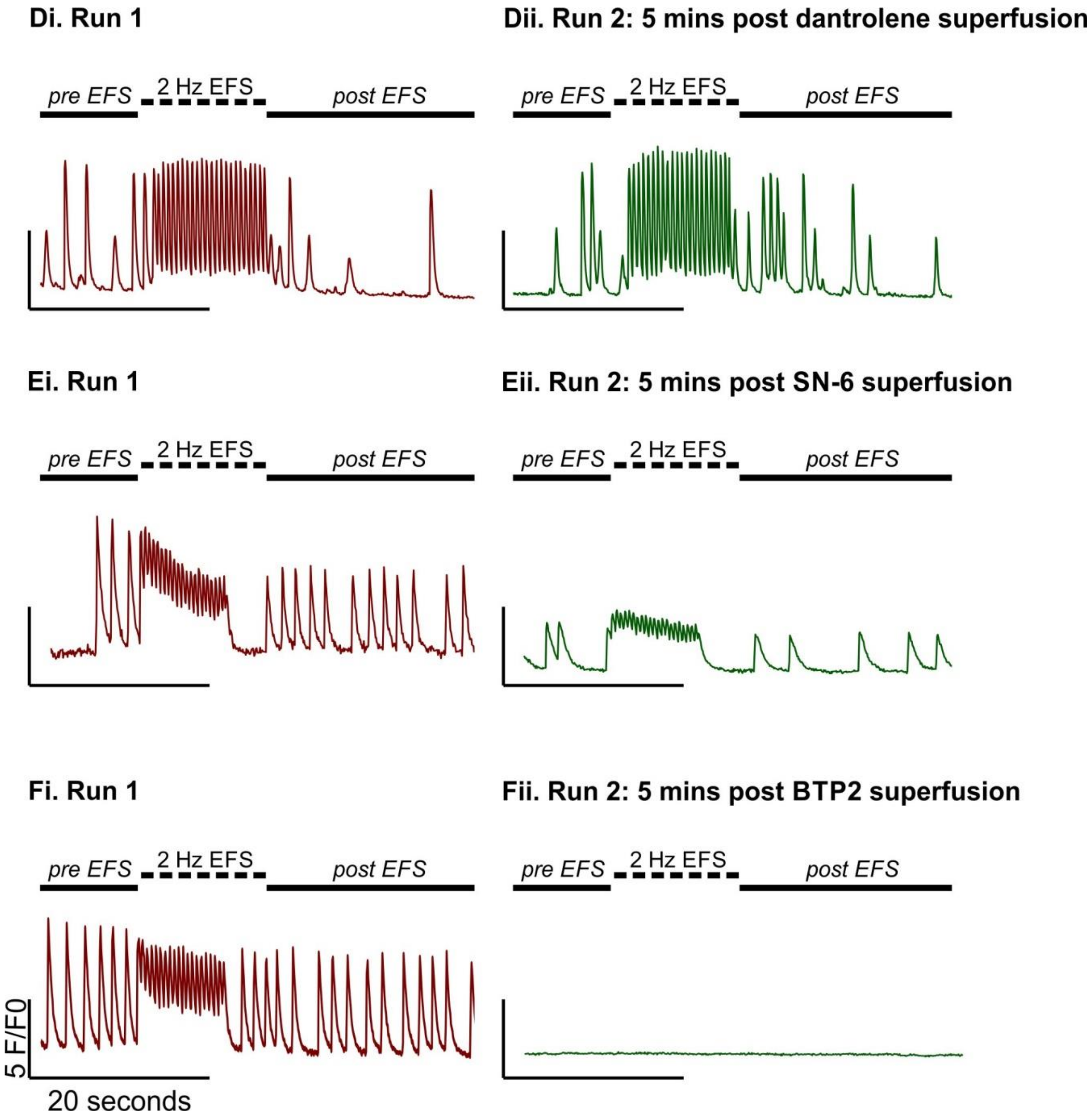

Figure 4.6. Effects of various Ca^{2+} signalsome-affecting reagents on spontaneous Ca^{2+} signals and EFS responses in NRVMs. Panel **Ai** illustrates the stimulation protocol used in this experiment, and depicts a representative Ca^{2+} trace from a NRVM in the presence of HBSS. Between Run 1 and Run2 the NRVMs were superfused with fresh HBSS, incubated for 5 minutes on the stage of the microscope, and then Run 2 was initiated. Panel **Aii** shows cell's responses post HBSS superfusion. Panels **B – F** depict similar paired experiments in which different NRVMs populations were superfused with the reagents shown. A fresh coverslip bearing naive NRVMs was used for each of the reagents shown. The concentrations of reagents applied were 100 µM for JTV-519, carvedilol, dantrolene and BTP2, and 10 µM for SN-6.

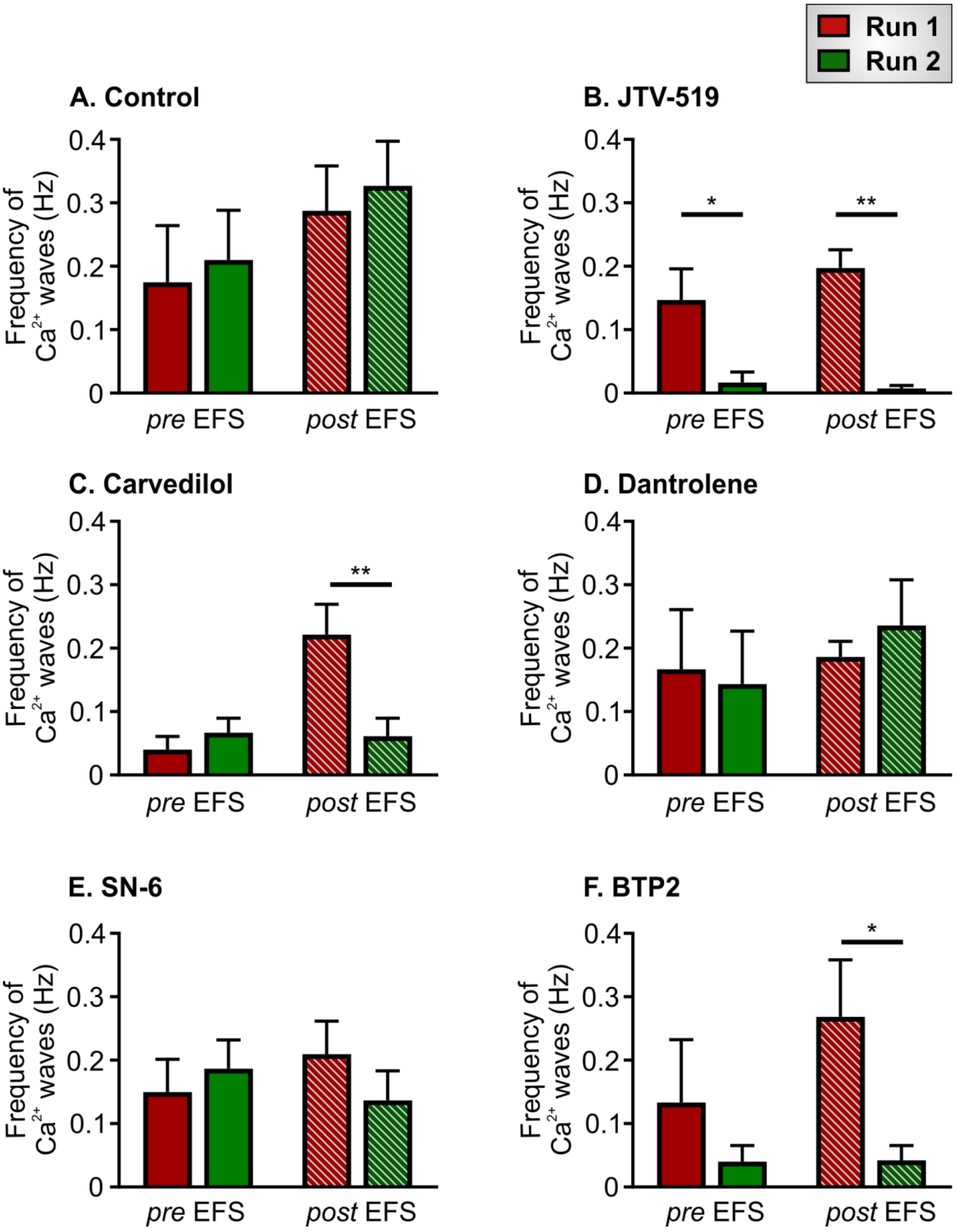

Figure 4.7. Effects of various Ca^{2+} signalsome-affecting reagents on the frequency of spontaneous Ca^{2+} signals in NRVMs. Panels **A – F** show the average frequency of spontaneous Ca^{2+} signals during Run 1 and Run 2 of the experiments depicted in Figure 4.6. The data are presented as mean ± S.E.M., and were analysed using paired *t*-tests. * and ** denote $P < 0.05$ and $P < 0.01$, respectively. *n* = 6 coverslips from 2 litters per reagent.

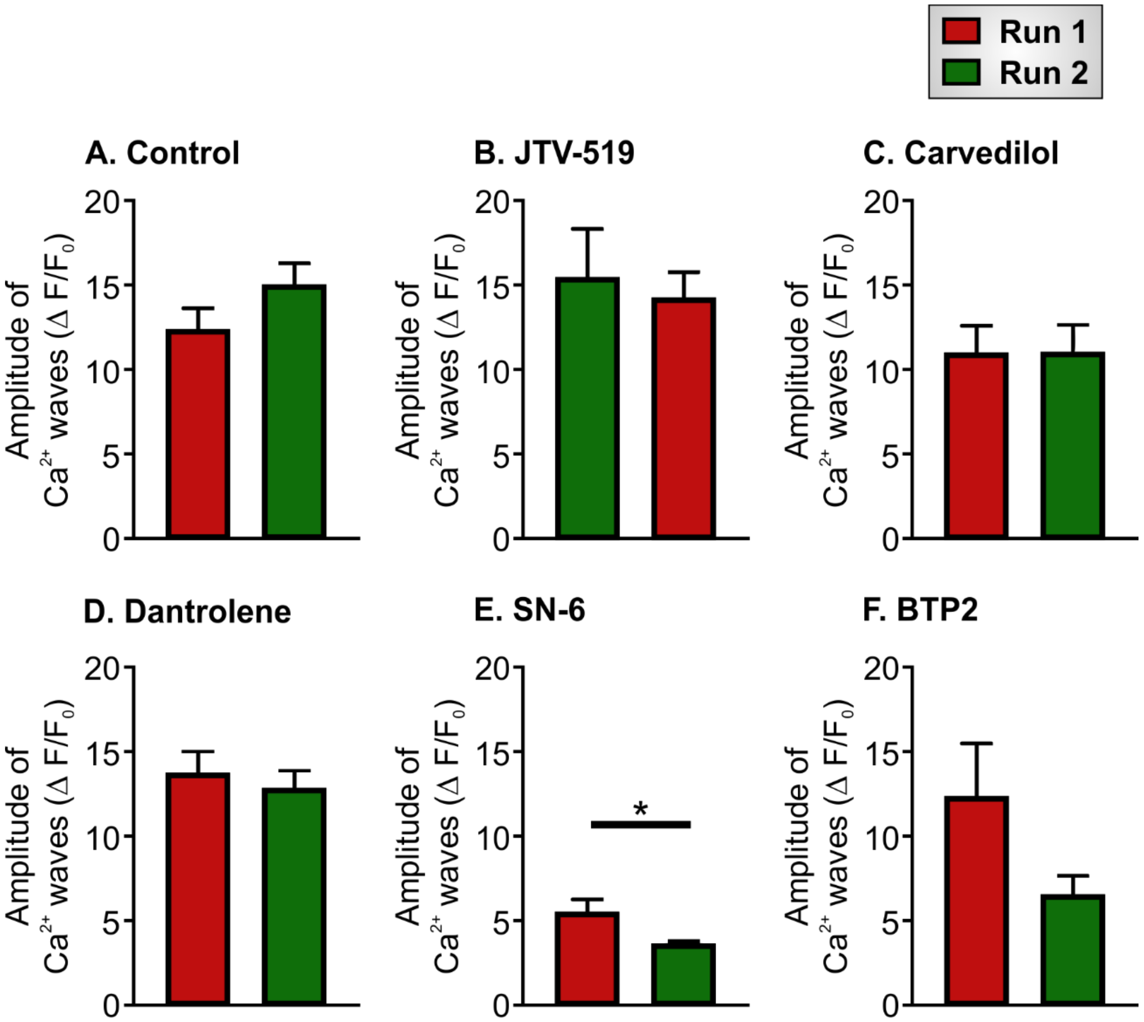

Figure 4.8. Effects of various Ca^{2+} signalsome-affecting reagents on the amplitude of spontaneous Ca^{2+} signals in NRVMS. Panels **A – F** show the average amplitude of spontaneous Ca^{2+} signals during Run 1 and Run 2 of the experiments depicted in Figure 4.6. The data are presented as mean ± S.E.M., and were analysed using paired *t*-tests. * denotes $P < 0.05$. *n* = 6 coverslips from 2 litters per reagent.

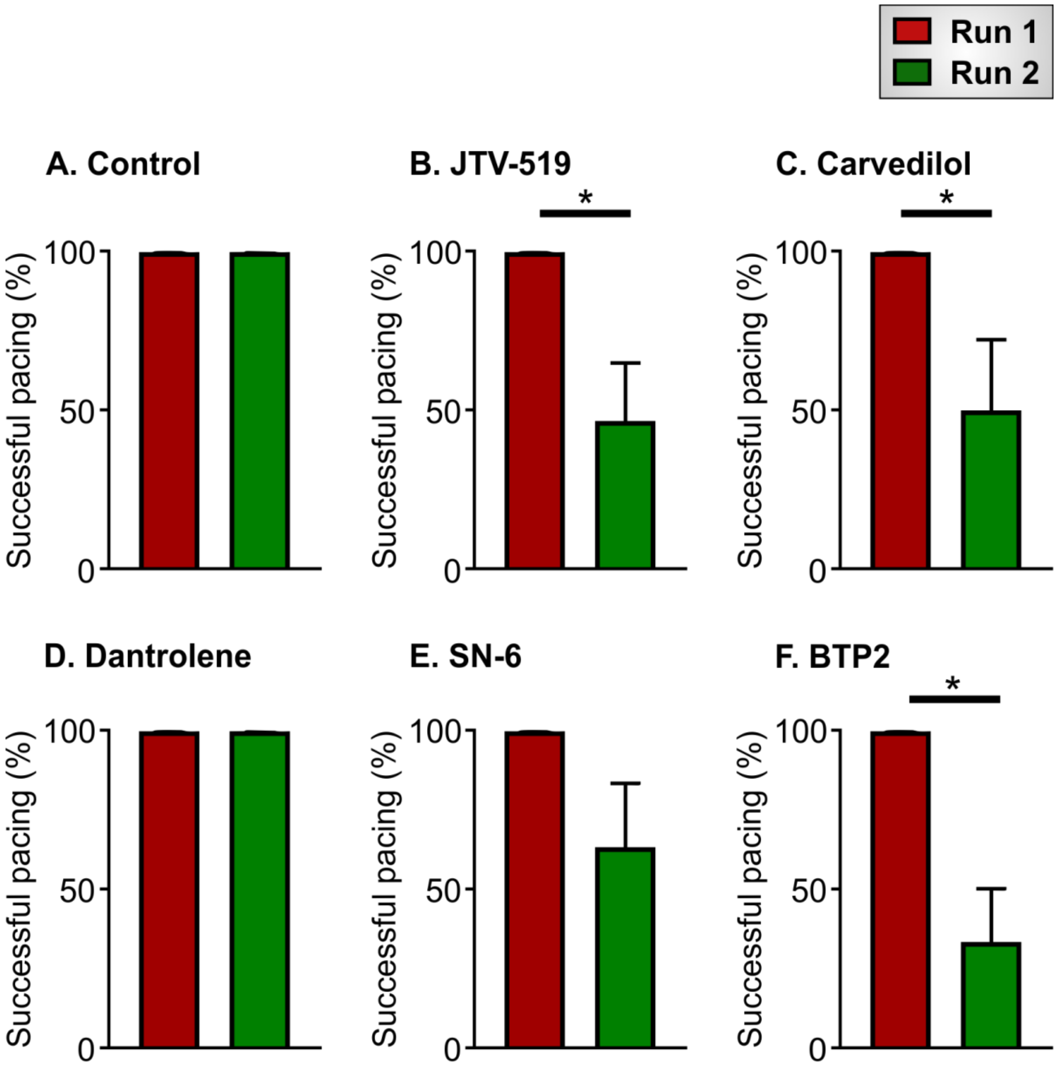

Figure 4.9. Effects of various Ca^{2+} signalsome-affecting reagents on ability of NRVMs to follow EFS pacing. Panels **A – F** show the percentage of NRVMs that followed EFS pulses during Run 1 and Run 2 of the experiments depicted in Figure 4.6. PVCs were considered to be 'successful paced' if they responded to all the EFS pulses in continuous train of pulses, and with consistent (+/- ≤ 10% of $\Delta F/F_0$ Ca^{2+} signal amplitudes). The data are presented as mean ± S.E.M., and were analysed using paired *t*-tests. * denotes $P < 0.05$. *n* = 6 coverslips from 2 litters per reagent.

4.4.2. Testing the role of different Ca^{2+} sources for spontaneous Ca^{2+} signals and EFS-induced Ca^{2+} transients in PVCs

Having assessed the effectiveness of the various reagents to alter Ca^{2+} signals in NRVMs, they were used advisedly on lung slices to examine whether they could reduce spontaneous Ca^{2+} signals and improve the fidelity of EFS pacing in PVCs. Verapamil was also used on lung slices, but was not tested on the NRVMs as it has already been established to be effective (Rietdorf *et al.*, 2014). A similar experimental design to that used with NRVMs, using two experimental runs (i.e. before and after a drug incubation period), was employed for the lung slices (Figure 4.6), but with some changes: a 10-minute incubation was used for the superfusion step to compensate for the likely slower dispersion of reagents within the tissue and line-scan imaging was performed using a confocal microscope to have a faster temporal resolution for the Ca^{2+} signals in PVCs.

Run 1:

1. **18-second line-scan recording of spontaneous activity.**
2. **18-second line-scan recording during application of 1Hz EFS.**

Following Run 1, a reagent (or HBSS as a control) was superfused over the lung slices whilst they were maintained on the microscope stage. Following a 10-minute incubation period, Run 2 was initiated.

Run 2:

1. **18-second line-scan recording of spontaneous activity.**
2. **18-second line-scan recording during application of 1Hz EFS.**

The experimental protocol was adopted to maximally preserve the Cal-520 fluorescence, since laser illumination during confocal imaging can lead to photobleaching. Just as with NRVMs, the robustness of the experimental paradigm was tested with control experiments in which HBSS was superfused over the lung slices for 10 minutes. An example of a control experiment is depicted in Figure 4.10. The line-scans and Ca^{2+} traces in Figure 4.10 show spontaneous Ca^{2+} signals and EFS-induced responses in two adjacent cells. Importantly, the frequency of the spontaneous Ca^{2+} signals did not change between the two periods of recording without EFS (i.e. part 1 in Run 1 and Run 2, respectively, in the protocol shown above) (Figure 4.10Bi and Ci). Moreover, the response of both cells to application of 1 Hz EFS was not altered by the 10-minute incubation with HBSS (part 2 in Run 1 and Run 2, respectively, in the protocol shown above) (Figure 4.4Bii and Cii).

In subsequent experiments, the reagents that were tested on NRVMs (and also verapamil) were applied to lung slices using the protocol described above and depicted in Figure 4.10. The concentrations of reagents used were 100 µM for verapamil, BTP2 and JTV-519, and 10 µM for SN-6. The effects of the reagents on the frequency, amplitude and duration of spontaneous Ca^{2+} signals within PVCs, and the ability of PVCs to follow EFS pulses are shown quantitatively in Figures 4.11 and 4.12.

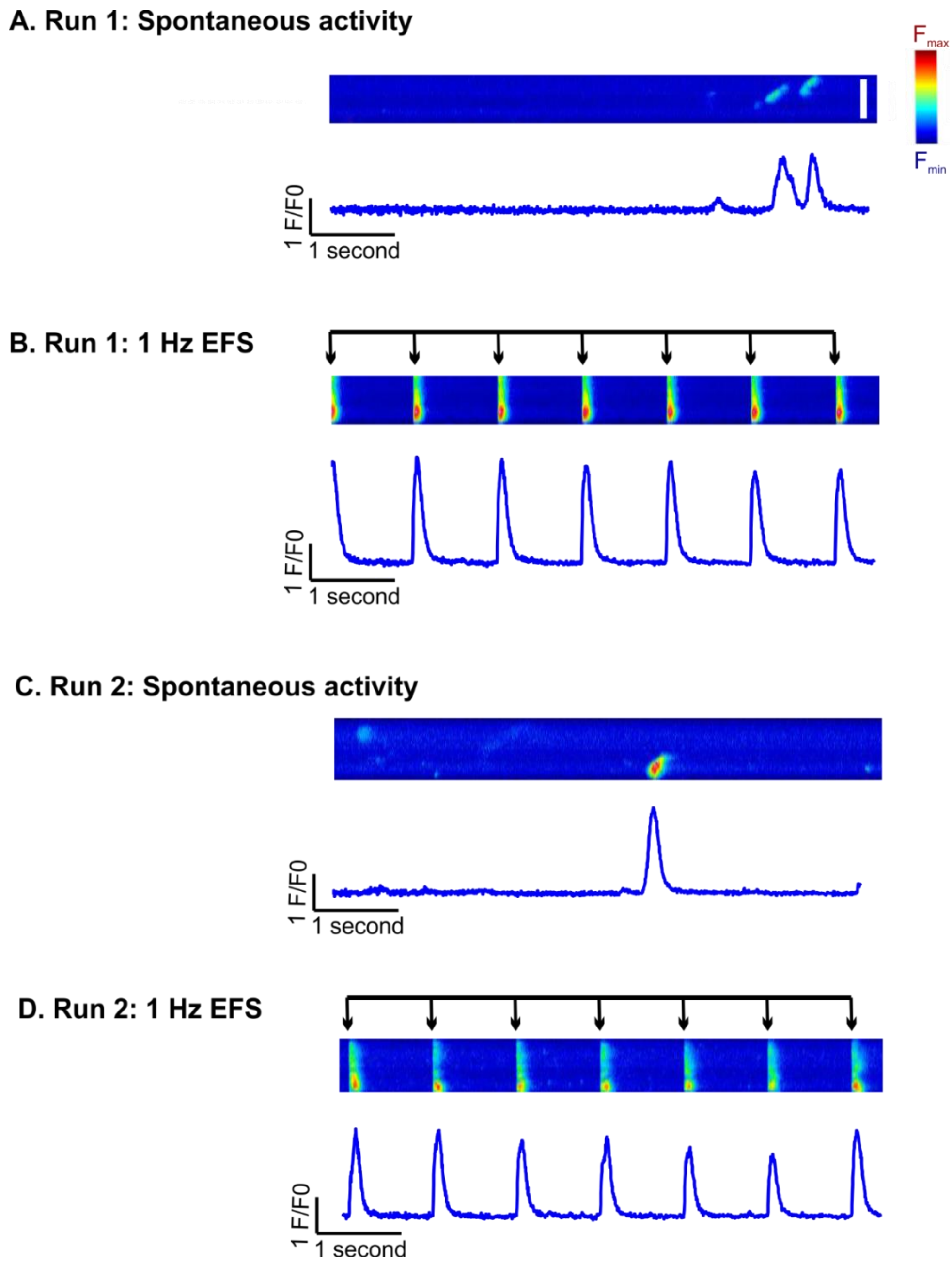

A. Run 1: Spontaneous activity

B. Run 1: 1 Hz EFS

C. Run 2: Spontaneous activity

D. Run 2: 1 Hz EFS

Figure 4.10. Control experiments exemplifying the protocol used to test the effect of Ca^{2+} signalsome-affecting reagents on spontaneous Ca^{2+} signals and responses to EFS in PVCs. Panels **A** and **B** represent ‘Run 1’ of the protocol described in the text. Whereas, Panels **C** and **D** represent ‘Run 2’ of the protocol. Panel **A** shows a line-scan plot and a Ca^{2+} trace illustrating the spontaneous Ca^{2+} signals observed within the PVC. The Ca^{2+} trace below the line-scan was derived from a region within the line-scan. Panel **B** shows the response of the PVCs to application of 1 Hz EFS. After the line-scan in Panel **B** was obtained, the lung slice was superfused with HBSS for 10 minutes. The line-scan plot and Ca^{2+} trace in panel **C** show the spontaneous Ca^{2+} signals observed after the HBSS incubation. Panel **D** illustrates that the PVCs displayed regular responses to a second series of 1 Hz EFS pulses. Scale bar denotes 30 µm.

Figure 4.11. Quantitation of the effect of Ca^{2+} signalsome-affecting reagents on spontaneous Ca^{2+} signals in PVCs. The bars in columns **A – E** show averaged data obtained from spontaneous Ca^{2+} signals occurring in Run 1, before the 10-minute superfusion with HBSS/reagent (red bars; Run 1 in the protocol described above), and from spontaneous Ca^{2+} signals occurring in Run 2, after the 10-minute superfusion with HBSS/reagent (green bars; Run 2 in the protocol described above). Panels **Ai - Ei** quantify the frequency of Ca^{2+} waves, Panels **Aii - Eii** show the frequency of local Ca^{2+} transients, Panels **Aiii - Eiii** depict the amplitude of the Ca^{2+} waves, and Panels **Aiv - Eiv** indicate the duration of Ca^{2+} waves. The data are presented as mean ± S.E.M., and were analysed using paired *t*-tests. *, ** and *** denote $P < 0.05$, $P < 0.01$, and $P < 0.001$, respectively. *n* = 10 – 18 slices from 4 animals per HBSS/reagent.

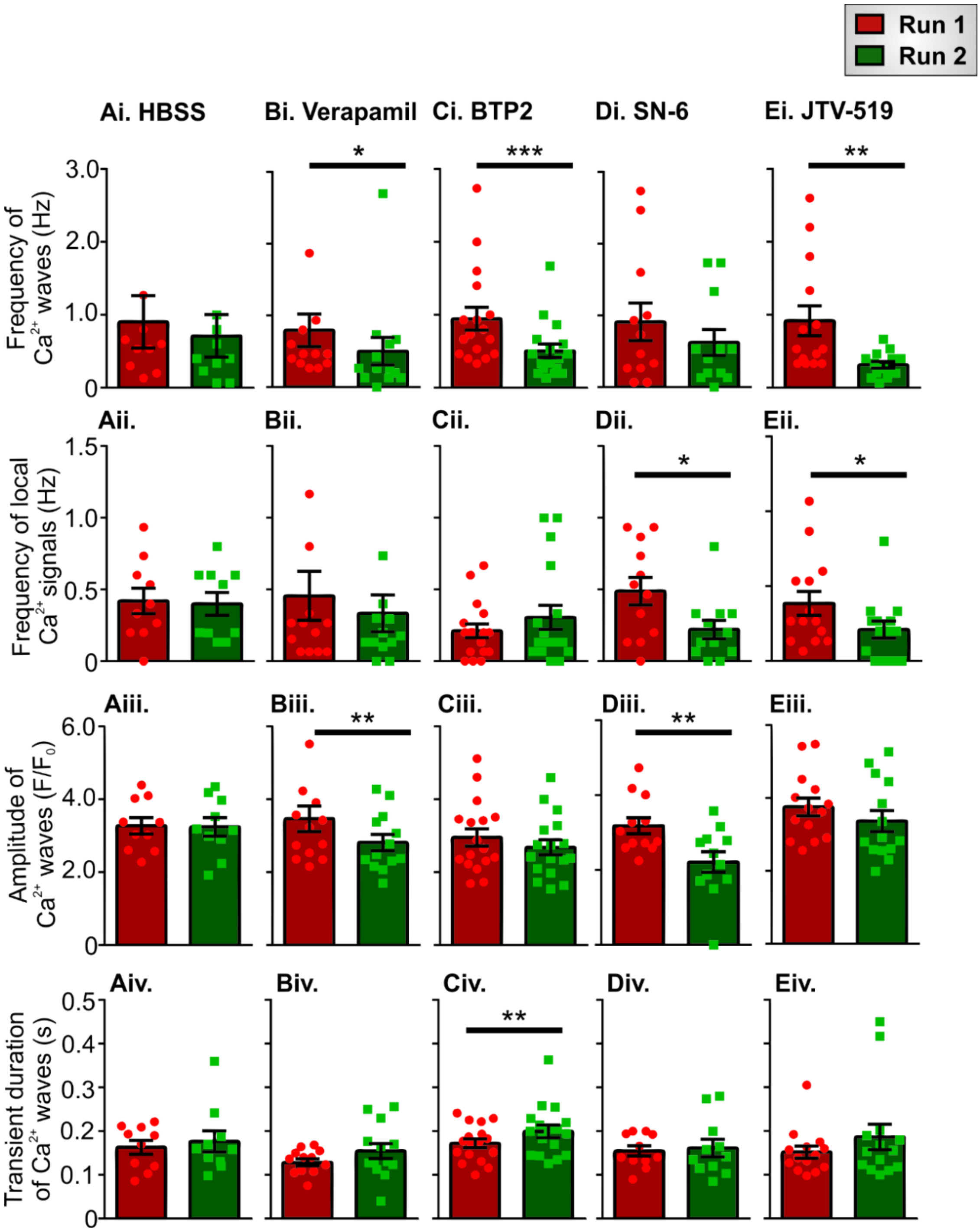

Run 1
Run 2
Ai. HBSS
Bi. Verapamil
Ci. BTP2
Di. SN-6
Ei. JTV-519
Frequency of Ca^{2+} waves (Hz)
3.0
2.0
1.0
0
*
***
**
Aii.
Bii.
Cii.
Dii.
Eii.
Frequency of local Ca^{2+} signals (Hz)
1.5
1.0
0.5
0
*
*
Aiii.
Biii.
Ciii.
Diii.
Eiii.
Amplitude of Ca^{2+} waves (F/F_0)
6.0
4.0
2.0
0
**
**
Aiv.
Biv.
Civ.
Div.
Eiv.
Transient duration of Ca^{2+} waves (s)
0.5
0.4
0.3
0.2
0.1
0
**

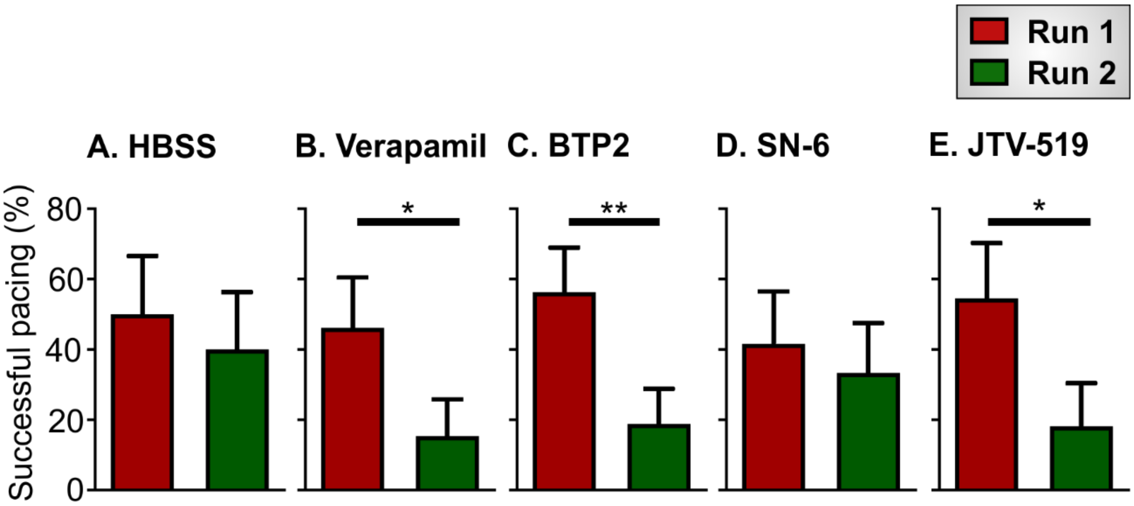

Figure 4.12. Quantitation of the effect of Ca^{2+} signalsome-affecting reagents on the ability of PVCs to follow 1 Hz EFS pacing. Panels **A - E** show the percentage of PVCs following 1 Hz EFS during Run 1 (red bars; Run 1 in the protocol described above) and Run 2 (green bars; Run 2 in the protocol described above), before and after a 10-minute addition of HBSS/reagent, respectively. The data are presented as mean ± S.E.M., and were analysed using paired *t*-tests. * and ** denote $P < 0.05$ and $P < 0.01$, respectively. *n* = 10 – 18 slices from 4 - 5 animals per HBSS/reagent.

The quantitative analysis of the effect of the different reagents indicated that they had disparate effects. Each of the reagents had a significant effect on one or more of the parameters depicted in Figures 4.11 and 4.12. BTP2, SN-6 and JTV-519 all significantly suppressed some aspect of spontaneous Ca^{2+} signalling within the PVCs (Figure 4.11). Since spontaneous Ca^{2+} signals have been shown to prevent PVCs from being regularly paced (Rietdorf *et al.,* 2014, Rietdorf *et al.,* 2015), the actions of BTP2, SN-6 and JTV-519 in reducing spontaneous Ca^{2+} signalling could be considered favourable and potentially anti-arrhythmic. However, both BTP2 and JTV-519 significantly decreased the proportion of PVCs that would follow regular EFS pulses (Figure 4.12). Only SN-6 was able to decrease spontaneous Ca^{2+} signalling (Figure 4.11) whilst PVCs were still able to respond to EFS pulses (Figure 4.12).

4.5. Characterisation of spontaneous Ca^{2+} signals and EFS-induced Ca^{2+} transients in PVCs from 3 month- and 24 month-old mice

The data discussed above illustrate the nature of spontaneous Ca^{2+} signals that occur in PVCs within lung slices obtained from 3 month-old mice, and experimental attempts to alleviate spontaneous Ca^{2+} signals using pharmacological reagents. To examine whether Ca^{2+} signalling or homeostasis changes in PVCs during ageing, a comparison was made using lung slices prepared from 3 month- and 24 month-old mice. Putative changes in Ca^{2+} signalling were analysed by measuring the frequency, velocity, amplitude, duration and number of initiation points of spontaneous Ca^{2+} waves, and the frequency of local Ca^{2+} signals. Additionally, the ability to pace the slices with EFS pulses at 1, 3 and 5 Hz was explored.

Representative line-scans recorded using PVCs obtained from 3 month-old (Figure 4.13A) and 24 month-old mice (Figure 4.13B and C) illustrate that spontaneous Ca^{2+} signals were evident at both ages. PVCs from the 3 month-old mice responded to 1, 3 and 5 Hz EFS, although the amplitude of the Ca^{2+} signals became progressively smaller as the stimulation frequency was increased (Figure 4.13Aii – Aiv). From the line-scans shown in Figure 4.13A, it is evident that the two adjacent cells differed in their responses to EFS. In particular, cell 1 displayed longer lasting EFS-induced Ca^{2+} transients at 1 and 3 Hz stimulation, compared to those seen in cell 2 (Figure 4.13Aii and Aiii). In addition, cell 1 displayed Ca^{2+} waves when the EFS frequency was increased to 5 Hz, whereas cell 2 maintained regular pacing (albeit with significantly reduced Ca^{2+} signal amplitude). With both cells, 3 Hz EFS pulses evoked alternans (Figure 4.13Aiii). In contrast to PVCs from 3 month-old mice, where many cells responded to 1 Hz EFS pulses, PVCs from 24 month-old mice did not respond well to application of EFS pulses. The line-scans presented in Figure 4.13B and C depict recordings from PVCs within two lung slices obtained from two 24 month-old mice. The cell in Panel B displayed spontaneous Ca^{2+} signals, but it did not respond to EFS pulses at 1, 3, or 5 Hz, whilst the cell in Panel C did follow the pacing with all three frequencies of EFS.

Quantitative analysis of spontaneous Ca^{2+} signals and EFS-evoked Ca^{2+} transients from experiments such as that shown in Figure 4.13 is presented in Figure 4.14. The characteristics of Ca^{2+} waves were significantly different between PVCs from 3 month- and 24 month-old animals in a number of ways; their frequency was increased (Figure 4.14Ai), their amplitude was reduced (Figure 4.14Aii) and they lasted longer (Figure 4.14iii). The frequency of local Ca^{2+} signals was not significantly different between PVCs from 3 month- and 24 month-old animals (Figure 4.14Aiv). Moreover, neither the proportions of cells with one, or more, Ca^{2+} wave initiation sites, nor their Ca^{2+} wave propagation velocities, were significantly different between PVCs from 3 month- and 24 month-old animals (Figure 4.14B-C).

A. 3 months

Ai. Spontaneous activity

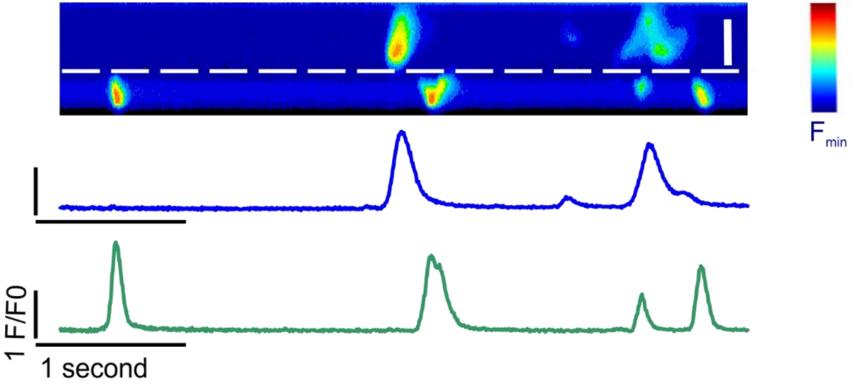

Aii. 1 Hz EFS

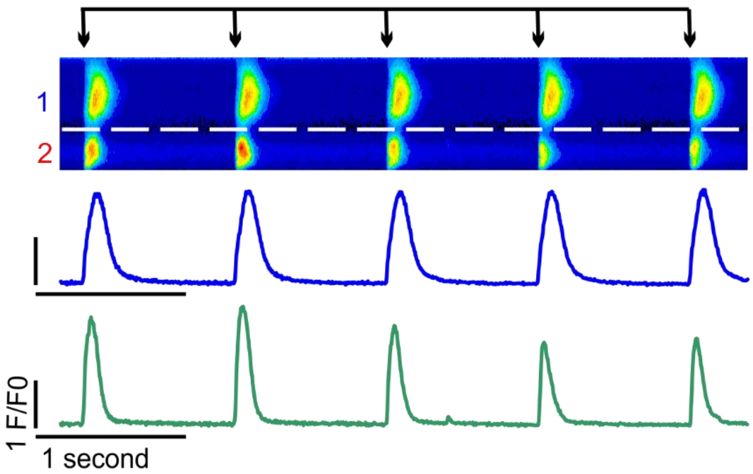

Aiii. 3 Hz EFS

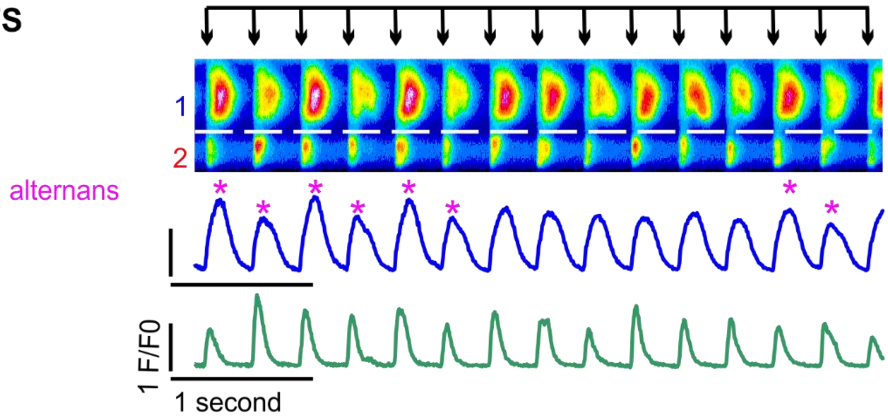

Aiv. 5 Hz EFS

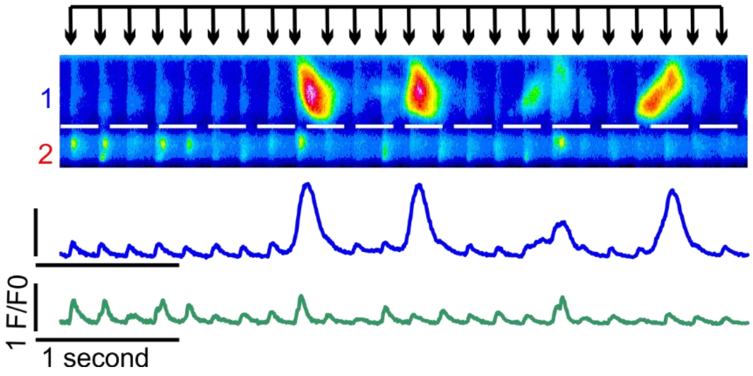

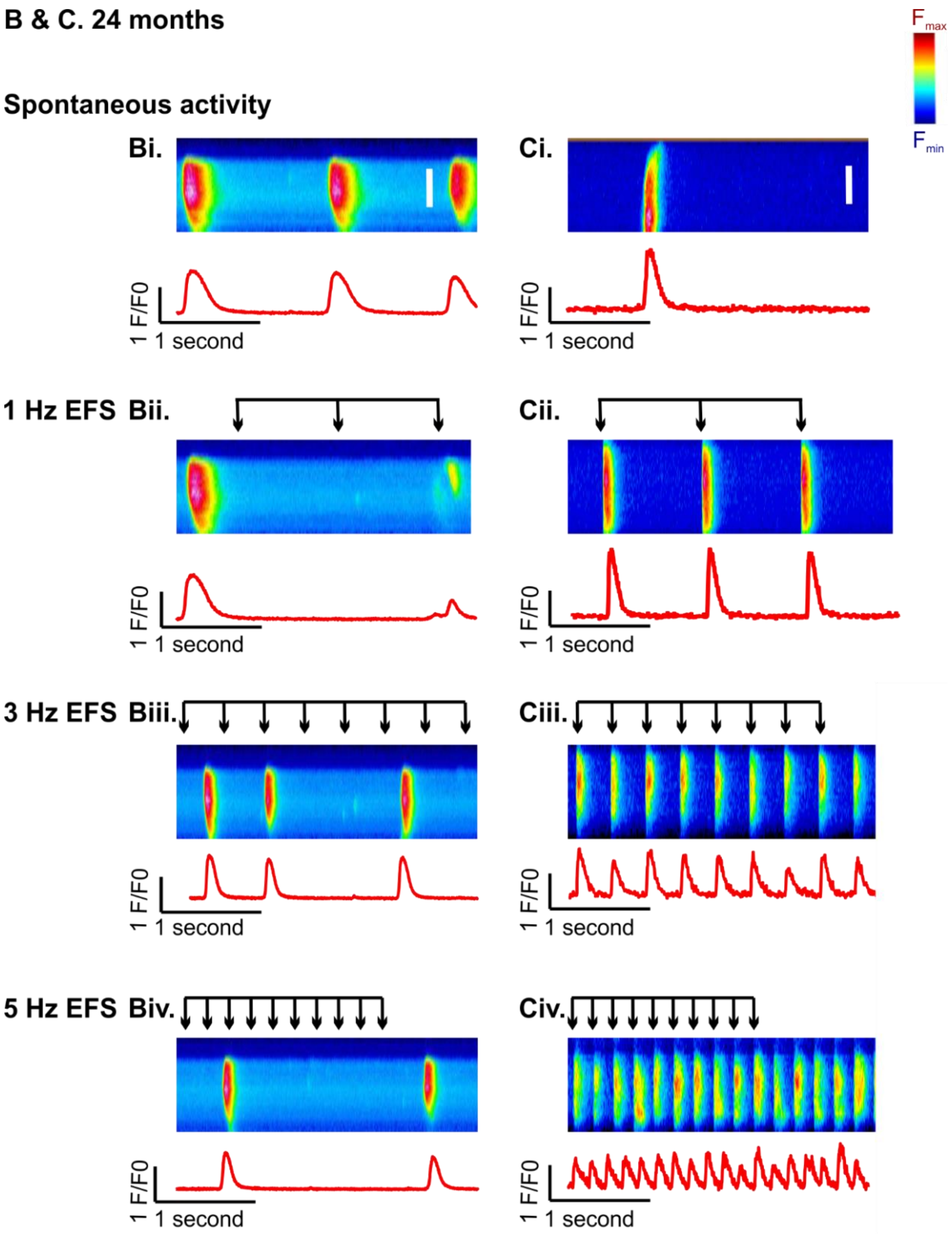

Figure 4.13. Spontaneous Ca^{2+} signals and EFS-induced Ca^{2+} transients in PVCs from 3 month- and 24 month-old mice. Panel **A** shows data recorded using PVCs obtained from a 3 month-old mouse. The line-scans and corresponding Ca^{2+} traces show spontaneous Ca^{2+} signals (**Ai**), and responses to 1, 3 and 5 Hz EFS pacing (**Aii - Aiv**). Panel **B** and **C** show data recorded using PVCs obtained from two 24 month-old mice. The line-scans and corresponding Ca^{2+} traces show spontaneous Ca^{2+} signals (**Bi** and **Ci**), and responses to 1, 3 and 5 Hz EFS pacing (**Bii – Biv**, **Cii-Civ**). The PVC in Panel **B** could not be paced, whilst the PVC in Panel **C** followed the electrical pacing. The scale bars in Panels **Ai, Bi** and **Ci** represent 30 µm.

Figure 4.14. Characteristics of spontaneous Ca^{2+} signals and EFS-induced Ca^{2+} transients in PVCs from 3 month- and 24 month-old mice.

The data presented in this figure were obtained from experiments such as that shown in Figure 4.13. The plots in Panels **Ai** – **Aiv,** and **B** – **C** show quantitative analyses of spontaneous Ca^{2+} signals that occurred in PVCs from 3 month- and 24 month-old mice. The spontaneous Ca^{2+} signals were recorded prior to application of EFS, as illustrated in Figure 4.13Ai & Bi. Panels **Ai** – **Aiii** and **B** – **C** represent analyses of Ca^{2+} waves, whilst Panel **Aiv** shows the frequency of local Ca^{2+} transients. Panels **D – E** show the correlation between the spontaneous Ca^{2+} signals and the ability to follow 1 Hz electrical pacing in PVCs from 3 month- and 24 month-old mice. The plot in Panel **G** shows quantitative analyses of EFS-induced pacing in PVCs from 3 month- and 24 month-old mice, with data obtained from experiments such as those shown in Figure 4.13Aii – iv and Bii - iv. The data in Panels **A** - **E** are presented as mean ± S.E.M., and were analysed using unpaired *t*-tests. The data shown in Panels **F - G** were compared using a Fisher's Test. * and ** indicate $P < 0.05$ and $P < 0.01$, respectively. *n* = 10 – 82 slices from 4 – 11 animals for both 3 month- and 24 month-old mice.

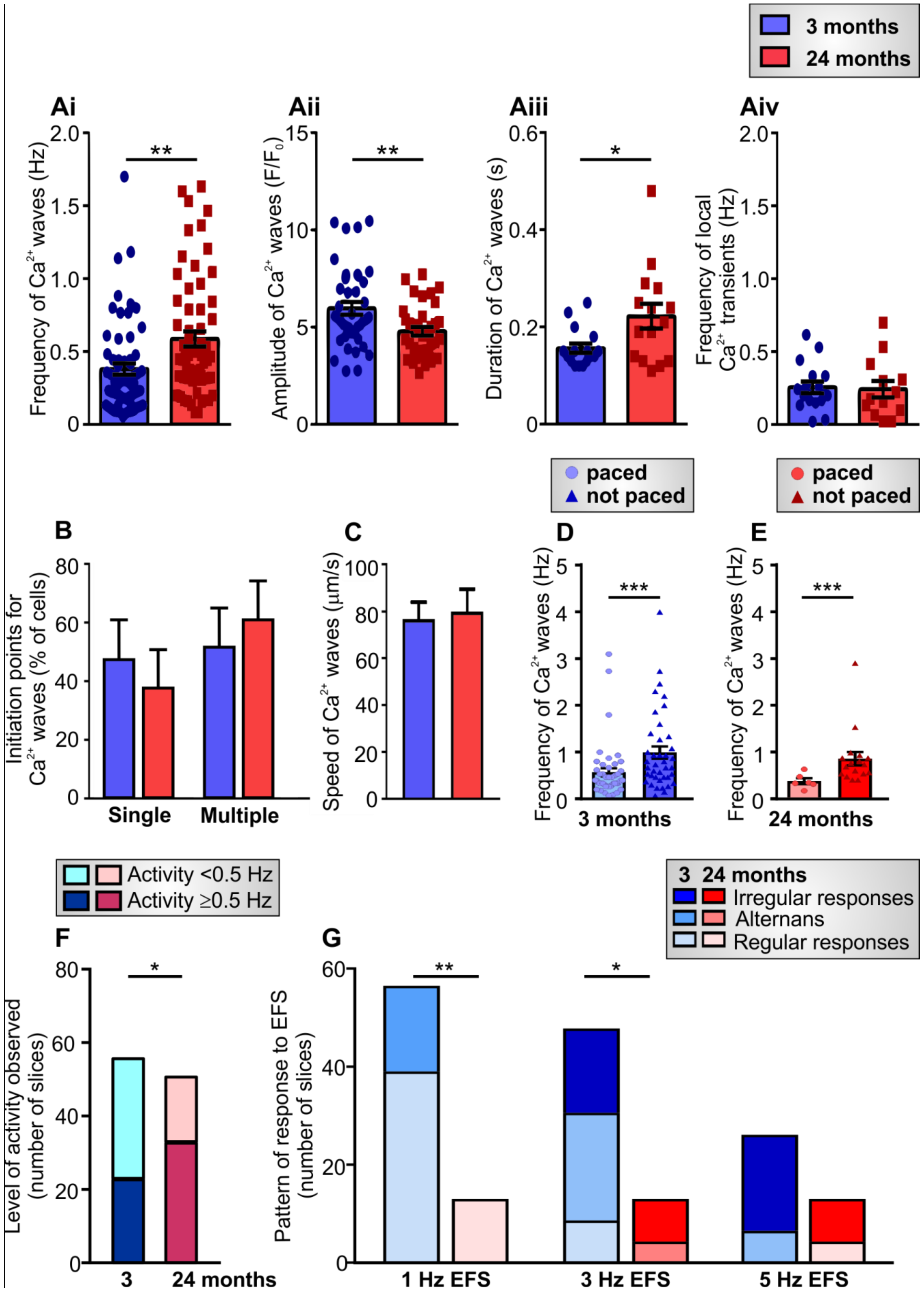
3 months
24 months
Ai
Frequency of Ca²⁺ waves (Hz)
**
Aii
Amplitude of Ca²⁺ waves (F/F₀)
**
Aiii
Duration of Ca²⁺ waves (s)
*
Aiv
Frequency of local Ca²⁺ transients (Hz)
paced
not paced
paced
not paced
B
Initiation points for Ca²⁺ waves (% of cells)
Single
Multiple
C
Speed of Ca²⁺ waves (µm/s)
D
Frequency of Ca²⁺ waves (Hz)
***
3 months
E
Frequency of Ca²⁺ waves (Hz)
***
24 months
Activity <0.5 Hz
Activity ≥0.5 Hz
F
Level of activity observed (number of slices)
*
3
24 months
3 24 months
Irregular responses
Alternans
Regular responses
G
Pattern of response to EFS (number of slices)
**
*
1 Hz EFS
3 Hz EFS
5 Hz EFS

The ability of EFS to pace PVCs from 3 month- and 24 month-old mice was analysed by applying a train of EFS pulses for 12 seconds as shown in Figure 4.13, and then examining the characteristics of Ca^{2+} signals triggered by each EFS pulse. It was noted that EFS application evoked multiple, distinctive outcomes, as follows:

1. **Regular responses** represent situations where PVCs responded to all the EFS pulses in continuous train of pulses, and with consistent Ca^{2+} signal amplitudes.

2. **Alternans** denote situations where PVCs responded to EFS pulses with alternating large and small Ca^{2+} signal amplitudes.

3. **Irregular responses** indicate situations where PVCs did not respond to each EFS pulse in continuous train of pulses, and/or showed Ca^{2+} signals with variable amplitudes, i.e. (+/- ≥ 50% $\Delta F/F_0$).

4. **No response** designates situations were PVCs did not respond to any EFS pulse in continuous train of pulses.

The quantitative analysis of EFS-induced Ca^{2+} signals is presented in Figure 4.14C, with the blue- and red-coloured bars indicating responses in PVCs from 3 month- and 24 month-old animals, respectively. It is evident that a greater proportion of PVCs from 3 month-old mice reacted to EFS with any form of response, compared to PVCs from 24 month-old animals. The PVCs from 3 month-old animals responded best to 1 Hz EFS pulses, with ~38% of cells showing regular responses. Increasing the EFS frequency from 1 Hz to 3 or 5 Hz changed the nature of the outcomes in 3 month-old PVCs so that fewer cells responded, and alternans and irregular responses were more prominent. The proportion of PVCs from 24 month-old mice that reacted to EFS was the same at 1, 3 or 5 Hz, but there were more alternans and irregular responses with 3 or 5 Hz.

It should be noted that pacing PVCs within lung slices using EFS was not simple to achieve despite great care being taken in the handling of the slices, superfusion of the tissue and placement of electrodes. Indeed, in the best case, with PVCs from 3 month-old mice paced with 1 Hz EFS, only 56 % of cells responded in any way (Figure 4.14F). The reason why the remainder of the PVCs did not respond to EFS pulses at all is unclear, but may reflect a lack of penetration of the electrical signal within the 180 μm-thick lung slices. Interestingly, there was a significant difference between the ability to pace PVCs from 3 month and 24 month-old mice (Figure 4.14F). The reasons why PVCs from 24 month-old animals were harder to pace using EFS pulses is unclear. It is important to point out that the cells were vital; they loaded to similar levels with Cal-520, had similar resting Cal-520 intensities (i.e. similar basal Ca^{2+} levels), and showed spontaneous Ca^{2+} signals indicative of functional Ca^{2+} stores, channels and ATPases. Furthermore, the experiments presented within this chapter were performed using slices from 3 month- and 24 month-old mice that had identical genetic backgrounds. The 3 month- and 24 month-old animals were nurtured in the same facility (The Open University's Biological Response Unit) over the same period of time. Furthermore, lung slices from both age groups were prepared for use on the same days to limit the variability within the experiments. It is therefore unlikely that differences in husbandry or treatment of the mice, lung slice preparation, stimulation conditions or experimental solutions were responsible for the discrepant EFS-induced pacing of PVCs from young and old animals. Rather, it is plausible to suggest that ageing was somehow responsible for the differences in responses of 3 month- and 24 month-old PVCs.

4.6. Characterisation of the role of RyR and adrenoceptors for Ca^{2+} transients in PVCs from 3 month- and 24 month-old mice

4.6.1. Effect of RyR2 inhibition using JTV-519 on spontaneous Ca^{2+} signals in PVCs from 3 month- and 24 month-old mice

JTV-519 was found to significantly reduce spontaneous Ca^{2+} signals in both NRVMs (Figures 4.6 and 4.7) and PVCs from 3 month-old mice (Figure 4.11). As discussed above, inhibition of spontaneous Ca^{2+} signals may plausibly help with the pacing of cardiac myocytes. Therefore, since PVCs from 24 month-old mice were found to have a higher frequency of spontaneous Ca^{2+} signals (Figure 4.14), the effect of JTV-519 was tested to examine whether it could similarly suppress spontaneous Ca^{2+} signals in PVCs from old animals.

To examine the effect of JTV-519 on spontaneous Ca^{2+} signals in PVCs from 3 month- and 24 month-old animals the following experimental protocol was used:

Run 1:

1. **35-second recording of spontaneous activity.**

Following Run 1, 100 µM JTV-519 (or HBSS as a control) was superfused over the lung slices whilst they were maintained on the microscope stage. Following a 10-minute incubation period, Run 2 was initiated.

Run 2:

1. **35-second recording of spontaneous activity.**

This protocol was repeated using PVCs from 3 month- and 24 month-old animals. For these experiments, spontaneous Ca^{2+} signals were recorded using 2D confocal imaging at 10 Hz. The reason for using 2D confocal imaging rather than line-scanning was to ensure that spontaneous Ca^{2+} signals were not missed through sampling a limited area of the PVCs. Examples of spontaneous Ca^{2+} signals recorded using the experimental protocol described above are shown in Figure 4.15. As discussed earlier, PVCs from both 3 month- and 24 month-old animals displayed spontaneous Ca^{2+} signals, with a mix of Ca^{2+} waves and local Ca^{2+} transients being evident.

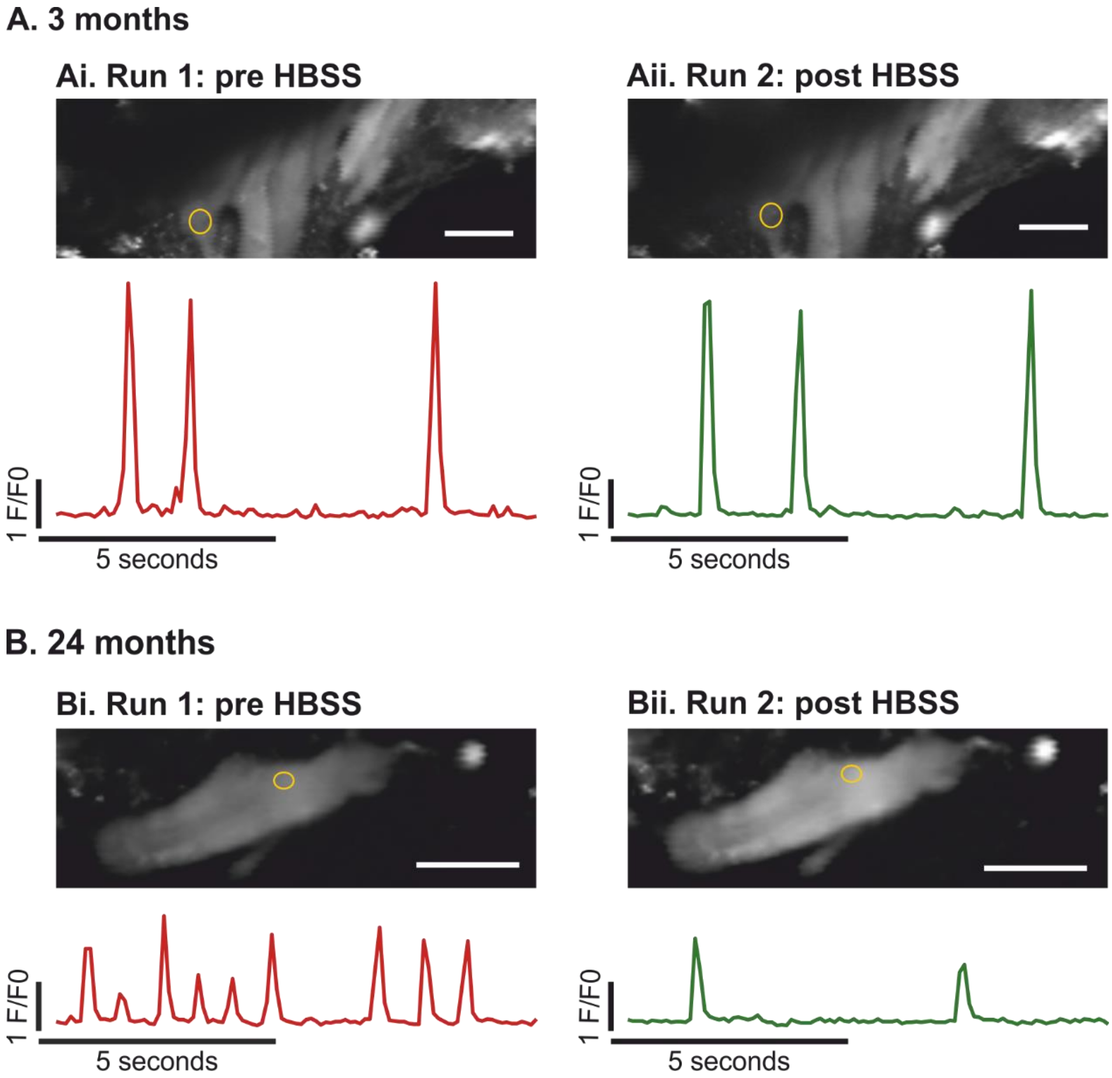

Figure 4.15. Protocol used to test the effects of drugs on the Ca^{2+} signalsome in PVCs from 3 month- and 24 month-old mice. Panels **A** and **B** show images of Cal-520-loaded PVCs and Ca^{2+} traces obtained by recording the Cal-520 fluorescence within the cells. Panel A depict recordings performed using PVCs from 3 month-old mice. Panel **Ai** show the activities of cells prior to a 10-minute incubation with HBSS (Run 1), panel **Aii** that after a 10-minute incubation with HBSS (Run 2). Panels Bi and Bii depict recordings performed using PVCs from 24 month-old mice. The yellow circles in the cell images show cellular regions used to obtain the Ca^{2+} traces. The scale bars represent 10 µm.

Quantitative analysis of experiments such as that depicted in Figure 4.15 is shown in Figure 4.16. The control experiments, with superfusion of HBSS, indicated that the frequency of spontaneous Ca^{2+} signals in both age groups was similar in Run 1 and Run 2 (i.e. before and after a 10-minute HBSS superfusion interval; Figure 4.16).

Variability in the nature and frequency of spontaneous Ca^{2+} signals is characteristic of PVCs (Rietdorf *et al.,* 2014 and as described above in 4.3.1). As described in Chapter 2, all possible procedures were used to minimise the variability within and between experiments. Control and reagent-testing experiments were performed using lung slices prepared at the same time, and from the same batches of mice. However, it is obvious from the data presented in Figure 4.16Ai and 4.16Bi that there was a substantial variation in the frequency of spontaneous Ca^{2+} signals during the first 35-second recordings from the PVCs, and it was considered that this variability may have obscured significant effects that might be caused by the drugs used. Therefore, to analyse the action of drugs on spontaneous Ca^{2+} signals further the data presented in Figure 4.16Ai and 4.16Bi were re-categorised. The re-categorisation defined PVCs based on their spontaneous Ca^{2+} signal frequency during Run 1 (i.e. prior to the 10-minute superfusion interval), as follows:

1. PVCs with a frequency of spontaneous Ca^{2+} signals ≥ 0.5 Hz before HBSS superfusion were categorised as 'high frequency' cells.
2. PVCs with a frequency of spontaneous Ca^{2+} signals < 0.5 Hz before HBSS superfusion were categorised as 'low frequency' cells.

This re-categorisation was applied to the data from both the 3 month- and 24 month-old PVCs, and is depicted in Figures 4.16Aii, Aiii, Bii and Biii. Sorting the PVCs into high and low frequency categories revealed no differences in the control experiments, but will however applied throughout the following series of experiment investigating the effects of drugs on the Ca^{2+} signalsome in PVCs.

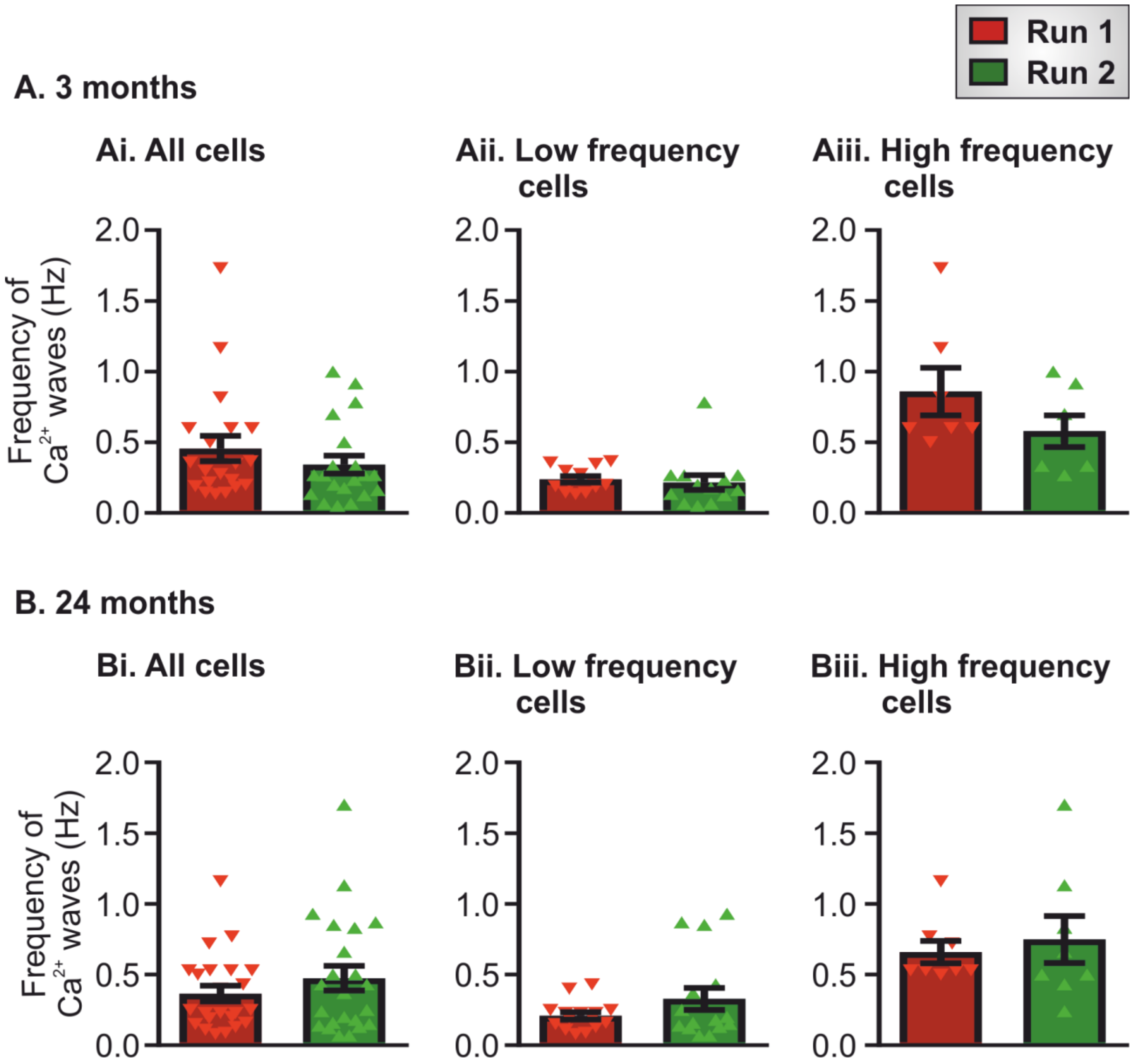

Figure 4.16. Effect of HBSS (control) on spontaneous Ca^{2+} signals in PVCs from 3 month- and 24 month-old mice. The data were obtained from experiments such as those depicted in Figure 4.15. Panels **A** and **B** show the frequency of spontaneous Ca^{2+} signals in PVCs from 3 month- and 24 month-old mice, respectively. The data are presented as mean ± S.E.M., and were analysed using paired *t*-tests. * indicates $P < 0.05$. $n = 15 - 17$ slices from 8 – 9 animals for both 3 month- and 24 month-old mice.

JTV-519 significantly reduced the frequency of spontaneous Ca^{2+} signals in PVCs from 24 month-old mice (Figure 4.17Bi). As presented, the data in Figure 4.17Ai suggest that the PVCs from 3 month-old mice used in these experiments did not show a significant reduction in the frequency of spontaneous Ca^{2+} signals following incubation with JTV-519 (Figure 4.17Ai), in contrast to the results presented in Figure 4.11. Categorising the data into low (Figures 4.17 Aii and Bii) and high (Figures 4.17 Aiii and Biii) frequency cells establishes a significant effect of JTV-519.

JTV-519 did indeed reduce the frequency of spontaneous events in PVCs from both 3 month- and 24 month-old mice. However, the action of JTV-519 was limited to PVCs that displayed a high frequency of spontaneous Ca^{2+} signals at the onset of the experiment (3 month- *vs.* 24 month-old PVCs; 0.7 ± 0.05 *vs.* 1.3 ± 0.16 Hz respectively). JTV-519 did not appear to affect PVCs of either age that had a low frequency of spontaneous Ca^{2+} signals (3 month- *vs.* 24 month-old PVCs; 0.21 ± 0.04 *vs.* 0.23 ± 0.03 Hz respectively).

The frequency of spontaneous Ca^{2+} signals during Run 2 (i.e. after the 10-minute JTV-519 superfusion) was typically between 0.2 – 0.3 Hz for PVCs from PVCs from both 3 month- and 24 month-old mice (Figures 4.16 and 4.17). These observations indicate that JTV-519 can reduce the occurrence of spontaneous Ca^{2+} signals by 50 – 84%, but it is only effective in situations where PVCs are highly spontaneously active (Figure 4.17Aiii – 4.17Biii).

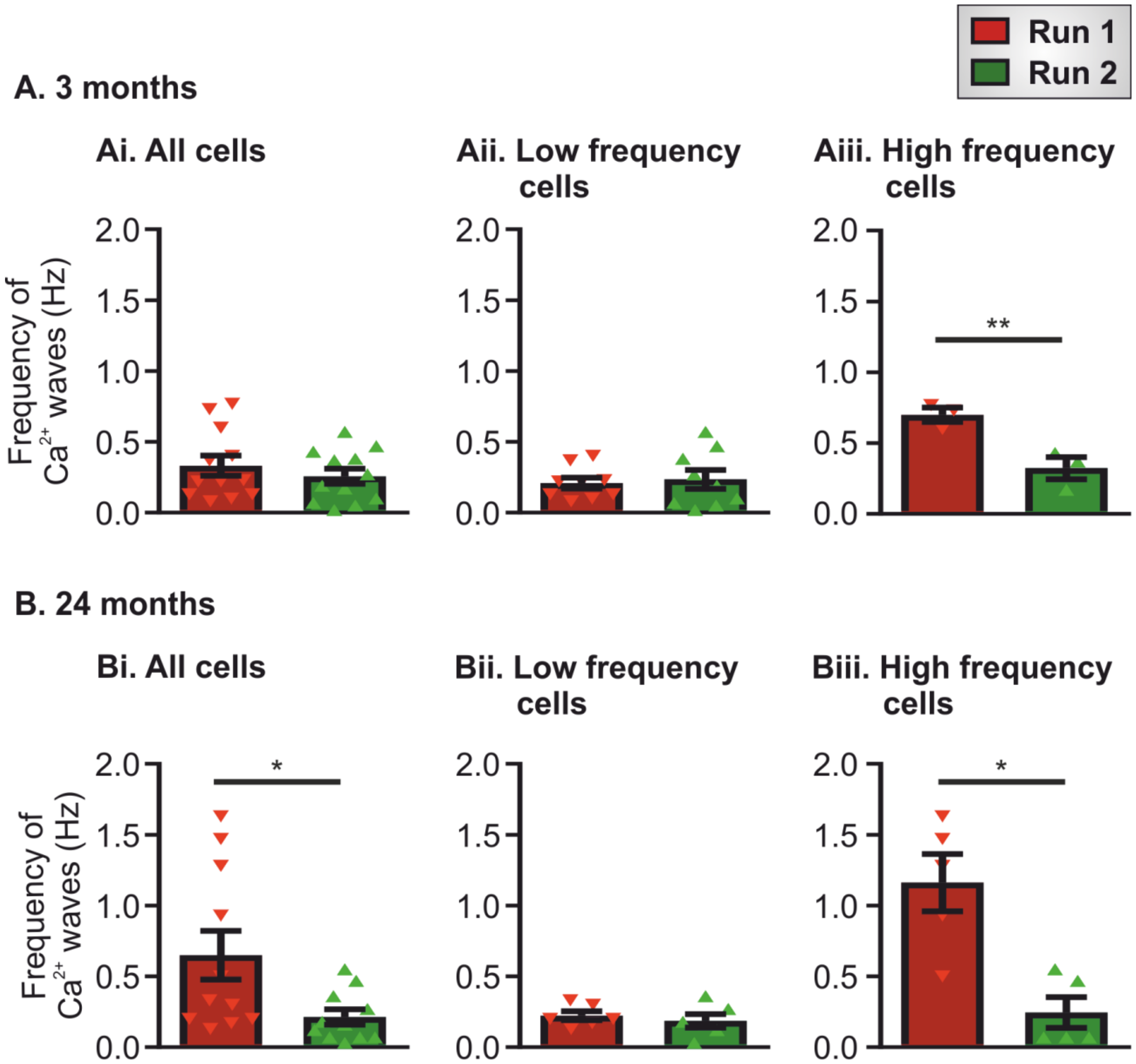

Figure 4.17. Effect of JTV-519 on spontaneous Ca^{2+} signals in PVCs from 3 month- and 24 month-old mice. The data were obtained from experiments such as those depicted in Figure 4.15, but with superfusion of 100 μM JTV-519. Panels **Ai** and **Bi** show the effect of JTV-519 on the frequency of spontaneous Ca^{2+} signals in PVCs from 3 month- and 24 month-old mice, respectively. Panels **Aii-Aiii** and **Bii-Biii** show the effect of JTV-519 on the frequency of spontaneous Ca^{2+} signals in PVCs from 3 month- and 24 month-old mice following categorisation of the cells into those that initially showed either low (< 0.5 Hz) or high (≥ 0.5 Hz) frequency of spontaneous Ca^{2+} signals. The data are presented as mean ± S.E.M., and were analysed with paired Student's *t*-tests. * and ** indicate P < 0.05 and P < 0.01, *n* = 10 slices from 4 animals.

4.6.2. Effect of RyR2 inhibition using dantrolene on spontaneous Ca^{2+} signals in PVCs from 3 month- and 24 month-old mice

Although dantrolene was found to be ineffective in reducing spontaneous Ca^{2+} signals in NRVMs (Figures 4.6 and 4.7), it was tested on PVCs in case it was more efficacious on fully differentiated cells. The same experimental protocol described in Section 4.6.1 was used:

Run 1:

1. **35-second recording of spontaneous activity.**

Following Run 1, 100 µM dantrolene (or HBSS as a control) was superfused over the lung slices whilst they were maintained on the microscope stage. Following a 10-minute incubation period, Run 2 was initiated.

Run 2:

1. **35-second recording of spontaneous activity.**

This protocol was repeated using PVCs from 3 month- and 24 month-old animals. For these experiments, spontaneous Ca^{2+} signals were recorded using 2D confocal imaging at 10 Hz. The quantitative analyses of the effects of dantrolene superfusion are presented in Figure 4.18.

Collectively plotting all the data obtained from the experiments involving dantrolene indicated that there was no significant effect of the reagent on the frequency of spontaneous Ca^{2+} signals in PVCs obtained from either 3 month- or 24 month-old mice (Figure 4.18A and B). Moreover, categorising the PVCs into ‘low frequency’ or ‘high frequency’ cells based on their initial frequency of spontaneous Ca^{2+} signals (as was done for the results with JTV-519 above) did not reveal any significant effect of dantrolene superfusion (Figure 4.18Aiii and 4.18Biii).

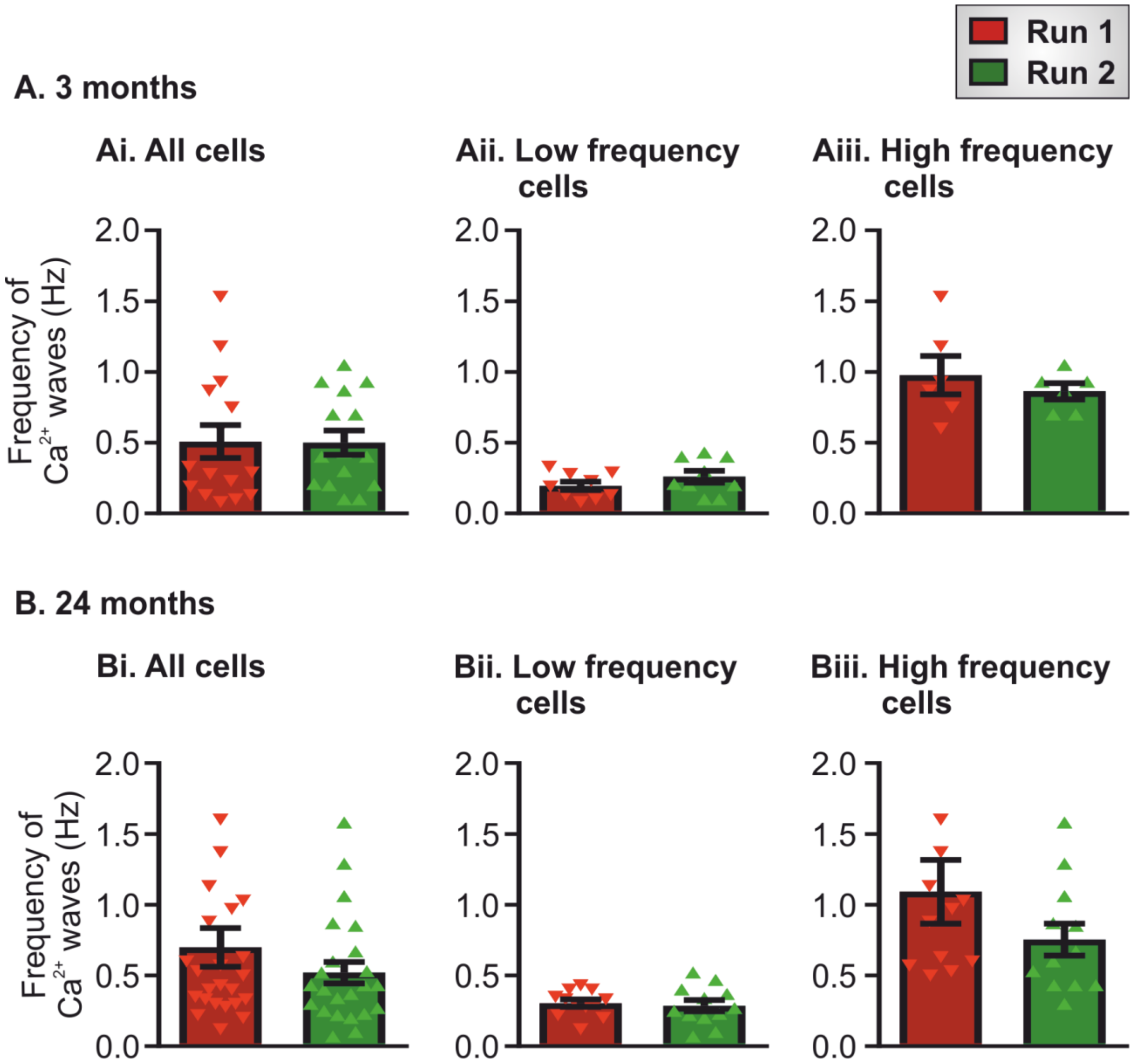

Figure 4.18. Effect of dantrolene on spontaneous Ca^{2+} signals in PVCs from 3 month- and 24 month-old mice. The data were obtained from experiments such as those depicted in Figure 4.15, but with superfusion of 100 µM dantrolene. Panels **Ai** and **Bi** show the effect of dantrolene on the frequency of spontaneous Ca^{2+} signals in PVCs from 3 month- and 24 month-old mice, respectively. Panels **Aii-Aiii** and **Bii-Biii** show the effect of dantrolene on the frequency of spontaneous Ca^{2+} signals in PVCs from 3 month- and 24 month-old mice following categorisation of the cells into those that initially showed either low (< 0.5 Hz) or high (≥ 0.5 Hz) frequency of spontaneous Ca^{2+} signals. The data are presented as mean ± S.E.M., and were analysed with paired Student's *t*-tests. *n* = 13 – 15 from 5 animals per age group in Panels **A** and **B**.

4.6.3. Effect of RyR2 inhibition with carvedilol in PVCs from 3 and 24 month-old mice

Since the two RyR inhibitors used in the experiments described above, JTV-519 and dantrolene, had differing effects on spontaneous Ca^{2+} signals in PVCs, a third RyR inhibitor, carvedilol, was also tested. Carvedilol has been used extensively in treating cardiovascular diseases (Zhou *et al.,* 2011), but has not been tested in PVCs. However, unlike JTV-519 which mainly targets RyR2, the action of carvedilol is less specific. In addition to RyR2 inhibition, carvedilol antagonises α- and β-adrenoceptors. Indeed, one of the principle clinical applications of carvedilol is as a 'beta blocker' to reduce hypertension (Farha *et al.,* 2017).

The same experimental protocol described in Section 4.6.1 was used:

Run 1:

1. **35-second recording of spontaneous activity.**

Following Run 1, 100 µM carvedilol (or HBSS as a control) was superfused over the lung slices whilst they were maintained on the microscope stage. Following a 10-minute incubation period, Run 2 was initiated.

Run 2:

1. **35-second recording of spontaneous activity.**

This protocol was repeated using PVCs from 3 month- and 24 month-old animals. For these experiments, spontaneous Ca^{2+} signals were recorded using 2D confocal imaging at 10 Hz. The quantitative analysis of the effects of carvedilol superfusion are presented in Figure 4.19.

Collectively plotting all the data obtained from the experiments involving carvedilol indicated that there was a significant reduction of the frequency of spontaneous Ca^{2+}

signals in PVCs obtained from 3 month-old mice (Figure 4.19A), but not in PVCs obtained from 24 month-old mice (Figure 4.19B). PVCs were categorised into ‘low frequency’ (< 0.5 Hz) or ‘high frequency’ (≥ 0.5 Hz) cells based on their initial frequency of spontaneous Ca^{2+} signals (as was done for the results with JTV-519 and dantrolene above). This categorisation revealed that carvedilol superfusion had a significant effect on PVCs obtained from both 3 month- and 24 month-old mice that had a high initial frequency of spontaneous Ca^{2+} signals (Figure 4.19Aiii and 4.19Biii).

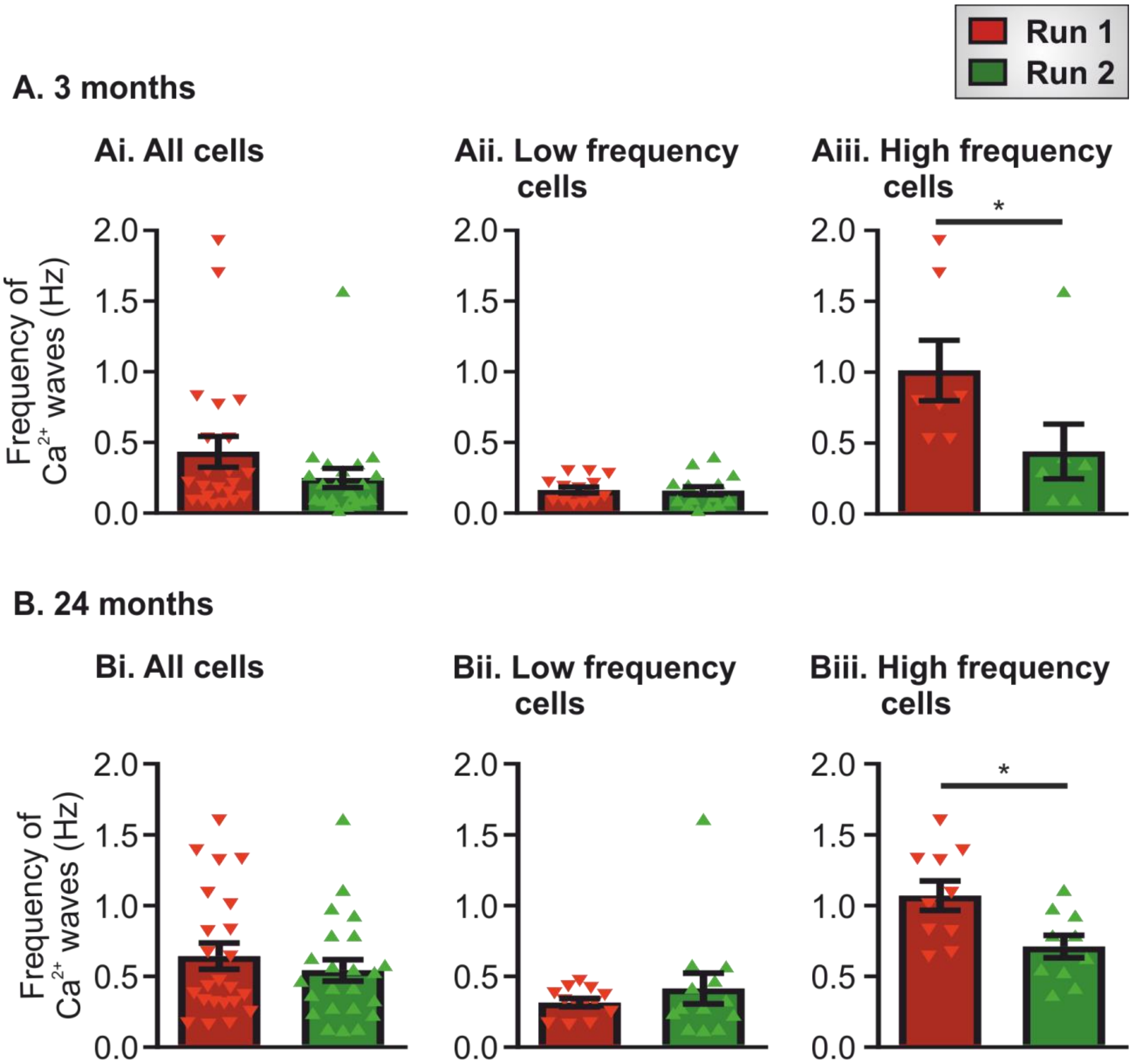

Figure 4.19. Effect of carvedilol on spontaneous Ca^{2+} signals in PVCs from 3 month- and 24 month-old mice. The data were obtained from experiments such as those depicted in Figure 4.15, but with superfusion of 100 µM carvedilol. Panels **Ai** and **Bi** show the effect of carvedilol on the frequency of spontaneous Ca^{2+} signals in PVCs from 3 month- and 24 month-old mice, respectively. Panels **Aii-Aiii** and **Bii-Biii** show the effect of carvedilol on the frequency of spontaneous Ca^{2+} signals in PVCs from 3 month- and 24 month-old mice following categorisation of the cells into those that initially showed either low (< 0.5 Hz) or high (≥ 0.5 Hz) frequency of spontaneous Ca^{2+} signals. The data are presented as mean ± S.E.M., and were analysed with paired Student's *t*-tests. * and ** indicate $P < 0.05$ and $P < 0.01$, respectively. *n* = 17 - 18 from 6 animals per age group in Panels **A** and **B**.

4.6.3. Effect of propranolol on PVCs from 3 and 24 month-old mice

As mentioned previously, carvedilol is not solely a RyR inhibitor, but also acts as an antagonist of α- and β-adrenoceptors (α/β-adrenoceptors). Moreover, it has been previously reported that the spontaneous electrical activity (firing rate) in PVCs could be increased by stimulating α/β-adrenoceptors using 10 nM and 1 µM isoproterenol (Chen *et al.,* 2008, Chen *et al.,* 2014). A potential contribution of α/β-adrenoceptors to the generation of spontaneous Ca^{2+} signals observed in PVCs was therefore examined using propranolol, which is a specific α/β-adrenoceptors antagonist and has been shown not to affect RyR2s in cardiac myocytes (Zhou *et al.*, 2011).

Run 1:

1. **35-second recording of spontaneous activity.**

Following Run 1, 100 µM propranolol (or HBSS as a control) was superfused over the lung slices whilst they were maintained on the microscope stage. Following a 10-minute incubation period, Run 2 was initiated.

Run 2:

1. **35-second recording of spontaneous activity.**

This protocol was repeated using PVCs from 3 month- and 24 month-old animals. For these experiments, spontaneous Ca^{2+} signals were recorded using 2D confocal imaging at 10 Hz. The quantitative analysis of the effects of propranolol superfusion are presented in Figure 4.20.

Collectively plotting all the data obtained from the experiments involving propranolol indicated that there was no significant effect of the reagent on the frequency of spontaneous Ca^{2+} signals in PVCs obtained from either 3 month- or 24 month-old mice

(Figure 4.20A and B). Moreover, categorising the PVCs into ‘low frequency’ or ‘high frequency’ cells based on their initial frequency of spontaneous Ca^{2+} signals (as was done for the results with JTV-519 above). This categorisation revealed that propranolol superfusion had no significant effect on PVCs obtained from both 3 month- and 24 month-old mice that had a high initial frequency of spontaneous Ca^{2+} signals (Figure 4.20Aiii and 4.20Biii).

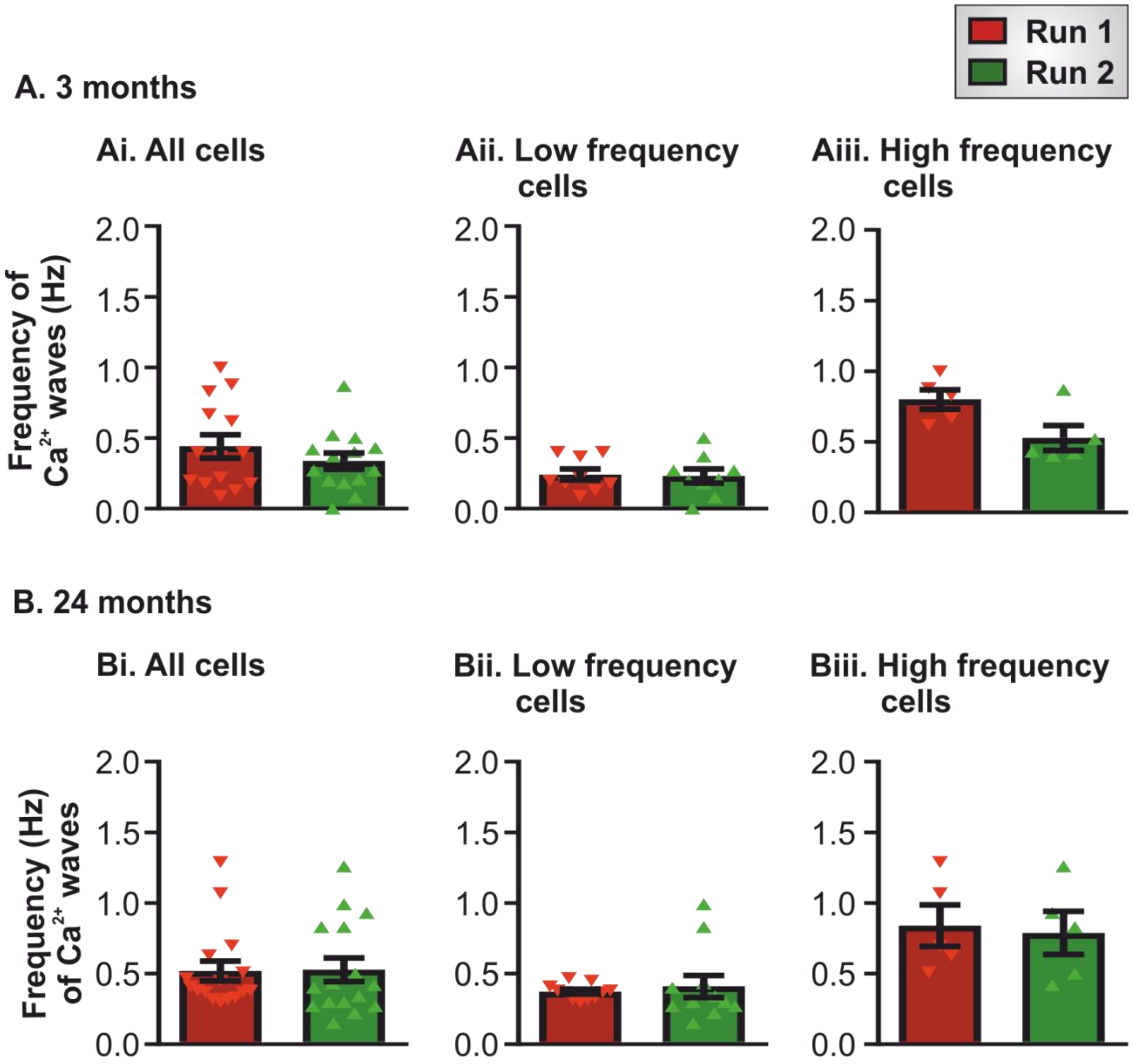

Figure 4.20. Effect of propranolol on spontaneous Ca^{2+} signals in PVCs from 3 month- and 24 month-old mice. The data were obtained from experiments such as those depicted in Figure 4.15, but with superfusion of 100 µM propranolol. Panels **Ai** and **Bi** show the effect of propranolol on the frequency of spontaneous Ca^{2+} signals in PVCs from 3 month- and 24 month-old mice, respectively. Panels **Aii-Aiii** and **Bii-Biii** show the effect of propranolol on the frequency of spontaneous Ca^{2+} signals in PVCs from 3 month- and 24 month-old mice following categorisation of the cells into those that initially showed either low (< 0.5 Hz) or high (≥ 0.5 Hz) frequency of spontaneous Ca^{2+} signals. The data are presented as mean ± S.E.M., and were analysed with paired Student's *t*-tests. *n* = 10 – 11 slices from 4 animals per age group in Panels **A** and **B**.

4.6.4. Activation of adrenoceptors in PVCs from 3 and 24 month-old mice

To further investigate the putative role of α/β-adrenoceptors in causing spontaneous Ca^{2+} signals within PVCs, lung slices were superfused with a combination of norepinephrine (100 µM) and isoprenaline (100 µM).

To examine the effects of norepinephrine (100 µM) and isoprenaline (100 µM), the following protocol was protocol was carried out:

Run 1

35-second recording of spontaneous activity

Following Run 1, norepinephrine (100 µM) and isoprenaline (100 µM) (or HBSS as a control) were superfused over the lung slices whilst they were maintained on the microscope stage. Following a 10-minute incubation period, Run 2 was initiated.

Run 2

35-second recording of spontaneous activity

This protocol was repeated using PVCs from 3 month- and 24 month-old animals. For these experiments, spontaneous Ca^{2+} signals were recorded using 2D confocal imaging at 10 Hz. The quantitative analysis of the effects of 100 µM isoprenaline and 100 µM norepinephrine superfusion are presented in Figure 4.21.

There was no change in the frequency of spontaneous Ca^{2+} signals in PVCs from 3 month- and 24 month-old mice following 10 minutes of norepinephrine and isoprenaline superfusion (Figure 4.21). Together with the observations made using propranolol (Figure 4.20), these data suggest that the effects of carvedilol presented in Figure 4.19 were caused by inhibition of RyRs, rather than being due to antagonism of α/β-adrenoceptors.

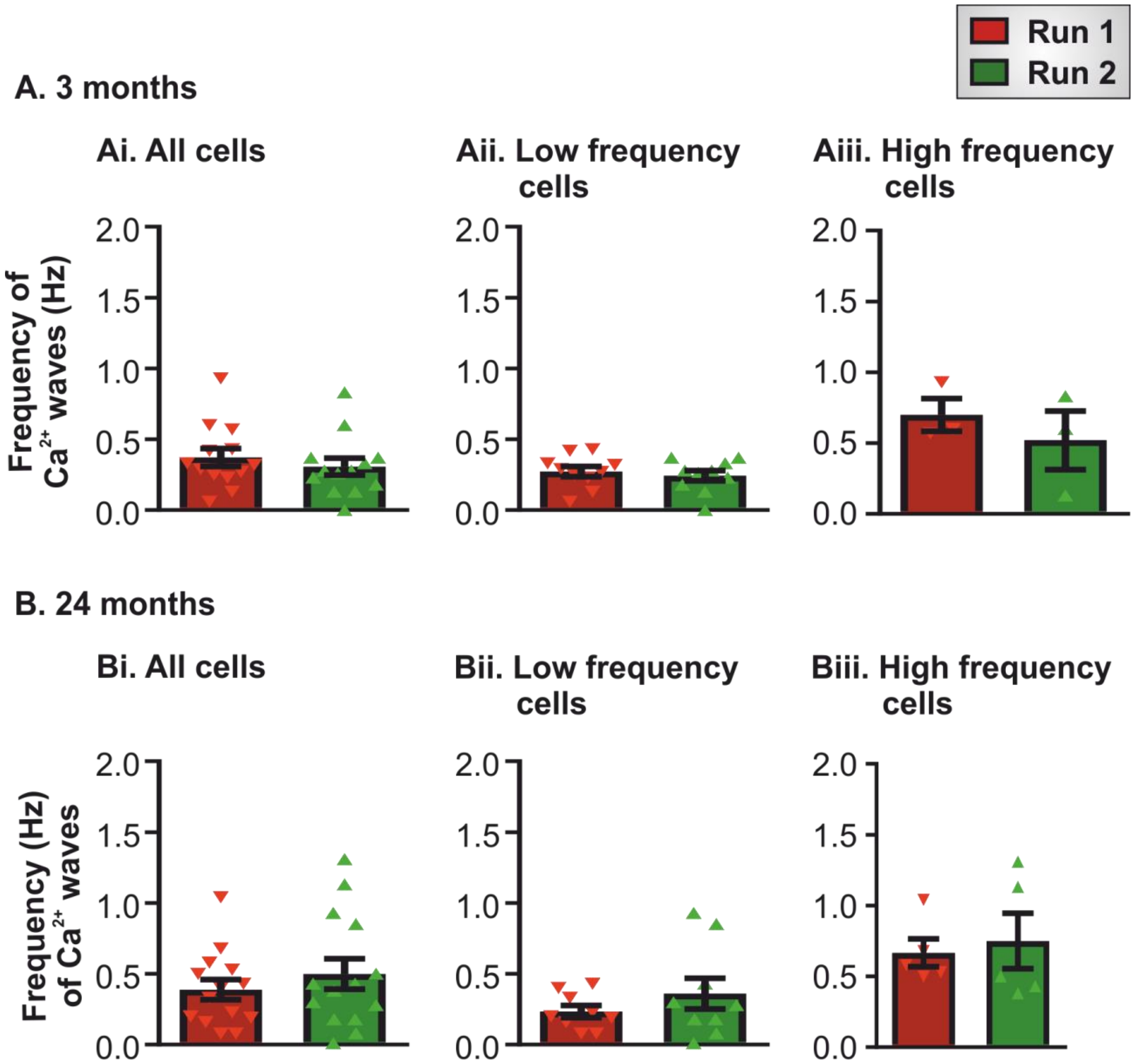

Figure 4.21. Effect of norepinephrine and isoprenaline on spontaneous Ca^{2+} signals in PVCs from 3 month- and 24 month-old mice. The data were obtained from experiments such as those depicted in Figure 4.15, but with superfusion of norepinephrine and isoprenaline (100 µM of each). Panels **Ai-Aiii** and **Bi-Biii** show the effect of norepinephrine and isoprenaline on the frequency of spontaneous Ca^{2+} signals in PVCs from 3 month- and 24 month-old mice, respectively. The data are presented as mean ± S.E.M., and were analysed with paired Student's *t*-tests. *n* = 10 slices from 4 animals per age group.

4.7. Assessing the production of reactive oxygen species production in PVCs from 3 month- and 24 month-old mice

The production of reactive oxygen species (ROS) has been reported to increase during ageing in ventricular myocytes (Cooper *et al.*, 2013). In particular, a deterioration of mitochondria during ageing often leads to an increased ROS production (Turdi *et al.,* 2010). The data presented in Chapter 3 showed alterations in mitochondrial characteristics in PVCs from 24 month-old mice, consistent with a change in mitochondrial function. These observations provoke the question whether an increase in ROS was responsible for some of the differences in the frequency of spontaneous Ca^{2+} signals in PVCs from 3 month- and 24 month-old mice. To assess ROS production, slices from both 3 month- and 24 month-old mice were incubated with 50 µM ROS Brite (a fluorescence ROS indicator) for 30 minutes at 37°C before collecting images on the Zeiss 510 META laser scanning microscope. When loaded into cells, ROS Brite increases its fluorescence intensity when modified by various ROS. Care was taken to ensure that the ROS Brite loading and imaging conditions were exactly the same in all experiments so that ROS production could be compared in PVCs obtained from 3 month- and 24 month-old mice.

Images of ROS Brite-loaded PVCs are presented in Figure 4.22A-C. It was evident that PVCs from 3 month-old mice (Figure 4.22A) displayed a significantly lower ROS Brite fluorescence than cells from 24 month-old animals (Figure 4.22B and C). The bright structure with a wavy appearance in the ROS Brite images is collagen, which exhibits substantial autofluorescence. The ROS levels within the PVCs were quantified by placing a ROI over whole cells within lung slice from 3 month- and 24 month-old mice and sampling the ROS Brite fluorescence intensity (Figure 4.22C). ROS Brite fluorescence was significantly greater in PVCs obtained from 24 month-old mice compared to that recorded in cells from 3 month-old mice (Figure 4.22D).

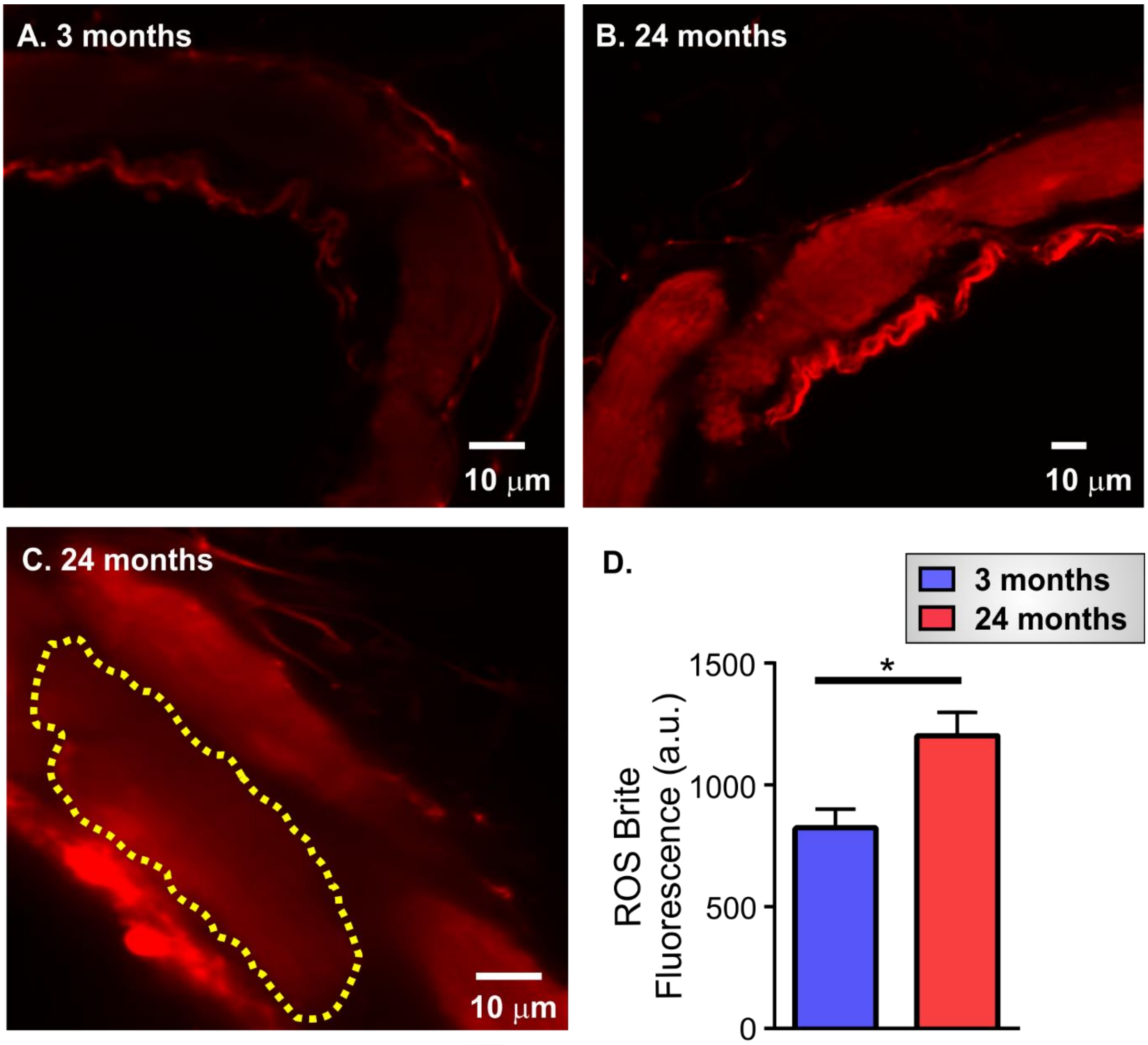

Figure 4.22. Quantitative assessment of ROS production in PVCs from 3 month- and 24 month-old mice. Panel **A** shows a representative image of PVCs from 3 month-old mice loaded with the fluorescent ROS indicator ROS Brite. Panel **B** shows a representative image of ROS Brite-loaded PVCs from 24 month-old mice. Panel **C** illustrates an example of a PVC outlined to measure ROS fluorescence. Panel **D** indicates the average ROS Brite fluorescence in PVCs from 3 month- and 24 month-old animals. The data presented as mean ± S.E.M., and were analysed using an unpaired Student's *t*-test, * indicates $P < 0.05$. *n* = 34 – 35 cells, 9 slices from 4 animals per age group.

The data presented in this study, and in others (Honjo *et al.,* 2003, Wang *et al.,* 2005, Logantha *et al.,* 2010), have clearly shown that stochastic RyR activity is responsible the spontaneous Ca^{2+} signals observed in PVCs. It is widely accepted that ROS induces activation of RyR2 in cardiac myocytes (Cooper *et al.* 2013), and it is therefore plausible that increased ROS production contributed to the greater frequency of spontaneous Ca^{2+} signals in PVCs from older animals. This hypothesis was examined by increasing the ROS-buffering capacity of PVCs by loading them with the ROS scavenger Trolox (100 µM), and then subsequently characterising the frequency of spontaneous Ca^{2+} signals and fidelity of pacing in response to EFS pulses.

To analyse the effects of 100 µM Trolox in PVCs, lung slices were incubated in either (HBSS with/without 100 µM Trolox) for 24 hours at 37°C prior imaging. The following day, the protocol below was carried-out.

1. 18-second line-scan recording of spontaneous activity in either (HBSS +/- 100 µM Trolox).

2. 18-second line-scan recording during application of 1 Hz in (HBSS +/- 100 µM Trolox).

3. 18-second line-scan recording during application of 3 Hz in (HBSS +/- 100 µM Trolox).

4. 18-second line-scan recording during application of 5 Hz in (HBSS +/- 100 µM Trolox).

Cal-520-loaded PVCs were imaged using confocal line-scanning at 333 Hz. PVCs were incubated in (HBSS +/- 100 µM Trolox) throughout the recording period whilst they were maintained on the stage of the microscope.

As described in section 4.5, spontaneous Ca^{2+} signals occurred with a high frequency in PVCs obtained from 24 month-old mice, compared to those from 3 month-old animals

(Figure 4.23A). Incubation of lung slices with Trolox significantly decreased the frequency of spontaneous Ca^{2+} signals in PVCs from both young and old animals (Figure 4.24A).

Consistent with results presented in section 4.3.2, PVCs within lung slices obtained from 24 month-old animals were more difficult to successfully pace with EFS than cells from 3 month-old animals (Figure 4.23B - D). Moreover, similar to the results presented in section 4.3.2 the ability to successful pace the PVCs declined at both ages if the stimulation frequency was increased from 1 Hz to 3 or 5 Hz (Figure 4.23B - D). Incubation of slices with Trolox did not significantly increase the proportion of cells at either age that were successfully paced at a specific EFS frequency (i.e. 1, 3 or 5 Hz). However, for PVCs from 24 month-old mice, there was a trend for Trolox to improve the proportion of cells that were successfully paced at each of the frequencies tested. Due to a lack of 24 month-old animals, these experiments could not be sufficiently repeated to have the same n number as in other protocols, and likely obtain statistical significance. It is intended that future studies will complete the data set.

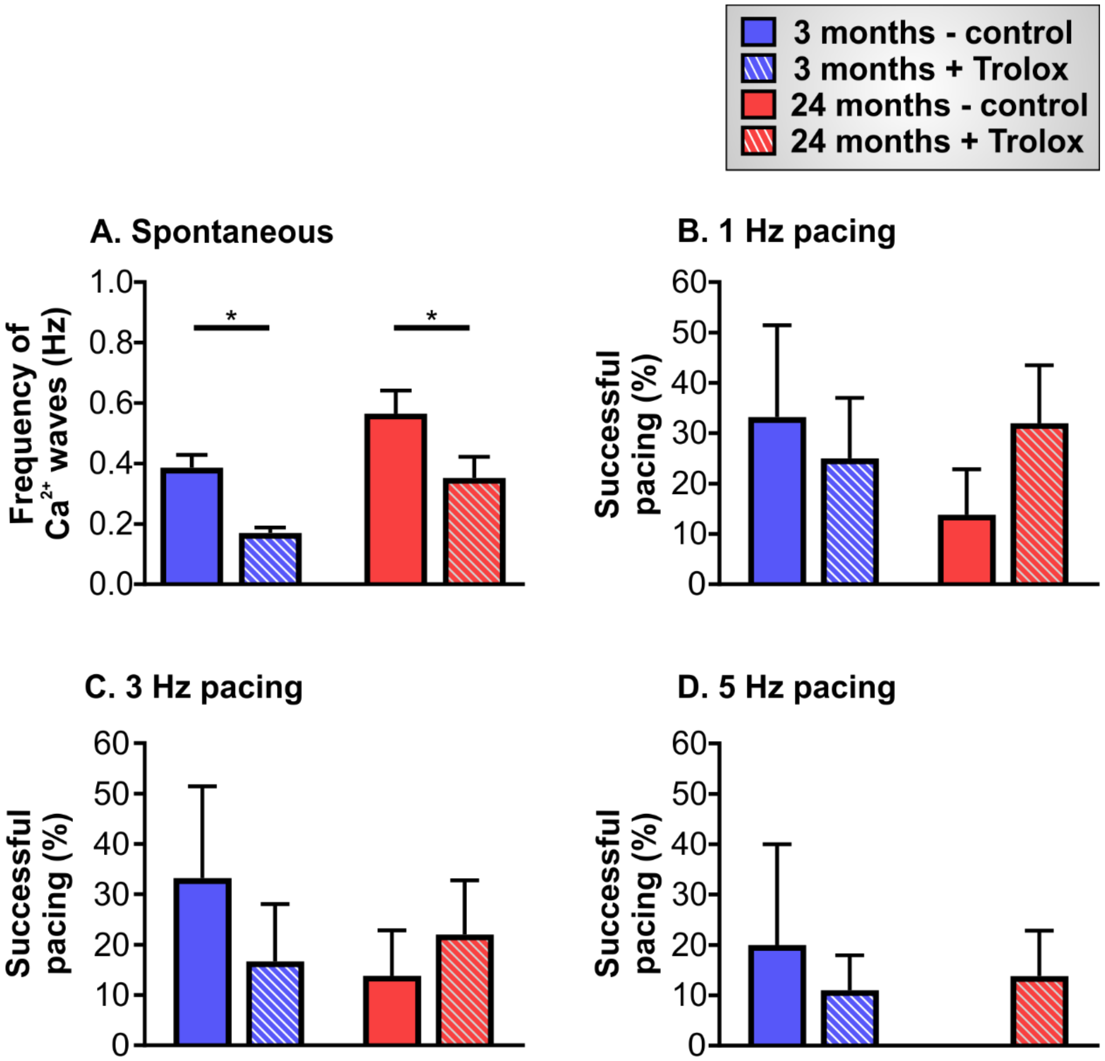

Figure 4.23. Effects of the ROS scavenger Trolox on the spontaneous Ca^{2+} signals in PVCs from 3 month- and 24 month-old mice. Panel **A** shows the frequency of spontaneous Ca^{2+} signals in PVCs from 3 month- and 24 month-old mice, either without or following incubation with 100 µM Trolox for 24 hours. Panels **B – D** show the percentage of regions within lung slices from 3 month- and 24 month-old mice that were successfully paced with 1, 3 or 5 Hz EFS, either without or following incubation with 100 µM Trolox for 24 hours. The data are presented as mean ± S.E.M., and were analyses using an unpaired Student's *t*-test. * denotes $P < 0.05$. *n* = 8 slices from 4 animals per age group.

4.8. Analysis of mitochondrial function in PVCs from 3 month- and 24 month-old mice

To assess the mitochondrial function in PVCs from 3 month- and 24 month-old mice, lung slices from both age groups were treated with 5 µM antimycin and 5 µM oligomycin (hereafter denoted 'anti/oligo'). Together, these reagents lead to mitochondrial depolarisation, prevent mitochondrial respiration, and abrogate ATP production or consumption by the F_1F_0 ATP synthase (Hung *et al.*, 2012, Zhao *et al.,* 2013, Leonard *et al.,* 2014). As a control, 5 µM oligomycin was added by itself to solely inhibit the F_1F_0 ATP synthase without mitochondrial depolarisation. The effects of anti/oligo on spontaneous Ca^{2+} signals in PVCs, and the ability of PVCs to be paced by EFS, was analysed using a similar protocol to that presented in section 4.4.2, as follows:

Run 1:

1. **18-second line-scan recording of spontaneous activity.**
2. **18-second recording during application of 1 Hz EFS.**

Following Run 1, anti/oligo (or HBSS as a control) was superfused over the lung slices whilst they were maintained on the microscope stage. Following a 5-minute incubation period, Run 2 was initiated.

Run 2:

1. **18-second line-scan recording of spontaneous activity.**
2. **18-second recording during application of 1 Hz EFS.**

Cal-520-loaded PVCs were imaged using confocal line-scanning at 333 Hz. Anti/oligo and oligomycin solutions were superfused over the cells while they were maintained on the stage of the microscope.

Line-scans and Ca^{2+} traces of the spontaneous Ca^{2+} signals in PVCs from 3 month- and 24 month-old mice, and responses to EFS pulses, are presented in Figure 4.24. In keeping with the data described earlier in this study, both Ca^{2+} waves and local Ca^{2+} transients were observed in the PVCs (Figure 4.24Ai and Bi). For the examples shown, the PVCs from both the 3 month- and 24 month-old animals both displayed regular responses to 1 HZ EFS application (Figure 4.24Aii and Bii).

Quantitative analyses of the effect of anti/oligo on spontaneous Ca^{2+} signals in PVCs from 3 month- and 24 month-old animals, and their ability of PVCs to be paced by EFS, are presented in Figure 4.25. Anti/oligo treatment had inconsistent effects on spontaneous Ca^{2+} signals in PVCs from 3 month- and 24 month-old animals, although there was a notable decrease in the frequency and/or amplitude of Ca^{2+} waves. There was a significant reduction in the ability of PVCs from 3 month-old mice slices to follow 1 Hz EFS after anti/oligo treatment (Figure 4.25Aiv, whereas PVCs from 24 month-old animals were not affected (Figure 4.25Biv).

The fact that the treatment with oligomycin alone, thus inhibiting the ATP production without affecting the mitochondrial membrane potential, generally did not affect the Ca^{2+} signalling parameters measured (apart from the frequency of Ca^{2+} waves, Figure 4.25Ai) indicates that the observed effects are caused by the changes in the mitochondrial membrane potential. The duration of spontaneous Ca^{2+} signals was not affected by anti/oligo superfusion (Figure 4.26).

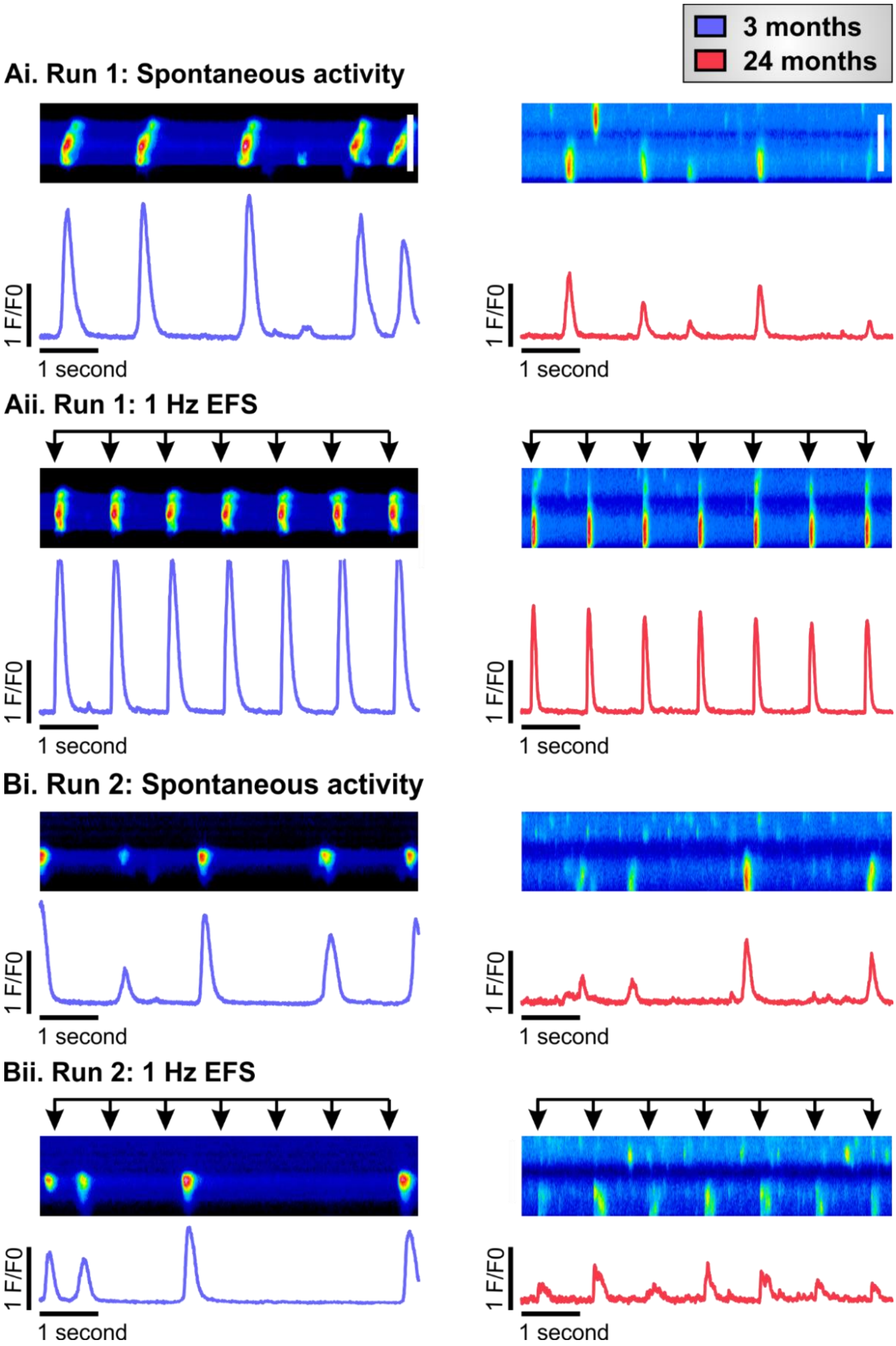

Figure 4.24. Effects of oligomycin + antimycin treatment on spontaneous Ca^{2+} signals and EFS pacing in PVCs from 3 month- and 24 month-old mice. Panels **Ai** and **Aii** show spontaneous Ca^{2+} signals and EFS-induced Ca^{2+} transients prior to superfusion with a solution containing 5 µM oligomycin and 5 µM antimycin for 5 minutes in PVCs from both age groups. Panels **Bi** and **Bii** show spontaneous Ca^{2+} signals and EFS-induced Ca^{2+} transients following the superfusion with a solution containing 5 µM oligomycin and 5 µM antimycin for 5 minutes. All scale bars represent 20 µm.

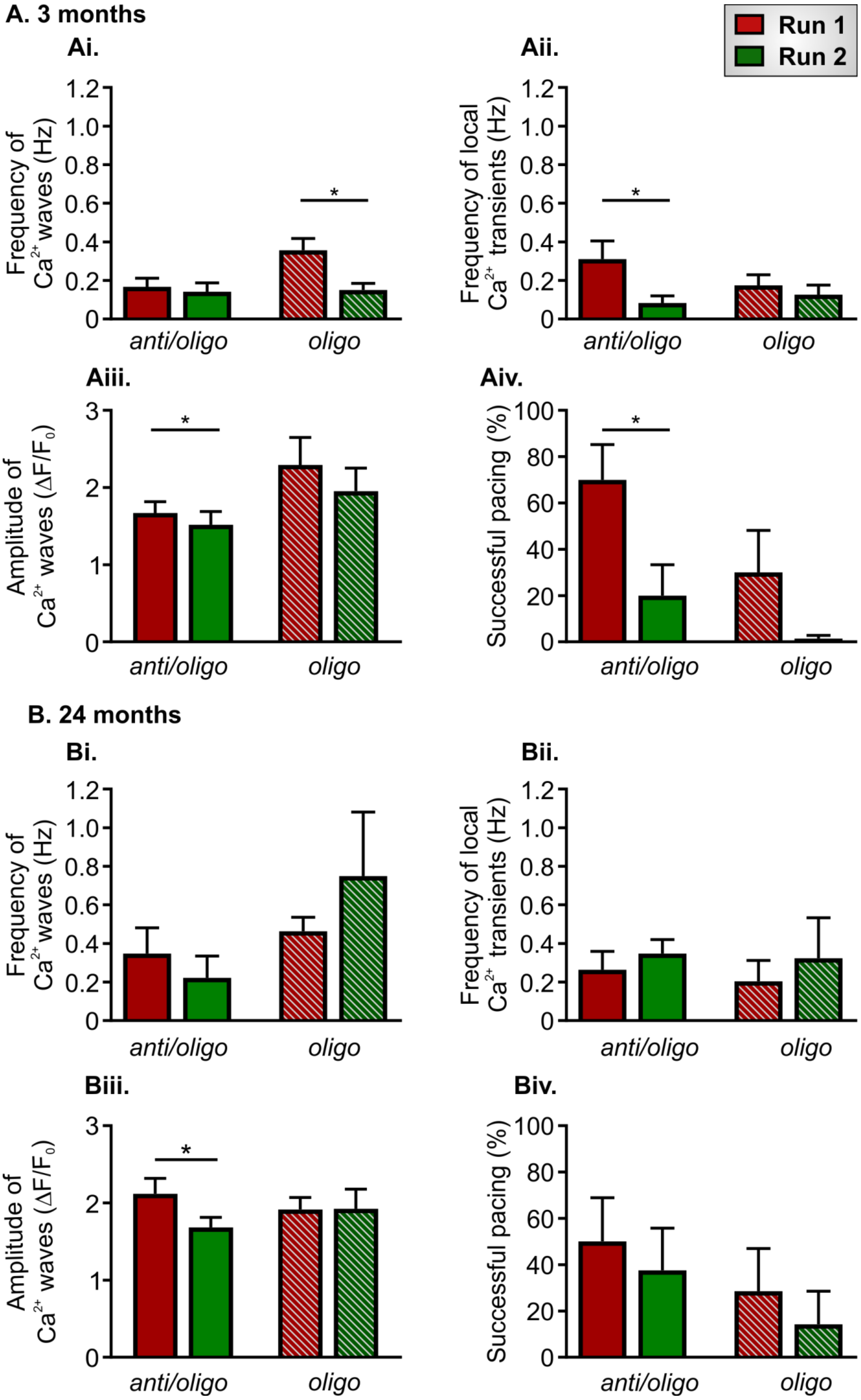
A. 3 months
Run 1
Run 2
Ai.
Frequency of Ca^{2+} waves (Hz)
1.2
1.0
0.8
0.6
0.4
0.2
0
*
anti/oligo
oligo
Aii.
Frequency of local Ca^{2+} transients (Hz)
*
anti/oligo
oligo
Aiii.
Amplitude of Ca^{2+} waves ($\Delta F/F_0$)
3
2
1
0
*
anti/oligo
oligo
Aiv.
Successful pacing (%)
100
80
60
40
20
0
*
anti/oligo
oligo
B. 24 months
Bi.
Frequency of Ca^{2+} waves (Hz)
anti/oligo
oligo
Bii.
Frequency of local Ca^{2+} transients (Hz)
anti/oligo
oligo
Biii.
Amplitude of Ca^{2+} waves ($\Delta F/F_0$)
*
anti/oligo
oligo
Biv.
Successful pacing (%)
anti/oligo
oligo

Figure 4.25. Effect of antimycin and oligomycin, or oligomycin alone, on Ca^{2+} signals in PVCs from 3 month- and 24 month-old mice. Panels **Ai** and **Bi** show the frequency of Ca^{2+} waves. Panels **Bi** and **Bii** illustrate the frequency of local Ca^{2+} transients. Panels **Aiii** and **Biii** show the amplitude of Ca^{2+} waves. Panels Aiv and Biv represent the percentage of slices following 1 Hz EFS from 3 month- and 24 month-old mice before or after superfusion with a combination of antimycin and oligomycin, or oligomycin only. The data are presented as mean ± S.E.M., and were analysed using paired *t*-tests, * indicates $P < 0.05$. $n = 7 – 11$ slices from 3 animals per age group.

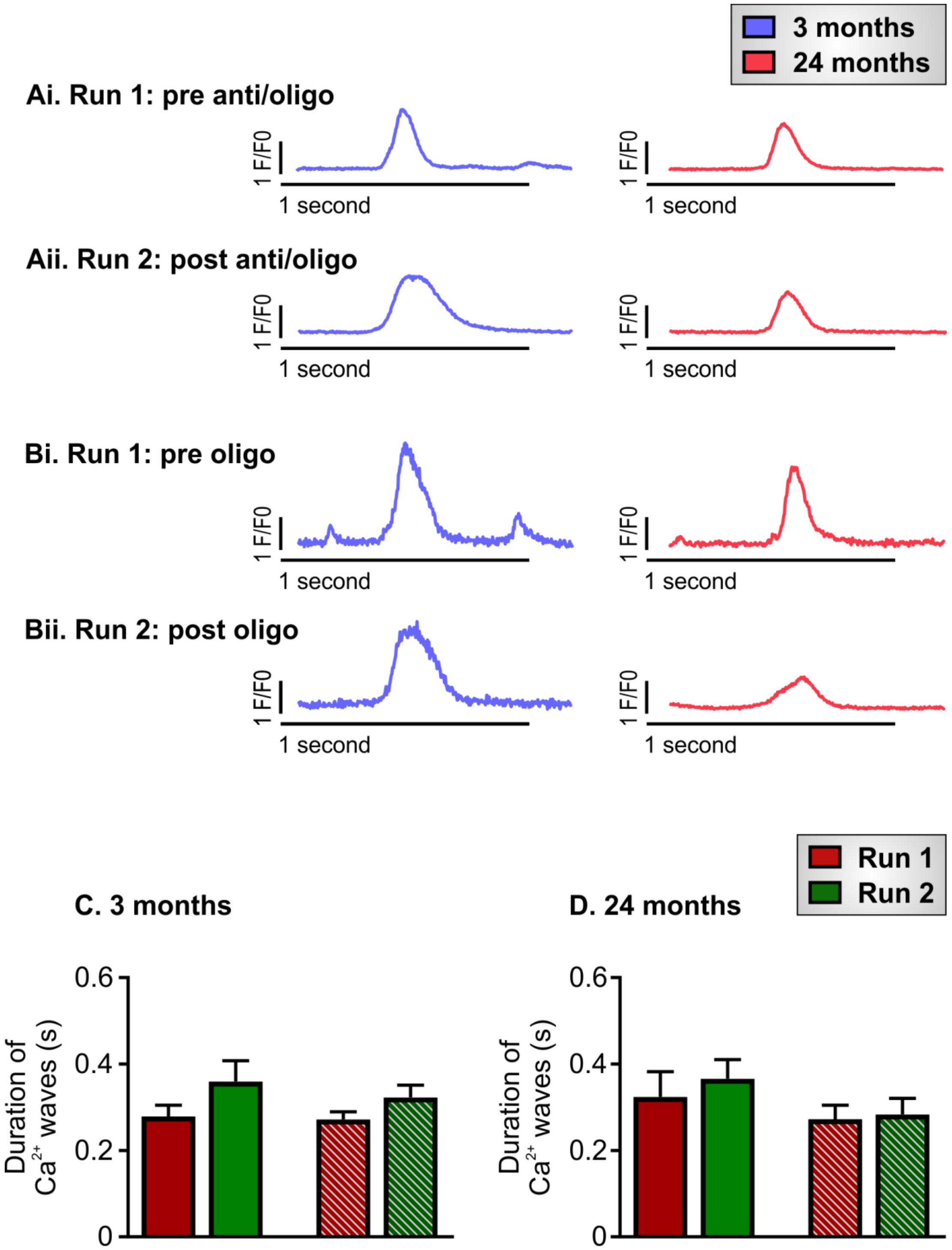

Figure 4.26. Effects of antimycin and oligomycin, or oligomycin alone, on the duration of Ca^{2+} transients in PVCs from 3month- and 24 month-old animals. Panels **Ai** and **Bi** show representative examples of Ca^{2+} waves in PVCs from 3 month- and 24 month-old mice before and after superfusion with 5 µM anti/oligo. Panels **Aii** and **Bii** show representative examples of Ca^{2+} waves in PVCs from 3 month- and 24 month-old mice before and after superfusion with 5 µM oligomycin. Panels **C** and **D** quantify the durations of Ca^{2+} transients in PVCs from 3 month- and 24 month-old mice before and after superfusion with 5 µM anti/oligo, or oligomycin alone. The data are presented as mean ± S.E.M., and were analysed using paired *t*-tests. *n* = 8 – 10 slices from 3 animals per age group.

4.9. Summary

1. Lung slices are a viable way to study PVC function; the PVCs maintain cell-cell contacts, organisation and orientation, they have low basal Ca^{2+} levels, display frequent spontaneous Ca^{2+} signals and demonstrate excitation-contraction coupling.
2. Ca^{2+} signals occurring in PVCs within lung slices from 3 month- and 24 month-old mice could be readily visualised using confocal imaging. The single wavelength Ca^{2+} indicator Cal-520 was ideal for visualising both spontaneous Ca^{2+} signals and EFS-induced Ca^{2+} transients. For reasons that are not fully known, PVCs preferentially loaded with Cal-520 (compared to their neighbouring endothelial and smooth muscle cells), which aided their identification and visualisation in imaging experiments.
3. PVCs displayed heterogeneous, complex patterns of spontaneous Ca^{2+} signals ranging from localised events occurring over a few micrometers and lasting for a hundreds of milliseconds, as well as Ca^{2+} waves that initiate as local signals but can propagate throughout the entirety of a PVC. Although most PVCs behaved as isolated Ca^{2+} signalling entities, a Ca^{2+} wave in one cell could occasionally trigger a response in an adjacent cell.
4. The spontaneous Ca^{2+} signals (local Ca^{2+} signals and Ca^{2+} waves) and EFS-induced Ca^{2+} transients could be distinguished on the basis of amplitude and kinetics, as well as their appearance in line-scans and 2D images.
5. In addition to their heterogeneity in spontaneous Ca^{2+} signals, PVCs show differing responses to EFS. Adjacent cells, which are likely to receive the same degree of electrical stimulation, do not show the same patterns of pacing in response to a train of EFS pulses.

6. NRVMs were used to test the efficacy of reagents that affect cardiac myocyte Ca^{2+} signals. JTV-519, carvedilol and BTP2 had significant effects on the occurrence of spontaneous Ca^{2+} transients in NRVMs, but also negatively affected the proportion of cells that could be paced by EFS.
7. After testing on NRVMs, the Ca^{2+} signalsome-affecting reagents were applied to PVCs in order to establish whether spontaneous Ca^{2+} signals could be inhibited with a concomitant improvement in the fidelity of EFS pacing. The results obtained using PVCs were broadly similar to those observed with NRVMs; some of the reagents (e.g. JTV-519 and BTP2) reduced various aspects of spontaneous Ca^{2+} signals, but they also caused significant decrease in the ability of PVCs to follow EFS pacing.
8. PVCs from 24 month-old mice displayed a significantly high frequency of spontaneous Ca^{2+} signals compared to PVCs from 3 month-old mice, and were more difficult to pace using EFS.
9. PVCs from 24 month-old mice tended to show more Ca^{2+} signal alternans and irregular responses than PVCs from 3 month-old mice.
10. Ca^{2+} signalsome-affecting reagents were used to investigate whether they could reduce the spontaneous Ca^{2+} signals in PVCs from 24 month-old mice. JTV-519 and carvedilol both significantly reduced the occurrence of spontaneous Ca^{2+} signals. However, they were only effective on cells that had a high frequency of spontaneous Ca^{2+} signals prior to reagent superfusion.
11. PVCs from 24 month-old mice displayed a higher rate of ROS production than PVCs from 3 month-old mice.
12. Application of the Trolox to PVCs to buffer ROS production significantly reduced the frequency of spontaneous Ca^{2+} signals in cells from both 3 month- and 24

month-old animals. However, while there was a trend for improved EFS-induced pacing of the PVCs from 24 month-old mice, it was not statistically significant with the data set available in this study.

13. Using a combination of antimycin + oligomycin to cause inhibition of mitochondrial electron transport, concomitant with mitochondrial depolarisation, altered some aspects of spontaneous Ca^{2+} signals in PVCs from 3 month-old mice, but also significantly reduced the ability of the cells to follow EFS pacing. PVCs from 24 month-old mice we much less affected by application of antimycin + oligomycin.

4.10. Discussion

It is established that electrical activity arising from PVCs in the pulmonary veins causes AF (Haissaguerre *et al.*, 1998, Chen *et al.,* 1999, Sueda *et al.,* 2005). However, the mechanism(s) underlying the generation of ectopic action potentials within PVCs are not clear. A number of studies have proposed that spontaneous Ca^{2+} signals contribute to the pro-arrhythmic activity of cardiac myocytes (Vest *et al.,* 2005, Neef *et al.,* 2010, Tsuneoka *et al.,* 2012, Voigt *et al.,* 2012). Indeed, altered Ca^{2+} homeostasis in atrial cardiac myocytes is one of the factors thought to contribute to the development and maintenance of AF during ageing (Lai *et al.,* 1999; Vest *et al.*, 2005; Zhu *et al.*, 2005; Wongcharoen *et al.,* 2007; Voigt *et al.*, 2012). Consequently, the work described in this Chapter characterised aspects of Ca^{2+} signalling in PVCs to help elucidate the pro-arrhythmic nature of these cells. Since the incidence of AF increases with age (Hayashi *et al.,* 2002, Nattel *et al.,* 2008), differences in Ca^{2+} signalling between PVCs from 3 month- and 24 month-old mice were examined to gain an insight into the changes that may occur during ageing.

PVCs utilise the same excitation-contraction coupling machinery as atrial and ventricular myocytes (Tsuneoka *et al.,* 2012, Rietdorf *et al.,* 2014). However, they appear to have a greater propensity to show spontaneous Ca^{2+} signals (Logantha *et al.,* 2010, Rietdorf *et al.,* 2014, Rietdorf *et al.,* 2015). The first observation of spontaneous activity involving PVCs was reported in 1876, when Brunton and Fayrer observed an independent pulsation of a rabbit pulmonary vein after all motion had ceased in the heart (Brunton and Fayrer, 1876). Since then, a number of studies have characterised the structure of PVCs, as well as their electrophysiological and Ca^{2+}-handling properties (Ho *et al.,* 2001, Chen *et al.,* 2002, Ehrlich *et al.,* 2003, Okamoto *et al.*, 2008, Schotten *et al.,* 2011), but as yet a definitive mechanism for the spontaneous Ca^{2+} signalling in PVCs is unclear. While the mechanism causing spontaneous Ca^{2+} signals may be unclear, previous work has demonstrated that such spontaneous events can prevent PVCs from being electrically paced (Rietdorf *et al.,* 2014, Rietdorf *et al.,* 2015). Principle aims of this study were to probe the cellular Ca^{2+} sources of that are responsible for spontaneous Ca^{2+} signals in PVCs, and to examine whether it is possible to prevent these events in order to promote fidelity in EC-coupling. In addition to corrupting pacing, spontaneous Ca^{2+} signals can lead to arrhythmias via a variety of mechanisms, such as the triggering of electrical events, as described in Chapter 1. It is therefore beneficial to gain a clear understanding of how spontaneous Ca^{2+} signals may occur in PVCs in order to develop therapies to prevent the induction of AF.

The data presented in this Chapter shows that blocking the supply of Ca^{2+} from different sources within PVCs can reduce various aspects of spontaneous Ca^{2+} signalling. Of the reagents used, verapamil, BTP2 and JTV-519 were the most efficacious in reducing the frequency of spontaneous Ca^{2+} signals in PVCs from 3 month-old mice (see section 4.4 above). However, whilst these compounds reduced spontaneous Ca^{2+} signalling, they had a negative impact on EC-coupling because fewer cells responded to EFS pulses (Figure 4.9). These data indicate that it may be difficult to dissociate the Ca^{2+} sources that promote spontaneous Ca^{2+} signals from those Ca^{2+} sources required for EC-coupling. Further experiments could use lower concentrations of the reagents employed in this study, in order to preserve EC-coupling. However, even at the relatively high reagent concentrations used in this study, there was sometimes a modest inhibition of spontaneous Ca^{2+} signalling (see sections 4.4 and 4.6.1). It is therefore unlikely that lower concentrations of the reagents would have a significant effect on spontaneous Ca^{2+} signals and deter them from interfering with pacing of PVCs.

The contribution of VOCCs to spontaneous Ca^{2+} signalling in PVCs was investigated using verapamil (100 µM), which caused a significant reduction in the frequency and amplitude of Ca^{2+} waves (Figure 4.7). These findings agree with previous results where the VOCCs antagonist nifedipine (100 µM) also reduced spontaneous Ca^{2+} signalling (Rietdorf *et al.*, 2014). In that earlier study, it was observed that spontaneous Ca^{2+} signalling continued in the presence of nifedipine, but the Ca^{2+} signals progressively declined in amplitude and frequency over tens of minutes. These observations indicate that spontaneous Ca^{2+} signalling in PVCs is not directly triggered by Ca^{2+} influx via VOCCs, but that VOCCs are needed to sustain the spontaneous Ca^{2+} signals, plausibly by supplying Ca^{2+} to replenish the SR. This notion is further supported by the previous findings that removal of Ca^{2+} from extracellular medium caused a progressive reduction in the frequency and amplitude of Ca^{2+} waves (Logantha *et al.*, 2010, Rietdorf *et al.*, 2014). The results presented in this study did not differentiate between different sub-types of VOCCs that may be involved in the generation of spontaneous Ca^{2+} signals. Verapamil has been shown to inhibit both L-type and T-type Ca^{2+} channels (Bergson *et al.*, 2011), and PVCs have been shown to express both L-type and T-type Ca^{2+} channels (Chen *et al.,* 2004, Logantha *et al.,* 2010). It is plausible that either, or both, types of VOCCs could be involved in the maintenance of spontaneous Ca^{2+} signals. It would be of interest, in future studies, to examine if spontaneous Ca^{2+} signals are more susceptible to inhibition of a particular VOCCs sub-type.

The pyrazole derivative BTP2 was used in this study to explore the possible contribution of SOCE to PVC Ca^{2+} signalling. BTP2 has been used in other studies as a SOCE antagonist and has been shown to block Ca^{2+} influx without affecting K^+ transport or VOCCs (Zitt *et al.*, 2004, He *et al.,* 2005). BTP2 has also been used to inhibit SOCE and was able to reduce SR Ca^{2+} content and firing rate in SA node cells (Liu *et al.*, 2015). In non-electrically excitable cells, SOCE is activated by depletion of Ca^{2+} from intracellular stores, which causes the formation of a signalling complex involving members of the STIM1 and Orai protein families (Hogan *et al.,* 2015). STIM1 and STIM2 function as sensors of Ca^{2+} within intracellular stores, and following depletion of Ca^{2+} stores they interact with Orai1, Orai2 and Orai3 proteins on the plasma membrane to form channels (often denoted 'CRAC' for Ca^{2+} release-activated channel) that allow Ca^{2+} into the cytosol (Vig *et al.,* Feske *et al.*, 2005; Feske *et al.*, 2006). In non-electrically excitable cells, SOCE has been established as a key source of Ca^{2+} and its role is to replenish endoplasmic reticulum Ca^{2+} after activation of channels such as inositol 1,4,5-trisphosphate receptors (Mathews *et al.,* 1989). However, although the molecular components responsible for SOCE (STIM1, STIM2 and Orai channels) are expressed in cardiac myocytes, the role of SOCE in the heart is unclear (Bootman and Rietdorf, 2017). Nevertheless, recent studies have shown that SOCE plays a role in Ca^{2+} homeostasis in some excitable cell types (Touchberry *et al.*, 2011; Liu *et al.*, 2015). For example, SOCE plays an important role in vascular contraction; Ca^{2+} influx induced by store depletion activated pulmonary artery and arterial smooth muscle contraction (Snetkov *et al.*, 2003; Bergdahl *et al.*, 2005). Additionally, SOCE is involved in maintaining pacemaker currents in SA node cells (Liu *et al.*, 2015).

At present, it is unclear what role SOCE may play, if any, in PVCs. Moreover, it remains to be established whether PVCs express STIM and Orai proteins (although their expression is near ubiquitous in mammalian tissues). The results presented here show that BTP2 significantly reduced the frequency of spontaneous Ca^{2+} signals, increased the duration of spontaneous Ca^{2+} waves and inhibited electrical pacing (Figures 4.5, 4.7, 4.8). However, whilst it is possible that there may be a role for SOCE as a source of Ca^{2+} for PVCs, it is not realistic to develop firm conclusions based on the use of one reagent. Moreover, the fact that BTP2 could completely inhibit both spontaneous Ca^{2+} signals and EFS-induced Ca^{2+}

transients (Figure 4.6) suggests that the reagent is not fully specific for SOCE, and should be used with caution (at least for studies involving cardiac myocytes).

NCX is the dominant mechanisms for extrusion of Ca^{2+} out of electrically excitable cells (Bassani *et al.,* 1994, Pieske *et al.,* 1999, Bers 2002, 2008). In its forward electrogenic mode, the NCX extrudes 1 Ca^{2+} in exchange for 3 Na^{+}, thus generating a net inward electrical current that depolarises the membrane potential. Conversely, immediately after a myocyte depolarises, the exchanger generates an outward current due to its reverse mode i.e. an increased in the efflux of Na^{+} and an influx of Ca^{2+}. This outward current contributes to the initial repolarisation phase (Bers, 2000). NCX expression has been shown to be upregulated in AF, contributing to the generation of EADs and DADs, and thereby promoting arrhythmias (Patterson *et al.*, 2006; Venetucci *et al.*, 2007; Okamoto *et al.*, 2012). Previous studies have established that NCX plays a role in extruding Ca^{2+} in PVCs, and may be involved in the generation of spontaneous electrical activity (Patterson *et al.*, 2006; Namekata *et al.*, 2009; Okamoto *et al.*, 2012). For example, it was shown that the forward mode of NCX is activated in PVCs by increasing the SR Ca^{2+} load using the Na^{+}/K^{+} ATPase inhibitor Ouabain, leading to spontaneous electrical events (Namekata *et al.*, 2009). Moreover, inhibiting Ca^{2+} release from the SR within PVCs using 10 μM Ryanodine prevented both NCX current activation and EADs (Patterson *et al.*, 2006).

In this study, SN-6 (10 μM) was used to inhibit NCX-mediated Ca^{2+} transport. SN-6 did not affect the frequency of Ca^{2+} waves, but it did reduce that of the local Ca^{2+} transients (Figure 4.7). In addition, SN-6 significantly reduced the amplitude of Ca^{2+} in waves, but did not significantly alter the ability of PVCs to follow 1 Hz EFS (Figure 4.8). Similar to our findings, Ghandi *et al.,* (2013) showed that 10 μM SN-6 reduced spontaneous peak amplitude of Ca^{2+} transients (Gandhi *et al.*, 2013). However, they also showed that SN-6 also inhibited L-type VOCCs. In this study, the VOCCs inhibitor verapamil and the NCX inhibitor SN-6 were the only two reagents that reduced the amplitude of Ca^{2+} waves, raising the possibility that Ca^{2+} influx via VOCCs somehow specifically enhances the amplitude of these signals. Further studies are required to elucidate the roles of VOCCs and NCX for Ca^{2+} signalling in PVCs.

It has been established that the spontaneous Ca^{2+} signals in PVCs occur due the activation of RyRs (Honjo *et al.,* 2003, Wang *et al.,* 2005, Logantha *et al.,* 2010). Therefore, the effects JTV-519, a RyR inhibitor that is currently used in clinical trials, were examined. JTV-519 has been shown to inhibit RyR2 activation by increasing the binding of FK506-binding proteins (FKBPs) to RyR2 (Shou *et al.*, 1998; Vest *et al.*, 2005; Dobrev *et al.*, 2012). A number of studies have demonstrated that both FKBP12 and FKBP12.6 can regulate RyR2 activity by stabilising the channel in a closed state, and thereby decreasing both the open probability and Ca^{2+} flux (Timerman *et al.*, 1993, Galfré *et al.*, 2012). FKBPs have been shown to be tightly associated with RyRs, with up to 4 FKBPs per channel (Jayaraman *et al.,* 1992). Further insights into the role of FKBP12s in regulating RyRs came with the development of FKBP12 and FKBP12.6 knockout mice. In particular, FKBP12.6 knockout mice showed significantly increased RyR2 open probability and channel conductance (Shou *et al.,* 1999, Vest *et al.* 2005). Although most studies suggest that FKBP12.6 binds to RyR2 and stabilises the channel in a closed state, thereby reducing the open probability of the channel, this topic still remains controversial and others have found different results (Galfré *et al.*, 2012). Nonetheless, expression of FKBP12.6 has been shown to decrease in left atrial and PVCs, thereby resulting in an increased SR Ca^{2+} leak. JTV-519, a RyR2 stabiliser which facilitates the binding of RyR2 and FKBP12.6 was demonstrated to attenuate induction of AF in a canine model and PVCs (Kumagai *et al.*, 2003; Chen *et al.*, 2008). JTV-519 inhibits RyR2 openings and thereby reduces SR Ca^{2+} leak that may induce

DADs, spontaneous firing rates and results in arrhythmias (Kumagai *et al.*, 2003; Chen *et al.*, 2008). Our results shows that JTV-519 significantly reduces the frequency of both local and Ca^{2+} waves in PVCs (Figure 4.7), but also significantly affected the ability of slices to follow EFS (Figure 4.8). The utility of JTV-519 for controlling spontaneous Ca^{2+} signals within PVCs requires further studies to establish if there are conditions in which spontaneous events could be preferentially abrogated.

A summary of the Ca^{2+} signalsome-affecting reagents used in this study and their putative targets are illustrated in Figure 4.27.

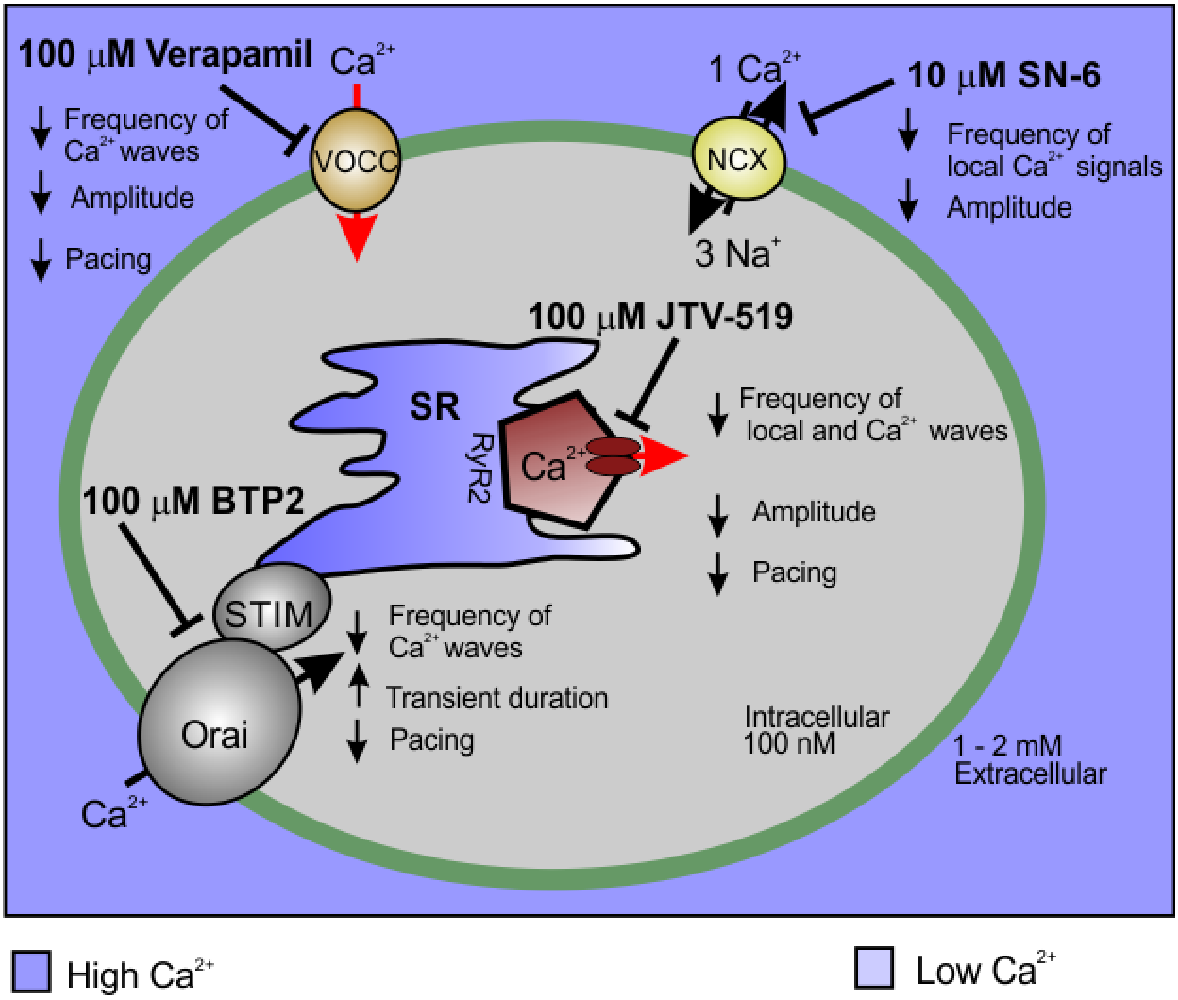

Figure 4.27. Summary of the pharmacological tools used to inhibit excitation-contraction coupling in PVCs. Inhibiting Ca^{2+} influx from extracellular medium by inhibiting VOCCs with verapamil or CRAC channel with BTP2 reduced the frequency of global Ca^{2+} transients and the pacing success rate. Interestingly, inhibiting Ca^{2+} influx by blocking NCX reduced the frequency of local Ca^{2+} transients, but not that of Ca^{2+} waves and did not affect pacing. Additionally, both verapamil and SN-6 reduced the amplitude of Ca^{2+} waves whereas BTP2 did not. Unlike the others, BTP2 is the only drug that increased the transient duration of Ca^{2+} waves. Inhibiting SR Ca^{2+} release with JTV-519 had the most profound effects on excitation-contraction coupling and reduced the frequency of both Ca^{2+} waves and local Ca^{2+} transients, the amplitude and the pacing success rate.

The comparison of Ca^{2+} signalling in PVCs from 3 month- and 24 month-old mice indicated that spontaneous Ca^{2+} signals were more prevalent in the older animals (Figures 4.13 and 4.14). Such spontaneous Ca^{2+} signalling was observed in the atrial cardiac myocytes of AF patients, and was attributed to enhanced RyR2 opening probability (Neef *et al.*, 2010). In addition to their increased frequency in PVCs from 24 month-old mice, the spontaneous Ca^{2+} waves had significantly lower amplitudes and longer durations (Figures 4.9 and 4.10). Further studies are required to establish why spontaneous Ca^{2+} signals occur more frequently, and with altered properties, in PVCs from 24 month-old mice. In particular, it would be important to establish whether the RyRs have altered covalent modifications and gating characteristics, and if the PVCs from older animals have changes in NCX or Ca^{2+} ATPase activity causing them to be less efficient in transporting Ca^{2+}. The reduction in SERCA2a activity and an increase in NCX forward current have also been found in other studies of ageing in cardiac myocytes (Hatch *et al.*, 2011; Herraiz-Martinez *et al.*, 2015). Similarly, Wongcharoen *et al.,* 2007 found a decreased expression of SERCA2a and increase in NCX and RyR expressions in PV tissues from aged rabbits. Based on these results and others, Wongcharoen *et al.,* 2007 suggested that SR Ca^{2+} leak is increased via stimulated RyR2 activity that stimulated the occurrence of DADs and may promote arrhythmias in PV from aged tissues. The results presented here show that JTV-519 and carvedilol reduced the frequency of spontaneous Ca^{2+} waves in PVCs that had a higher level of activity (≥ 0.5 Hz) regardless of the age group (Figures 4.17 and 4.19). Since a greater proportion of PVCs from 24 month-old mice had a spontaneous Ca^{2+} signals with a frequency ≥ 0.5 Hz, the effects of JTV-519 and carvedilol were more prominent with cells from older mice. Surprisingly, opposite to the results described here, ryanodine, another blocker of the RyR, induced spontaneous firing rates and incidence of DADs in PVs from young and aged rabbits rather than reducing DADs (Wongcharoen *et al.,* 2007).

The ability of these compounds to have a more selective action on PVCs with a higher level of spontaneous activity could be potentially useful in terms of therapeutic intervention to assist cells maintaining rhythmic pacing. However, further studies are needed as previous studies have reported different results in PVCs.

An intriguing observation was that PVCs from 24 month-old animals were significantly more difficult to pace using EFS than their 3 month-old counterparts (Figure 4.14). As described above, this difference was not due to the animals being treated any differently, or variation in the preparation of the cells. It would be informative to establish whether there are changes in the expression of proteins involved in responding to APs and triggering Ca^{2+} signals during EC-coupling. The major differences in spontaneous and EFS-induced Ca^{2+} signals, and the effects of inhibiting RyR2 are summarised below in Table 4.2 below.

3 months vs. 24 months	***24 months vs. 3 months***
1. Frequency of spontaneous Ca^{2+} waves (lower). 2. Amplitude of spontaneous Ca^{2+} waves (higher). 3. Transient duration of spontaneous Ca^{2+} waves (faster). 4. EFS (efficient).	1. Frequency of spontaneous Ca^{2+} waves (Higher). 2. Amplitudes of spontaneous Ca^{2+} waves (lower). 3. Transient duration of spontaneous Ca^{2+} waves (slower). 4. EFS (less efficient).
5. Carvedilol (only in PVCs with frequency ≥ 0.5 Hz spontaneous Ca^{2+} waves).	5. Carvedilol (only in PVCs with frequency ≥ 0.5 Hz spontaneous Ca^{2+} waves).
6. JTV-519 (only in PVCs with frequency ≥ 0.5 Hz spontaneous Ca^{2+} waves).	JTV-519 effects (only in PVCs with frequency ≥ 0.5 Hz spontaneous Ca^{2+} waves).
7. Dantrolene (no effects).	7. Dantrolene (no effects).

Table 4.2. Summary of the changes in Ca^{2+} homeostasis and the effects of RyR2 inhibition in 3 and 24 month-old mice.

One limitation of this study is that all experiments were conducted at room temperature (RT). Other studies have reported better potency of various compounds when experiments are undertaken at 37°C (de Tombe and ter Keurs, 1990, Chung and Campbell, 2003, Kanaya *et al.,* 2005). The major disadvantages of performing the experiments at 37°C are a greater loss of the fluorescent Ca^{2+} indicator (Malgaroli *et al.*, 1987; Bootman *et al.*, 2013), and difficulties in maintaining a steady temperature without gradients. The imaging performed in this study utilised inverted microscopes, and the objective lens that comes close to the lung slice is a substantial heat sink. Importantly, a previous study has shown that the frequency of the spontaneous activity in PVCs is not different at RT and 37 °C (Rietdorf *et al.*, 2014).

3 months	***24 months***
1. ROS levels (lower).	1. ROS levels (Higher).
2. Trolox (ROS scavenger) 2 (a) spontaneous Ca^{2+} waves (decreased). 2 (b) Pacing (No significant effects).	2. Trolox (ROS scavenger) 2 (a) spontaneous Ca^{2+} waves (decreased). 2 (b) Pacing (No significant effects).
3. Oligomycin + antimycin (a) Spontaneous local Ca^{2+} signals (reduced). (b) Amplitude (Reduced). (c) Pacing (Inhibited).	3. Oligomycin + antimycin (a) Spontaneous local Ca^{2+} signals (No effects). (b) Amplitude (Reduced). (c) Pacing (Not affected).

Table 4.3. The effects of Trolox and mitochondrial inhibition of Ca2+ homeostasis in PVCs from 3 and 24 month-old mice.

Measurements using ROS Brite indicated that PVCs from 24 month-old mice had significantly higher basal ROS production than PVCs from young mice (Figure 4.22, Table 4.3). These findings concur with previous studies that showed increased ROS production during ageing (Cooper *et al.*, 2013; Dorighello *et al.*, 2017). It is also interesting to note that increased ROS production has been reported during AF (Huang *et al.*, 2017) and in stressful conditions such as heart failure and obesity (Niemann *et al.*, 2011; Guo *et al.*, 2013). The potential source(s) of ROS in PVCs were not investigated in this study, and require further work. However, increased ROS production has been linked to mitochondrial dysfunction (Xi *et al.,* 2005, Yang *et al.,* 2006, Cooper *et al.,* 2003, Ni *et al.,* 2016). Mitochondria in cardiac myocytes have been shown to deteriorate during ageing and stressful conditions such as diabetes; they can be enlarged with disrupted cristae, and become more heterogeneous in shape (Feldman *et al.*, 1981; Gupta *et al.*, 2010).

An increase in ROS production has been shown to affect Ca^{2+} homeostasis by modulating the opening of channels that are cysteine rich through redox modification (Cooper *et al.*, 2013). For example, RyR2 has been shown to be activated by ROS (Cooper *et al.*, 2013). Moreover, post-translational thiol oxidation of RyRs caused by mitochondrial ROS production during ageing caused a significantly increased SR Ca^{2+} leak (Cooper *et al.*, 2013). To examine the consequences of ROS production on Ca^{2+} homeostasis, PVCs were incubated with the ROS scavenger Trolox, which significantly reduced the frequency of Ca^{2+} waves in PVCs from both 3 month- and 24 month-old mice (Figure 4.23, Table 4.3).

Taken together with the data presented in Chapter 3, the results of this study support a hypothesis in which PVCs have deteriorating function as they age. The myofibres and mitochondria are less organised in PVCs from old animals, and they display significantly more spontaneous Ca^{2+} signals and are harder to stimulate using EFS. Moreover, PVCs produce more ROS as they age, potentially as a consequence of mitochondrial dysfunction. The increased ROS production promotes spontaneous Ca^{2+} signals that can negatively affect the ability of PVCs to follow electrical pacing. Whilst it is difficult to control spontaneous Ca^{2+} signals in PVCs by using Ca^{2+} signalsome-affecting reagents without also affecting EC-coupling, ameliorating mitochondrial changes or ROS production may be helpful preventing pro-arrhythmic events.

Chapter 5: Development of a cellular model of cardiac ageing using chemical induction

5.1. Introduction

As outlined in Chapter 1, ageing studies in animals are typically conducted via protracted longitudinal experiments that compare cells, tissues or samples from young and old animals, or by using progeroid (usually mouse) models. Although these studies are effective, they are expensive and time-consuming. Moreover, it may be difficult to ensure that the growth environments of the young and old animals are exactly alike over prolonged periods. Previous studies have shown that acute treatment with hydroxyurea (HU) can induce cellular senescence and ageing phenotypes in both isolated cells (Park *et al.*, 2000; Yeo *et al.*, 2000; Narath *et al.*, 2007) and animals (Banh *et al.*, 2013). For example, HU was used to establish a model of neuronal ageing, using neural stem cells (Dong *et al.*, 2014). For the reasons given above, an acute ageing model would be valuable research tool. To date, no attempt has been made to acutely age cardiac myocytes, for example by using HU. The studies described in this Chapter therefore sought to explore whether an acute, chemically-induced, cellular model of cardiac ageing could be established using cultured neonatal rat ventricular myocytes (NRVMs).

5.1.1. Using NRVMs to develop a cellular model of cardiac ageing

A putative cellular model of cardiac ageing was created by treating NRVMs with HU for up to 7 days. NRVMs were used for this study, since they are a more tractable system than PVCs. Moreover, there are some experimental parameters that are difficult to assess when using PVCs. For example, measuring SR Ca^{2+} is difficult with PVCs because they do not show the typical fast release of Ca^{2+} from the SR following the application of a high caffeine concentration (Rietdorf *et al.*, 2014). As a result, SR Ca^{2+} content was not measured using the PVCs from 3 month- and 24 month-old mice that were described in

Chapter 4. In contrast, NRVMs responded to caffeine application with a rapid release of Ca^{2+} from the SR. Autophagy was also difficult to measure in PVCs within lung slices. The commercial kits that are currently available to stain autophagosomes were tested using PVCs, but did give a poor outcome due to significant background labelling. However, autophagy levels were readily characterised in NRVMs. Generally, autophagy is upregulated in stress (Russell *et al.*, 2014), but downregulated in cardiac myocytes from aged animals (Shirakabe *et al.*, 2016), so reduced autophagic flux was expected in HU-treated NRVMs if this treatment induces an ageing phenotype.

Based on the previous work discussed in Chapter 1, the results from the structural study in PVCs, atrial and ventricular myocytes (Chapter 3) and the functional study in PVCs (Chapter 4), it was anticipated that many cellular changes would be apparent in an ageing phenotype. In particular, it was considered plausible that the following aspects of NRVMs would be altered.

(1) Ca^{2+} homeostasis:

- The frequency of spontaneous Ca^{2+} signals would *increase.*
- The percentage of cells that successfully follow pacing with EFS would *decrease*.
- The SR Ca^{2+} content and the rate of SR Ca^{2+} re-uptake would be affected.

(2) Mitochondria will show functional changes.

(3) ROS production (basal and inducible) would be *increased*.

(4) Autophagy would be *decreased.*

(5) Structural changes:

- Appearance of cellular ageing markers (e.g. lipofuscin) would be *increased.*
- The number and size of mitochondria would be *changed (although unclear whether increased or decreased).*

5.2. Aims of the Chapter

The work presented in this Chapter compared Ca^{2+} signalling, mitochondrial function, ROS production, autophagy and structural changes in control and HU-treated NRVMs. The principal aims were to characterise the physiological effects of HU-treatment, and compare them to features seen in naturally aged animals. The specific aims were:

(1) Characterise Ca^{2+} homeostasis in control and HU-treated cells. In particular, the following aspects were investigated:

- Frequency of spontaneous Ca^{2+} signals
- Percentage of cells that successfully followed pacing with 2 Hz EFS
- SR Ca^{2+} content and the rate of SR Ca^{2+} re-uptake

(2) Compare the mitochondrial membrane potential in control and HU-treated cells.

(3) Examine the basal and inducible ROS production in control and HU-treated cells.

(4) Characterise autophagy and autophagic flux in control and HU-treated cells.

(5) Investigate structural changes in control and HU-treated cells, with special attention to the:

- Appearance of cellular ageing markers (e.g. lipofuscin)
- Number and size of mitochondria

5.3. Changes in spontaneous Ca^{2+} signals and EFS-induced Ca^{2+} signals in HU-treated cells compared to control cells

The effects of HU treatment on Ca^{2+} homeostasis were analysed by studying the frequency of spontaneous Ca^{2+} signals, and the ability of NRVMs to follow pacing with 2 Hz EFS, in control and HU-treated cells. NRVMs were imaged on a widefield fluorescence microscope, as described in Chapter 4, Figures 4.6 – 4.9. Whereas line-scanning was largely used for studies of PVCs, as described in the previous Chapter, widefield imaging was sufficient to record Ca^{2+} signals in monolayers of NRVMs. To visualise Ca^{2+} signals, NRVMs were loaded with Cal-520 and imaged at 12 Hz, similar to the experiments shown in Chapter 4, Section 4.4.1, Time-lapse widefield videos of all cells in a field of view were collected. ROIs were placed within the individual NRVMs, and Ca^{2+} traces were obtained for each of the individual ROIs using ImageJ, as described in Chapter 2 (Figure 2.3). For this Chapter, spontaneous Ca^{2+} signals were not categorised into local Ca^{2+} transients and Ca^{2+} waves. Successful responses to EFS pacing were classified according to the timing of the responses relative to an EFS pulse, and the rate of rise of the Ca^{2+} signal. As shown in Chapter 4, Figure 4.2D, EFS-induced Ca^{2+} transients had a faster rate of rise than Ca^{2+} waves.

The experimental protocol used for these experiments is illustrated in Figure 5.1A. The imaging experiments lasted 30 seconds and were performed as follows:

1. 10 seconds recording of spontaneous activity (***pre*** **EFS**).
2. 10 seconds with 2 Hz EFS (**EFS**).
3. 10 seconds recording of spontaneous activity (***post*** **EFS**).

This protocol was repeated on days 1, 4 and 7 days following addition of either 50 or 500 µM HU to the NRVM growth medium. The first part of the recording, *pre* EFS, established the spontaneous Ca^{2+} signals activity in the cells prior to the application of EFS pacing. The second phase of the recording, during EFS, showed whether the HU-treatment of the cells affected their ability to follow electrical pacing, and the third and final part of the recording, post EFS, was used to assess whether the pacing affected the spontaneous Ca^{2+} signal activity in the cells. The frequency and amplitude of spontaneous Ca^{2+} signals (largely Ca^{2+} waves in the NRVMs), and the ability of the cells to follow EFS pacing were analysed by comparing these values between the different treatments, and on the different days post HU addition.

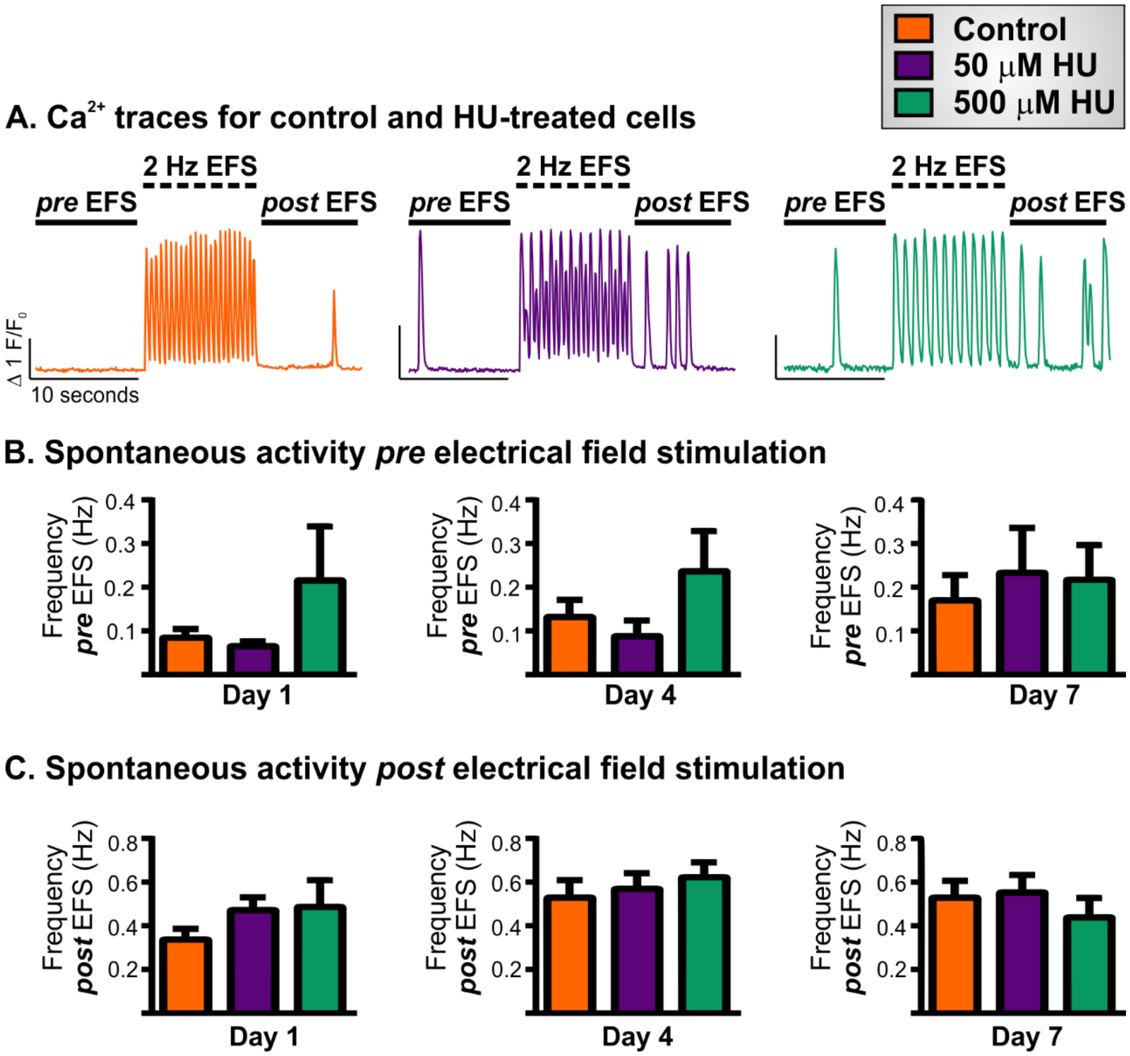

Figure 5.1. Spontaneous Ca^{2+} signals and EFS-induced Ca^{2+} signals in HU-treated NRVMs.

Panel **A** illustrates the imaging and EFS stimulation protocol used, and shows representative Ca^{2+} traces obtained from control NRVMs, and cells incubated with 50 or 500 µM HU for 4 days. Panel **B** quantifies the average frequency of spontaneous Ca^{2+} signals *pre* EFS for cells incubated with 0, 50 or 500 µM HU for 1, 4 or 7 days. Panel **C** quantifies the average frequency of spontaneous Ca^{2+} signals *post* EFS for cells incubated with 0, 50 or 500 µM HU for 1, 4 or 7 days. The data are presented as mean ± S.E.M., and were analysed using one-way ANOVA. *n* = 9 coverslips from 3 litters per treatment.

The Ca^{2+} traces shown in Figure 5.1A were derived from representative NRVMs on day 4 of HU incubation, and illustrate the imaging protocol used. In all three conditions (0, 50 and 500 µM HU), NRVMs displayed a low frequency of spontaneous Ca^{2+} signals (typically <1 Hz). Similar to the results observed when applying EFS pulses to PVCs (Chapter 4, Section 4.5, Figures 4.13 – 4.14), NRVMs showed regular responses and alternans during EFS pacing. Contrary to the observations made using PVCs, irregular responses were never observed in NRVMs. The Reponses of NRVMs were therefore classified into two types:

1. **Regular responses.** Ca^{2+} transients during regular responses were elicited by every EFS pulse, and had similar pulse-to-pulse amplitudes.
2. **Alternans.** During alternans, cells also responded to every EFS pulse, but the amplitude of the Ca^{2+} transients alternated between large and small.

The control cells (orange trace on the left-hand side of Figure 5.1A) responded to 2 Hz EFS with regular Ca^{2+} transients. In contrast, the representative NRVM treated with 50 µM HU showed alternans (purple trace in the middle of Figure 5.1A). The representative NRVM treated with 500 µM HU only responded to every other EFS pulse (green trace on the right- hand side of Figure 5.1A). The frequency of spontaneous Ca^{2+} signals appeared to be lowest in control cells, greatest in NRVMs treated with 500 µM HU, and the frequency generally increased with duration of HU incubation (Figure 5.1B and C), but these differences are not statistically significant.

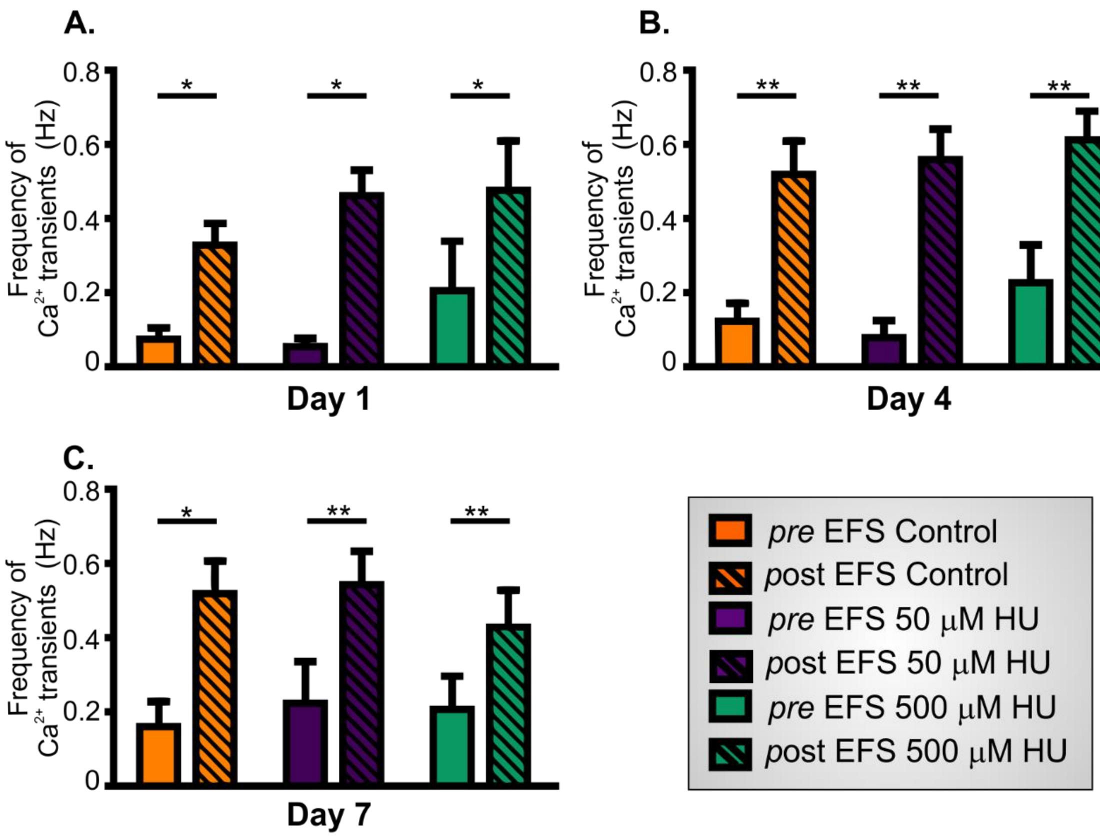

Figure 5.2. Frequency of spontaneous Ca^{2+} signals before and after application of 2 Hz EFS in HU-treated NRVMs. Panel **A** shows the frequency of spontaneous Ca^{2+} signals pre and post 2 Hz EFS on day 1 in control and HU-treated NRVMs. Panels **B** and **C** show the frequencies of spontaneous Ca^{2+} signals pre and post 2 Hz EFS on days 4 and 7. The data are presented as mean ± S.E.M., and were analysed using paired *t*-tests. * and ** denote $P < 0.05$ and $P < 0.01$, respectively. *n* = 9 coverslips from 3 litters.

A direct comparison of the spontaneous activity in the three treatments *pre*- and *post* EFS showed that the frequency of spontaneous Ca^{2+} signals increased following application of 2 Hz EFS (Figure 5.2). This effect was independent of the duration of NRVM incubation with HU. The responses of control and HU-treated cells to 2 Hz EFS were classified into regular pacing or alternans, as shown in Figure 5.3.

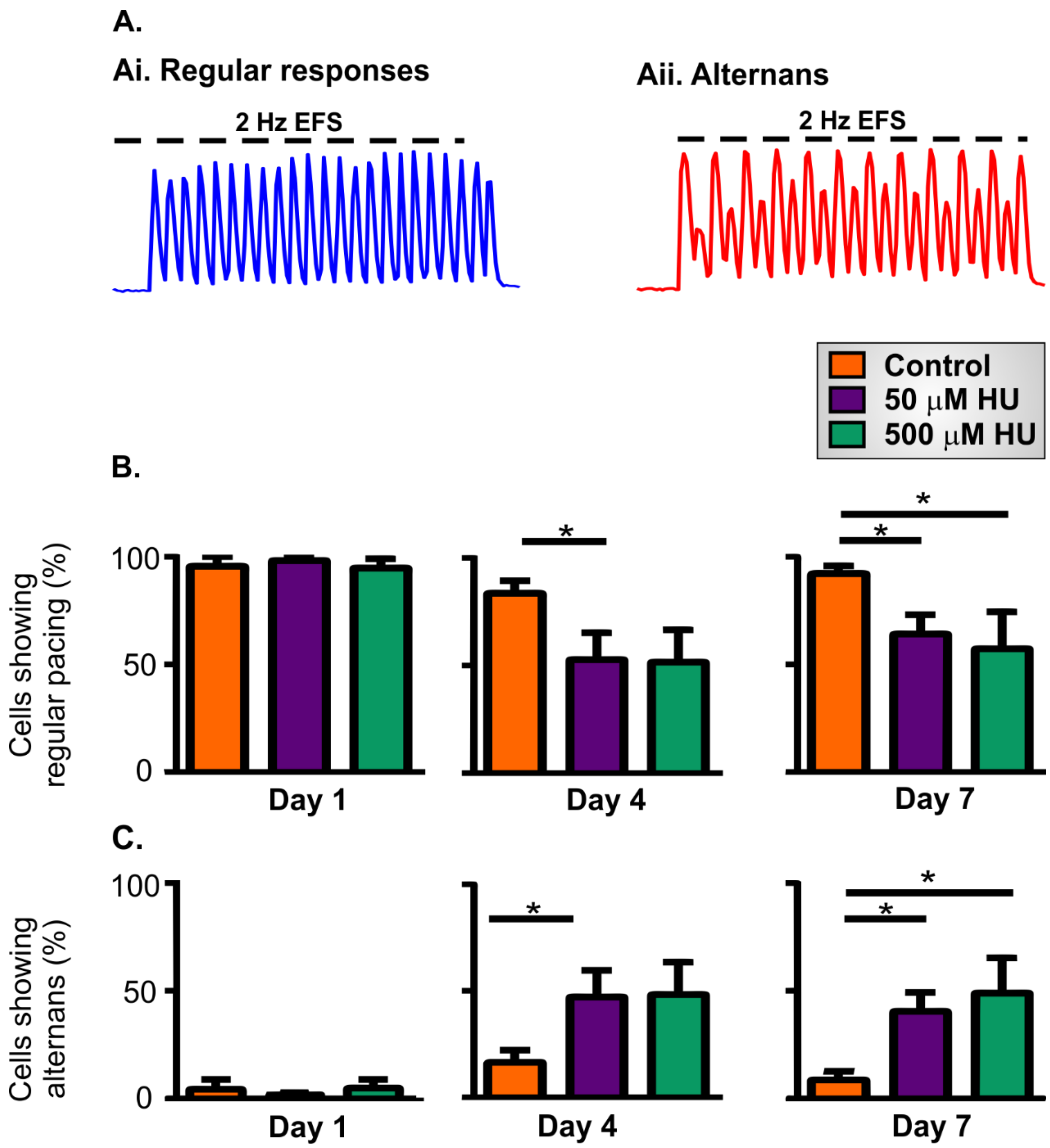

Figure 5.3. EFS elicited either regular responses or alternans in HU-treated NRVMs.

Panel **A** illustrates regular responses during EFS application **(Ai)** and alternans **(Aii)**. Panel **B** shows the percentage of NRVMs that displayed regular responses to EFS on different days of incubation with HU. Panel **C** illustrates the percentage of NRVMs that responded to EFs with alternans. The data are presented as mean ± S.E.M., and were analysed using one-way ANOVA. * denotes $P < 0.05$. *n* = 9 coverslips from 3 litters.

Almost all NRVMS, whether HU-treated or control, showed regular pacing when applying 2 Hz EFS on day 1 (Figure 5.3B). The majority of control cells continued to show regular responses to EFS pacing on days 4 and 7 (Figure 5.3B). In contrast, the number of HU-treated NRVMs that showed regular responses to EFS pulses was reduced on days 4 and 7 of HU incubation (Figure 5.3B).

On day 1, neither control nor HU-treated cells showed an abundant occurrence of alternans (<5 % of cells, Figure 5.3C). Moreover, under control conditions, few cells showed alternans on days 4 or 7. In contrast, the occurrence of alternans increased by day 4 in NRVMs treated with 50 µM HU, and on day 7 cells significantly more cells treated with 50 or 500 µM HU responded to EFS with alternans (Figure 5.3C). The observation that changes in the responses of NRVMs to EFS were not evident following 1 day of incubation with HU suggested that these effects were not due to an acute action of the reagent, but rather that they appeared as a consequence of cellular remodelling over time.

5.4. Comparison of SR Ca^{2+} uptake and Ca^{2+} content in control and HU-treated NRVMs

The decreased ability of NRVMs to follow EFS in HU-treated NRVMs pointed to a change in either Ca^{2+} homeostasis or the expression of proteins involved in EC-coupling. One possible reason for dysregulated Ca^{2+} homeostasis in cardiac myocytes would be a change in the SR Ca^{2+} concentration (Trafford *et al*., 2000), for example caused by alterations in activity of the SERCA2a Ca^{2+} ATPase. To test whether this occurred in HU-treated NRVMs, the rate of SR Ca^{2+} uptake in control and HU-treated cells was measured.

For these experiments, the SR Ca^{2+} store was emptied with caffeine, and the characteristics of the caffeine-induced Ca^{2+} transient were assessed. The imaging experiment lasted 120 seconds and was performed by continuously recording the following three parts as follows:

1. 20 seconds recording of the spontaneous activity.
2. 30 seconds superfusion with Ca^{2+} free imaging buffer containing the Ca^{2+} chelator EGTA (500 µM).
3. 30 seconds superfusion with 1 mM caffeine.

During the first part of the recording, the basal Ca^{2+} concentration and spontaneous Ca^{2+} signalling within the cells were measured, thereby establishing that the cells were viable and showed typical Ca^{2+} signalling. During the second part of the recording, lasting 30 seconds, extracellular Ca^{2+} was removed, thereby ensuring that only Ca^{2+} release from the SR was measured in the last part of the recording, and also causing the spontaneous Ca^{2+} signals in the NRVMs to cease. During the third and final part of the recording, caffeine was added to the cells for 30 seconds. At the concentration used (1 mM), caffeine added in phase 3 of the recording caused a rapid increase of cytosolic Ca^{2+} concentration due to activation of RyRs on the SR (Figure 5.4A). As expected, the caffeine-induced increase in cytosolic Ca^{2+} concentration was transient. The Ca^{2+} removal was due to the action of various Ca^{2+} transport processes, including export of Ca^{2+} across the sarcolemma by NCX and plasma membrane Ca^{2+} ATPases, and Ca^{2+} uptake into mitochondria. The parameters analysed for the caffeine-induced Ca^{2+} transient were illustrated in Figure 5.4B. The rate of Ca^{2+} clearance was characterised by fitting a one-phase exponential decay curve, and by measuring the transient duration at half-maximal amplitude (Figure 5.3B). In addition, the integrated caffeine-induced Ca^{2+} signal (hereafter denoted ‘area under the curve’; AUC) was used as an estimate for the total SR Ca^{2+} content (Díaz *et al.*, 1997; Greensmith *et al.*, 2014), and the maximal change in the peak amplitude for the Ca^{2+} release was calculated.

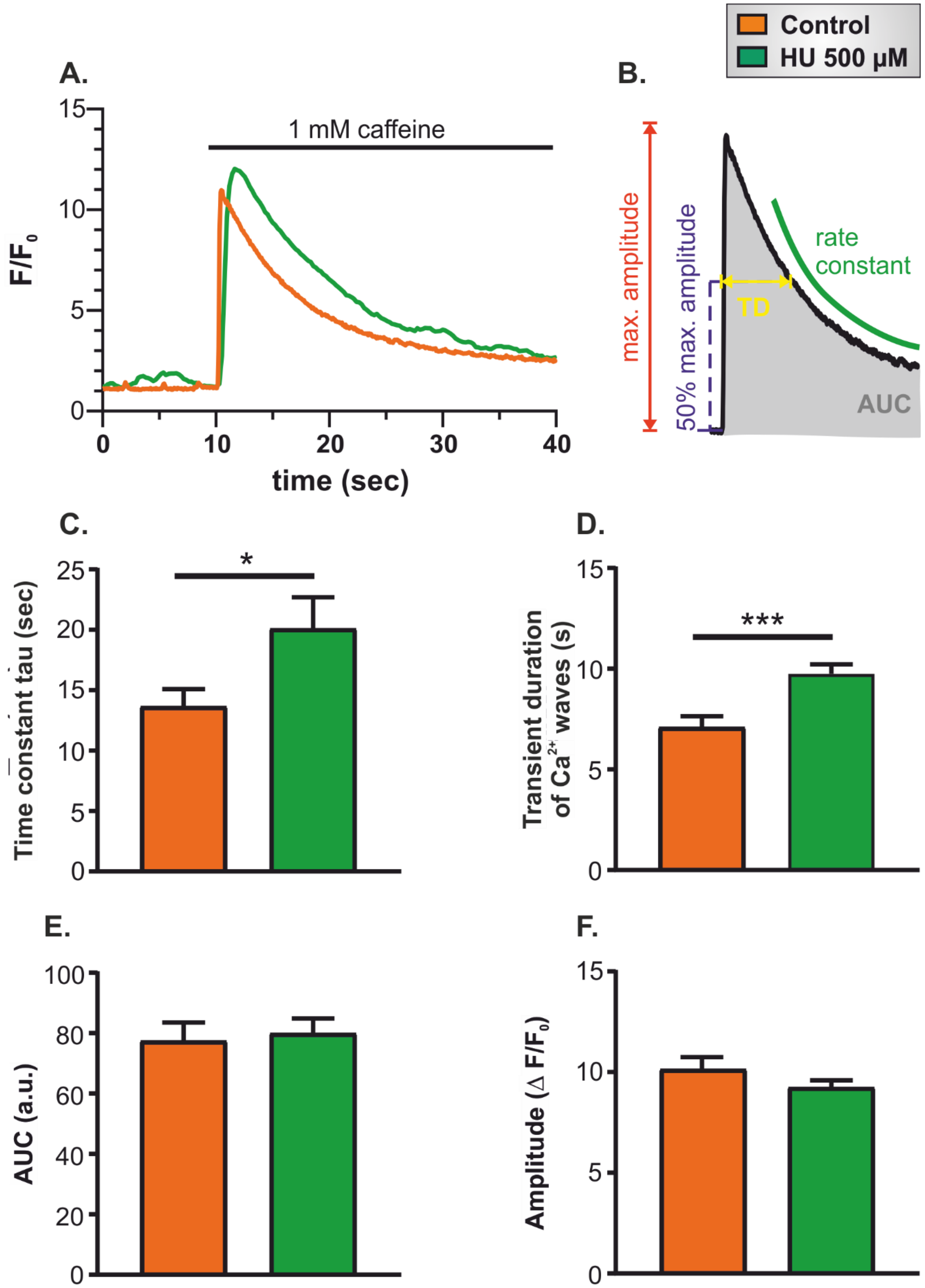
Control
HU 500 µM
A.
1 mM caffeine
F/F0
15
10
5
0
0
10
20
30
40
time (sec)
B.
max. amplitude
50% max. amplitude
TD
rate constant
AUC
C.
Time constant tau (sec)
25
20
15
10
5
0
*
D.
Transient duration of Ca2+ waves (s)
15
10
5
0
***
E.
AUC (a.u.)
100
80
60
40
20
0
F.
Amplitude (∆ F/F0)
15
10
5
0

Figure 5.4. Comparison of recovery of caffeine-induced Ca^{2+} transients and SR Ca^{2+} content in control and HU-treated NRVMs. Panel **A** shows representative caffeine-induced Ca^{2+} transients in control and HU-treated cells. Panel **B** illustrates the parameters quantified in order to characterise the caffeine-induced Ca^{2+} signals. TD denotes transient duration. Panel **C** shows quantification of the time constant, tau, derived from fitting mono-exponential decay curves to the caffeine-induced Ca^{2+} signals. Panel **D** shows quantification of the transient duration, measured as full-width at half-maximal amplitude. Panel **E** shows quantification of the AUC. Panel **F** indicates the maximum amplitude ($\Delta F/F_0$) of caffeine-induced Ca^{2+} transients in control and 500 µM HU-treated cells. The data present were all obtained on day 4 of HU incubation. The data are presented as mean ± S.E.M., and were analysed using unpaired *t*-tests. * and *** denote $P < 0.05$ and $P < 0.001$, respectively. $n = 7$ coverslips from 7 litters per group.

The transient duration (measured at 50 % of the maximum amplitude) and the time constant tau (Figure 5.4C and D) were both significantly increased in HU-treated NRVMs. These data indicate that the HU treatment slowed the rate of decay of the Ca^{2+} transient. In contrast, neither the AUC nor the maximum amplitude of the Ca^{2+} transient were different between control and HU-treated NRVMs (Figure 5.4E and F). The results observed here suggest that HU did not alter the SR Ca^{2+} content. Although this study found no change in the SR Ca^{2+} content, there might be still be alterations in either SERCA2a and/or NCX activity or in the Ca^{2+} leak from the SR. The fact that there were significant increases in the rate constant (5.4C) and transient duration (5.4D) in HU treated cells supported this further, but more studies are needed to establish whether SERCA2a and NCX activity are altered with HU treatment.

5.5. Assessing mitochondrial membrane potential in control and HU-treated NRVMs

To understand the mechanisms underlying the changes in Ca^{2+} signalling found in HU-treated NRVMs, experiments were performed to measure the mitochondrial membrane potential in control and HU-treated cells. The mitochondrial membrane potential was quantified using the ratiometric fluorescent indicator JC-10 (Kustiawan *et al.,* 2017, Wang *et al.,* 2016). This indicator emits green or red fluorescence during excitation with 488 nm. The colour of the emission depends on presence of monomeric or aggregated forms of JC-10 within the mitochondrial matrix. In normally respiring cells, JC-10 accumulates within mitochondria and forms aggregates that have a red fluorescence emission. An example of the accumulation of red-emitting JC-10 aggregates is shown in Figure 5.5Ai. The JC-10 aggregates are in equilibrium with JC-10 monomers, which have a green fluorescence emission. An example of the green emission from JC-10 monomers within the same cells is shown in Figure 5.5Bi.

Depolarisation of the mitochondrial membrane potential, for example using antimycin, causes the red-emitting JC-10 aggregates to dissipate into green-emitting JC-10 monomers. An example of the effects of 10 µM antimycin on the red and green emission profiles of JC-10 is depicted in Figure 5.5A and B. It is evident that addition of antimycin caused a rapid decrease in the red emission, whilst simultaneously increasing the intensity of the green emission. JC-10 can be used to monitor mitochondrial membrane potential by assessing either the red or green fluorescence emission (Figure 5.5Ci), or by calculating the ratio of red to green fluorescence (Figure 5.5 Cii). Note that whilst the green emission from JC-10 initially increases after dissociation of the red-emitting aggregates, prolonged depolarisation of the mitochondrial membrane potential leads to the eventual loss of green-emitting monomers too.

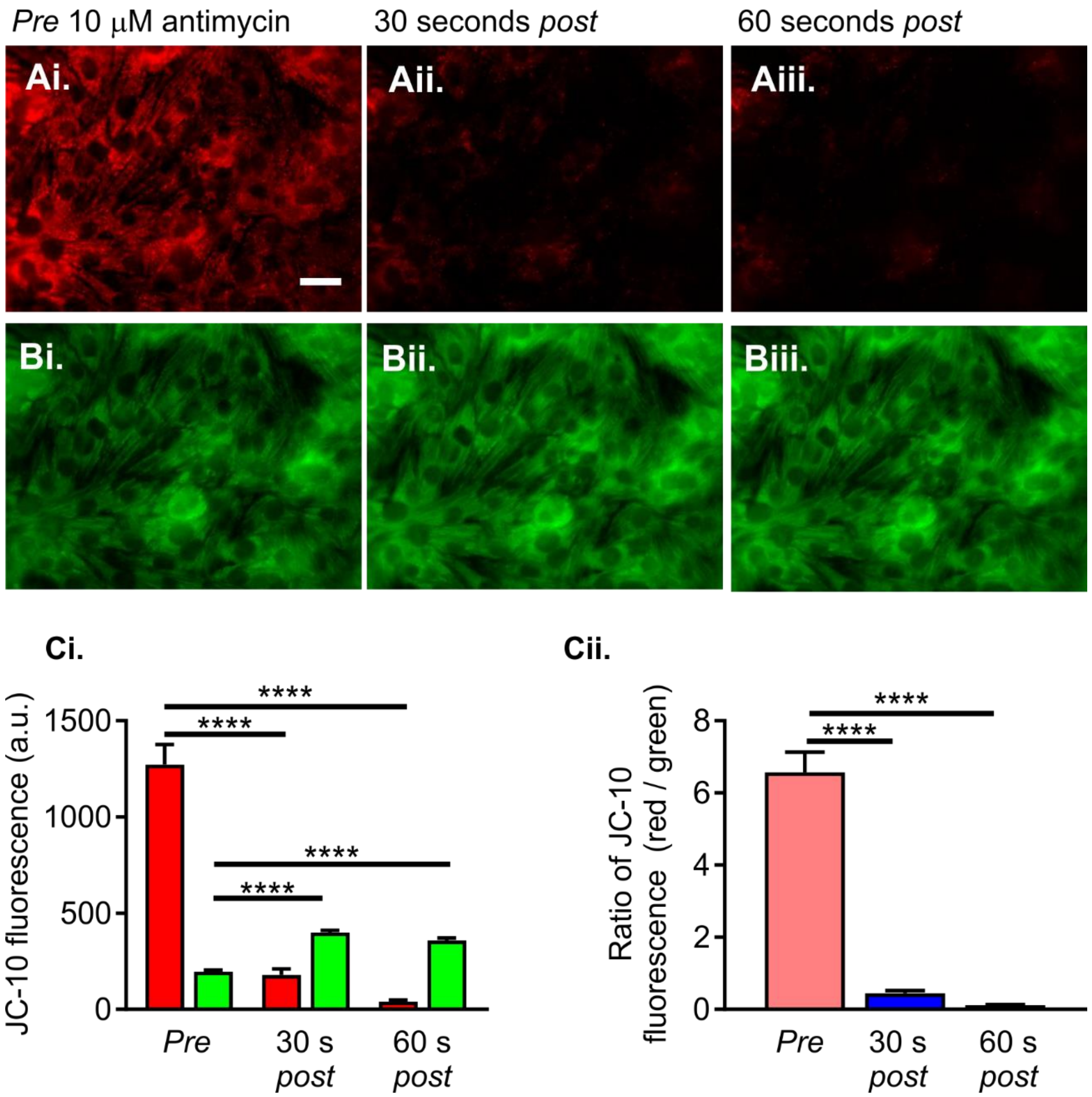

Figure 5.5. Using ratiometric fluorescent indicator JC-10 to determine mitochondrial membrane potential in NRVMs. Panels **A** shows the red fluorescence of JC-10 aggregates before **(Ai)** and after **(Aii and Aiii)** addition of 10 μM antimycin. Panel **B** shows the green fluorescence of JC-10 monomers before **(Bi)** and after **(Bii and iii)** addition of antimycin. Panel Ci illustrates the fluorescence (a.u.) of JC-10 monomers (green bars) and aggregates (red bars) before *(pre)* and after *(post)* addition of antimycin. The ratio of the red/green JC-10 fluorescence is presented in Panel **Cii**. The data presented as mean ± S.E.M., and were analysed using one-way ANOVA. **** denotes P < 0.0001. *n* = 16 cells from one litter. The scale bar represents 20 μm.

JC-10 was used to compare the mitochondrial membrane potential in control cells with that of NRVMs on days 1, 4 and 7 of incubation with 50 µM or 500 µM HU (Figure 5.6). For these experiments, cells were co-loaded with MitoTracker Red (> 650 nm emission to avoid overlap with JC-10) to control the correct mitochondrial localisation of JC-10. The MitoTracker fluorescence was used to focus on the cells to allow the regions to be chosen unbiased, and to avoid photo bleaching of the JC-10 fluorescence prior to the image acquisition. After focussing on the cells, images for the green and the red JC-10 fluorescence emission, and the MitoTracker fluorescence emission, were obtained.

The representative images in Figure 5.6A show NRVMs on day 7. Control cells displayed substantial green and red JC-10 fluorescence emission profiles (Figure 5.6A, top row). The correct mitochondrial localisation of JC-10 was confirmed by co-loading the cells with MitoTracker Red. In contrast, NRVMs incubated with HU showed almost no red JC-10 fluorescence emission, and a lesser green fluorescence (Figure 5.6A, middle and bottom rows). The MitoTracker Red labelling was also reduced.

In order to quantitate JC-10 fluorescence, 5 regions per coverslip were chosen by their MitoTracker Red staining, and the intensity of JC-10 green and red emission in those regions was recorded. Quantification of the JC-10 fluorescence indicated that incubation with either 50 µM or 500 µM HU caused a significant reduction in the JC-10 fluorescence.

Surprisingly, the JC-10 fluorescence was increased on day 1 for cells treated with HU (Figure 5.6Bi). On day 4 NRVMs treated with 500 showed a reduced JC-10 fluorescence, indicating the presence of more depolarised mitochondria (Figure 5.6Bii). This is even more evident on day 7 when both groups of HU-treated NRVMs showed a reduction in the JC-10 fluorescence (Figure 5.6Biii). Unexpectedly, the JC-10 fluorescence in control cells on day 7 was higher than that on day 4 and 1.

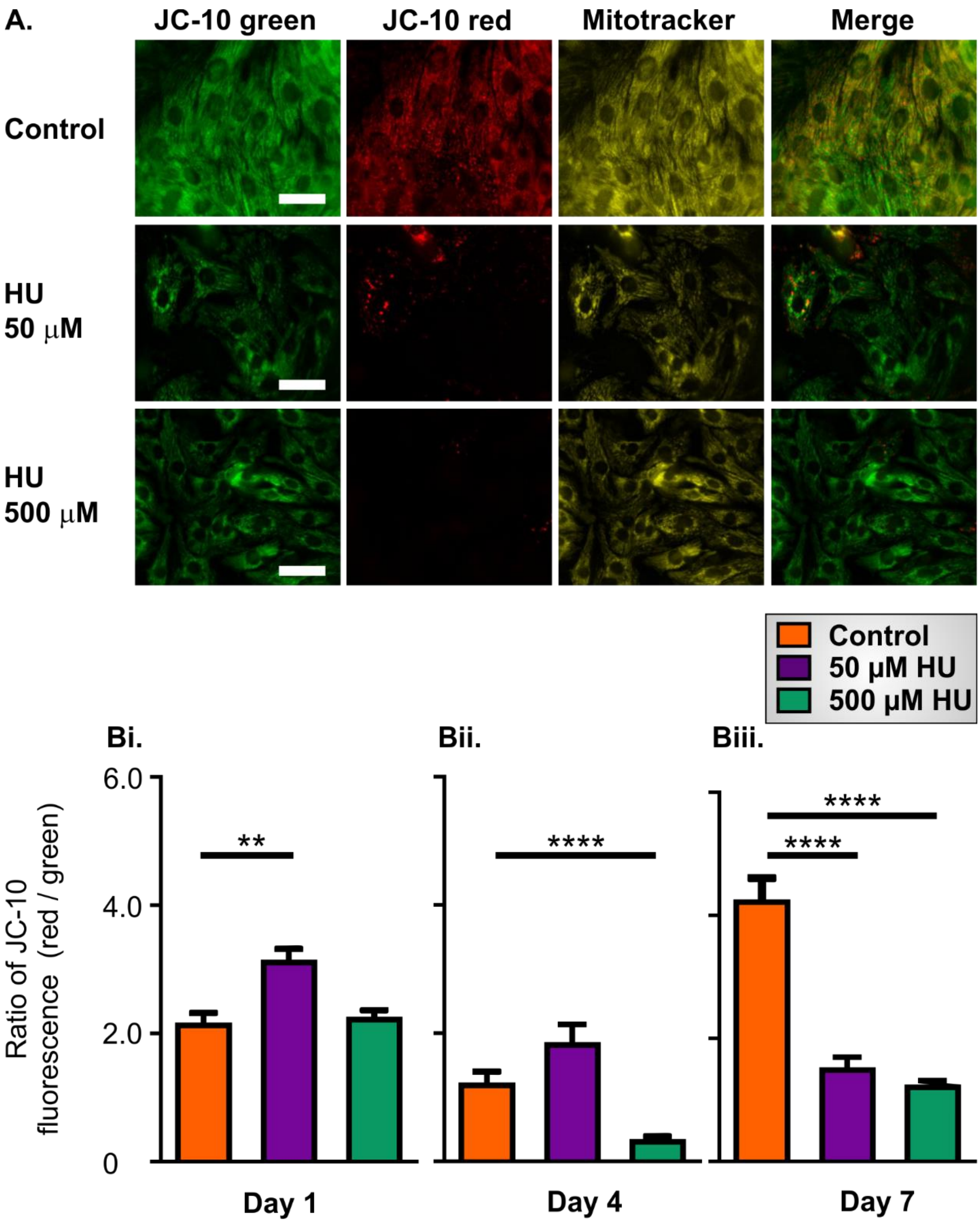

Figure 5.6. Assessment of the mitochondrial membrane potential in control and HU-treated NRVMs using JC-10. Panel **A** shows representative JC-10 and Mitotracker Red fluorescence images of NRVMs on day 7. MitoTracker Red was used to confirm that the JC-10 staining was localised in mitochondria. The scale bar represents 10 µm. Panels **Bi - Biii** summarise the data collected on days 1, 4 and 7. The red/green ratio changes in proportion with the mitochondrial membrane potential. The data are presented as mean ± S.E.M., and were analysed using one-way ANOVA. * denotes $P < 0.05$. *n* = 9 coverslips from 3 litters.

5.6. Measurement of basal and inducible ROS levels in control and HU-treated NRVMs

Basal ROS production was found to be significantly higher in PVCs from 24 month-old mice compared to cells from 3 month-old mice (Chapter 4, Section 4.7, Figure 4.22). Depolarised mitochondria have been shown to have an increased ROS production (Zhao *et al.,* 2013). To test whether the decrease in the mitochondrial membrane potential found in HU-treated cells was associated with a change in the cellular ROS production, control and HU-treated NRVMs were loaded with the fluorescent ROS indicator ROS Brite. Images of ROS Brite-loaded NRVMs were captured on a widefield fluorescence microscope. The experimental protocol for these experiments was:

1. 10-second recording of ROS Brite fluorescence within control or HU-treated NRVMs.
2. Addtion of 10 µM antimycin, followed by imaging of ROS Brite fluorescence for 120 seconds at 25 Hz.

The basal ROS levels were analysed by comparing the mean fluorescence in the first 5 images that were acquired. The inducible ROS production was analysed by calculating the mean ROS Brite fluorescence within control or HU-treated NRVMs at 10-second intervals. Control and 500 µM HU-treated NRVMs on day 4 after the treatment were chosen for this experiment, since 500 µM HU incubation for 4 days significantly altered mitochondrial membrane (Section 5.5, Figure 5.6Bii). NRVMs were co-loaded with MitoTracker Red to identify the cells (Figure 5.7Ai) since ROS Brite only showed a minimal fluorescence at the initiation of experiments (Figure 5.7Aii). The inducible ROS production was measured as illustrated in Figure 5.7B. After 10 seconds of collecting the baseline values, 10 µM antimycin was added and the inducible ROS production was measured over a 120 seconds period (Figure 5.7B). The ROS Brite fluorescence increased strongly after addition of 10 µM antimycin (Figure 5.7Aiii). The change in ROS Brite fluorescence was normalised to the starting level within each cell. Collapsing the mitochondrial membrane potential caused a greater increase in ROS Brite fluorescence in HU-treated NRVMs compared to the control cells. This difference was evident from 20 seconds after the antimycin addition until the end of the experiment when the ROS levels were still increasing (Figure 5.7B). Despite the increased capacity of HU-treated cells to produce ROS after antimycin application, the basal ROS levels at the start of the experiment were not different in control and HU-treated cells (Figure 5.7C).

These results suggested that HU treatment of NRVMs decreased their mitochondrial membrane potential, and increased the production of ROS when the mitochondria were further depolarised, but without altering the basal ROS levels within the cells. Both, the changes in mitochondrial membrane potential and the increased ROS levels can affect the cellular Ca^{2+} homeostasis (Cooper *et al.,* 2003, Niemann *et al.*, 2011; Guo *et al.*, 2013, Huang *et al.*, 2017).

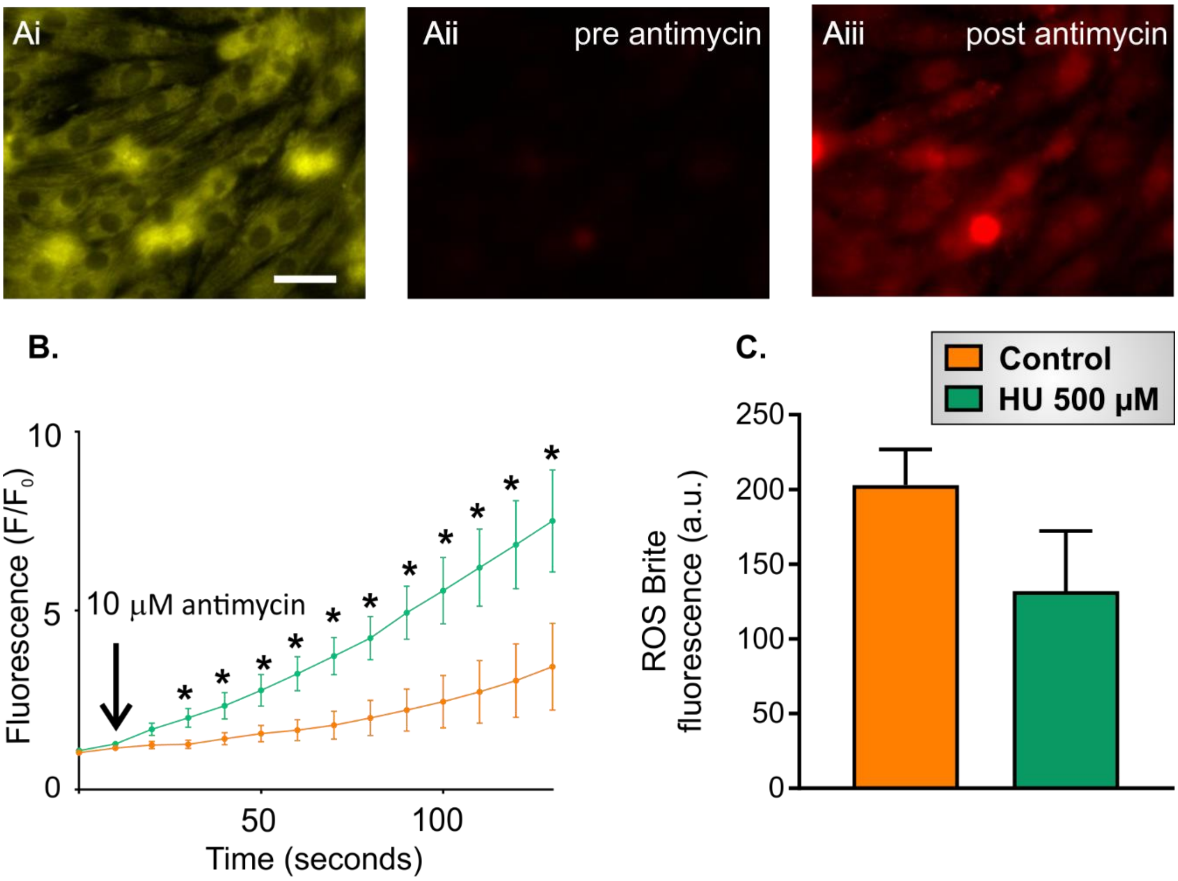

Figure 5.7. Basal and inducible ROS production in control and HU-treated NRVMs.

Panel **Ai** shows an image of NRVMs stained with MitoTracker Red. Panels **Aii** and **Aiii** show ROS Brite fluorescence in the same cells *pre* and 120 seconds *post* antimycin treatment, respectively. The scale bar represents 20 μm. Panel **B** shows changes in the ROS Brite fluorescence *pre* and *pos*t antimycin addition in control and 500 μM HU-treated cells on day 4 post HU treatment. The data presented as mean ± SEM., and were analysed using unpaired *t*-tests for the individual time points. Panel **C** compares the basal ROS levels in control and 500 μM HU-treated cells. The data are presented as mean ± S.E.M., and were analysed using an unpaired *t*-test. * denotes $P < 0.05$. *n* = 5 coverslips from 2 litters per group.

5.7. Effects of HU treatment on autophagy

Autophagy is a housekeeping process by which a cell recycles damaged and dysfunctional organelles and other molecules. In cardiac myocytes, increased autophagy was found in stressful conditions, but generally, the levels of autophagy were found to be reduced during ageing (De Meyer *et al*., 2010). A widely accepted method for quantifying basal autophagy is to count the number of autophagic vesicles in a cell after staining them with a fluorescent probe (e.g. CytoID kit, Enzo) (Klionsky *et al.*, 2007; Mauvezin *et al.*, 2014). Therefore, if HU treatment recapitulated an ageing phenotype a lesser number of autophagosomes would be expected in HU-treated cells compared to control cells (Shirakabe *et al*., 2016). To assess autophagy in the NRVMs, cells were loaded with the CytoID reagent for 30 minutes at 37°C degrees, and images were subsequently acquired using a widefield fluorescence microscope. For each coverslip, 5 - 10 regions were imaged and the mean number of autophagosomes per region was calculated.

After staining with the CytoID reagent, the autophagosomes within NRVMs were evident as green fluorescent vesicles (Figure 5.9A). The number of autophagosomes was similar in control and HU-treated cells on day 1 (Figure 5.8Bi). Independent of the treatment, the number of autophagosomes increased over time. However, the increase was more pronounced in the HU-treated cells (Figure 5.8Bii and Biii).

These results suggest that the HU treatment caused an induction of autophagy was not acute, but rather developed over time. The fact that the number of autophagosomes increased over time in control NRVMs was a sign that the conditions in which the cells were kept caused some stress to the cells, which was increased by HU.

A better measure for autophagy is to characterise autophagic flux by observing the effects of inhibiting autophagosome production using the PI3-kinase inhibitor 3-MA, and inhibiting autophagosome degradation using bafilomycin-A1 or chloroquine. However, these experiments were not achievable within this study. The preliminary results are presented in the context of future work in Chapter 6.

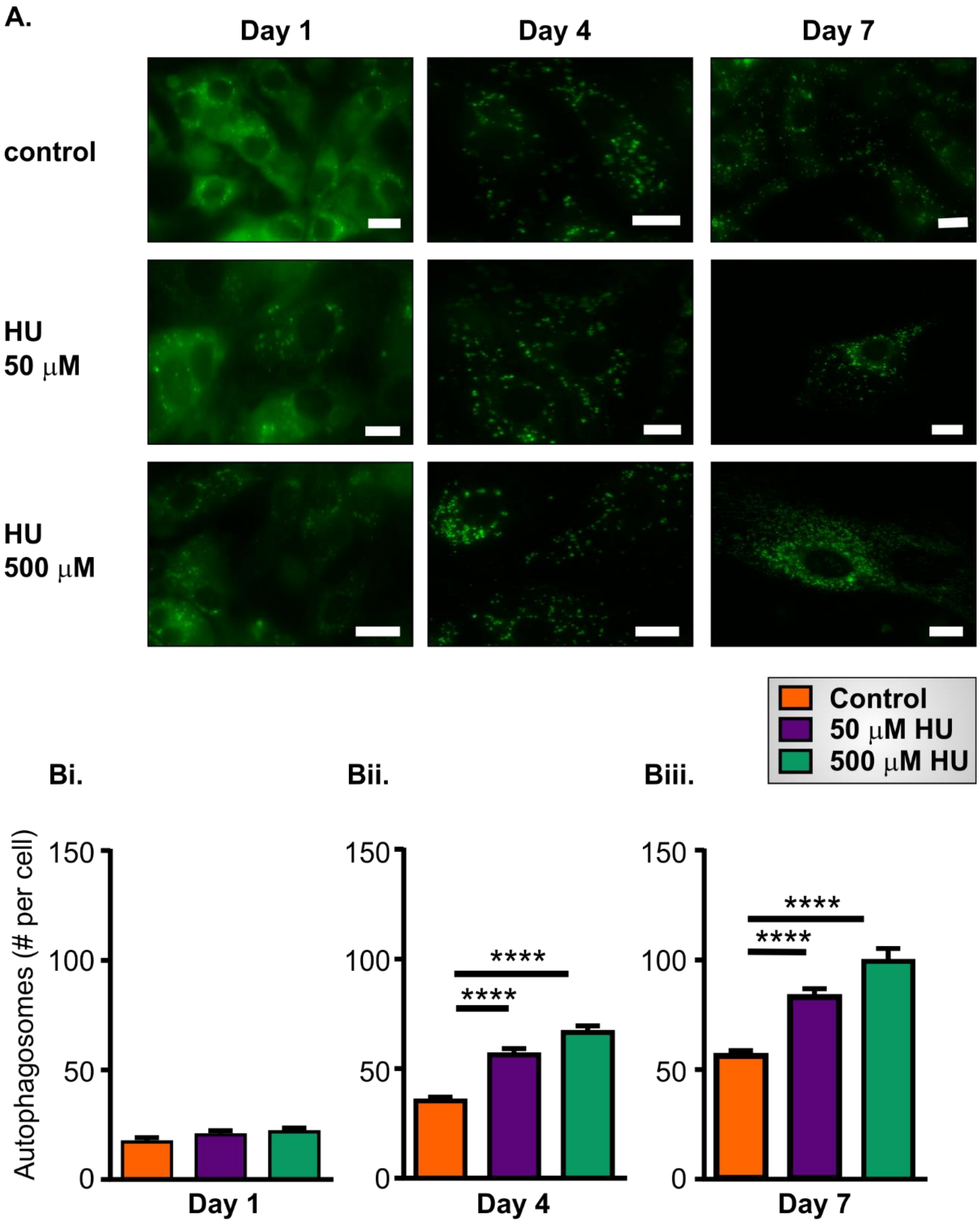

Figure 5.8. Effects of HU treatment on the level of autophagy in NRVMs. Panel **A** shows representative images of autophagosomes stained with the CytoID kit in control and HU-treated cells. The scale bar represents 10 μm. Panels **Bi - Biii** show quantitation of autophagosome numbers in control cells and HU-treated NRVMs on days 1, 4 and 7. The data are presented as mean ± S.E.M., and were analysed using one-way ANOVA. **** denotes P < 0.0001, respectively. *n* = 20 - 60 regions from 3 litters.

5.8. Structural changes in HU-treated compared to control NRVMs

Cardiac myocytes from old mice showed changes in their structure in TEM images (Chapter 3), with the organisation of their myofilaments and/or the number and size of mitochondria being different from those in young mice (Section 3.7.1, Figures 3.25 and 3.26, Tables 3.1-3.3). As this study was intended to establish a cellular model of cardiac ageing, it was of interest whether markers of cellular stress or ageing appeared in HU-treated cells. To investigate this, the structure of control cells and NRVMs treated with 500 µM HU for 7 days was compared using TEM. The day 7 time point was chosen as it was expected to show the biggest difference between the treatments.

TEM images of control NRVMs (Figure 5.9A-C) showed typical structures seen in cardiac myocytes: myofilaments with Z-lines (Figure 5.9A), abundant mitochondria in between the myofilaments (Figure 5.9A) and intercalated disks between the myocytes (Figure 5.9B). The myofilaments in NRVMs appeared less densely packed than in ventricular myocytes (Chapter 3.6.3, Figures 3.20 and 3.21), and were more comparable to those found in atrial myocytes (see Chapter 3.6.2, Figures 3.14 and 3.15) or PVCs (Chapter 3.6.1, Figures 3.10 and 3.11).

NRVMs treated with 500 µM HU for 7 days showed the same characteristic cardiac myocyte structure with myofilaments and intercalated discs (Figure 5.9D). However, they also contained structures that were less frequently seen in the untreated control cells (Figure 5.9E). In particular, there was an increase in the abundance of reticular membranes (plausibly ER or SR) decorated with ribosomes that were less evident in controls cells (Figure 5.9E and Figure 5.10D). These ribosome-associated reticular structures appeared around the sarcolemma and perinuclear area of the HU-treated NRVMs. In addition, HU-treated cells displayed autophagosomes and 'membranous cytoplasmic bodies', which are circular lipid aggregates linked to ganglioside accumulation in various lysosomal storage diseases (Ferreira and Gahl 2017 (Figure 5.9E).

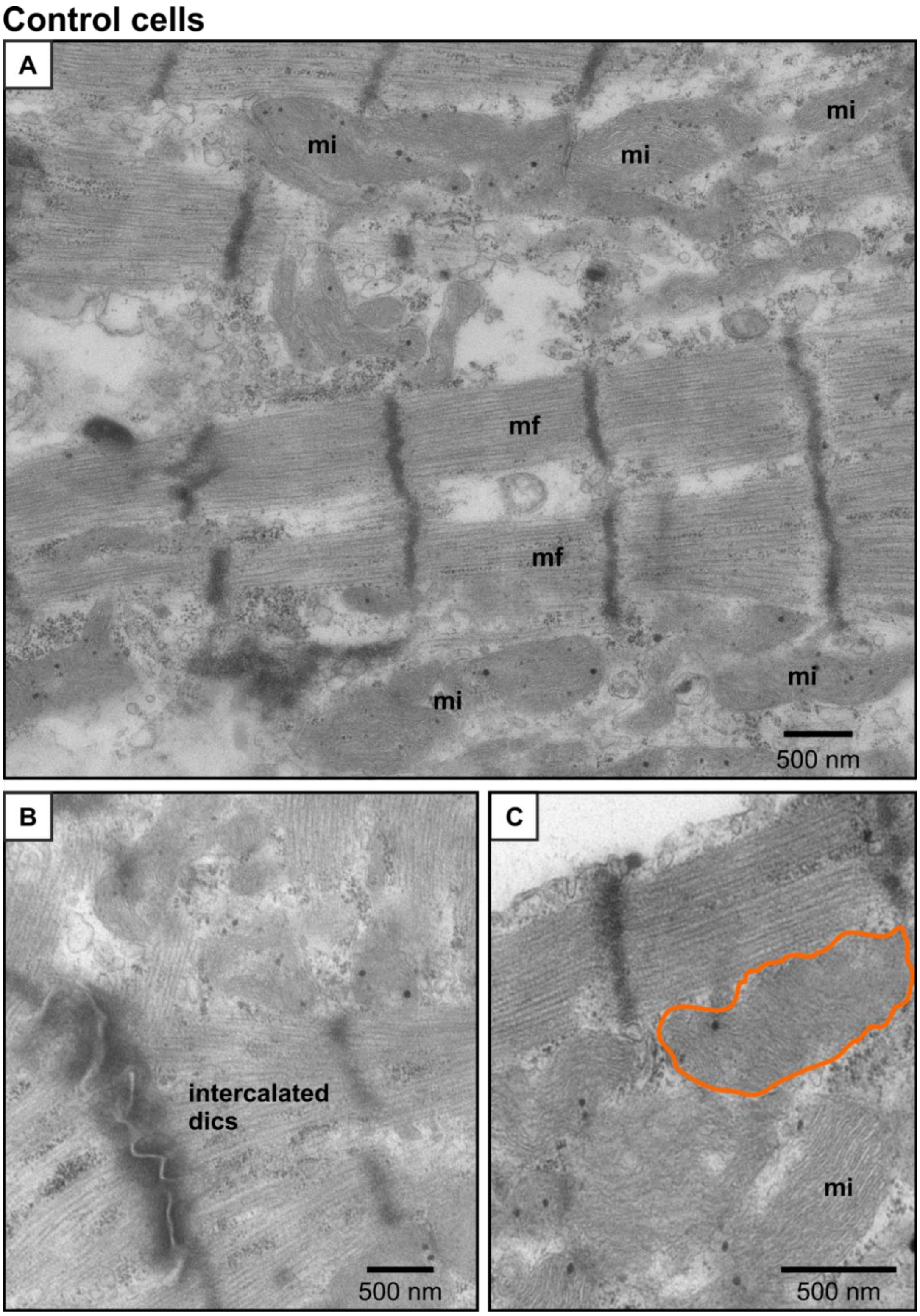

Figure 5.9. TEM images of control and HU-treated cells. Panels **A - C** show representative TEM images of control cells on day 7, illustrating the presence of myofilaments (mf), intercalated discs and mitochondria (mi) with preserved cristae (outlined in orange). Panels **D** and **E** are representative images from 500 µM HU-treated cells on day 7, showing the presence of mitochondria with disrupted cristae, outlined in green (Panel **D**), ribosome-associated reticular membranes (r-a RM), membranous cytoplasmic bodies (MCB) and autophagosomes (au) (Panel E).

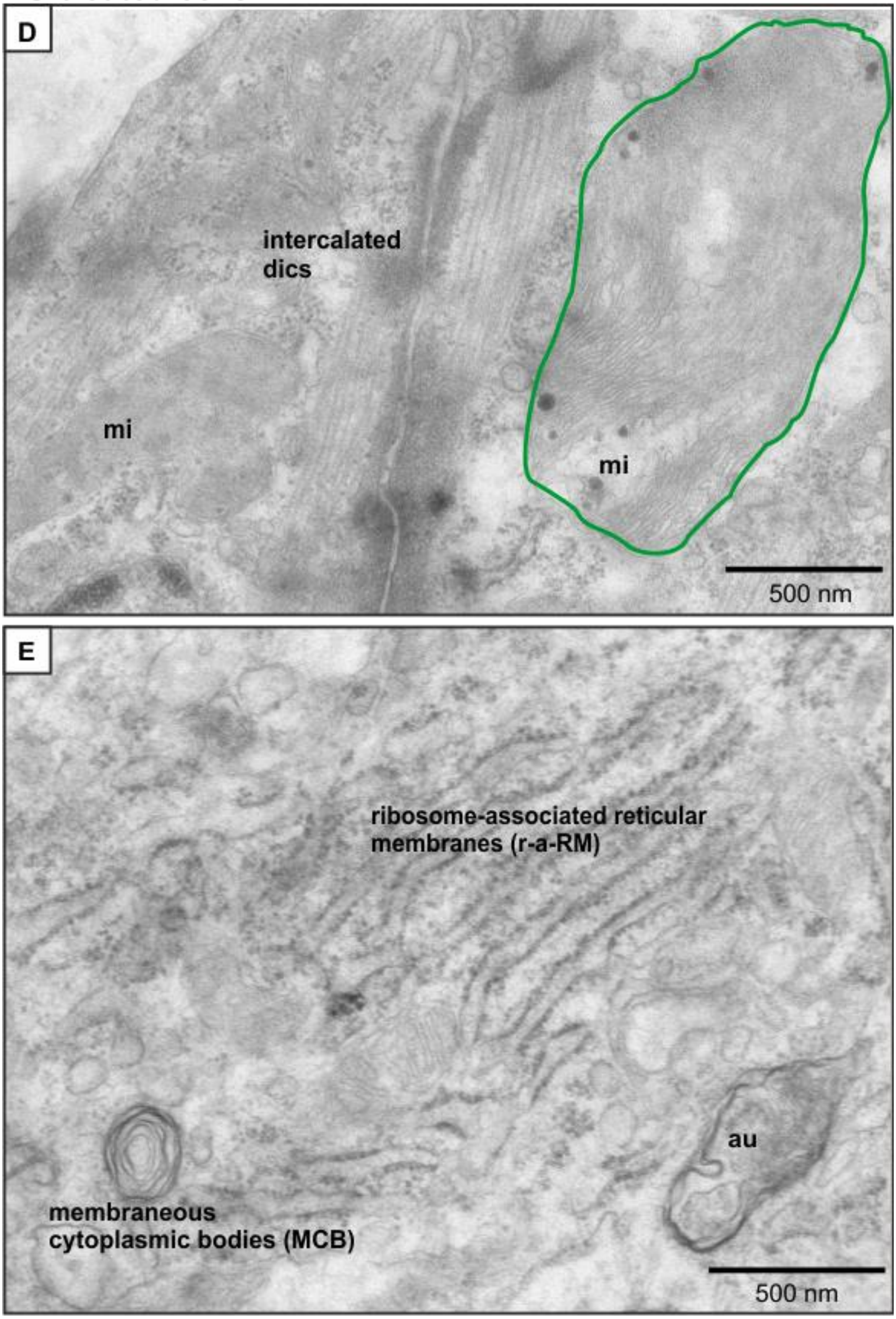

HU-treated cells

The increased appearance of autophagosomes in TEM images from HU-treated cells accord with the data presented in section 5.7 (Figure 5.9) that reported an increased number of autophagosomes found with live cell staining. In contrast to PVCs, atrial and ventricular myocytes from 24 month-old mice, no lipofuscin was seen in the HU-treated NRVMs.

The size of individual mitochondrial was not different following the HU treatment (Figure 5.9C and D, Figure 5.10A). The size of mitochondria was similar to that found in ventricular myocytes from 3 month- and 24 month-old animals, and to that in PVCs from 24 month-old animals (Chapter 3, Section 3.7.2 and Figure 3.26). HU treatment reduced the number of mitochondria found in NRVMs (Figure 5.10B).

NRVMs contained the smallest number of mitochondria: control NRVMs contained 8 ± 1 mitochondria per 50 μm^2, whilst the other cardiac myocytes from 3 month-old animals showed between 28.4 ± 1.8 (PVCs) and 43.8 ± 1.8 (atrial myocytes) per 50 μm^2 (see Chapter 3, Tables 3.1 – 3.3, in which the number is given per 25 μm^2).

One structural sign for damaged/dysfunctional mitochondria is a disruption of the cristae (Terman *et al.*, 2004a). An increase in the space in-between individual cristae in mitochondria was used to classify the mitochondria in 'intact cristae' or 'disrupted cristae', with a space of 100 nm cristae width as a threshold value. This analysis showed that HU treatment almost doubled the number of mitochondria that contained disrupted cristae (Figure 5.10C).

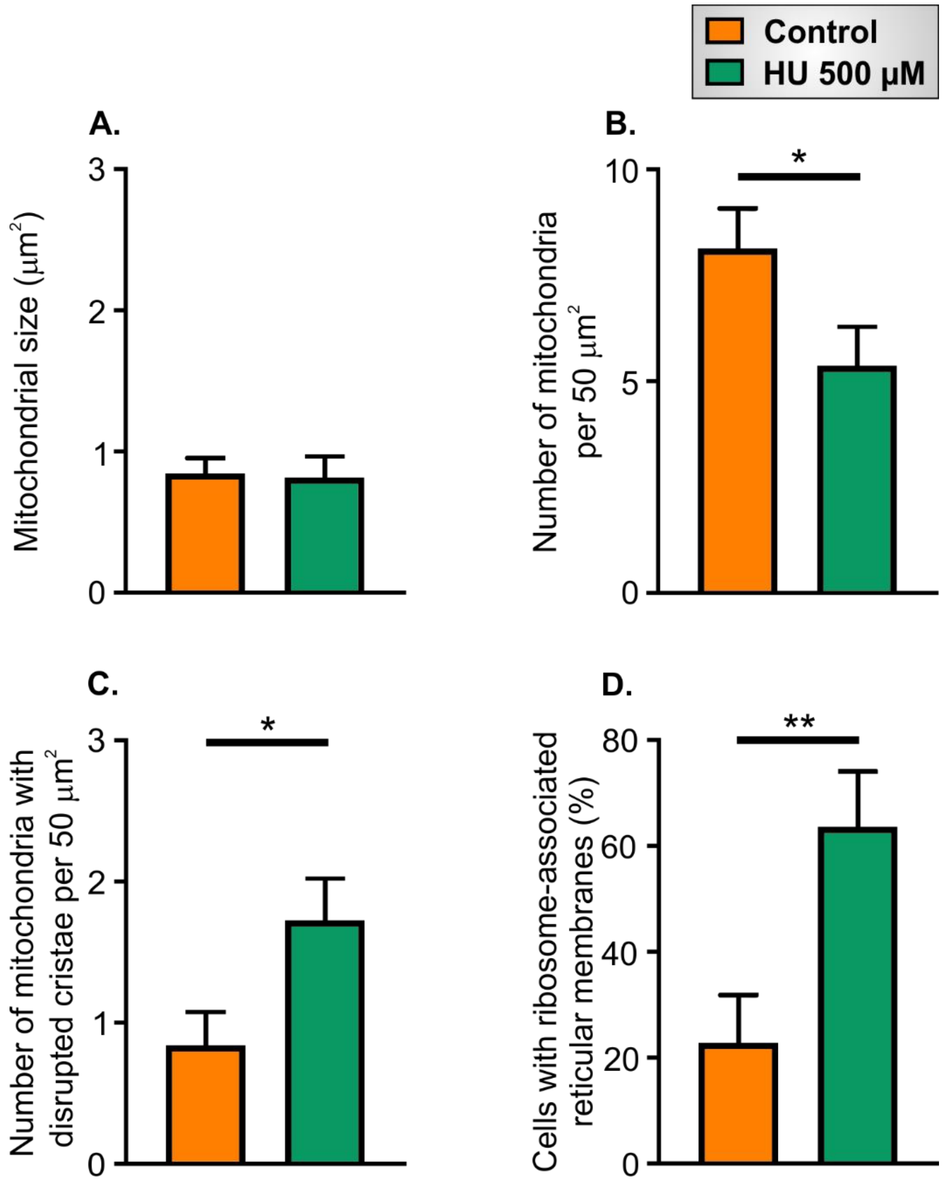

Figure 5.10. Quantification of the size and total number of mitochondria, and appearance of mitochondria with disrupted cristae, and the percentage of NRVMs containing ribosome-associated membranes in HU-treated NRVMs compared to control cells. Panel **A** shows mitochondrial size. Panel **B** shows mitochondrial number per 50 µm². Panel **C** shows the number of mitochondria with disrupted cristae per 50 µm². Panel **D** shows the percentage of NRVMs containing ribosome-associated membranes in control and HU-treated cells. The data are presented as mean ± S.E.M., and were analysed using unpaired *t*-tests. * and ** denote $P < 0.05$ and $P < 0.01$, respectively. *n* = 22 images from 2 litters.

5.10. Summary of the chapter

1. The frequency of spontaneous Ca^{2+} signals in NRVMs before or after application of EFS was not affected by HU treatment. Independent of the treatment, NRVMs showed a higher frequency of Ca^{2+} signals after a period of EFS application (section 5.3).

2. HU treatment decreased the percentage of NRVMs that show regular responses to EFS pulses, and increased the percentage of cells showing alternans over time (section 5.3).

3. The rate of decline of the cytosolic Ca^{2+} signal after addition of caffeine was decreased after HU treatment. The amount of Ca^{2+} in the SR, measured via the area under the curve for the caffeine release, and the maximum amplitude of the caffeine-induced Ca^{2+} transient, was not affected by HU treatment (section 5.4).

4. The mitochondrial membrane potential was measured using the fluorescent indicator JC-10. HU treatment of NRVMs caused mitochondrial depolarisation over time (section 5.5).

5. ROS levels were measured using the fluorescent indicator ROS Brite. ROS production was induced by depolarising mitochondria with 10 µM antimycin. Antimycin-inducible ROS production was increased in HU-treated cells (section 5.6).

6. Autophagy was not affected by HU treatment on day 1. Accumulation of autophagic vesicles increased over time of NRVMs being in culture, and was greater in HU-treated cells than in control cells (section 5.7).

7. An analysis of TEM images from control cells and NRVMs incubated with 500 µM HU for 7 days revealed an increased number of ribosome-associated reticular membranes after HU treatment. Membranous cytoplasmic bodies, presumably an accumulation of gangliosides, and autophagosomes were present in the HU-treated cells. Lipofuscin was not present in either control or HU-treated NRVMs (section 5.8)

8. The size of mitochondria, measured in TEM images, was not changed by HU treatment, and was similar to that in ventricular myocytes from 3 month- and 24 month-old mice (section 5.8).

9. HU treatment reduced the number of mitochondria in NRVMs. In comparison to the other types of cardiac myocytes, NRVMs contained less than half the number of mitochondria per 50 μm^2 (section 5.8).

10. An increased proportion of mitochondria with disrupted cristae was found in HU-treated NRVMs (section 5.8).

5.11. Discussion

5.11.1. Cellular Model of Cardiac Ageing

5.11.1.1. Why would a cellular model of cardiac ageing be useful?

Investigating ageing using longitudinal studies of 'naturally' aged animals or genetically modified progeroid mouse models requires a long lead-time, administrative work and is expensive. Working with isolated primary cardiac myocytes is quicker and more flexible. However, adult myocytes do not survive for long in culture and so cannot be used for longitudinal ageing studies. NRVMs will survive in culture for much longer than adult myocytes, but cells isolated from neonates are the opposite of an 'aged' cell.

Acute models of ageing have been used before to circumvent the issues with longitudinal studies. For example, mice models that show accelerated ageing induced by D-Galactose have been used to study neurological and behavioural effects of ageing (Wang *et al.*, 2009; Nam *et al.*, 2014) and the loss of muscle strength (Chang *et al.*, 2014), but their success depends on the exact conditions and age of the mice used for the treatment (Parameshwaran *et al.*, 2010). A so-called cellular model of ageing in which an ageing phenotype is induced by addition of HU was been established for neural stem cells (Dong *et al.*, 2014), but not for cardiac myocytes. Such a cellular model would allow the study of certain cellular aspects of ageing in cardiac in a more flexible manner.

5.11.1.2. How does chemical induction of ageing work?

HU is widely used in the treatment of sickle cell anaemia and as a tumour therapeutic agent. It exerts its effects by inhibiting DNA synthesis, increasing cellular ROS and causing growth arrest and senescence by inducing cell cycle inhibitors. These cellular effects of HU are believed to lead to a cellular phenotype similar to that observed in physiological ageing in animals or cells treated with HU (Krakoff *et al.,* 1968, Park, Jeong *et al.,* 2000).

5.11.1.3. How can a cellular model of cardiac ageing be validated?

To validate a cellular model of cardiac ageing it is important to show that the effects of the HU addition are mimicking those of natural ageing, and are not merely caused by cellular stress. The intention of this chapter was to compare the phenotype of HU-treated NRVMs with the structural (Chapter 3) and functional (Chapter 4) changes found in cardiac myocytes from old mice.

Based on the results from Chapters 3 and 4, the following changes were expected in NRVMs if the HU addition mimicked ageing as it was seen in 24 month-old mice:

- Increased frequency of spontaneous Ca^{2+} signals and occurrence of alternans
- Elevated basal ROS levels
- Diminished mitochondrial membrane potential
- Dysregulated autophagy
- Disrupted structure of myofilaments and mitochondrial changes

Additional measures would be necessary for a comprehensive validation of an ageing model, but characterising these parameters would suggest whether it is worth pursuing this goal in future studies. Figure 5.11 summarises the results from Chapter 5, and compares them with findings presents in Chapters 3 and 4.

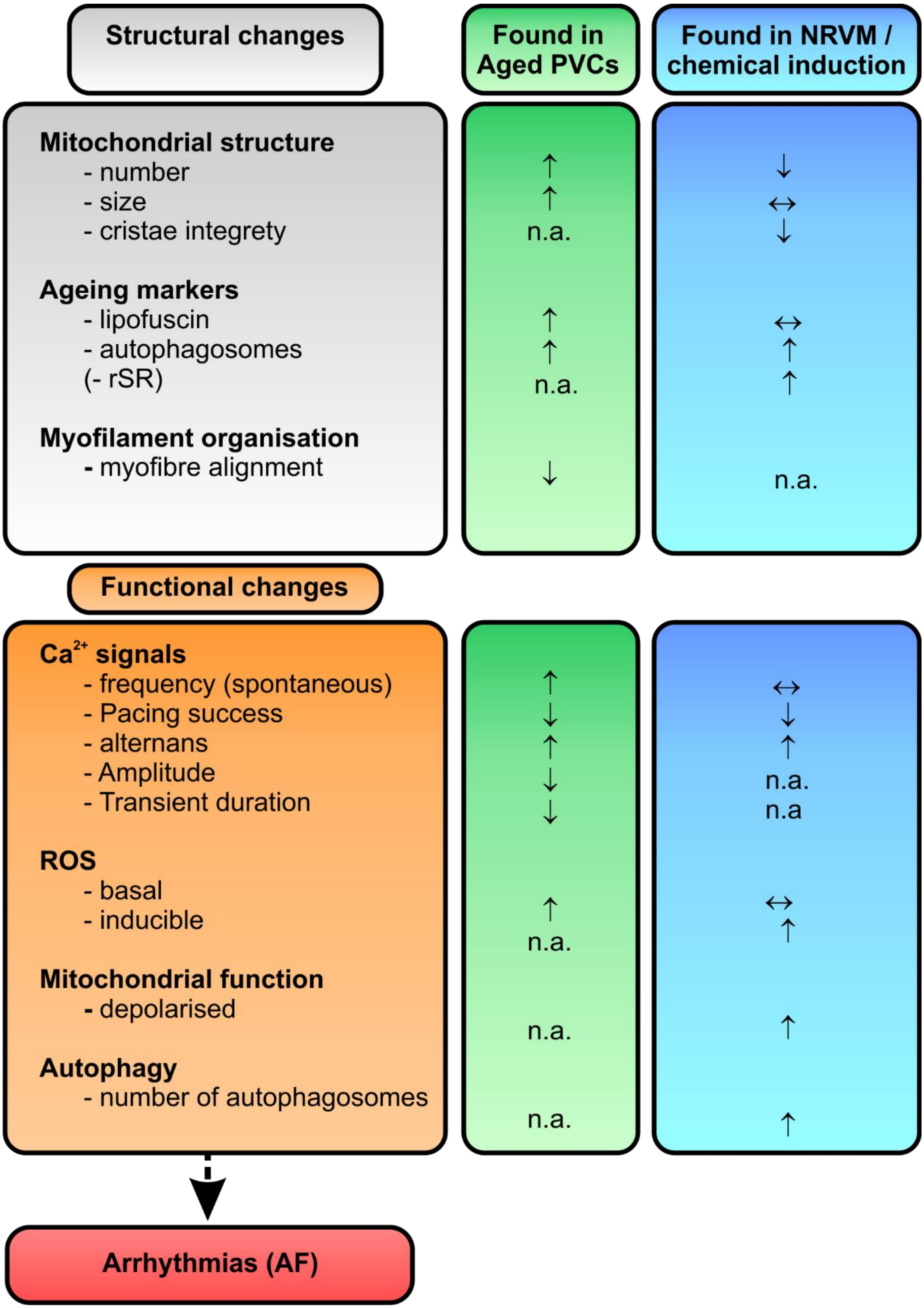

Structural changes	Found in Aged PVCs	Found in NRVM / chemical induction
Mitochondrial structure		
- number	↑	↓
- size	↑	↔
- cristae integrety	n.a.	↓
Ageing markers		
- lipofuscin	↑	↔
- autophagosomes	↑	↑
(- rSR)	n.a.	↑
Myofilament organisation		
- myofibre alignment	↓	n.a.
Functional changes		
Ca^{2+} signals		
- frequency (spontaneous)	↑	↔
- Pacing success	↓	↓
- alternans	↑	↑
- Amplitude	↓	n.a.
- Transient duration	↓	n.a
ROS		
- basal	↑	↔
- inducible	n.a.	↑
Mitochondrial function		
- depolarised	n.a.	↑
Autophagy		
- number of autophagosomes	n.a.	↑

Figure 5.11. Summary of the changes in naturally aged PVCs and in chemically induced NRVMs. Changes in the ultrastructure, Ca^{2+} handling and ROS during ageing resemble those found in HU-treated cells which may be caused by either cellular ageing or cellular stress. All of changes may actually be facilitating the occurrence of AF.

5.11.2. HU effects on Ca^{2+} homeostasis

5.11.2.1. Measurement of Ca^{2+} signals and EFS responses

ROIs were placed inside the cells and the changes in fluorescence over time in were analysed in ImageJ and plotted as Ca^{2+} traces.

The experimental paradigm was to measure the spontaneous activity for 10 seconds, then applies 2 Hz EFS for 10 seconds, followed by recording the spontaneous activity for another 10 second period.

Successful responses to EFS pulses were identified by the fast rate of rise of the Ca^{2+} transient, as it was explained in Section 4.3.1.1 (Figure 4.2). For each day and treatment, the responses to EFS were classified into two groups: percentage of cells showing regular responses and percentage of cells showing alternans. Irregular responses, as described for PVCs, were not seen in NRVMs.

5.11.2.2. Changes in the frequency of Ca^{2+} signals

NRVMs displayed a lower frequency of Ca^{2+} signals before EFS application than after the pacing period (Figure 5.2), independent of the HU treatment or number of days in culture. Before EFS application, NRVMs showed generally a lower frequency of Ca^{2+} signals than PVCs: ~ 0.1 Hz in NRVMs (Figures 5.1 and 5.2), and ~ 0.4 Hz in PVCs from 3 month-old animals (Chapter 4, Figures 4.7 and 4.14). However, following the EFS application, the frequency of Ca^{2+} signals in NRVMs increased and matched that seen in PVCs or was potentially higher (range between 0.3-0.6 Hz, Figure 5.2).

A possible explanation for the increased frequency of Ca^{2+} signals following the EFS application is that during the period of EFS responses, whilst the cells showed synchronous Ca^{2+} transients with a large amplitude, the content of the SR Ca^{2+} store was refilled, allowing for more frequent Ca^{2+} signals (Diaz e*t al.,* 2004).

5.11.2.3. Changes in the EFS responses in HU-treated NRVMs

Control cells responded to 2 HZ EFS with regular responses on days 1, 4 and 7. HU treatment reduced the percentage of cells that showed regular responses to pacing on day 4 and 7 after the HU addition (Figure 5.3). The cells not showing regular responses to the EFS responded with alternans; no irregular responses were observed. The fact that the occurrence of alternans was only significantly increased from day 4 onward indicated that the HU effects were not acute. A similar increase in alternans was seen in naturally aged PVCs, as discussed in Chapter 4 (Figures 4.9 and 4.10). Alternans were shown to be important for the development of arrhythmia (Kanaporis and Blatter, 2017). The occurrence of irregular pacing and alternans has been described in both, stressful conditions and during ageing (Narayan *et al.,* 2011; Cutler *et al.,* 2009; Narayan *et al.,* 2002), and thus do not allow the distinction of whether HU addition caused an ageing phenotype or merely cellular stress.

5.11.2.4. Changes in SR Ca^{2+} uptake and SR Ca^{2+} content in HU-treated NRVMs

The SR Ca^{2+} content was estimated by opening the RyRs on the SR with caffeine in the absence of extracellular Ca^{2+}. The maximum amplitude of the caffeine-induced Ca^{2+} transient and the AUC were not different between the control and 500 µM HU-treated cells (Figure 5.4E and F). At any given time, the SR Ca^{2+} content is affected by several parameters, e.g. the size of the SR, the rate of Ca^{2+} loss via leaky RyRs and the rate of Ca^{2+}

uptake via the SERCA2a activity. Therefore, the maximum amplitude and the AUC are only rough estimates of the SR Ca^{2+} content, but they indicate that HU-treatment did not strongly affect the SR Ca^{2+} content. More detailed experiments, outlined in Chapter 6 Section 6.2 'Future directions', would be needed to test for changes in the leakiness of RyRs or SERCA2a activity, as it has been described to occur in AF (Neef *et al.*, 2010, Hatch *et al.,* 2011, Herraiz-Martinez *et al.,* 2015). However, the rate of Ca^{2+} clearance was significantly longer in HU-treated cells (Figure 5.4C and D). The most important channel causing Ca^{2+} clearance in cardiac myocytes is the SERCA2a, estimated to remove 70 % - 90 % (Lipskaia *et al.,* 2010). The remaining Ca^{2+} is either removed over the sarcolemma via the NCX, PMCA, or taken up into mitochondria (Bassani *et al.,* 1994, Pieske *et al.,* 1999, Bers 2008, Lipskaia *et al.,* 2010). Further experiments are necessary to test which of these processes was affected by the HU-treatment, and to establish whether the SERCA2a activity might be affected by HU. Taking into account that HU-treated cells had a larger proportion of depolarised mitochondria (Figure 5.6), that had a disturbed structure (Figure 5.9D – cristae), it is likely that Ca^{2+} uptake into the mitochondria is reduced in the HU-treated cells. If this is the case, application of antimycin and oligomycin to depolarise the mitochondria as it is the case in HU-treated cells should mimic the HU-effects in control NRVMs.

However, changes in the level or activity of the NCX could also explain the quicker rate of Ca^{2+} clearance from the cytoplasm seen in control cells (Herraiz-Martinez *et al.,* 2015; Hatch *et al.,* 2011), and control experiments need to be performed to establish whether HU treatment affects the expression and/or activity of SERCA2a or the NCX.

5.11.3. HU induced changes in the mitochondrial membrane potential

Changes in the mitochondrial membrane potential were investigated using the fluorescent indicator JC-10. A significant decrease of the mitochondrial membrane potential was found on days 4 and 7 in HU-treated cells (Figure 5.6).

It had previously been shown that the mitochondrial membrane potential collapsed during ageing, calorific restrictions and p53-induced senescence (Pieri *et al.*, 1994; Sugrue *et al.*, 1999; Terman *et al.*, 2004a; Niemann *et al.*, 2011), which agrees with the results in HU-treated NRVMs. As a consequence, mitochondria cannot provide energy, in form of ATP, to the cell. Depolarised mitochondria also produce more ROS (Lin *et al.*, 2017).

5.11.4. Changes in basal and inducible ROS levels in NRVMs

The basal ROS levels in HU-treated NRVMs were not different to those in control cells when measured using the fluorescent ROS indicator ROS Brite (Figure 5.7C). After collapsing the mitochondrial membrane with antimycin, HU-treated NRVMs showed a higher (inducible) ROS production than the control cells (Figure 5.7B).

Both, ageing and stressful conditions have been shown to increase ROS levels as discussed before in Chapter 4 (Niemann *et al.,* 2011, Cooper *et al.,* 2013, Sag *et al.,* 2014, Tribulova *et al.,* 2015). In NRVMs, an age-dependent increase in lipofuscin granules and ROS levels coupled with a decrease in the mitochondrial membrane potential was found after keeping the cells in culture for up to 3 months (Terman *et al.*, 2004a; Terman *et al.*, 2005).

Cellular ROS can have many origins. Without further controls it is not possible to determine the cellular origin of the ROS measured here, but because the increase was measured acutely after the antimycin addition on the microscope stage, it likely originates from the mitochondria, but this will need to be proven in future experiments. HU itself was shown to lead to the production of hydroxyl radicals and hydrogen peroxide inside cells (Banh & Hales, 2013). It was therefore surprising that HU treatment did not affect the basal ROS levels, rather, it only induced a temporary increase in the ROS production by inducing NRVMs to produce ROS after antimycin addition. Again, these results indicate that over time, HU treatment induced either cellular stress or senescence in the NRVMs, but it was impossible to distinguish between the two.

5.11.5. Autophagy in HU-treated NRVMs

This study highlighted that autophagy, measured by counting autophagic vesicles, was increased whilst NRVMs were kept in culture, and that the level of autophagy was significantly higher in HU-treated cells compared to control cells on day 4 and 7 (Figure 5.9). Generally, studies have found that the level of autophagy in cardiac myocytes decreased with age. Increasing the rate of autophagy was found to alleviate the effects of ageing (Del Rosso *et al.,* 2003, De Meyer *et al.,* 2010, LaRocca *et al.,* 2012, Shirakabe *et al.*, 2016). In addition to ageing, long lasting external stress can also reduce autophagy and its cardioprotective effects (Nishida *et al.*, 2015), whilst cells tend to respond to short term stress with an upregulation of autophagy (Russell *et al.*, 2014).

Therefore, the increased basal autophagy found here is more likely a sign for stress than an ageing phenotype. However, the experiments presented in this thesis only measure the total number of autophagosomes at one point in time, whilst autophagy has to be assessed as a balance of the production and degradation of autophagosomes (i.e. 'autophagic flux'). All steps of the autophagic flux are impaired by ageing (De Meyer *et al.*, 2010). An increased number of autophagic vesicles could be explained if the rate of autophagosome degradation is slower than the rate of production, even if the overall level of autophagy in the cells is low. Attempts were made to characterise the autophagic flux (as illustrated in Chapter 1, Figure 1.8). The preliminary results are presented in Chapter 6 'Future Experiments'. However, the experiments have not yet been conclusive and need further optimisation. Therefore it is at this time impossible to comment on which part of the autophagic flux was affected by the HU treatment.

5.11.6. Structural changes in HU-treated NRVMs

To validate whether the HU treatment mimics processes occurring during physiological ageing, the structure of NRVMs was studied in TEM images. Particular attention was paid to changes of the mitochondria, after their number and size was changed when comparing TEM images of cardiac myocytes from young and old mice in Chapter 3. Only differences between control and 500 µM HU-treated NRVMs on day 7 on were studied in this part of the thesis.

5.11.6.1. Appearance of structures that indicate cellular stress and/or ageing in HU-treated NRVMs

The appearance of rough ER/SR indicates that HU-treated NRVMs might have a higher level of protein synthesis compared to the control cells. Protein synthesis and the number of ribosomes are usually reduced with increasing age in cardiac myocytes (Terman *et al.*, 2007), so the increased amount of rough SR could be a response to cellular stress (Han *et al.,* 2013, Antonucci *et al.,* 2015).

An upregulation of the level of autophagy was shown in HU-treated NRVMs using live-cell staining (Figure 5.8). This was confirmed by the more frequent appearance of autophagosomes in TEM images from the HU-treated cells compared to the control NRVMs. Autophagosomes were also more frequently seen in TEM images of the 24 month-old mice, but not frequent enough to be reliably quantified. The apparent contradiction that autophagy is declining with age (Del Rosso *et al.,* 2003, De Meyer *et al.,* 2010, LaRocca *et al.,* 2012, Shirakabe *et al.,* 2016), but autophagosomes are observed more frequently in TEM images could be due to the fact that these are actually dysfunctional autophagosomes accumulate during ageing, whilst smaller autophagosomes that are processed normally have not been seen in the images as we did not intend to quantify them. These dysfunctional autophagosomes are larger and more obvious in a TEM image, and contain material that can no longer be properly degraded, including lipofuscin (Terman *et al.*, 2007).

Another structure that was obvious in many images of the HU-treated NRVMs were membranous cytoplasmic bodies. These structures are most likely formed by ganglioside accumulations, and are a product of a defective lipid metabolism and a type of lipid storage product that is found in old cells and is a prominent marker in some lysosomal storage diseases (Ferreira and Gahl 2017). Like autophagosomes, membranous cytoplasmic bodies have also been observed in some TEM images of PVCs from 24 month-old mice. However, neither of them appeared frequently enough to be quantified in the study of physiologically aged mice (Chapter 3), or in this chapter.

None of the TEM images of control or HU-treated NRVMs showed the common ageing marker lipofuscin. Lipofuscin is an aggregation of non-degradable products that accumulate in the cell over time (Jung *et al.*, 2007). Even if HU treatment accelerated an ageing process, the experiments presented here might not be sufficiently long to allow the accumulation of lipofuscin. This highlights that not all phenotypes of ageing could be recapitulated in an accelerated model of ageing.

5.11.6.2. Changes in size and number of mitochondria in HU-treated NRVMs

HU-treated NRVMs showed a significant reduction in the number of mitochondria, but not change in their size. The different types of cardiac myocytes from adult mice showed different changes in the number and size of mitochondria: In PVCs, both, number and size of mitochondria were increased in, whilst atrial myocytes showed an increase in the size of mitochondria (Chapter 3, Table 3.1 and 3.2). The reduction in the number of mitochondria found in HU-treated NRVMs was therefore opposite to the changes observed in physiologically aged mice. The total number of mitochondria in control NRVMs appeared to be lower than that found in all three types of cardiac myocytes from adult mice. Control NRVMs contained ~ 8 mitochondria per 50 μm^2, whilst the myocytes from adult mice contained between 28 – 44 mitochondria in the same area (PVCs and atrial myocytes from 3 month-old animals, respectively).

As discussed in Chapter 3, previous studies reported variable alterations in the number and size of mitochondria, and within one disease opposing results can be found in different models, e.g. an increased mitochondrial size in atrial myocytes of a dog model of AF (Morillo *et al*., 1995) but a decreased mitochondrial size and increased mitochondrial number and in a goat model of AF (Ausma *et al*., 1997). Variable changes were also reported from other cardiac diseases, during ageing and in stressful conditions (Furuoka *et al.,* 2001, Gupta *et al.,* 2010).

This indicates that the number and size of mitochondria were not a reliable indicators whether the observed in NRVMs reflect ageing or merely a stress response.

5.11.6.3. Disruption of the mitochondrial cristae

The space between individual cristae, measured in the TEM images, was used as an indicator for intact or disrupted cristae. HU treatment increased the number of mitochondria that showed disrupted cristae. HU treatment also reduced the absolute number of mitochondria in the NRVMs. As a consequence, not only were fewer mitochondria present to deliver the ATP for the cell homeostasis in HU-treated NRVMs, but these also showed structural changes that are likely to lead to a dysfunction of the mitochondria. Previous studies have also reported disruption of cristae in aged animals compared to control ones. In some cases, mitochondrial cristae were found to be concentrated in some areas within the mitochondrion and absent from other areas (Feldman *et al.*, 1981; Terman *et al.*, 2004b, Gupta *et al.*, 2010).

5.11.7. Does HU treatment induce cellular stress or ageing?

As mentioned before, the main purpose of this chapter was to gain further understanding of the changes that are happening in cardiac myocytes after treatment with HU to scope whether this treatment can be used to establish a cellular model of cardiac ageing. If it were successful, a cellular model of ageing should be able to reduce animal use, reduce costs and administrative work, and it can be available in a matter of weeks rather than years.

Based on the comparison of cellular signalling in cardiac myocytes from 3 month- and 24 month-old mice, the following parameters were chosen to judge whether HU treatment caused changes similar to those seen in ageing:

Parameter	**Change observed with age in mice / *described in the literature***	**Observed change in chemically induced ageing**	**Criterion for ageing met**
Frequency of Ca^{2+} signals	Increased	Unchanged	No
Successful pacing	Decreased	Decreased	Yes
Occurrence of alternans	Increased	Increased	Yes
Mitochondria with collapsed membrane potential	Increased	Increased	Yes
Basal ROS levels	Increased	unchanged	No
Level of autophagy	*Decreased (literature)*	*Increased*	No
Appearance of structural markers of ageing (TEM)	Increased gangliosides and autophagosomes	Increased	Yes
Appearance of structural markers of ageing (TEM)	Increased lipofuscin	Absent	No
Mitochondrial size	Changed / more variable	Unchanged	No
Mitochondrial number	Changed / more variable	Reduced	Yes
Disrupted cristae in mitochondria	*Increased (literature)*	*Increased*	Yes

Table 5.1. Summary of the parameters studied in aged mice (Chapter 3 and 4), or if not investigated in mice, taken from the literature, and whether the changes in HU-treated NRVMs are similar or different to the expected changes.

Some of the observed changes, summarised in Table 5.1, are similar to those seen in aged mice, whilst others are different. One explanation for the results would be that HU induced cellular stress and NRVMs became weaker over time, as has been suggested for the ageing models (Park *et al.*, 2000; Yeo *et al.*, 2000; Narath *et al.*, 2007). To decipher whether HU treatment really caused an ageing phenotype, a characterisation beyond the cellular signalling parameters measured here is required. It would be of particular importance to focus on markers that are affected by ageing but not stress (or vice versa).

In conclusion, the data collected at this point do not distinguish between HU inducing cellular stress or an ageing phenotype. However, it could be argued that ageing causes cellular stress and vice versa, and therefore an ageing model will always show signs of increased cellular stress. Further work is required to determine whether or not it is worth pursuing chemically-induced ageing models such as that described here.

Chapter 6. General discussion

The heart is a muscular organ that beats continuously to pump blood and supply oxygen to the lungs and the rest of the body in mammals. To achieve this enormous task, the heart contains various cardiac myocytes that are structured in a highly ordered manner. In the heart, Ca^{2+} acts as a mediator between the electrical depolarisation of the cell and excitation-contraction coupling that results in contractions of the heart to pump the blood and ultimately blood flow. Therefore, maintenance of the heart's structure and Ca^{2+} homeostasis are crucial to allow its function. Sadly, during ageing or in disease states like in AF, structural and Ca^{2+} handling remodelling in cardiac myocytes appear that results in a deficient cardiac output (Lai *et al.,* 1999, Ausma *et al.,* 2002, Klein *et al.,* 2003, Van der Velden *et al.,* 2003, Boldt *et al.,* 2006, Sun *et al.,* 2008). It is now widely accepted that structural and functional remodelling in atrial myocytes and PVCs are some factors that facilitate AF (Ausma *et al.,* 1997, Thijssen *et al.,* 2000, Ausma *et al.,* 2001, Schotten *et al.,* 2003, Gaborit *et al.,* 2005). As ageing is a major risk factor for the development of AF, this thesis focused on the changes in the structural and Ca^{2+} homeostasis changes in PVCs during ageing, and how these changes can facilitate arrhythmias like AF.

6.1. Overview of chapters 3, 4 and 5

The work presented in Chapter 3 compared the changes in structure in PVCs, atrial and ventricular myocytes during ageing. The localisation of RyR2, Cx40 and Cx43 was compared in PVCs from 3 and 24 month-old mice and found a reduction of the Cx40 expression in old mice. Electrical coupling of cardiac myocytes is critical for a smooth signal propagation and alteration of the Cx40 expression levels and localisations have been reported to occur in AF (Chaldoupi *et al.,* 2009, Tribulova *et al.,* 2015). The most obvious structural changes in PVCs, atrial and ventricular myocytes from 3 and 24 month-old mice regarded the number and size of mitochondria, the organisation of the myofibres and the appearance of lipofuscin. Mitochondria are of importance for cardiac myocytes to deliver the energy for the constant contractions, and a reduced number or impaired function would seriously affect the ability of a cardiac myocytes to contract. Changes in number and/or size of mitochondria of PVCs and atrial myocytes from 24 month-old mice were found. Whether these result in an impaired mitochondrial function could only be tested for PVCs (Chapter 4). This thesis established a method to quantify the organisation of myofibres within a cardiac myocyte, and reported a better organisation in ventricular myocytes compared to atrial myocytes and PVCs. This could reflect that the main force to pump blood through the body and lungs is delivered by the ventricular myocytes. However, this organisation deteriorated and ventricular myocytes from 24 month-old mice had an organisation comparable to that in atrial myocytes and PVCs from 3 and 24 month-old mice, potentially explaining the reduced ability to pump blood found in hearts from aged animals (Mongensen *et al.,* 2017; Nanayakkara *et al.*, 2017). For all three cell types, there was a significant increase in the 'ageing pigment' lipofuscin during ageing.

To link the structural changes with alterations in Ca^{2+} homeostasis in PVCs during ageing, chapter 4 investigated changes in Ca^{2+} handling, contribution of mitochondria to the Ca^{2+} homeostasis and ROS production PVCs during ageing. Perhaps the most intriguing feature of murine PVCs is the occurrence of spontaneous Ca^{2+} transients both locally and globally, without an electrical input from the SA node cells. Therefore chapter 4 started by describing the features and channels involved in the development of spontaneous local Ca^{2+} transients and Ca^{2+} waves, and in the responses to EFS. Ageing of PVCs did not affect the speed, Ca^{2+} wave directions and the characteristics of initiation points. Activity of RyR2 is critical for all Ca^{2+} waves and EFS responses in PVCs from both age groups.

The Ca^{2+} waves from 3- and 24 month-old mice showed several differences: They occurred at a higher frequency in PVCs from 24 month-old mice, had reduced amplitude and a longer transient duration. Especially the combination of a higher frequency with a prolonged transient duration is likely to disrupt the ability of cardiac myocytes to respond to the next incoming AP (Hatch *et al.*, 2011, Rietdorf *et al.,* 2014, Herraiz-Martinez *et al.*, 2015, Rietdorf *et al.,* 2015) as the cells would still be in a refractory period. In general, PVCs from 24 month-old mice were less able to follow pacing with 1, 3 and 5 Hz EFS when compared to PVCs from 3 month-old mice. In an animal, this may facilitate the occurrence of irregular heartbeats and impair the cardiac output.

To investigate which components of the Ca^{2+} signalsome are causing the observed changes in the Ca^{2+} waves, a pharmacological study was performed, investigating the function of RyRs, NCX and SOCE. However, these did not show conclusive differences which channels cause the increased activity in PVCs from 24 month-old animals. In contrast, it highlighted the importance of the frequency of the spontaneous activity for the effectiveness of the drugs. Chapter 4 revealed that JTV-519 and carvedilol reduced the spontaneous activity in PVCs with ≥ 0.5 Hz basal activity regardless of the age group. As PVCs from 24 month-old mice had a higher proportion of PVCs with frequency of spontaneous activity ≥ 0.5 Hz, JTV and carvedilol were more potent on PVCs from 24 month-old mice. The increase in spontaneous Ca^{2+} signals in PVCs with age facilitates the occurrence of DADs and hinders their ability to follow electrical pacing (Hatch *et al.*, 2011, Rietdorf *et al.,* 2014, Herraiz-Martinez *et al.*, 2015, Rietdorf *et al.,* 2015). The average spontaneous activity reported herein is lower than the average spontaneous activity reported by Rietdorf *et al.,* 2014 which could be attributed to the differences in mouse strains used in the two studies.

Chapter 4 also demonstrated that basal ROS levels were significantly higher in PVCs from 24 month-old mice compared to 3 month-old ones. Reducing cellular ROS levels, e.g. by antioxidant treatment, is frequently discussed as a way to prevent typical ageing-induced changes (Yasuo *et al.*, 2006; Sun *et al.*, 2010), and indeed treating PVCs of both age groups with the ROS-scavenger Trolox significantly reduced the frequency of Ca^{2+} waves, which suggested that ROS may activate RyRs opening as previously suggested (Cooper *et al.*, 2013). It is unclear what the ROS source was, but one possibility would be dysfunctional mitochondria (Cooper *et al.,* 2003, Xi *et al.,* 2005, Yang *et al.,* 2006, Ni *et al.,* 2016).

After seeing an increased in number and size of mitochondria in PVCs in TEM images from 24 month-old mice (Chapter 3), the work in Chapter 4 examined whether this affected their function. An accumulation of defective mitochondria, often with an increased size and collapsed membrane potential, is typical for ageing (Feldman *et al.*, 1981; Gupta *et al.*, 2010) and ways of maintaining mitochondrial function are considered to prevent the development of cardiac dysfunctions (Graham *et al.,* 2009, Javadov *et al.,* 2009, Sun and Yang, 2017). For methodological reasons, was not possible to investigate whether there were differences in the mitochondrial membrane potential in PVCs from 3 and 24 month-old mice inside lung slices. However, it was possible to inhibit the mitochondrial function in both age groups by addition of a combination of anti- and oligomycin and study the effects on the Ca^{2+} signalling. This treatment significantly reduced the frequency of local Ca^{2+} transients, affected successful pacing and inhibited the amplitude of Ca^{2+} waves. These effects were more pronounced in PVCs from 3 month-old mice. This might indicate that the function of a proportion of mitochondria in PVCs from 24 month-old mice was already impaired so that a further inhibition had less of an impact. However, this theory would need further experimental proof before it could be accepted.

The work presented in Chapters 3 & 4 demonstrated changes in the structure and Ca^{2+} signalling during ageing that are similar to those reported as facilitating arrhythmias like in AF, and highlighting the importance of PVCs as a pro-arrhythmic cell type. However, as will be outlined in Section 6.2 'Future Directions', a more detailed study will be needed to deepen the understanding of the function of PVCs and help to identify potential new drug targets.

Performing the experiments that were presented in Chapter 3 and 4 highlighted some problems of working with naturally aged animals, namely the long delays between the availability of animals, and the problems if further experiments needed to be performed at the end of an experimental period. Because ageing is a very popular research topic, e.g. a PubMed search of 'cardiac ageing' limited to 2017 found 2164 publications, ways of accelerating ageing to study it in an easier manner have been developed. These are e.g. progeroid mouse models or models using chemical induction of ageing (see Chapter 1, Section 1.8). The work presented in Chapter 5 was aimed to provide evidence whether or not the addition of HU could cause an ageing phenotype in NRVMs, or whether possible phenotypic changes were only caused by cellular stress. For this, Ca^{2+} signalling, mitochondrial function, ROS production and structure of control and HU-treated NRVMs were characterised and compared to those found in Chapters 3 and 4 or the literature. Similar to the findings in naturally aged cardiac myocytes, the HU-treated cells showed a reduced ability to follow electrical pacing, an increased occurrence of alternans and more mitochondria with a collapsed membrane potential. All of these are pro-arrhythmic occurrences. Parameters that were not investigated in the PVC study, but were changed in HU-treated NRVMs included a higher proportion of dysfunctional mitochondria (indicated by a wider cristae width), increased inducible ROS production and an increase in the number of autophagosomes. Most of the parameters measured are affected in both, ageing and stress, making it difficult to distinguish between the two processes and validate the HU-treatment as a model of cellular ageing. Factors other than the cellular signalling processes investigated will have to be studied further to distinguish between the two. This could include markers for genetic instability, telomere attrition, epigenetic alterations like histone modifications or DNA methylation, loss of proteostasis (Lopez-Otin *et al.,* 2013). It was intended to study the protein expression levels of proteins that change more profoundly in senescence than with stress (p53, PARP and advanced glycation end products), but the analysis was not successful (see Section 6.2 'Future directions'). However, seeing that ageing is putting the cell in a stressful situation, a certain amount of overlap of both processes is to be expected.

In summary, the most significant results when comparing the natural and chemically-induced ageing were:

- Altered structure in both, naturally aged PVCs and chemically induced NRVMs. Both of these changes manifest during ageing as well as in cellular stress conditions that hinder the cardiac output.

- Pro-arrhythmic changes in the Ca^{2+} homeostasis were found in naturally aged PVCs and HU-treated NRVMs.

- Basal and inducible ROS production was increased in PVCs from 24 month-old mice and HU-treated NRVMs, respectively. These may affect Ca^{2+} homeostasis.

- Accumulation of structural ageing markers: lipofuscin in naturally aged PVCs; rSR, in HU-treated NRVMs; autophagosomes and gangliosides in both cell types.

- Changes in the number (PVCs), size (PVCs and HU-treated NRVMs) and cristae width (HU-treated NRVMs), which might disrupted the normal Ca^{2+} homeostasis.

6.2. Future directions

The data presented in this thesis demonstrate that changes in structure as well as Ca^{2+} signalling occur in PVCs during ageing. EM analysis carried out in Chapter 3 demonstrated poor mitochondrial integrity, an increased presence of lipofuscin granules and dis-organised myofilaments in PVCs from aged mice compared to young ones (Figures 3.9 – 3.12). To further confirm these changes especially in mitochondrial size and number, a 3D analysis on mitochondrial number and size in PVCs during ageing should be of great interest. Furthermore, more detailed study of connexins, including the localisation (end or lateral in the cells) that has been found to change in PVCs and including Cx45 that is found in other cells of the cardiac conductive system. Presence of Cx45 in PVCs is unclear, found to be present in PVCs (Kugler *et al.,* 2017) or absent (Yamamoto *et al.,* 2006). Potentially also test the functional importance of gap junction connectivity by blocking/opening gap junctions in functional studies.

Whilst Chapter 4 revealed that verapamil; BTP2 and JTV-519 were successful in reducing the frequency of spontaneous Ca^{2+} signalling, they also reduced the ability of PVCs to follow electrical pacing (Figure 4.9). These data suggest reagents used affected the spontaneous activity and had negative effects on excitation-contraction coupling. This makes it difficult to pick out the Ca^{2+} sources involves in generating the spontaneous Ca^{2+} transients. Further studies are needed to be able to establish this particularly with BTP2 reagent. BTP2 has been used in other studies to inhibit SOCE in SA node cells (Liu *et al.,* 2015). In this study, BTP2 significantly reduced the frequency of spontaneous Ca^{2+} waves, increased the duration of spontaneous Ca^{2+} waves and inhibited electrical pacing (Figures 4.5, 4.7, 4.8). These data may indicate the possibility of SOCE role in generating spontaneous Ca^{2+} signals but the fact that it affected both spontaneous and EFS-induced

Ca^{2+} transients, this suggests that BTP2 may not be fully specific. Additionally, it still remains to be established whether PVCs express STIM and Orai proteins. Therefore, future studies investigating the role of SOCE in PVCs either during ageing or in AF should be desirable. Similarly, more detailed study of the role of the NCX in PVCs is needed, especially seeing that it reduced the frequency of local Ca^{2+} transients without affecting the ability of the cells to follow EFS, making it potentially interesting for the treatment of arrhythmia.

Another interesting finding in Chapter 4 was the increased frequency of spontaneous Ca^{2+} transients in PVCs from aged mice compared to young mice (Figures 4.9 and 4.10). This data could indicate SR Ca^{2+} leakage but such conclusions cannot be made at the moment and further studies are needed to be carried-out looking at altered gating properties of RyR2s, protein and mRNA. This would mean that PVCs have to be isolated, which proved difficult in this study after considerable amount of time and efforts was spent in trying to isolate PVCs.

The HU-treatment caused a prolonged rate of recovery after a caffeine-induced Ca^{2+} release from the SR, but didn’t show gross differences in the SR Ca^{2+} content. The experiments performed in this thesis do not distinguish between the different molecules that could cause the slowing down of the recovery: a reduced expression or activity of the NCX, the PMCA or the Ca^{2+} uptake into mitochondria. Taking into account the effects the HU treatment had onto mitochondria, it is likely that an impaired mitochondrial function contributed to the slower rate of Ca^{2+} clearance. However, this needs to be addressed in experiments specifically targeting the mitochondria (antimycin and oligomycin treatment before caffeine addition) or the NCX (NCX inhibition before the caffeine addition). Analysing the SERCA2a activity by measuring the rate of rise of the Ca^{2+} transient after blocking SERCA2a with CPA would also contribute to a better understanding of the changes in SR Ca^{2+} handling seen after the HU treatment. Apart from structural and signalling changes, Chapter 5 also investigated the effects of HU treatment on autophagy. One of the widely accepted methods to investigate autophagy is to count the number of autophagosomes using fluorescence kits Klionsky *et al.*, 2007; Mauvezin *et al.*, 2014). By counting the number of fluorescently tagged autophagosomes, Chapter 5 demonstrated that basal autophagy was up-regulated in both control and HU-treated cells on day 4 and 7 *post* HU treatment (Figure 5.8). However, this increase is significantly higher in HU-treated cells compared to control cells on day 4 and 7 after HU incubation (Figure 5.8). To fully comment on the effect of HU treatment on autophagy, it is necessary to conduct further studies looking at the autophagic flux by monitoring the degradation and production of autophagosomes. It was intended to characterise the autophagic flux by using the mTORC1 / mTORC2 inhibitor PP242 to induce autophagy, 3-MA to prevent the production of autophagosomes and bafilomycin A1 or chloroquine to prevent the degradation of autophagosomes. However, the optimisation of the experiments was not achievable within the timeframe of this thesis. In this study, pp242 was used to induce the production of autophagosomes. Preliminary results in this thesis suggest an increase in autophagosomes with 5 µM pp242 in both control and HU-treated cells (Figure 6.1). However, as measures to prevent autophagosome formation using 3-MA were not done, and the inhibition of their degradation with bafilomycin or chloroquine were not consistent, it was difficult to draw any possible conclusion thus far and further studies investigating autophagic flux in control and HU-treated NRVMs are needed. The preliminary results collected so far are presented in Figure 6.1.

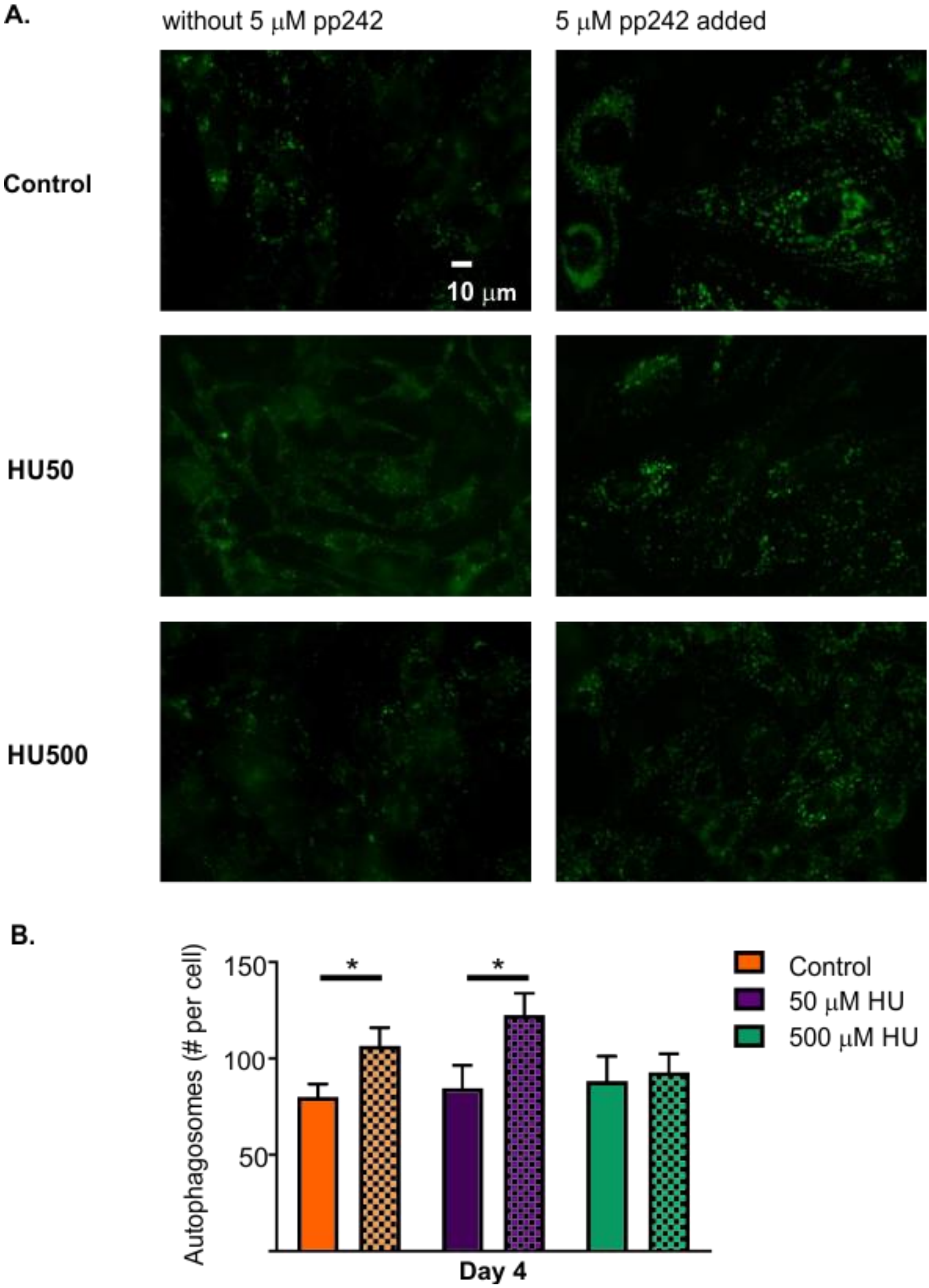

Figure 6.1. mTOR inhibition with pp242 increases the level of autophagy in control and HU-treated cells. Panel **A** shows representative images of autophagosomes in control and HU-treated cells with and without 5 µM pp242. Scale bar 10 µm. Panel **B** illustrates that pp242 can induce autophagy on day 4 in control, 50 µM HU, but not in 500 µM HU-treated cells. A one way ANOVA, *P < 0.05. *n* = 3 coverslips from 3 litters. Data presented as means ± S.E.M.

Furthermore, Chapter 5 also revealed that HU treatment in NRVMs did not change AUC or maximum peak amplitude, but it slowed the clearance of Ca^{2+} (Figure 5.4). Although no attempts were made to directly measure the SERCA2a activity, considerable efforts were put in this thesis to quantify SERCA2a protein levels of control and HU-treated cells on day 1, 4 and 7. Unfortunately, data in this are not fully conclusive due to technical problems whilst harvesting cells, extracting sufficient quantities of protein and most importantly getting consistent loading. Troponin T was used as a loading control and did not give consistent loading for the various samples (Figures 6.2A and 6.3 A). It is therefore difficult to say whether the expression of SERCA2a changed over time, or whether there were problems with the sample loading (Figure 6.2). Therefore, quantifying SERCA2a protein levels in control and HU-treated cells should be of great interest.

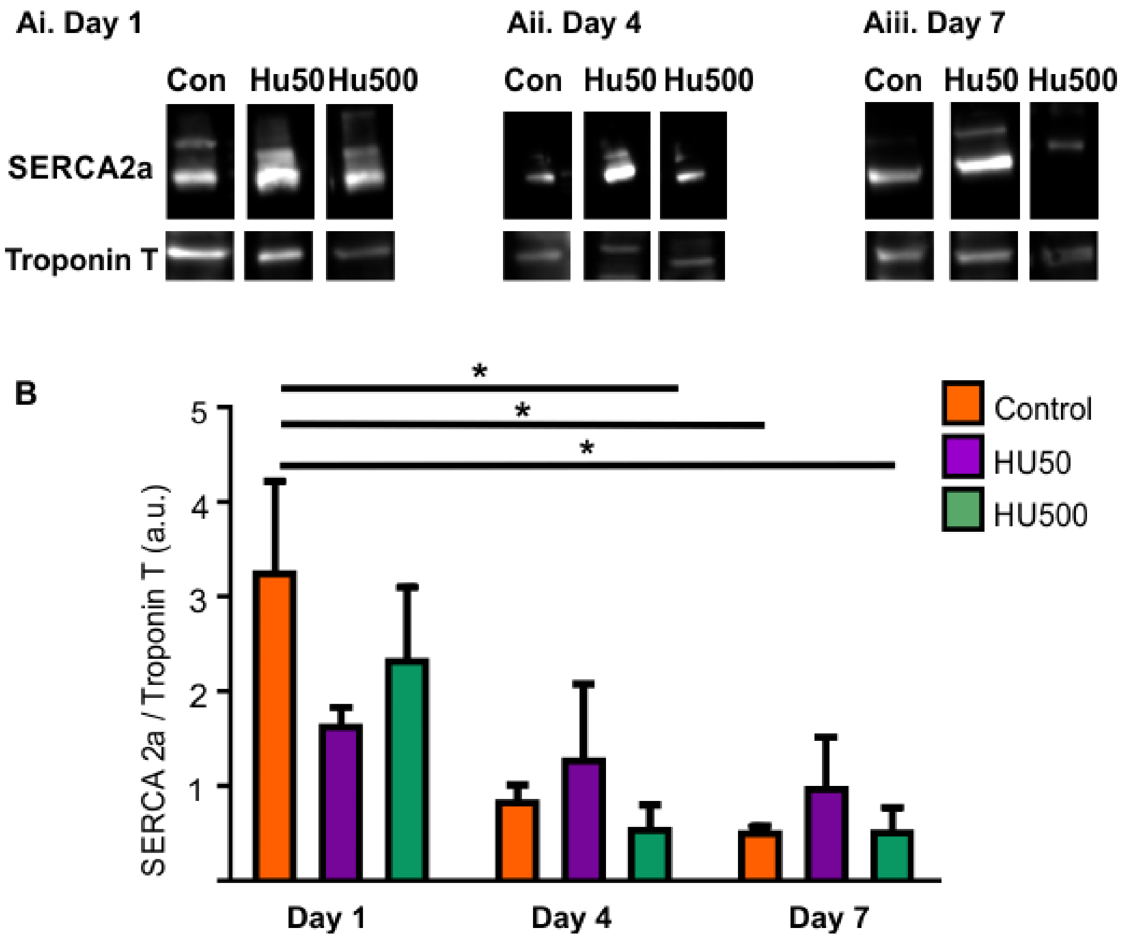

Figure 6.2. Down-regulation of SERCA2a in both control and HU-Treated cells with no significant changes between the groups. Panel **Ai** shows representative blots of control and HU-treated cells showing representative bands of SERCA2a and Troponin T on day 1 **(Ai)**, day 4 **(Aii)** and day 7 **(Aiii).** Panel **B** summarises the relative protein levels of SERCA2a normalised to Troponin T of control and HU-treated cells on day 1, 4 and 7. Data presented as means ± S.E.M., a one way ANOVA, * P < 0.05, *n* = 3 litters per group.

Finally, Chapter 5 demonstrated changes in the structure and Ca^{2+} signalling which are similar to those found in naturally aged PVCs. However, to fully establish whether HU treatment affected NRVMs down to the molecular level, a Western Blotting study was performed to analyse the effects of HU on protein levels of some ageing markers which include, p53, PARP-1 and advanced glycation end products. These suffered from the same methodological difficulties as described for studying the SERCA2a expression levels, and are therefore also inconclusive. The preliminary results and Western Blots are shown in

Figure 6.3. Hence further studies are needed on analysing either mRNA or protein levels of ageing markers.

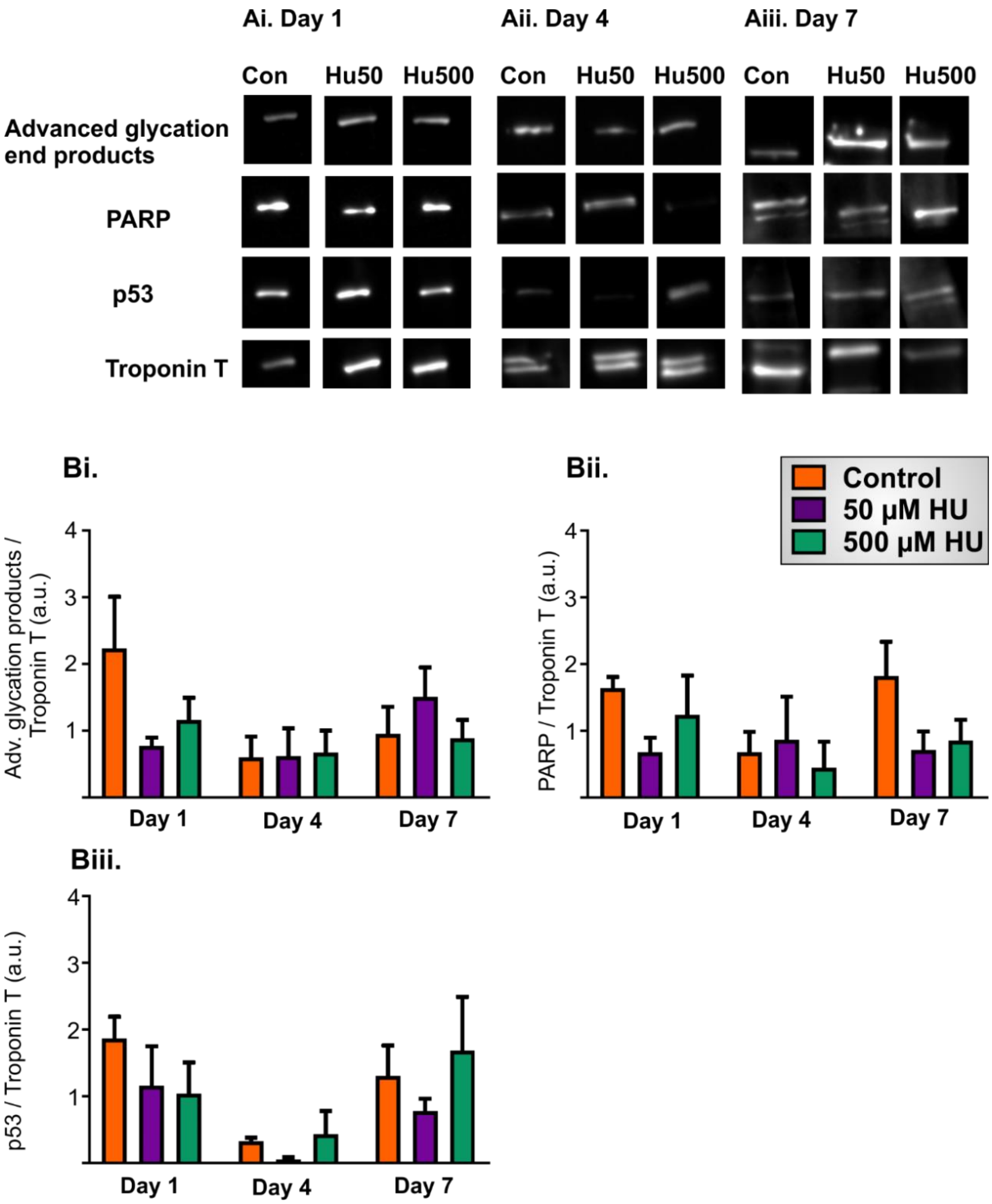

Figure 6.3. No change in the levels of proteins linked to ageing in control and HU-treated cells. Panel **A** shows representative immunoblots of advanced glycation end products, PARP-1, p53 and Troponin T of control and HU-treated cells on day 1, panel **Aii** (day 4) and **Aiii** (day 7). Panel **Bi** summarises the relative protein levels of advanced glycation end products normalised to Troponin T in control and HU-treated cells on day 1, 4 and 7. Panel **Bii** represents relative protein level of PARP-1 and Panel **Biii** shows p53 protein levels. A one way ANOVA, *n* = 3 litters per group, data presented as means ± S.E.M.

6.3. Limitations

Perhaps the biggest obstacle of this study was not being able to isolate PVCs from mice. A modified Langendorff preparation to isolate PVCs was attempted several times but did not yield viable PVCs. Studying cells whilst they are in their normal tissue environment, like in the lung slice preparation, has several advantages (Sanderson, 2011), but also limitations. For example, it did not allow to load certain indicators (e.g. JC-10, CytoID to measure autophagy) to study the function of PVCs from aged mice and compare them to HU-treated cells.

Studying murine PVCs only allows access to very limited amounts of material. For example, it would be difficult to obtain enough material for a PCR analysis or even a Western Blot.

Mice and rats have a very high resting heart rate and do not naturally develop AF. The spontaneous activity so typical for murine PVCs is not commonly observed in larger animals. The easy access to murine PVCs in lung slices makes these a good model to study their basic signalling, but it would be desirable to move these studies to a larger animal model.

6.4. Wider implications of the results

Ageing is a complex process which leads to an increased damage of molecules, cells, tissues and organelles that is characterised by a progressive decline in the function and rise in susceptibility in diseases. Advancing age is associated with the onset of cardiovascular and neurological diseases. As the proportion of the ageing population increases, the prevalence of ageing associated diseases will also increase. Results presented in this thesis demonstrated that ageing is associated with structural remodelling and disturbed Ca^{2+} handling in cardiac myocytes. Changes in the structure and function of mitochondria, an increased appearance of lipofuscin granules, higher ROS levels and an altered Ca^{2+} homeostasis were described to occur in PVCs during ageing. These changes are not confined just in cardiac myocytes, but similar changes have also been reported in the brain (Pearce *et al.*, 1997; Smith *et al.*, 2010).

This thesis has shown that altered Ca^{2+} homeostasis is a complex matter that involves a range of organelles, channels and pathways. This provides us the means to develop pharmacological interventions to target a range of channels and organelles to tackle the changes that manifest during ageing. Finding a PVC-specific target would allow AF treatment without off-target effects on atrial and ventricular myocytes. So far, most drugs that are used to treat AF are Na^{+} channels inhibitors, beta-blockers, Ca^{2+} channel blockers, K^{+} channel blockers and sodium-potassium ATPase blockers (see Chapter 1.1 for AF pharmacological treatments). Although these drugs are effective in relieving AF symptoms, they are associated with severe side-effects and in some cases in-effective (Camm *et al.*, 2010). This reinforces the need for better and more specific treatments. Our study has demonstrated connexin remodelling in PVCs, the appearance of dysfunctional mitochondria and elevated ROS levels during ageing which in turn may interfere with the Ca^{2+} homeostasis. Hence, targeting ROS production and mitochondrial dysfunction provides other means of tackling altered Ca^{2+} homeostasis during ageing.

New drugs are now being developed and tested that target gap-junctions. One such drug is 9f (GAP-134) that is currently in phase I clinical trials for the treatment of AF. This drug has been shown to significantly prolong the time to AV block in the mouse $CaCl_2$ arrhythmia model after oral administration (Butera *et al.*, 2009). Another antiarrhythmic peptide rotigaptide (ZP-123) increased gap junction intercellular communication in cardiac myocytes expressing Cx43 (Clarke *et al.*, 2006). Additionally, other sets of anti-ageing drugs that are emerging are natural phenolic compounds that targets ROS. Amongst these is resveratrol which is found largely in the skins of red grapes, nuts and pomegranates, is a ROS scavenger and has been shown to improve cell survival (Yasuo *et al.*; Baur *et al.*, 2006; Sun *et al.*, 2010). Additionally, other natural compounds including omega-3 that is in fish oil have also been shown to have protective effects in patients with arrhythmias (Leaf *et al.*, 2005; Brouwer *et al.*, 2009). However, results from clinical trials in patients with arrhythmias have produced conflicting results, and hence need further investigations (Leaf *et al.*, 2005; Brouwer *et al.*, 2009). With regards to mitochondrial dysfunction, preventive measures are surfacing that seek to inhibit this reduction by re-strengthening the already weakened antioxidant mechanisms. Glutathione which is an intracellular thiol compound, which is produced in the cytosol of mammalian cells, is the main antioxidant mechanism form of defence against ROS and electrophiles. Previous studies have reported reduced levels of glutathione in the brains of patients with Parkinson's disease (Pearce *et al.*, 1997) and in the ageing brains of mice (Mo *et al.*, 1995). Dietary supplements that include vitamins have been found to protect against the development of AF (Carnes *et al.*, 2001; Lin *et al.*, 2010). (Carnes *et al.*, 2001) showed that Vitamin C attenuated pacing-induced atrial remodelling atrial peroxynitrite production. However, (Shiroshita-Takeshita *et al.*, 2004) did not find the protective effects of vitamins C and E against AF. Therefore, maintaining these antioxidants could be another protective measure to protect against AF, but further studies are still needed.

In conclusion, this thesis has shown that PVCs undergo structural remodelling and develop abnormal Ca^{2+} handling during ageing, which facilitate the maintenance of AF. Whilst most of the available pharmacological treatments in AF rely on classical channel inhibitors, there is a still a lack of drugs that target ROS, mitochondrial dysfunction and gap junctional changes, all of which are shown to be dysregulated during ageing and in AF.

References

Ames, A. and W. G. Stevenson (2006). "Cardiology patient page. Catheter ablation of atrial fibrillation." *Circulation* **113**(13): e666-668.

Antonucci, L., Fagman, J. B., Kim, J. Y., Todoric, J., Gukovsy, I., Mackey, M., Ellisman, M. H. & Karin, M. 2015. Basal autophagy maintains pancreatic acinar cell homeostasis and protein synthesis and prevents ER stress. *Proc Natl Acad Sci* USA, 112, e6166-74.

Arora, R., S. Verheule, L. Scott, A. Navarrete, V. Katari, E. Wilson, D. Vaz and J. E. Olgin (2003). "Arrhythmogenic Substrate of the Pulmonary Veins Assessed by High-Resolution Optical Mapping." *Circulation* **107**(13): 1816.

Ausma, J., N. Litjens, M. H. Lenders, H. Duimel, F. Mast, L. Wouters, F. Ramaekers, M. Allessie and M. Borgers (2001). "Time course of atrial fibrillation-induced cellular structural remodeling in atria of the goat." *J Mol Cell Cardiol* **33**(12): 2083-2094.

Ausma, J., H. M. van der Velden, M. H. Lenders, E. P. van Ankeren, H. J. Jongsma, F. C. Ramaekers, M. Borgers and M. A. Allessie (2003). "Reverse structural and gap-junctional remodeling after prolonged atrial fibrillation in the goat." *Circulation* **107**(15): 2051-2058.

Ausma, J., M. Wijffels, F. Thoné, L. Wouters, M. Allessie and M. Borgers (1997). "Structural Changes of Atrial Myocardium due to Sustained Atrial Fibrillation in the Goat." *Circulation* **96**(9): 3157.

Ayettey, A. S. and V. Navaratnam (1978). "The T-tubule system in the specialized and general myocardium of the rat." *Journal of Anatomy* **127**(Pt 1): 125-140.

Banh S, Hales BF (2013). Hydroxyurea exposure triggers tissue-specific activation of p38 mitogen-activated protein kinase signaling and the DNA damage response in organogenesis-stage mouse embryos. *Toxicological sciences: an official journal of the Society of Toxicology* 133: 298-308.

Bassani, J. W., R. A. Bassani and D. M. Bers (1994). "Relaxation in rabbit and rat cardiac cells: species-dependent differences in cellular mechanisms." *The Journal of_Physiology* **476**(2): 279-293.

Baughman, J. M., F. Perocchi, H. S. Girgis, M. Plovanich, C. A. Belcher-Timme, Y. Sancak, X. R. Bao, L. Strittmatter, O. Goldberger, R. L. Bogorad, V. Koteliansky and V. K. Mootha (2011). "Integrative genomics identifies MCU as an essential component of the mitochondrial calcium uniporter." *Nature* **476**(7360): 341-345.

Baur JA, Pearson KJ, Price NL, Jamieson HA, Lerin C, Kalra A (2006). Resveratrol improves health and survival of mice on a high-calorie diet. *Nature* 444: 337-342.

Benacquista, B. L., M. R. Sharma, M. Samsó, F. Zorzato, S. Treves and T. Wagenknecht (2000). "Amino acid residues 4425-4621 localized on the three-dimensional structure of the skeletal muscle ryanodine receptor." *Biophysical Journal* **78**(3): 1349-1358.

Bergdahl A, Gomez MF, Wihlborg A-K, Erlinge D, Eyjolfson A, Xu S-Z*, et al.* (2005). Plasticity of TRPC expression in arterial smooth muscle: correlation with store-operated Ca^{2+} entry. *American Journal of Physiology - Cell Physiology* 288**:** C872.

Bergson P, Lipkind G, Lee SP, Duban M-E, Hanck DA (2011). Verapamil Block of T-Type Calcium Channels. *Molecular Pharmacology* 79**:** 411-419.

Berridge, M. J. (1997). "Elementary and global aspects of calcium signalling." *Journal of Experimental Biology* **200**(2): 315.

Berridge, M. J. (2002). "The endoplasmic reticulum: a multifunctional signaling organelle." *Cell Calcium* **32**(5): 235-249.

Berridge, M. J., M. D. Bootman and P. Lipp (1998). "Calcium -- a life and death signal." *Nature* **395**(6703): 645.

Bers, D. M. (2008). "Calcium cycling and signaling in cardiac myocytes." *Annu Rev Physiol* **70**: 23-49.

Bhupathy, P., G. J. Babu and M. Periasamy (2007). "Sarcolipin and phospholamban as regulators of cardiac sarcoplasmic reticulum Ca^{2+} ATPase." *Journal of Molecular and Cellular Cardiology* **42**(5): 903-911.

Blatter, L. A., J. Kockskämper, K. A. Sheehan, A. V. Zima, J. Hüser and S. L. Lipsius (2003). "Local calcium gradients during excitation-contraction coupling and alternans in atrial myocytes." *The Journal of Physiology* **546**(1): 19-31.

Blayney, L. M. and F. A. Lai (2009). "Ryanodine receptor-mediated arrhythmias and sudden cardiac death." *Pharmacology & Therapeutics* **123**(2): 151-177.

Boldt, A., A. Scholl, J. Garbade, M. E. Resetar, F. W. Mohr, J. F. Gummert and S. Dhein (2006). "ACE–inhibitor treatment attenuates atrialstructural remodeling in patients with lonechronic atrial fibrillation." *Basic Research in Cardiology* **101**(3): 261-267.

Boldt, A., U. Wetzel, J. Lauschke, J. Weigl, J. Gummert, G. Hindricks, H. Kottkamp and S. Dhein (2004). "Fibrosis in left atrial tissue of patients with atrial fibrillation with and without underlying mitral valve disease." *Heart* **90**(4): 400-405.

Bootman, M. D., D. R. Higazi, S. Coombes and H. L. Roderick (2006). "Calcium signalling during excitation-contraction coupling in mammalian atrial myocytes." *J Cell_Sci* **119**(Pt 19): 3915-3925.

Boyle, A. J., J. Hwang, J. Ye, H. Shih, K. Jun, Y. Zhang, Q. Fang, R. Sievers, Y. Yeghiazarians and R. J. Lee (2013). "The Effects of Aging on Apoptosis Following Myocardial Infarction." *Cardiovascular Therapeutics* **31**(6): e102-e110.

Boyman, L., A. C. Chikando, G. S. Williams, R. J. Khairallah, S. Kettlewell, C. W. Ward, G. L. Smith, J. P. Kao and W. J. Lederer (2014). "Calcium movement in cardiac mitochondria." *Biophys J* **107**(6): 1289-1301.

Brochet, D. X., D. Yang, H. Cheng and W. J. Lederer (2012). "Elementary calcium release events from the sarcoplasmic reticulum in the heart." *Adv Exp Med Biol* 740: 499-509.

Brouwer IA, Raitt MH, Dullemeijer C, Kraemer DF, Zock PL, Morris C, et al. (2009). Effect of fish oil on ventricular tachyarrhythmia in three studies in patients with implantable cardioverter defibrillators. *European Heart Journal* 30: 820-826.

Brundel, B. J. J. M., I. C. Van Gelder, R. H. Henning, A. E. Tuinenburg, L. E. Deelman, R. G. Tieleman, J. G. Grandjean, W. H. Van Gilst and H. J. G. M. Crijns (1999). "Gene expression of proteins influencing the calcium homeostasis in patients with persistent and paroxysmal atrial fibrillation." *Cardiovascular Research* **42**(2): 443-454.

Brunton TL & Fayrer J (1876). Note on independent pulsations of the pulmonary veins and vena cava. *Proc Roy Soc London* 25, 174–176

Bull, R. and J. J. Marengo (1993). "Sarcoplasmic reticulum release channels from frog skeletal muscle display two types of calcium dependence." *FEBS Letters* **331**(3): 223-227.
Cai, L., Y. Yin, Z. Ling, L. Su, Z. Liu, J. Wu, H. Du, X. Lan, J. Fan, W. Chen, Y. Xu, P. Zhou, J. Zhu and B. Zrenner (2013). "Predictors of late recurrence of atrial fibrillation after catheter ablation." *Int J Cardiol* **164**(1): 82-87.

Butera JA, Larsen BD, Hennan JK, Kerns E, Di L, Alimardanov A, et al. (2009). Discovery of (2S,4R)-1-(2-Aminoacetyl)-4-benzamidopyrrolidine-2-carboxylic Acid Hydrochloride (GAP-134)13, an Orally Active Small Molecule Gap-Junction Modifier for the Treatment of Atrial Fibrillation. *Journal of Medicinal Chemistry* 52: 908-911.

Camm, A. J., P. Kirchhof, G. Y. H. Lip, U. Schotten, I. Savelieva, S. Ernst, I. C. Van Gelder, N. Al-Attar, G. Hindricks, B. Prendergast, H. Heidbuchel, O. Alfieri, A. Angelini, D. Atar, P. Colonna, R. De Caterina, J. De Sutter, A. Goette, B. Gorenek, M. Heldal, S. H. Hohloser, P. Kolh, J.-Y. Le Heuzey, P. Ponikowski, F. H. Rutten, A. Vahanian, A. Auricchio, J. Bax, C. Ceconi, V. Dean, G. Filippatos, C. Funck-Brentano, R. Hobbs, P. Kearney, T. McDonagh, B. A. Popescu, Z. Reiner, U. Sechtem, P. A. Sirnes, M. Tendera, P. E. Vardas, P. Widimsky, P. E. Vardas, V. Agladze, E. Aliot, T. Balabanski, C. Blomstrom-Lundqvist, A. Capucci, H. Crijns, B. Dahlöf, T. Folliguet, M. Glikson, M. Goethals, D. C. Gulba, S. Y. Ho, R. J. M. Klautz, S. Kose, J. McMurray, P. Perrone Filardi, P. Raatikainen, M. J. Salvador, M. J. Schalij, A. Shpektor, J. Sousa, J. Stepinska, H. Uuetoa, J. L. Zamorano and I. Zupan (2010). "Guidelines for the management of atrial fibrillationThe Task Force for the Management of Atrial Fibrillation of the European Society of Cardiology (ESC)." *European Heart_Journal* **31**(19): 2369-2429.

Capes, E. M., R. Loaiza and H. H. Valdivia (2011). "Ryanodine receptors." *Skelet_Muscle* **1**(1): 18.

Carnes CA, Chung MK, Nakayama T, Nakayama H, Baliga RS, Piao S, et al. (2001). Ascorbate Attenuates Atrial Pacing-Induced Peroxynitrite Formation and Electrical Remodeling and Decreases the Incidence of Postoperative Atrial Fibrillation. *Circulation Research* 89: e32.

Catterall, W. A. (2011). "Voltage-Gated Calcium Channels." *Cold Spring Harbor Perspectives in Biology* **3**(8): a003947.

Catterall, W. A. and T. M. Swanson (2015). "Structural Basis for Pharmacology of Voltage-Gated Sodium and Calcium Channels." *Molecular Pharmacology* **88**(1): 141.

Chakraborti, S., & Dhalla, Naranjan S. (2016). Regulation of Ca^{2+} -ATPases, V-ATPases and F-ATPases (1st ed. 2016. ed., *Advances in Biochemistry in Health and Disease*; 14).

Chaldoupi, S. M., P. Loh, R. N. Hauer, J. M. de Bakker and H. V. van Rijen (2009). "The role of connexin40 in atrial fibrillation." *Cardiovasc Res* **84**(1): 15-23.

Chang L, Liu X, Liu J, Li H, Yang Y, Liu J, et al. (2014). D-galactose induces a mitochondrial complex I deficiency in mouse skeletal muscle: potential benefits of nutrient combination in ameliorating muscle impairment. *Journal of medicinal food* 17: 357-364.

Chen, Y.-C., S.-A. Chen, Y.-J. Chen, C.-T. Tai, P. Chan and C.-I. Lin (2004). "T-Type Calcium Current in Electrical Activity of Cardiomyocytes Isolated from Rabbit Pulmonary Vein." *Journal of Cardiovascular Electrophysiology* **15**(5): 567-571.

Chen, Y.-J., S.-A. Chen, Y.-C. Chen, H.-I. Yeh, M.-S. Chang and C.-I. Lin (2002). "Electrophysiology of single cardiomyocytes isolated from rabbit pulmonary veins: implication in initiation of focal atrial fibrillation." *Basic Research in Cardiology* **97**(1): 26-34.

Chen, J. H., Hales, C. N. & Ozanne, S. E. 2007. DNA damage, cellular senescence and organismal ageing: causal or correlative? *Nucleic Acids Res,* 35**,** 7417-28.

Chen, Y. J., Y. C. Chen, W. Wongcharoen, C. I. Lin and S. A. Chen (2008). "Effect of K201, a novel antiarrhythmic drug on calcium handling and arrhythmogenic activity of pulmonary vein cardiomyocytes." *Br J Pharmacol* **153**(5): 915-925.

Cheng, H. and W. J. Lederer (2008). "Calcium sparks." *Physiol Rev* **88**(4): 1491-1545.

Cheng, H., W. J. Lederer and M. B. Cannell (1993). "Calcium sparks: elementary events underlying excitation-contraction coupling in heart muscle." *Science* **262**: 740+.

Cheng, W., X. Altafaj, M. Ronjat and R. Coronado (2005). "Interaction between the dihydropyridine receptor Ca^{2+} channel β-subunit and ryanodine receptor type 1 strengthens excitation-contraction coupling." *Proceedings of the National Academy of Sciences of the United States of America* **102**(52): 19225-19230.

Cheung, D. W. (1981). "Electrical activity of the pulmonary vein and its interaction with the right atrium in the guinea-pig." *The Journal of Physiology* **314**(1): 445-456.

Chu, A., M. Fill, E. Stefani and M. L. Entman (1993). "Cytoplasmic Ca^{2+} does not inhibit the cardiac muscle sarcoplasmic reticulum ryanodine receptor Ca2+ channel, although Ca^{2+}-induced Ca^{2+} inactivation of Ca^{2+} release is observed in native vesicles." *The Journal of Membrane Biology* **135**(1): 49-59.

Chugh, S. S., R. Havmoeller, K. Narayanan, D. Singh, M. Rienstra, E. J. Benjamin, R. F. Gillum, Y. H. Kim, J. H. McAnulty, Jr., Z. J. Zheng, M. H. Forouzanfar, M. Naghavi, G. A. Colilla, S., A. Crow, W. Petkun, D. E. Singer, T. Simon and X. Liu (2013). "Estimates of current and future incidence and prevalence of atrial fibrillation in the U.S. adult population." *Am J Cardiol* **112**(8): 1142-1147.

Crouch, J., Schulte, B.A. 1996."Identification and cloning of site C splice variants of plasma membrane Ca-ATPase in the gerbil cochlea". *Hear Res* 101: 55-61.

Chung, C. S. & Campbell, K. S. 2013. "Temperature and transmural region influence functional measurements in unloaded left ventricular cardiomyocytes". *Physiol Rep,* 1**,** e00158.

Clarke TC, Thomas D, Petersen JS, Evans WH, Martin PEM (2006). The antiarrhythmic peptide rotigaptide (ZP123) increases gap junction intercellular communication in cardiac myocytes and HeLa cells expressing connexin 43. *British Journal of Pharmacology* 147: 486-495.

Colilla, S., Crow, A., Petkun, W., Singer, D. E., Simon, T. & Liu, X. 2013. Estimates of current and future incidence and prevalence of atrial fibrillation in the U.S. adult population. *Am J Cardiol,* 112**,** 1142-7.

Cooper, L. L., W. Li, Y. Lu, J. Centracchio, R. Terentyeva, G. Koren and D. Terentyev (2013). "Redox modification of ryanodine receptors by mitochondria-derived reactive oxygen species contributes to aberrant Ca2+ handling in ageing rabbit hearts." *J Physiol* **591**(23): 5895-5911.

Cutler, M. J., X. Wan, K. R. Laurita, R. J. Hajjar and D. S. Rosenbaum (2009). "Targeted SERCA2a gene expression identifies molecular mechanism and therapeutic target for arrhythmogenic cardiac alternans." *Circ Arrhythm Electrophysiol* **2**(6): 686-694.

Czyż, A. and L. Kiedrowski (2003). "Inhibition of plasmalemmal Na^+/Ca^{2+} exchange by mitochondrial Na^+/Ca^{2+} exchange inhibitor 7-chloro-5-(2-chlorophenyl)-1,5-dihydro-4,1-benzothiazepin-2(3H)-one (CGP-37157) in cerebellar granule cells." *Biochemical Pharmacology* **66**(12): 2409-2411.

De Maat, G. E., I. C. Van Gelder, M. Rienstra, A. F. Quast, E. S. Tan, A. C. Wiesfeld, A. Pozzoli and M. A. Mariani (2014). "Surgical vs. transcatheter pulmonary vein isolation as first invasive treatment in patients with atrial fibrillation: a matched group comparison." *Europace* **16**(1): 33-39.

De Meyer, G. R., De Keulenaer, G. W. & Martinet, W. 2010. Role of autophagy in heart failure associated with aging. *Heart Fail Rev,* 15**,** 423-30.

De Souza, E. J., W. Ahmed, V. Chan, R. Bashir and T. Saif (2013). "Cardiac myocytes' dynamic contractile behavior differs depending on heart segment." *Biotechnol Bioeng* **110**(2): 628-636.

De Stefani, D., A. Raffaello, E. Teardo, I. Szabo and R. Rizzuto (2011). "A forty-kilodalton protein of the inner membrane is the mitochondrial calcium uniporter." *Nature* **476**(7360): 336-340.

Deter, R. L. and C. De Duve (1967). "Influence of glucagon, an inducer of cellular autophagy, on some physical properties of rat liver lysosomes." *J Cell Biol.* **33**(2): 437-449

De Tombe, P. and ter Keurs, H (1990). "Force and velocity of sarcomere shortening in Trabeculae from rat hearts". *Circulation Research* 66: 1239-1254.

Dedkova, E. N. and L. A. Blatter (2013). "Calcium signaling in cardiac mitochondria." *J Mol Cell Cardiol* **58**: 125-133.

Díaz ME, Trafford AW, O'Neill SC, Eisner DA (1997). Measurement of sarcoplasmic reticulum Ca^{2+} content and sarcolemmal Ca^{2+} fluxes in isolated rat ventricular myocytes during spontaneous Ca^{2+} release. *The Journal of physiology* 501 (Pt 1)**:** 3.

Dibb, K. M., J. D. Clarke, D. A. Eisner, M. A. Richards and A. W. Trafford (2013). "A functional role for transverse (t-) tubules in the atria." *J Mol Cell Cardiol* **58**: 84-91.

Dobrev, D., L. Carlsson and S. Nattel (2012). "Novel molecular targets for atrial fibrillation therapy." *Nat Rev Drug Discov* **11**(4): 275-291.

Dong, C. M., Wang, X. L., Wang, G. M., Zhang, W. J., Zhu, L., Gao, S., Yang, D. J., Qin, Y., Liang, Q. J., Chen, Y. L., Deng, H. T., Ning, K., Liang, A. B., Gao, Z. L. & Xu, J. 2014. A stress-induced cellular aging model with postnatal neural stem cells. *Cell Death Dis,* 5**,** e1116.

Dorighello GG, Paim BA, Leite ACR, Vercesi AE, Oliveira HCF (2017). Spontaneous experimental atherosclerosis in hypercholesterolemic mice advances with ageing and correlates with mitochondrial reactive oxygen species. *Experimental Gerontology*.

Drago, I., D. De Stefani, R. Rizzuto and T. Pozzan (2012). "Mitochondrial Ca^{2+} uptake contributes to buffering cytoplasmic Ca^{2+} peaks in cardiomyocytes." *Proc Natl Acad Sci U S A* **109**(32): 12986-12991.

Drago, I., D. De Stefani, R. Rizzuto and T. Pozzan (2012). "Mitochondrial Ca^{2+} uptake contributes to buffering cytoplasmic Ca^{2+} peaks in cardiomyocytes." *Proceedings of the National Academy of Sciences* **109**(32): 12986-12991.

Duncan, M. E., A. Pitcher and M. J. Goldacre (2014). "Atrial fibrillation as a cause of death increased steeply in England between 1995 and 2010." *Europace* **16**(6): 797-802.

Ehrlich, J. R., T. J. Cha, L. Zhang, D. Chartier, P. Melnyk, S. H. Hohnloser and S. Nattel (2003). "Cellular electrophysiology of canine pulmonary vein cardiomyocytes: action potential and ionic current properties." *J Physiol* **551**(Pt 3): 801-813.

Eisner, D. A., J. L. Caldwell, K. Kistamas and A. W. Trafford (2017). "Calcium and Excitation-Contraction Coupling in the Heart." *Circ Res* **121**(2): 181-195.

Elliott, E. B., Hasumi, H., Otani, N., Matsuda, T., Matsuda, R., Kaneko, N., Smith, G. L. & Loughrey, C. M. 2011. K201 (JTV-519) alters the spatiotemporal properties of diastolic $Ca^{(2+)}$ release and the associated diastolic contraction during beta-adrenergic stimulation in rat ventricular cardiomyocytes. *Basic Res Cardiol,* 106, 1009-22.

Fahlstrom, A., Yu, Q. & Ulfhake, B. 2011. Behavioral changes in aging female C57BL/6 mice. *Neurobiol Aging,* 32**,** 1868-80.

Farha, S., Saygin, D., Park, M. M., Cheong, H. I., Asosingh, K., Comhair, S. A., Stephens, O. R., Roach, E. C., Sharp, J., Highland, K. B., Defilippo, F. P., Neumann, D. R., Tang, W. H. W. & Erzurum, S. C. 2017. Pulmonary arterial hypertension treatment with carvedilol for heart failure: a randomized controlled trial. *JCI Insight,* 2.

Fearnley, C. J., H. L. Roderick and M. D. Bootman (2011). "Calcium signaling in cardiac myocytes." *Cold Spring Harb Perspect Biol* **3**(11): a004242.

Feldman, M. L. and V. Navaratnam (1981). "Ultrastructural changes in atrial myocardium of the ageing rat." *Journal of Anatomy* **133**(Pt 1): 7-17.

Feridooni, H. A., K. M. Dibb and S. E. Howlett (2015). "How cardiomyocyte excitation, calcium release and contraction become altered with age." *J Mol Cell Cardiol* **83**: 62-72.

Ferreira CR, Gahl WA (2017). Lysosomal storage diseases. *Translational science of rare diseases* 2: 1-71.

Feske S, Prakriya M, Rao A, Lewis RS (2005). A severe defect in CRAC $Ca^{(2+)}$ channel activation and altered $K^{(+)}$ channel gating in T cells from immunodeficient patients. *The Journal of Experimental Medicine* 202: 651-662.

Feske S, Gwack Y, Prakriya M, Srikanth S, Puppel S-H, Tanasa B, et al. (2006). A mutation in Orai1 causes immune deficiency by abrogating CRAC channel function. *Nature* 441: 179-185.

Fhadil, S. and P. Wright (2015). "The role of anti-arrhythmic drugs for AF rhythm control." *British Journal of Cardiac Nursing* **10**(4): 179-182.

Frisk, M., J. T. Koivumaki, P. A. Norseng, M. M. Maleckar, O. M. Sejersted and W. E. Louch (2014). "Variable t-tubule organization and Ca^{2+} homeostasis across the atria." *Am J Physiol Heart Circ Physiol* **307**(4): H609-620.

Fruen, B. R., Mickelson, J. R., Louis, C. F. (1997). Dantrolene inhibition of sarcoplassmic reticulum Ca^{2+} release by direct and specific action at skeletal muscle Ryanodine receptors" *The Journal of Biological Chemistry* **272**(43): 26965 - 26971.

Fulda, S. 2012. Autophagy and cell death. *Autophagy,* 8**,** 1250-1.

Furuoka, H., Yagi, S., Murakami, A., Honma, A., Kobayashi, Y., Matsui, T., Miyahara, K. & Taniyama, H. 2001. Hereditary dilated cardiomyopathy in Holstein-Friesian cattle in

Japan: association with hereditary myopathy of the diaphragmatic muscles. *J Comp Pathol,* 125, 159-65.

Gaborit, N., M. Steenman, G. Lamirault, N. Le Meur, S. Le Bouter, G. Lande, J. Léger, F. Charpentier, T. Christ, D. Dobrev, D. Escande, S. Nattel and S. Demolombe (2005). "Human Atrial Ion Channel and Transporter Subunit Gene-Expression Remodeling Associated With Valvular Heart Disease and Atrial Fibrillation." *Circulation* **112**(4): 471.

Galfré, E., S. J. Pitt, E. Venturi, M. Sitsapesan, N. R. Zaccai, K. Tsaneva-Atanasova, S. O'Neill and R. Sitsapesan (2012). "FKBP12 Activates the Cardiac Ryanodine Receptor Ca^{2+}-Release Channel and Is Antagonised by FKBP12.6." *PLOS ONE* **7**(2): e31956.

Gandhi A, Siedlecka U, Shah AP, Navaratnarajah M, Yacoub MH, Terracciano CM (2013). The effect of SN-6, a novel sodium-calcium exchange inhibitor, on contractility and calcium handling in isolated failing rat ventricular myocytes. *Cardiovasc Ther* 31: e115-124.

Graham, D., Huynh, N. N., Hamilton, C. A., Beattie, E., Smith, R. A., Cocheme, H. M., Murphy, M. P. & Dominiczak, A. F. 2009. Mitochondria-targeted antioxidant MitoQ10 improves endothelial function and attenuates cardiac hypertrophy. *Hypertension* 54, 322-8.

Greensmith DJ, Galli GLJ, Trafford AW, Eisner DA (2014). Direct measurements of SR free Ca reveal the mechanism underlying the transient effects of RyR potentiation under physiological conditions. *Cardiovascular Research* 103: 554-563.

Gaztañaga, L., F. E. Marchlinski and B. P. Betensky (2012). "Mechanisms of Cardiac Arrhythmias." *Revista Española de Cardiología (English Edition)* **65**(2): 174-185.

Gherghiceanu, M., M. E. Hinescu, F. Andrei, E. Mandache, C. E. Macarie, M.-S. Faussone-Pellegrini and L. M. Popescu (2008). "Interstitial Cajal-like cells (ICLC) in myocardial sleeves of human pulmonary veins." *Journal of Cellular and Molecular Medicine* **12**(5a): 1777-1781.

Giorgio, V., L. Guo, C. Bassot, V. Petronilli and P. Bernardi (2017). "Calcium and regulation of the mitochondrial permeability transition." *Cell Calcium.*

Go, A. S., E. M. Hylek, K. A. Phillips and et al. (2001). "Prevalence of diagnosed atrial fibrillation in adults: National implications for rhythm management and stroke prevention: the anticoagulation and risk factors in atrial fibrillation (atria) study." *JAMA* **285**(18): 2370-2375.

Graef, M. & Nunnari, J. 2011. Mitochondria regulate autophagy by conserved signalling pathways. *EMBO J,* 30**,** 2101-14.

Grant, A. O. (2009). "Cardiac ion channels." *Circ Arrhythm Electrophysiol* **2**(2): 185-194.

Greensmith DJ, Galli GLJ, Trafford AW, Eisner DA (2014). Direct measurements of SR free Ca reveal the mechanism underlying the transient effects of RyR potentiation under physiological conditions. *Cardiovascular Research* 103**:** 554-563.

Greiser, M., H.-R. Neuberger, E. Harks, A. El-Armouche, P. Boknik, S. de Haan, F. Verheyen, S. Verheule, W. Schmitz, U. Ravens, S. Nattel, M. A. Allessie, D. Dobrev and U.

Greiser, M. and U. Schotten (2013). "Dynamic remodeling of intracellular $Ca^{(2)(+)}$ signaling during atrial fibrillation." *J Mol Cell Cardiol* 58: 134-142.

Guerrero-Hernandez, A., G. Avila and A. Rueda (2014). "Ryanodine receptors as leak channels." *Eur J Pharmacol* 739: 26-38.

Guerrero-Hernandez, A., Avila, G. & Rueda, A. 2014. Ryanodine receptors as leak channels. *Eur J Pharmacol,* 739**,** 26-38.

Guerini D, Zecca-Mazza A, Carafoli E (2000). "Single amino acid mutations in trans membrane domain 5 confer to the plasma membrane Ca^{2+} pump properties typical of the Ca^{2+} pump of endo(sarco)plasmic reticulum. *J Biol Chem* 275:31361–31368.

Guerini, D., Coletto, L., Carafoli, E. 2005. "Exporting calcium from cells". *Cell Calcium* 38: 281-289.

Guerrini, R., P. Menegazzi, R. Anacardio, M. Marastoni, R. Tomatis, F. Zorzato and S. Treves (1995). "Calmodulin Binding Sites of the Skeletal, Cardiac, and Brain Ryanodine Receptor Ca^{2+} Channels: Modulation by the Catalytic Subunit of cAMP-Dependent Protein Kinase?" *Biochemistry* **34**(15): 5120-5129.

Guo, X., S. Yuan, Z. Liu and Q. Fang (2014). "Oxidation- and CaMKII-mediated sarcoplasmic reticulum $Ca^{(2+)}$ leak triggers atrial fibrillation in aging." *J Cardiovasc_Electrophysiol* **25**(6): 645-652.

Gupta, A., S. Gupta, D. Young, B. Das, J. McMahon and S. Sen (2010). "Impairment of ultrastructure and cytoskeleton during progression of cardiac hypertrophy to heart failure." *Lab Invest* **90**(4): 520-530.

Györke, I. and S. Györke (1998). "Regulation of the cardiac ryanodine receptor channel by luminal Ca^{2+} involves luminal Ca^{2+} sensing sites." *Biophysical Journal* **75**(6): 2801-2810.

Györke, I., N. Hester, L. R. Jones and S. Györke (2004). "The Role of Calsequestrin, Triadin, and Junctin in Conferring Cardiac Ryanodine Receptor Responsiveness to Luminal Calcium." *Biophysical Journal* **86**(4): 2121-2128.

Han, J., Back, S. H., Hur, J., Lin, Y. H., Gildersleeve, R., Shan, J., Yuan, C. L., Krokowski, D., Wang, S., Hatglou, M., Kilberg, M. S., Sartor, M. A. & Kaufman, R. J. 2013. ER-stress-induced transcriptional regulation increases protein synthesis leading to cell death. *Nat Cell Biol,* 15, 481-90.

Hassink, R. J., H. T. Aretz, J. Ruskin and D. Keane (2003). "Morphology of atrial myocardium in human pulmonary veins: A postmortem analysis in patients with and without atrial fibrillation." *Journal of the American College of Cardiology* **42**(6): 1108-1114.

Hatch, F., M. K. Lancaster and S. A. Jones (2011). "Aging is a primary risk factor for cardiac arrhythmias: disruption of intracellular Ca^{2+} regulation as a key suspect." *Expert Review of Cardiovascular Therapy* **9**(8): 1059-1067.

Hayashi, H., C. Wang, Y. Miyauchi, C. Omichi, H.-N. Pak, S. Zhou, T. Ohara, W. J. Mandel, S.-F. Lin, M. C. Fishbein, P.-S. Chen and H. S. Karagueuzian (2002). "Aging-Related Increase to Inducible Atrial Fibrillation in the Rat Model." *Journal of Cardiovascular Electrophysiology* **13**(8): 801-808.

He LP, Hewavitharana T, Soboloff J, Spassova MA, Gill DL (2005). A functional link between store-operated and TRPC channels revealed by the 3,5-bis(trifluoromethyl)pyrazole derivative, BTP2. *J Biol Chem* 280: 10997-11006.

Heeringa, J., D. A. van der Kuip, A. Hofman, J. A. Kors, G. van Herpen, B. H. Stricker, T. Stijnen, G. Y. Lip and J. C. Witteman (2006). "Prevalence, incidence and lifetime risk of atrial fibrillation: the Rotterdam study." *Eur Heart J* **27**(8): 949-953.

Herraiz-Martinez, A., J. Alvarez-Garcia, A. Llach, C. E. Molina, J. Fernandes, A. Ferrero-Gregori, C. Rodriguez, A. Vallmitjana, R. Benitez, J. M. Padro, J. Martinez-Gonzalez, J. Cinca and L. Hove-Madsen (2015). "Ageing is associated with deterioration of calcium homeostasis in isolated human right atrial myocytes." *Cardiovasc Res* **106**(1): 76-86.

Hirose, M. and K. R. Laurita (2007). "Calcium-mediated triggered activity is an underlying cellular mechanism of ectopy originating from the pulmonary vein in dogs." *Am J Physiol Heart Circ Physiol* **292**(4): H1861-1867.

Ho, S., J. Cabrera, V. Tran, J. Farre, R. Anderson and D. Sanchez-Quintana (2001). "Architecture of the pulmonary veins: relevance to radiofrequency ablation." *Heart* **86**(3): 265-270.

Hocini, M., S. Y. Ho, T. Kawara, A. C. Linnenbank, M. Potse, D. Shah, P. Jaïs, M. J. Janse, M. Haïssaguerre and J. M. T. de Bakker (2002). "Electrical Conduction in Canine Pulmonary Veins." *Circulation* **105**(20): 2442.

Hogan PG, Rao A (2015). Store-operated calcium entry: Mechanisms and modulation. *Biochem Biophys Res Commun* 460: 40-49.

Honjo, H., Boyett, M. R., Niwa, R., Inada, S., Yamamoto, M., Mitsui, K., Horiuchi, T., Shibata, N., Kamiya, K. & Kodama, I. 2003. Pacing-induced spontaneous activity in myocardial sleeves of pulmonary veins after treatment with ryanodine. *Circulation,* 107**,** 1937-43.

Hoppel, C. L., Tandler, B., Fujioka, H. & Riva, A. 2009. Dynamic organization of mitochondria in human heart and in myocardial disease. *Int J Biochem Cell Biol,* 41**,** 1949-56.

Hove-Madsen, L., A. Llach, A. Bayes-Genis, S. Roura, E. Rodriguez Font, A. Aris and J. Cinca (2004). "Atrial fibrillation is associated with increased spontaneous calcium release from the sarcoplasmic reticulum in human atrial myocytes." *Circulation* **110**(11): 1358-1363.

Huang, S. Y., Y. C. Chen, Y. H. Kao, M. H. Hsieh, Y. K. Lin, S. A. Chen and Y. J. Chen (2017). "Redox and Activation of Protein Kinase A Dysregulates Calcium Homeostasis in Pulmonary Vein Cardiomyocytes of Chronic Kidney Disease." *J Am Heart Assoc* **6**(7).

Huang, X., B. Fruen, D. T. Farrington, T. Wagenknecht and Z. Liu (2012). "Calmodulin-binding locations on the skeletal and cardiac ryanodine receptors." *J Biol Chem* **287**(36): 30328-30335.

Hüser, J., L. A. Blatter and S. L. Lipsius (2000). "Intracellular $Ca^{(2+)}$ release contributes to automaticity in cat atrial pacemaker cells." *The Journal of Physiology* **524**(Pt 2): 415-422.

Inoue Y, Ito K, Sakaue T, Iwamoto T, Kita S (2004). Characterization of SN-6, a novel exchange inhibitor and its renal protective effect. *Clin Calcium*; 14:84–91.

Izzo, V., J. M. Bravo-San Pedro, V. Sica, G. Kroemer and L. Galluzzi (2016). "Mitochondrial Permeability Transition: New Findings and Persisting Uncertainties." *Trends in Cell Biology* **26**(9): 655-667.

Janssen B.J., Smits J.F. 2002. Autonomic control of blood pressure in mice: basic physiology and effects of genetic modification. *Am J Physiol Regul Integr Comp Physiol,* **282**(6), pp. 1545–1564.

Javadov, S., Rajapurohitam, V., Kilic, A., Zeidan, A., Choi, A. & Karmazyn, M. 2009. Anti-hypertrophic effect of NHE-1 inhibition involves GSK-3beta-dependent attenuation of mitochondrial dysfunction. *J Mol Cell Cardiol*, 46, 998-1007.

Jones, W. K., A. Sánchez and J. Robbins (1994). "Murine pulmonary myocardium: Developmental analysis of cardiac gene expression." *Developmental Dynamics* **200**(2): 117-128.

Juhaszova, M., C. Rabuel, D. B. Zorov, E. G. Lakatta and S. J. Sollott (2005). "Protection in the aged heart: preventing the heart-break of old age?" *Cardiovasc Res* **66**(2): 233-244.

Jung, C. B., Moretti, A., Mederos Y Schnitizler, M., Iop, L., Storch, U., Bellin, M., Dorn, T., Rupenthal, S., Pfeiffer, S., Goedel, A., Dirschingher, R. J., Seyfarth, M., Lam, J. T., Sinnecker, D., Gudermann, T., Lipp, P. & Laugwitz, K. L. (2012). Dantrolene rescues arrhythmogenic RYR2 defect in a patient-specific stem cell model of catecholaminergic polymorphic ventricular tachycardia. *EMBO Mol Med*, 4, 180-91.

Jung T, Bader N, Grune T (2007). Lipofuscin: formation, distribution, and metabolic consequences. *Annals of the New York Academy of Sciences* 1119: 97-111.

Kanaporis, G. and L. A. Blatter (2017). "Alternans in atria: Mechanisms and clinical relevance." *Medicina (Kaunas)* **53**(3): 139-149.

Kanaya, N., Gable, B., Wickley, P., Murray, P.A., Damron, D.S (2005). Experimental conditions are important determinants of cardiac inotropic effects of Propofol" *Anesthesiology* 103: 1026-34.

Kasai, M. and T. Ide (1996). Regulation of Calcium Release Channel in Sarcoplasmic Reticulum. *Ion Channels.* T. Narahashi. Boston, MA, Springer US**:** 303-331.

Katra, R. P., T. Oya, G. S. Hoeker and K. R. Laurita (2007). "Ryanodine receptor dysfunction and triggered activity in the heart." *Am J Physiol Heart Circ Physiol* **292**(5): H2144-2151.

Kimura J, Kawahara M, Sakai E, Yatabe J, Nakanishi H (1999): Effects of a novel cardioprotective drug, JTV-519, on membrane currents of guinea pig ventricular myocytes. *Jpn J Pharmacol*; 79:275-281.

Klein, G., F. Schröder, D. Vogler, A. Schaefer, A. Haverich, B. Schieffer, T. Korte and H. Drexler (2003). "Increased open probability of single cardiac L-type calcium channels in patients with chronic atrial fibrillationRole of phosphatase 2A." *Cardiovascular Research* **59**(1): 37-45.

Klionsky, D. J. 2005. The molecular machinery of autophagy: unanswered questions. *J Cell Sci,* 118**,** 7-18.

Klionsky DJ, Cuervo AM, Seglen PO (2007). Methods for Monitoring Autophagy from Yeast to Human. *Autophagy* 3**:** 181-206.

Klionsky, D. J., K. Abdelmohsen, A. Abe, M. J. Abedin, H. Abeliovich, A. Acevedo Arozena, H. Adachi, C. M. Adams, P. D. Adams, K. Adeli, P. J. Adhihetty, S. G. Adler, G. Agam, R. Agarwal, M. K. Aghi, M. Agnello, P. Agostinis, P. V. Aguilar, J. Aguirre-Ghiso, E. M. Airoldi, S. Ait-Si-Ali, T. Akematsu, E. T. Akporiaye, M. Al-Rubeai, G. M. Albaiceta, C. Albanese, D. Albani, M. L. Albert, J. Aldudo, H. Algul, M. Alirezaei, I. Alloza, A. Almasan, M. Almonte-Beceril, E. S. Alnemri, C. Alonso, N. Altan-Bonnet, D. C. Altieri, S. Alvarez, L. Alvarez-Erviti, S. Alves, G. Amadoro, A. Amano, C. Amantini, S. Ambrosio, I. Amelio, A. O. Amer, M. Amessou, A. Amon, Z. An, F. A. Anania, S. U. Andersen, U. P. Andley, C. K. Andreadi, N. Andrieu-Abadie, A. Anel, D. K. Ann, S. Anoopkumar-Dukie, M. Antonioli, H. Aoki, N. Apostolova, S. Aquila, K. Aquilano, K. Araki, E. Arama, A. Aranda, J. Araya, A. Arcaro, E. Arias, H. Arimoto, A. R. Ariosa, J. L. Armstrong, T. Arnould, I. Arsov, K. Asanuma, V. Askanas, E. Asselin, R. Atarashi, S. S. Atherton, J. D. Atkin, L. D. Attardi, P. Auberger, G. Auburger, L. Aurelian, R. Autelli, L. Avagliano, M. L. Avantaggiati, L. Avrahami, S. Awale, N. Azad, T. Bachetti, J. M. Backer, D. H. Bae, J. S. Bae, O. N. Bae, S. H. Bae, E. H. Baehrecke, S. H. Baek, S. Baghdiguian, A. Bagniewska-Zadworna, H. Bai, J. Bai, X. Y. Bai, Y. Bailly, K. N. Balaji, W. Balduini, A. Ballabio, R. Balzan, R. Banerjee, G. Banhegyi, H. Bao, B. Barbeau, M. D. Barrachina, E. Barreiro, B. Bartel, A. Bartolome, D. C. Bassham, M. T. Bassi, R. C. Bast, Jr., A. Basu, M. T. Batista, H. Batoko, M. Battino, K. Bauckman, B. L. Baumgarner, K. U. Bayer, R. Beale, J. F. Beaulieu, G. R. Beck, Jr., C. Becker, J. D. Beckham, P. A. Bedard, P. J. Bednarski, T. J. Begley, C. Behl, C. Behrends, G. M. Behrens, K. E. Behrns, E. Bejarano, A. Belaid, F. Belleudi, G. Benard, G. Berchem, D. Bergamaschi, M. Bergami, B. Berkhout, L. Berliocchi, A. Bernard, M. Bernard, F. Bernassola, A. Bertolotti, A. S. Bess, S. Besteiro, S. Bettuzzi, S. Bhalla, S. Bhattacharyya, S. K. Bhutia, C. Biagosch, M. W. Bianchi, M. Biard-Piechaczyk, V. Billes, C. Bincoletto, B. Bingol, S. W. Bird, M. Bitoun, I. Bjedov, C.

Blackstone, L. Blanc, G. A. Blanco, H. K. Blomhoff, E. Boada-Romero, S. Bockler, M. Boes, K. Boesze-Battaglia, L. H. Boise, A. Bolino, A. Boman, P. Bonaldo, M. Bordi, J. Bosch, L. M. Botana, J. Botti, G. Bou, M. Bouche, M. Bouchecareilh, M. J. Boucher, M. E. Boulton, S. G. Bouret, P. Boya, M. Boyer-Guittaut, P. V. Bozhkov, N. Brady, V. M. Braga, C. Brancolini, G. H. Braus, J. M. Bravo-San Pedro, L. A. Brennan, E. H. Bresnick, P. Brest, D. Bridges, M. A. Bringer, M. Brini, G. C. Brito, B. Brodin, P. S. Brookes, E. J. Brown, K. Brown, H. E. Broxmeyer, A. Bruhat, P. C. Brum, J. H. Brumell, N. Brunetti-Pierri, R. J. Bryson-Richardson, S. Buch, A. M. Buchan, H. Budak, D. V. Bulavin, S. J. Bultman, G. Bultynck, V. Bumbasirevic, Y. Burelle, R. E. Burke, M. Burmeister, P. Butikofer, L. Caberlotto, K. Cadwell, M. Cahova, D. Cai, J. Cai, Q. Cai, S. Calatayud, N. Camougrand, M. Campanella, G. R. Campbell, M. Campbell, S. Campello, R. Candau, I. Caniggia, L. Cantoni, L. Cao, A. B. Caplan, M. Caraglia, C. Cardinali, S. M. Cardoso, J. S. Carew, L. A. Carleton, C. R. Carlin, S. Carloni, S. R. Carlsson, D. Carmona-Gutierrez, L. A. Carneiro, O. Carnevali, S. Carra, A. Carrier, B. Carroll, C. Casas, J. Casas, G. Cassinelli, P. Castets, S. Castro-Obregon, G. Cavallini, I. Ceccherini, F. Cecconi, A. I. Cederbaum, V. Cena, S. Cenci, C. Cerella, D. Cervia, S. Cetrullo, H. Chaachouay, H. J. Chae, A. S. Chagin, C. Y. Chai, G. Chakrabarti, G. Chamilos, E. Y. Chan, M. T. Chan, D. Chandra, P. Chandra, C. P. Chang, R. C. Chang, T. Y. Chang, J. C. Chatham, S. Chatterjee, S. Chauhan, Y. Che, M. E. Cheetham, R. Cheluvappa, C. J. Chen, G. Chen, G. C. Chen, G. Chen, H. Chen, J. W. Chen, J. K. Chen, M. Chen, M. Chen, P. Chen, Q. Chen, Q. Chen, S. D. Chen, S. Chen, S. S. Chen, W. Chen, W. J. Chen, W. Q. Chen, W. Chen, X. Chen, Y. H. Chen, Y. G. Chen, Y. Chen, Y. Chen, Y. Chen, Y. J. Chen, Y. Q. Chen, Y. Chen, Z. Chen, Z. Chen, A. Cheng, C. H. Cheng, H. Cheng, H. Cheong, S. Cherry, J. Chesney, C. H. Cheung, E. Chevet, H. C. Chi, S. G. Chi, F. Chiacchiera, H. L. Chiang, R. Chiarelli, M. Chiariello, M. Chieppa, L. S. Chin, M. Chiong, G. N. Chiu, D. H. Cho, S. G. Cho, W. C. Cho, Y. Y. Cho, Y. S. Cho, A. M. Choi, E. J. Choi, E. K. Choi, J. Choi, M. E. Choi, S. I. Choi, T. F. Chou, S. Chouaib, D. Choubey, V. Choubey, K. C. Chow, K. Chowdhury, C. T. Chu, T. H. Chuang, T. Chun, H. Chung, T. Chung, Y. L. Chung, Y. J. Chwae, V. Cianfanelli, R. Ciarcia, I. A. Ciechomska, M. R. Ciriolo, M. Cirone, S. Claerhout, M. J. Clague, J. Claria, P. G. Clarke, R. Clarke, E. Clementi, C. Cleyrat, M. Cnop, E. M. Coccia, T. Cocco, P. Codogno, J. Coers, E. E. Cohen, D. Colecchia, L. Coletto, N. S. Coll, E. Colucci-Guyon, S. Comincini, M. Condello, K. L. Cook, G. H. Coombs, C. D. Cooper, J. M. Cooper, I. Coppens, M. T. Corasaniti, M. Corazzari, R. Corbalan, E. Corcelle-Termeau, M. D. Cordero, C. Corral-Ramos, O. Corti, A. Cossarizza, P. Costelli, S. Costes, S. L. Cotman, A. Coto-Montes, S. Cottet, E. Couve, L. R. Covey, L. A. Cowart, J. S. Cox, F. P. Coxon, C. B. Coyne, M. S. Cragg, R. J. Craven, T. Crepaldi, J. L. Crespo, A. Criollo, V. Crippa, M. T. Cruz, A. M. Cuervo, J. M. Cuezva, T. Cui, P. R. Cutillas, M. J. Czaja, M. F. Czyzyk-Krzeska, R. K. Dagda, U. Dahmen, C. Dai, W. Dai, Y. Dai, K. N. Dalby, L. Dalla Valle, G. Dalmasso, M. D'Amelio, M. Damme, A. Darfeuille-Michaud, C. Dargemont, V. M. Darley-Usmar, S. Dasarathy, B. Dasgupta, S. Dash, C. R. Dass, H. M. Davey, L. M. Davids, D. Davila, R. J. Davis, T. M. Dawson, V. L. Dawson, P. Daza, J. de Belleroche, P. de Figueiredo, R. C. de Figueiredo, J. de la Fuente, L. De Martino, A. De Matteis, G. R. De Meyer, A. De Milito, M. De Santi, W. de Souza, V. De Tata, D. De Zio, J. Debnath, R. Dechant, J. P. Decuypere, S. Deegan, B. Dehay, B. Del Bello, D. P. Del Re, R. Delage-Mourroux, L. M. Delbridge, L. Deldicque, E. Delorme-Axford, Y. Deng, J. Dengjel, M. Denizot, P. Dent, C. J. Der, V. Deretic, B. Derrien, E. Deutsch, T. P. Devarenne, R. J. Devenish, S. Di Bartolomeo, N. Di Daniele, F. Di Domenico, A. Di Nardo, S. Di Paola, A. Di Pietro, L. Di Renzo, A. DiAntonio, G. Diaz-Araya, I. Diaz-Laviada, M. T. Diaz-Meco, J. Diaz-Nido, C. A. Dickey, R. C. Dickson, M. Diederich, P. Digard, I. Dikic, S. P. Dinesh-Kumar, C. Ding, W. X. Ding, Z. Ding, L. Dini, J. H. Distler, A. Diwan, M. Djavaheri-Mergny, K. Dmytruk, R. C. Dobson, V. Doetsch, K. Dokladny, S. Dokudovskaya, M. Donadelli, X. C. Dong, X. Dong, Z. Dong, T. M. Donohue, Jr., K. S. Doran, G. D'Orazi, G. W. Dorn, 2nd, V. Dosenko, S.

Dridi, L. Drucker, J. Du, L. L. Du, L. Du, A. du Toit, P. Dua, L. Duan, P. Duann, V. K. Dubey, M. R. Duchen, M. A. Duchosal, H. Duez, I. Dugail, V. I. Dumit, M. C. Duncan, E. A. Dunlop, W. A. Dunn, Jr., N. Dupont, L. Dupuis, R. V. Duran, T. M. Durcan, S. Duvezin-Caubet, U. Duvvuri, V. Eapen, D. Ebrahimi-Fakhari, A. Echard, L. Eckhart, C. L. Edelstein, A. L. Edinger, L. Eichinger, T. Eisenberg, A. Eisenberg-Lerner, N. T. Eissa, W. S. El-Deiry, V. El-Khoury, Z. Elazar, H. Eldar-Finkelman, C. J. Elliott, E. Emanuele, U. Emmenegger, N. Engedal, A. M. Engelbrecht, S. Engelender, J. M. Enserink, R. Erdmann, J. Erenpreisa, R. Eri, J. L. Eriksen, A. Erman, R. Escalante, E. L. Eskelinen, L. Espert, L. Esteban-Martinez, T. J. Evans, M. Fabri, G. Fabrias, C. Fabrizi, A. Facchiano, N. J. Faergeman, A. Faggioni, W. D. Fairlie, C. Fan, D. Fan, J. Fan, S. Fang, M. Fanto, A. Fanzani, T. Farkas, M. Faure, F. B. Favier, H. Fearnhead, M. Federici, E. Fei, T. C. Felizardo, H. Feng, Y. Feng, Y. Feng, T. A. Ferguson, A. F. Fernandez, M. G. Fernandez-Barrena, J. C. Fernandez-Checa, A. Fernandez-Lopez, M. E. Fernandez-Zapico, O. Feron, E. Ferraro, C. V. Ferreira-Halder, L. Fesus, R. Feuer, F. C. Fiesel, E. C. Filippi-Chiela, G. Filomeni, G. M. Fimia, J. H. Fingert, S. Finkbeiner, T. Finkel, F. Fiorito, P. B. Fisher, M. Flajolet, F. Flamigni, O. Florey, S. Florio, R. A. Floto, M. Folini, C. Follo, E. A. Fon, F. Fornai, F. Fortunato, A. Fraldi, R. Franco, A. Francois, A. Francois, L. B. Frankel, I. D. Fraser, N. Frey, D. G. Freyssenet, C. Frezza, S. L. Friedman, D. E. Frigo, D. Fu, J. M. Fuentes, J. Fueyo, Y. Fujitani, Y. Fujiwara, M. Fujiya, M. Fukuda, S. Fulda, C. Fusco, B. Gabryel, M. Gaestel, P. Gailly, M. Gajewska, S. Galadari, G. Galili, I. Galindo, M. F. Galindo, G. Galliciotti, L. Galluzzi, L. Galluzzi, V. Galy, N. Gammoh, S. Gandy, A. K. Ganesan, S. Ganesan, I. G. Ganley, M. Gannage, F. B. Gao, F. Gao, J. X. Gao, L. Garcia Nannig, E. Garcia Vescovi, M. Garcia-Macia, C. Garcia-Ruiz, A. D. Garg, P. K. Garg, R. Gargini, N. C. Gassen, D. Gatica, E. Gatti, J. Gavard, E. Gavathiotis, L. Ge, P. Ge, S. Ge, P. W. Gean, V. Gelmetti, A. A. Genazzani, J. Geng, P. Genschik, L. Gerner, J. E. Gestwicki, D. A. Gewirtz, S. Ghavami, E. Ghigo, D. Ghosh, A. M. Giammarioli, F. Giampieri, C. Giampietri, A. Giatromanolaki, D. J. Gibbings, L. Gibellini, S. B. Gibson, V. Ginet, A. Giordano, F. Giorgini, E. Giovannetti, S. E. Girardin, S. Gispert, S. Giuliano, C. L. Gladson, A. Glavic, M. Gleave, N. Godefroy, R. M. Gogal, Jr., K. Gokulan, G. H. Goldman, D. Goletti, M. S. Goligorsky, A. V. Gomes, L. C. Gomes, H. Gomez, C. Gomez-Manzano, R. Gomez-Sanchez, D. A. Goncalves, E. Goncu, Q. Gong, C. Gongora, C. B. Gonzalez, P. Gonzalez-Alegre, P. Gonzalez-Cabo, R. A. Gonzalez-Polo, I. S. Goping, C. Gorbea, N. V. Gorbunov, D. R. Goring, A. M. Gorman, S. M. Gorski, S. Goruppi, S. Goto-Yamada, C. Gotor, R. A. Gottlieb, I. Gozes, D. Gozuacik, Y. Graba, M. Graef, G. E. Granato, G. D. Grant, S. Grant, G. L. Gravina, D. R. Green, A. Greenhough, M. T. Greenwood, B. Grimaldi, F. Gros, C. Grose, J. F. Groulx, F. Gruber, P. Grumati, T. Grune, J. L. Guan, K. L. Guan, B. Guerra, C. Guillen, K. Gulshan, J. Gunst, C. Guo, L. Guo, M. Guo, W. Guo, X. G. Guo, A. A. Gust, A. B. Gustafsson, E. Gutierrez, M. G. Gutierrez, H. S. Gwak, A. Haas, J. E. Haber, S. Hadano, M. Hagedorn, D. R. Hahn, A. J. Halayko, A. Hamacher-Brady, K. Hamada, A. Hamai, A. Hamann, M. Hamasaki, I. Hamer, Q. Hamid, E. M. Hammond, F. Han, W. Han, J. T. Handa, J. A. Hanover, M. Hansen, M. Harada, L. Harhaji-Trajkovic, J. W. Harper, A. H. Harrath, A. L. Harris, J. Harris, U. Hasler, P. Hasselblatt, K. Hasui, R. G. Hawley, T. S. Hawley, C. He, C. Y. He, F. He, G. He, R. R. He, X. H. He, Y. W. He, Y. Y. He, J. K. Heath, M. J. Hebert, R. A. Heinzen, G. V. Helgason, M. Hensel, E. P. Henske, C. Her, P. K. Herman, A. Hernandez, C. Hernandez, S. Hernandez-Tiedra, C. Hetz, P. R. Hiesinger, K. Higaki, S. Hilfiker, B. G. Hill, J. A. Hill, W. D. Hill, K. Hino, D. Hofius, P. Hofman, G. U. Hoglinger, J. Hohfeld, M. K. Holz, Y. Hong, D. A. Hood, J. J. Hoozemans, T. Hoppe, C. Hsu, C. Y. Hsu, L. C. Hsu, D. Hu, G. Hu, H. M. Hu, H. Hu, M. C. Hu, Y. C. Hu, Z. W. Hu, F. Hua, Y. Hua, C. Huang, H. L. Huang, K. H. Huang, K. Y. Huang, S. Huang, S. Huang, W. P. Huang, Y. R. Huang, Y. Huang, Y. Huang, T. B. Huber, P. Huebbe, W. K. Huh, J. J. Hulmi, G. M. Hur, J. H. Hurley, Z. Husak, S. N. Hussain, S. Hussain, J. J. Hwang, S. Hwang, T. I. Hwang, A. Ichihara, Y. Imai, C. Imbriano, M. Inomata, T. Into, V. Iovane, J. L. Iovanna, R. V. Iozzo, N. Y.

Ip, J. E. Irazoqui, P. Iribarren, Y. Isaka, A. J. Isakovic, H. Ischiropoulos, J. S. Isenberg, M. Ishaq, H. Ishida, I. Ishii, J. E. Ishmael, C. Isidoro, K. I. Isobe, E. Isono, S. Issazadeh-Navikas, K. Itahana, E. Itakura, A. I. Ivanov, A. K. Iyer, J. M. Izquierdo, Y. Izumi, V. Izzo, M. Jaattela, N. Jaber, D. J. Jackson, W. T. Jackson, T. G. Jacob, T. S. Jacques, C. Jagannath, A. Jain, N. R. Jana, B. K. Jang, A. Jani, B. Janji, P. R. Jannig, P. J. Jansson, S. Jean, M. Jendrach, J. H. Jeon, N. Jessen, E. B. Jeung, K. Jia, L. Jia, H. Jiang, H. Jiang, L. Jiang, T. Jiang, X. Jiang, X. Jiang, X. Jiang, Y. Jiang, Y. Jiang, A. Jimenez, C. Jin, H. Jin, L. Jin, M. Jin, S. Jin, U. K. Jinwal, E. K. Jo, T. Johansen, D. E. Johnson, G. V. Johnson, J. D. Johnson, E. Jonasch, C. Jones, L. A. Joosten, J. Jordan, A. M. Joseph, B. Joseph, A. M. Joubert, D. Ju, J. Ju, H. F. Juan, K. Juenemann, G. Juhasz, H. S. Jung, J. U. Jung, Y. K. Jung, H. Jungbluth, M. J. Justice, B. Jutten, N. O. Kaakoush, K. Kaarniranta, A. Kaasik, T. Kabuta, B. Kaeffer, K. Kagedal, A. Kahana, S. Kajimura, O. Kakhlon, M. Kalia, D. V. Kalvakolanu, Y. Kamada, K. Kambas, V. O. Kaminskyy, H. H. Kampinga, M. Kandouz, C. Kang, R. Kang, T. C. Kang, T. Kanki, T. D. Kanneganti, H. Kanno, A. G. Kanthasamy, M. Kantorow, M. Kaparakis-Liaskos, O. Kapuy, V. Karantza, M. R. Karim, P. Karmakar, A. Kaser, S. Kaushik, T. Kawula, A. M. Kaynar, P. Y. Ke, Z. J. Ke, J. H. Kehrl, K. E. Keller, J. K. Kemper, A. K. Kenworthy, O. Kepp, A. Kern, S. Kesari, D. Kessel, R. Ketteler, I. D. Kettelhut, B. Khambu, M. M. Khan, V. K. Khandelwal, S. Khare, J. G. Kiang, A. A. Kiger, A. Kihara, A. L. Kim, C. H. Kim, D. R. Kim, D. H. Kim, E. K. Kim, H. Y. Kim, H. R. Kim, J. S. Kim, J. H. Kim, J. C. Kim, J. H. Kim, K. W. Kim, M. D. Kim, M. M. Kim, P. K. Kim, S. W. Kim, S. Y. Kim, Y. S. Kim, Y. Kim, A. Kimchi, A. C. Kimmelman, T. Kimura, J. S. King, K. Kirkegaard, V. Kirkin, L. A. Kirshenbaum, S. Kishi, Y. Kitajima, K. Kitamoto, Y. Kitaoka, K. Kitazato, R. A. Kley, W. T. Klimecki, M. Klinkenberg, J. Klucken, H. Knaevelsrud, E. Knecht, L. Knuppertz, J. L. Ko, S. Kobayashi, J. C. Koch, C. Koechlin-Ramonatxo, U. Koenig, Y. H. Koh, K. Kohler, S. D. Kohlwein, M. Koike, M. Komatsu, E. Kominami, D. Kong, H. J. Kong, E. G. Konstantakou, B. T. Kopp, T. Korcsmaros, L. Korhonen, V. I. Korolchuk, N. V. Koshkina, Y. Kou, M. I. Koukourakis, C. Koumenis, A. L. Kovacs, T. Kovacs, W. J. Kovacs, D. Koya, C. Kraft, D. Krainc, H. Kramer, T. Kravic-Stevovic, W. Krek, C. Kretz-Remy, R. Krick, M. Krishnamurthy, J. Kriston-Vizi, G. Kroemer, M. C. Kruer, R. Kruger, N. T. Ktistakis, K. Kuchitsu, C. Kuhn, A. P. Kumar, A. Kumar, A. Kumar, D. Kumar, D. Kumar, R. Kumar, S. Kumar, M. Kundu, H. J. Kung, A. Kuno, S. H. Kuo, J. Kuret, T. Kurz, T. Kwok, T. K. Kwon, Y. T. Kwon, I. Kyrmizi, A. R. La Spada, F. Lafont, T. Lahm, A. Lakkaraju, T. Lam, T. Lamark, S. Lancel, T. H. Landowski, D. J. Lane, J. D. Lane, C. Lanzi, P. Lapaquette, L. R. Lapierre, J. Laporte, J. Laukkarinen, G. W. Laurie, S. Lavandero, L. Lavie, M. J. LaVoie, B. Y. Law, H. K. Law, K. B. Law, R. Layfield, P. A. Lazo, L. Le Cam, K. G. Le Roch, H. Le Stunff, V. Leardkamolkarn, M. Lecuit, B. H. Lee, C. H. Lee, E. F. Lee, G. M. Lee, H. J. Lee, H. Lee, J. K. Lee, J. Lee, J. H. Lee, J. H. Lee, M. Lee, M. S. Lee, P. J. Lee, S. W. Lee, S. J. Lee, S. J. Lee, S. Y. Lee, S. H. Lee, S. S. Lee, S. J. Lee, S. Lee, Y. R. Lee, Y. J. Lee, Y. H. Lee, C. Leeuwenburgh, S. Lefort, R. Legouis, J. Lei, Q. Y. Lei, D. A. Leib, G. Leibowitz, I. Lekli, S. D. Lemaire, J. J. Lemasters, M. K. Lemberg, A. Lemoine, S. Leng, G. Lenz, P. Lenzi, L. O. Lerman, D. Lettieri Barbato, J. I. Leu, H. Y. Leung, B. Levine, P. A. Lewis, F. Lezoualc'h, C. Li, F. Li, F. J. Li, J. Li, K. Li, L. Li, M. Li, M. Li, Q. Li, R. Li, S. Li, W. Li, W. Li, X. Li, Y. Li, J. Lian, C. Liang, Q. Liang, Y. Liao, J. Liberal, P. P. Liberski, P. Lie, A. P. Lieberman, H. J. Lim, K. L. Lim, K. Lim, R. T. Lima, C. S. Lin, C. F. Lin, F. Lin, F. Lin, F. C. Lin, K. Lin, K. H. Lin, P. H. Lin, T. Lin, W. W. Lin, Y. S. Lin, Y. Lin, R. Linden, D. Lindholm, L. M. Lindqvist, P. Lingor, A. Linkermann, L. A. Liotta, M. M. Lipinski, V. A. Lira, M. P. Lisanti, P. B. Liton, B. Liu, C. Liu, C. F. Liu, F. Liu, H. J. Liu, J. Liu, J. J. Liu, J. L. Liu, K. Liu, L. Liu, L. Liu, Q. Liu, R. Y. Liu, S. Liu, S. Liu, W. Liu, X. D. Liu, X. Liu, X. H. Liu, X. Liu, X. Liu, X. Liu, Y. Liu, Y. Liu, Z. Liu, Z. Liu, J. P. Liuzzi, G. Lizard, M. Ljujic, I. J. Lodhi, S. E. Logue, B. L. Lokeshwar, Y. C. Long, S. Lonial, B. Loos, C. Lopez-Otin, C. Lopez-Vicario, M. Lorente, P. L. Lorenzi, P. Lorincz, M. Los, M. T. Lotze, P. E. Lovat, B. Lu, B. Lu, J. Lu, Q. Lu, S. M. Lu, S. Lu, Y. Lu, F. Luciano, S. Luckhart, J. M. Lucocq, P. Ludovico, A. Lugea, N. W.

Lukacs, J. J. Lum, A. H. Lund, H. Luo, J. Luo, S. Luo, C. Luparello, T. Lyons, J. Ma, Y. Ma, Y. Ma, Z. Ma, J. Machado, G. M. Machado-Santelli, F. Macian, G. C. MacIntosh, J. P. MacKeigan, K. F. Macleod, J. D. MacMicking, L. A. MacMillan-Crow, F. Madeo, M. Madesh, J. Madrigal-Matute, A. Maeda, T. Maeda, G. Maegawa, E. Maellaro, H. Maes, M. Magarinos, K. Maiese, T. K. Maiti, L. Maiuri, M. C. Maiuri, C. G. Maki, R. Malli, W. Malorni, A. Maloyan, F. Mami-Chouaib, N. Man, J. D. Mancias, E. M. Mandelkow, M. A. Mandell, A. A. Manfredi, S. N. Manie, C. Manzoni, K. Mao, Z. Mao, Z. W. Mao, P. Marambaud, A. M. Marconi, Z. Marelja, G. Marfe, M. Margeta, E. Margittai, M. Mari, F. V. Mariani, C. Marin, S. Marinelli, G. Marino, I. Markovic, R. Marquez, A. M. Martelli, S. Martens, K. R. Martin, S. J. Martin, S. Martin, M. A. Martin-Acebes, P. Martin-Sanz, C. Martinand-Mari, W. Martinet, J. Martinez, N. Martinez-Lopez, U. Martinez-Outschoorn, M. Martinez-Velazquez, M. Martinez-Vicente, W. K. Martins, H. Mashima, J. A. Mastrianni, G. Matarese, P. Matarrese, R. Mateo, S. Matoba, N. Matsumoto, T. Matsushita, A. Matsuura, T. Matsuzawa, M. P. Mattson, S. Matus, N. Maugeri, C. Mauvezin, A. Mayer, D. Maysinger, G. D. Mazzolini, M. K. McBrayer, K. McCall, C. McCormick, G. M. McInerney, S. C. McIver, S. McKenna, J. J. McMahon, I. A. McNeish, F. Mechta-Grigoriou, J. P. Medema, D. L. Medina, K. Megyeri, M. Mehrpour, J. L. Mehta, Y. Mei, U. C. Meier, A. J. Meijer, A. Melendez, G. Melino, S. Melino, E. J. de Melo, M. A. Mena, M. D. Meneghini, J. A. Menendez, R. Menezes, L. Meng, L. H. Meng, S. Meng, R. Menghini, A. S. Menko, R. F. Menna-Barreto, M. B. Menon, M. A. Meraz-Rios, G. Merla, L. Merlini, A. M. Merlot, A. Meryk, S. Meschini, J. N. Meyer, M. T. Mi, C. Y. Miao, L. Micale, S. Michaeli, C. Michiels, A. R. Migliaccio, A. S. Mihailidou, D. Mijaljica, K. Mikoshiba, E. Milan, L. Miller-Fleming, G. B. Mills, I. G. Mills, G. Minakaki, B. A. Minassian, X. F. Ming, F. Minibayeva, E. A. Minina, J. D. Mintern, S. Minucci, A. Miranda-Vizuete, C. H. Mitchell, S. Miyamoto, K. Miyazawa, N. Mizushima, K. Mnich, B. Mograbi, S. Mohseni, L. F. Moita, M. Molinari, M. Molinari, A. B. Moller, B. Mollereau, F. Mollinedo, M. Mongillo, M. M. Monick, S. Montagnaro, C. Montell, D. J. Moore, M. N. Moore, R. Mora-Rodriguez, P. I. Moreira, E. Morel, M. B. Morelli, S. Moreno, M. J. Morgan, A. Moris, Y. Moriyasu, J. L. Morrison, L. A. Morrison, E. Morselli, J. Moscat, P. L. Moseley, S. Mostowy, E. Motori, D. Mottet, J. C. Mottram, C. E. Moussa, V. E. Mpakou, H. Mukhtar, J. M. Mulcahy Levy, S. Muller, R. Munoz-Moreno, C. Munoz-Pinedo, C. Munz, M. E. Murphy, J. T. Murray, A. Murthy, I. U. Mysorekar, I. R. Nabi, M. Nabissi, G. A. Nader, Y. Nagahara, Y. Nagai, K. Nagata, A. Nagelkerke, P. Nagy, S. R. Naidu, S. Nair, H. Nakano, H. Nakatogawa, M. Nanjundan, G. Napolitano, N. I. Naqvi, R. Nardacci, D. P. Narendra, M. Narita, A. C. Nascimbeni, R. Natarajan, L. C. Navegantes, S. T. Nawrocki, T. Y. Nazarko, V. Y. Nazarko, T. Neill, L. M. Neri, M. G. Netea, R. T. Netea-Maier, B. M. Neves, P. A. Ney, I. P. Nezis, H. T. Nguyen, H. P. Nguyen, A. S. Nicot, H. Nilsen, P. Nilsson, M. Nishimura, I. Nishino, M. Niso-Santano, H. Niu, R. A. Nixon, V. C. Njar, T. Noda, A. A. Noegel, E. M. Nolte, E. Norberg, K. K. Norga, S. K. Noureini, S. Notomi, L. Notterpek, K. Nowikovsky, N. Nukina, T. Nurnberger, V. B. O'Donnell, T. O'Donovan, P. J. O'Dwyer, I. Oehme, C. L. Oeste, M. Ogawa, B. Ogretmen, Y. Ogura, Y. J. Oh, M. Ohmuraya, T. Ohshima, R. Ojha, K. Okamoto, T. Okazaki, F. J. Oliver, K. Ollinger, S. Olsson, D. P. Orban, P. Ordonez, I. Orhon, L. Orosz, E. J. O'Rourke, H. Orozco, A. L. Ortega, E. Ortona, L. D. Osellame, J. Oshima, S. Oshima, H. D. Osiewacz, T. Otomo, K. Otsu, J. J. Ou, T. F. Outeiro, D. Y. Ouyang, H. Ouyang, M. Overholtzer, M. A. Ozbun, P. H. Ozdinler, B. Ozpolat, C. Pacelli, P. Paganetti, G. Page, G. Pages, U. Pagnini, B. Pajak, S. C. Pak, K. Pakos-Zebrucka, N. Pakpour, Z. Palkova, F. Palladino, K. Pallauf, N. Pallet, M. Palmieri, S. R. Paludan, C. Palumbo, S. Palumbo, O. Pampliega, H. Pan, W. Pan, T. Panaretakis, A. Pandey, A. Pantazopoulou, Z. Papackova, D. L. Papademetrio, I. Papassideri, A. Papini, N. Parajuli, J. Pardo, V. V. Parekh, G. Parenti, J. I. Park, J. Park, O. K. Park, R. Parker, R. Parlato, J. B. Parys, K. R. Parzych, J. M. Pasquet, B. Pasquier, K. B. Pasumarthi, D. Patschan, C.

Patterson, S. Pattingre, S. Pattison, A. Pause, H. Pavenstadt, F. Pavone, Z. Pedrozo, F. J. Pena, M. A. Penalva, M. Pende, J. Peng, F. Penna, J. M. Penninger, A. Pensalfini, S. Pepe, G. J. Pereira, P. C. Pereira, V. Perez-de la Cruz, M. E. Perez-Perez, D. Perez-Rodriguez, D. Perez-Sala, C. Perier, A. Perl, D. H. Perlmutter, I. Perrotta, S. Pervaiz, M. Pesonen, J. E. Pessin, G. J. Peters, M. Petersen, I. Petrache, B. J. Petrof, G. Petrovski, J. M. Phang, M. Piacentini, M. Pierdominici, P. Pierre, V. Pierrefite-Carle, F. Pietrocola, F. X. Pimentel-Muinos, M. Pinar, B. Pineda, R. Pinkas-Kramarski, M. Pinti, P. Pinton, B. Piperdi, J. M. Piret, L. C. Platanias, H. W. Platta, E. D. Plowey, S. Poggeler, M. Poirot, P. Polcic, A. Poletti, A. H. Poon, H. Popelka, B. Popova, I. Poprawa, S. M. Poulose, J. Poulton, S. K. Powers, T. Powers, M. Pozuelo-Rubio, K. Prak, R. Prange, M. Prescott, M. Priault, S. Prince, R. L. Proia, T. Proikas-Cezanne, H. Prokisch, V. J. Promponas, K. Przyklenk, R. Puertollano, S. Pugazhenthi, L. Puglielli, A. Pujol, J. Puyal, D. Pyeon, X. Qi, W. B. Qian, Z. H. Qin, Y. Qiu, Z. Qu, J. Quadrilatero, F. Quinn, N. Raben, H. Rabinowich, F. Radogna, M. J. Ragusa, M. Rahmani, K. Raina, S. Ramanadham, R. Ramesh, A. Rami, S. Randall-Demllo, F. Randow, H. Rao, V. A. Rao, B. B. Rasmussen, T. M. Rasse, E. A. Ratovitski, P. E. Rautou, S. K. Ray, B. Razani, B. H. Reed, F. Reggiori, M. Rehm, A. S. Reichert, T. Rein, D. J. Reiner, E. Reits, J. Ren, X. Ren, M. Renna, J. E. Reusch, J. L. Revuelta, L. Reyes, A. R. Rezaie, R. I. Richards, D. R. Richardson, C. Richetta, M. A. Riehle, B. H. Rihn, Y. Rikihisa, B. E. Riley, G. Rimbach, M. R. Rippo, K. Ritis, F. Rizzi, E. Rizzo, P. J. Roach, J. Robbins, M. Roberge, G. Roca, M. C. Roccheri, S. Rocha, C. M. Rodrigues, C. I. Rodriguez, S. R. de Cordoba, N. Rodriguez-Muela, J. Roelofs, V. V. Rogov, T. T. Rohn, B. Rohrer, D. Romanelli, L. Romani, P. S. Romano, M. I. Roncero, J. L. Rosa, A. Rosello, K. V. Rosen, P. Rosenstiel, M. Rost-Roszkowska, K. A. Roth, G. Roue, M. Rouis, K. M. Rouschop, D. T. Ruan, D. Ruano, D. C. Rubinsztein, E. B. Rucker, 3rd, A. Rudich, E. Rudolf, R. Rudolf, M. A. Ruegg, C. Ruiz-Roldan, A. A. Ruparelia, P. Rusmini, D. W. Russ, G. L. Russo, G. Russo, R. Russo, T. E. Rusten, V. Ryabovol, K. M. Ryan, S. W. Ryter, D. M. Sabatini, M. Sacher, C. Sachse, M. N. Sack, J. Sadoshima, P. Saftig, R. Sagi-Eisenberg, S. Sahni, P. Saikumar, T. Saito, T. Saitoh, K. Sakakura, M. Sakoh-Nakatogawa, Y. Sakuraba, M. Salazar-Roa, P. Salomoni, A. K. Saluja, P. M. Salvaterra, R. Salvioli, A. Samali, A. M. Sanchez, J. A. Sanchez-Alcazar, R. Sanchez-Prieto, M. Sandri, M. A. Sanjuan, S. Santaguida, L. Santambrogio, G. Santoni, C. N. Dos Santos, S. Saran, M. Sardiello, G. Sargent, P. Sarkar, S. Sarkar, M. R. Sarrias, M. M. Sarwal, C. Sasakawa, M. Sasaki, M. Sass, K. Sato, M. Sato, J. Satriano, N. Savaraj, S. Saveljeva, L. Schaefer, U. E. Schaible, M. Scharl, H. M. Schatzl, R. Schekman, W. Scheper, A. Schiavi, H. M. Schipper, H. Schmeisser, J. Schmidt, I. Schmitz, B. E. Schneider, E. M. Schneider, J. L. Schneider, E. A. Schon, M. J. Schonenberger, A. H. Schonthal, D. F. Schorderet, B. Schroder, S. Schuck, R. J. Schulze, M. Schwarten, T. L. Schwarz, S. Sciarretta, K. Scotto, A. I. Scovassi, R. A. Screaton, M. Screen, H. Seca, S. Sedej, L. Segatori, N. Segev, P. O. Seglen, J. M. Segui-Simarro, J. Segura-Aguilar, E. Seki, C. Sell, I. Selliez, C. F. Semenkovich, G. L. Semenza, U. Sen, A. L. Serra, A. Serrano-Puebla, H. Sesaki, T. Setoguchi, C. Settembre, J. J. Shacka, A. N. Shajahan-Haq, I. M. Shapiro, S. Sharma, H. She, C. J. Shen, C. C. Shen, H. M. Shen, S. Shen, W. Shen, R. Sheng, X. Sheng, Z. H. Sheng, T. G. Shepherd, J. Shi, Q. Shi, Q. Shi, Y. Shi, S. Shibutani, K. Shibuya, Y. Shidoji, J. J. Shieh, C. M. Shih, Y. Shimada, S. Shimizu, D. W. Shin, M. L. Shinohara, M. Shintani, T. Shintani, T. Shioi, K. Shirabe, R. Shiri-Sverdlov, O. Shirihai, G. C. Shore, C. W. Shu, D. Shukla, A. A. Sibirny, V. Sica, C. J. Sigurdson, E. M. Sigurdsson, P. S. Sijwali, B. Sikorska, W. A. Silveira, S. Silvente-Poirot, G. A. Silverman, J. Simak, T. Simmet, A. K. Simon, H. U. Simon, C. Simone, M. Simons, A. Simonsen, R. Singh, S. V. Singh, S. K. Singh, D. Sinha, S. Sinha, F. A. Sinicrope, A. Sirko, K. Sirohi, B. J. Sishi, A. Sittler, P. M. Siu, E. Sivridis, A. Skwarska, R. Slack, I. Slaninova, N. Slavov, S. S. Smaili, K. S. Smalley, D. R. Smith, S. J. Soenen, S. A. Soleimanpour, A. Solhaug, K. Somasundaram, J. H. Son, A. Sonawane, C. Song, F. Song, H. K. Song, J. X. Song, W. Song, K. Y. Soo, A. K. Sood, T.

W. Soong, V. Soontornniyomkij, M. Sorice, F. Sotgia, D. R. Soto-Pantoja, A. Sotthibundhu, M. J. Sousa, H. P. Spaink, P. N. Span, A. Spang, J. D. Sparks, P. G. Speck, S. A. Spector, C. D. Spies, W. Springer, D. S. Clair, A. Stacchiotti, B. Staels, M. T. Stang, D. T. Starczynowski, P. Starokadomskyy, C. Steegborn, J. W. Steele, L. Stefanis, J. Steffan, C. M. Stellrecht, H. Stenmark, T. M. Stepkowski, S. T. Stern, C. Stevens, B. R. Stockwell, V. Stoka, Z. Storchova, B. Stork, V. Stratoulias, D. J. Stravopodis, P. Strnad, A. M. Strohecker, A. L. Strom, P. Stromhaug, J. Stulik, Y. X. Su, Z. Su, C. S. Subauste, S. Subramaniam, C. M. Sue, S. W. Suh, X. Sui, S. Sukseree, D. Sulzer, F. L. Sun, J. Sun, J. Sun, S. Y. Sun, Y. Sun, Y. Sun, Y. Sun, V. Sundaramoorthy, J. Sung, H. Suzuki, K. Suzuki, N. Suzuki, T. Suzuki, Y. J. Suzuki, M. S. Swanson, C. Swanton, K. Sward, G. Swarup, S. T. Sweeney, P. W. Sylvester, Z. Szatmari, E. Szegezdi, P. W. Szlosarek, H. Taegtmeyer, M. Tafani, E. Taillebourg, S. W. Tait, K. Takacs-Vellai, Y. Takahashi, S. Takats, G. Takemura, N. Takigawa, N. J. Talbot, E. Tamagno, J. Tamburini, C. P. Tan, L. Tan, M. L. Tan, M. Tan, Y. J. Tan, K. Tanaka, M. Tanaka, D. Tang, D. Tang, G. Tang, I. Tanida, K. Tanji, B. A. Tannous, J. A. Tapia, I. Tasset-Cuevas, M. Tatar, I. Tavassoly, N. Tavernarakis, A. Taylor, G. S. Taylor, G. A. Taylor, J. P. Taylor, M. J. Taylor, E. V. Tchetina, A. R. Tee, F. Teixeira-Clerc, S. Telang, T. Tencomnao, B. B. Teng, R. J. Teng, F. Terro, G. Tettamanti, A. L. Theiss, A. E. Theron, K. J. Thomas, M. P. Thome, P. G. Thomes, A. Thorburn, J. Thorner, T. Thum, M. Thumm, T. L. Thurston, L. Tian, A. Till, J. P. Ting, V. I. Titorenko, L. Toker, S. Toldo, S. A. Tooze, I. Topisirovic, M. L. Torgersen, L. Torosantucci, A. Torriglia, M. R. Torrisi, C. Tournier, R. Towns, V. Trajkovic, L. H. Travassos, G. Triola, D. N. Tripathi, D. Trisciuoglio, R. Troncoso, I. P. Trougakos, A. C. Truttmann, K. J. Tsai, M. P. Tschan, Y. H. Tseng, T. Tsukuba, A. Tsung, A. S. Tsvetkov, S. Tu, H. Y. Tuan, M. Tucci, D. A. Tumbarello, B. Turk, V. Turk, R. F. Turner, A. A. Tveita, S. C. Tyagi, M. Ubukata, Y. Uchiyama, A. Udelnow, T. Ueno, M. Umekawa, R. Umemiya-Shirafuji, B. R. Underwood, C. Ungermann, R. P. Ureshino, R. Ushioda, V. N. Uversky, N. L. Uzcategui, T. Vaccari, M. I. Vaccaro, L. Vachova, H. Vakifahmetoglu-Norberg, R. Valdor, E. M. Valente, F. Vallette, A. M. Valverde, G. Van den Berghe, L. Van Den Bosch, G. R. van den Brink, F. G. van der Goot, I. J. van der Klei, L. J. van der Laan, W. G. van Doorn, M. van Egmond, K. L. van Golen, L. Van Kaer, M. van Lookeren Campagne, P. Vandenabeele, W. Vandenberghe, I. Vanhorebeek, I. Varela-Nieto, M. H. Vasconcelos, R. Vasko, D. G. Vavvas, I. Vega-Naredo, G. Velasco, A. D. Velentzas, P. D. Velentzas, T. Vellai, E. Vellenga, M. H. Vendelbo, K. Venkatachalam, N. Ventura, S. Ventura, P. S. Veras, M. Verdier, B. G. Vertessy, A. Viale, M. Vidal, H. Vieira, R. D. Vierstra, N. Vigneswaran, N. Vij, M. Vila, M. Villar, V. H. Villar, J. Villarroya, C. Vindis, G. Viola, M. T. Viscomi, G. Vitale, D. T. Vogl, O. V. Voitsekhovskaja, C. von Haefen, K. von Schwarzenberg, D. E. Voth, V. Vouret-Craviari, K. Vuori, J. M. Vyas, C. Waeber, C. L. Walker, M. J. Walker, J. Walter, L. Wan, X. Wan, B. Wang, C. Wang, C. Y. Wang, C. Wang, C. Wang, C. Wang, D. Wang, F. Wang, F. Wang, G. Wang, H. J. Wang, H. Wang, H. G. Wang, H. Wang, H. D. Wang, J. Wang, J. Wang, M. Wang, M. Q. Wang, P. Y. Wang, P. Wang, R. C. Wang, S. Wang, T. F. Wang, X. Wang, X. J. Wang, X. W. Wang, X. Wang, X. Wang, Y. Wang, Y. Wang, Y. Wang, Y. J. Wang, Y. Wang, Y. Wang, Y. T. Wang, Y. Wang, Z. N. Wang, P. Wappner, C. Ward, D. M. Ward, G. Warnes, H. Watada, Y. Watanabe, K. Watase, T. E. Weaver, C. D. Weekes, J. Wei, T. Weide, C. C. Weihl, G. Weindl, S. N. Weis, L. Wen, X. Wen, Y. Wen, B. Westermann, C. M. Weyand, A. R. White, E. White, J. L. Whitton, A. J. Whitworth, J. Wiels, F. Wild, M. E. Wildenberg, T. Wileman, D. S. Wilkinson, S. Wilkinson, D. Willbold, C. Williams, K. Williams, P. R. Williamson, K. F. Winklhofer, S. S. Witkin, S. E. Wohlgemuth, T. Wollert, E. J. Wolvetang, E. Wong, G. W. Wong, R. W. Wong, V. K. Wong, E. A. Woodcock, K. L. Wright, C. Wu, D. Wu, G. S. Wu, J. Wu, J. Wu, M. Wu, M. Wu, S. Wu, W. K. Wu, Y. Wu, Z. Wu, C. P. Xavier, R. J. Xavier, G. X. Xia, T. Xia, W. Xia, Y. Xia, H. Xiao, J. Xiao, S. Xiao, W. Xiao, C. M. Xie, Z. Xie, Z. Xie, M. Xilouri, Y. Xiong, C. Xu, C. Xu, F. Xu, H. Xu, H. Xu, J. Xu, J. Xu, J. Xu, L. Xu, X. Xu, Y. Xu, Y. Xu,

Z. X. Xu, Z. Xu, Y. Xue, T. Yamada, A. Yamamoto, K. Yamanaka, S. Yamashina, S. Yamashiro, B. Yan, B. Yan, X. Yan, Z. Yan, Y. Yanagi, D. S. Yang, J. M. Yang, L. Yang, M. Yang, P. M. Yang, P. Yang, Q. Yang, W. Yang, W. Y. Yang, X. Yang, Y. Yang, Y. Yang, Z. Yang, Z. Yang, M. C. Yao, P. J. Yao, X. Yao, Z. Yao, Z. Yao, L. S. Yasui, M. Ye, B. Yedvobnick, B. Yeganeh, E. S. Yeh, P. L. Yeyati, F. Yi, L. Yi, X. M. Yin, C. K. Yip, Y. M. Yoo, Y. H. Yoo, S. Y. Yoon, K. I. Yoshida, T. Yoshimori, K. H. Young, H. Yu, J. J. Yu, J. T. Yu, J. Yu, L. Yu, W. H. Yu, X. F. Yu, Z. Yu, J. Yuan, Z. M. Yuan, B. Y. Yue, J. Yue, Z. Yue, D. N. Zacks, E. Zacksenhaus, N. Zaffaroni, T. Zaglia, Z. Zakeri, V. Zecchini, J. Zeng, M. Zeng, Q. Zeng, A. S. Zervos, D. D. Zhang, F. Zhang, G. Zhang, G. C. Zhang, H. Zhang, H. Zhang, H. Zhang, H. Zhang, J. Zhang, J. Zhang, J. Zhang, J. Zhang, J. P. Zhang, L. Zhang, L. Zhang, L. Zhang, L. Zhang, M. Y. Zhang, X. Zhang, X. D. Zhang, Y. Zhang, Y. Zhang, Y. Zhang, Y. Zhang, Y. Zhang, M. Zhao, W. L. Zhao, X. Zhao, Y. G. Zhao, Y. Zhao, Y. Zhao, Y. X. Zhao, Z. Zhao, Z. J. Zhao, D. Zheng, X. L. Zheng, X. Zheng, B. Zhivotovsky, Q. Zhong, G. Z. Zhou, G. Zhou, H. Zhou, S. F. Zhou, X. J. Zhou, H. Zhu, H. Zhu, W. G. Zhu, W. Zhu, X. F. Zhu, Y. Zhu, S. M. Zhuang, X. Zhuang, E. Ziparo, C. E. Zois, T. Zoladek, W. X. Zong, A. Zorzano and S. M. Zughaier (2016). "Guidelines for the use and interpretation of assays for monitoring autophagy (3rd edition)." *Autophagy* **12**(1): 1-222.

Koller, M. L., S. K. G. Maier, A. R. Gelzer, W. R. Bauer, M. Meesmann and R. F. Gilmour (2005). "Altered Dynamics of Action Potential Restitution and Alternans in Humans With Structural Heart Disease." *Circulation* **112**(11): 1542.

Komatsu, M., Waguri, S., Ueno, T., Iwata, J., Murata, S., Tanida, I., Ezaki J., Mizushima, N., Ohsumi, Y., Uchiyama, Y., Kominami, E., Tanaka, K. & Chiba, T. 2005. Impairment of starvation-induced and constitutive autophagy in Atg7-deficient mice. *J Cell Biol,* 169**,** 425-34.

Kopecky , S. L., B. J. Gersh , M. D. McGoon , J. P. Whisnant , D. R. J. Holmes , D. M. Ilstrup and R. L. Frye (1987). "The Natural History of Lone Atrial Fibrillation." *New England Journal of Medicine* **317**(11): 669-674.

Koura, T., M. Hara, S. Takeuchi, K. Ota, Y. Okada, S. Miyoshi, A. Watanabe, K. Shiraiwa, H. Mitamura, I. Kodama and S. Ogawa (2002). Anisotropic conduction properties in canine atria analyzed by high-resolution optical mapping: Preferential direction of conduction block changes from longitudinal to transverse with increasing age. *Circulation,* **105**(17), pp. 2092-2098.

Kracklauer, M. P., H. Z. Feng, W. Jiang, J. L. Lin, J. J. Lin and J. P. Jin (2013). "Discontinuous thoracic venous cardiomyocytes and heart exhibit synchronized developmental switch of troponin isoforms." *FEBS J* **280**(3): 880-891.

Krakoff, I.H., Brown, N.C., Reichard, P., 1968. Inhibition of ribonucleoside diphosphate reductase by hydroxyurea. *Cancer Res.* 28, 1559–1565.

Kugler, S., N. Nagy, G. Racz, A. M. Tokes, B. Dorogi and A. Nemeskeri (2017). "Presence of cardiomyocytes exhibiting Purkinje-type morphology and prominent connexin 45 immunoreactivity in the myocardial sleeves of cardiac veins." *Heart Rhythm.*

Kumagai, K., H. Nakashima, N. Gondo and K. Saku (2003). "Antiarrhythmic Effects of JTV-519, a Novel Cardioprotective Drug, on Atrial Fibrillation/Flutter in a Canine Sterile Pericarditis Model." *Journal of Cardiovascular Electrophysiology* **14**(8): 880-884.

Kurz, T., Terman, A. & Brunk, U. T. 2007. Autophagy, ageing and apoptosis: the role of oxidative stress and lysosomal iron. *Arch Biochem Biophys,* 462**,** 220-30.

Kustiawan, P.M., Lirdprapamongkol, K., Palaga, T., Puthong, S., Phuwapraisirisan, P., Svasti, J., Chanchao, C. (2017). "*Molecular mechanism of cardol, isolated from Trigona incisa stingless bee propolis, induced apoptosis in the SW620 human colorectal cancer cell line". BMC Pharmacol Toxicol* **18**:32.

Kwak, H. B. (2013). "Aging, exercise, and extracellular matrix in the heart." *J Exerc Rehabil* **9**(3): 338-347.

Kwong KF, Schuessler RB, Green KG, Laing JG, Beyer EC, Boineau JP*, et al.* (1998). Differential expression of gap junction proteins in the canine sinus node. *Circulation research* 82**:** 604-612.

Laky, D., Parascan L., Càndea, V. (2011). "Atrial structural remodelling in patients with chronic fibrillations and in animal models." *Rom J Morphol Embryol* **52**(1):95-98.

Lai, L.-P., M.-J. Su, J.-L. Lin, F.-Y. Lin, C.-H. Tsai, Y.-S. Chen, S. K. S. Huang, Y.-Z. Tseng and W.-P. Lien (1999). "Down-regulation of L-type calcium channel and sarcoplasmic reticular Ca^{2+}-ATPase mRNA in human atrial fibrillation without significant change in the mRNA of ryanodine receptor, calsequestrin and phospholamban." *Journal of the American College of Cardiology* **33**(5): 1231-1237.

Larocca, T. J., Henson, G. D., Thorburn, A., Sindler, A. L., Pierce, G. L. & Seals, D. R. 2012. Translational evidence that impaired autophagy contributes to arterial ageing. *J Physiol,* 590**,** 3305-16.

Laver, D. R. (2007). "Ca^{2+} stores regulate ryanodine receptor Ca^{2+} release channels via luminal and cytosolic Ca^{2+} sites." *Biophys J* **92**(10): 3541-3555.

Leaf A, Albert CM, Josephson M, Steinhaus D, Kluger J, Kang JX, et al. (2005). Prevention of Fatal Arrhythmias in High-Risk Subjects by Fish Oil n-3 Fatty Acid Intake. *Circulation* 112: 2762.

Leem, C. H., W. T. Kim, J. M. Ha, Y. J. Lee, H. C. Seong, H. Choe, Y. J. Jang, J. B. Youm and Y. E. Earm (2006). "Simulation of Ca^{2+}-Activated Cl; Current of Cardiomyocytes in Rabbit Pulmonary Vein: Implications of Subsarcolemmal Ca^{2+} Dynamics." *Philosophical Transactions: Mathematical, Physical and Engineering Sciences* **364**(1842): 1223-1243.

Lehnart, S. E., C. Terrenoire, S. Reiken, X. H. T. Wehrens, L.-S. Song, E. J. Tillman, S. Mancarella, J. Coromilas, W. J. Lederer, R. S. Kass and A. R. Marks (2006). "Stabilization of cardiac ryanodine receptor prevents intracellular calcium leak and arrhythmias."

Proceedings of the National Academy of Sciences of the United States of America **103**(20): 7906-7910.

Levin, M. D., M. M. Lu, N. B. Petrenko, B. J. Hawkins, T. H. Gupta, D. Lang, P. T. Buckley, J. Jochems, F. Liu, C. F. Spurney, L. J. Yuan, J. T. Jacobson, C. B. Brown, L. Huang, F. Beermann, K. B. Margulies, M. Madesh, J. H. Eberwine, J. A. Epstein and V. V. Patel (2009). "Melanocyte-like cells in the heart and pulmonary veins contribute to atrial arrhythmia triggers." *The Journal of Clinical Investigation* **119**(11): 3420-3436.

Lilienbaum, A. (2013). "Relationship between the proteasomal system and autophagy." *Int J Biochem Mol Biol.* **4**(1): 1-26.

Lin, Y. K., Cheng, C. C., Tsai, M. C., Wu, P. Y., Chen, Y. A., Chen, Y. C., Chen, S. A. & Chen, Y. J. 2017. Mitochondrial dysfunction on sinoatrial node and pulmonary vein electrophysiological activities. *Exp Ther Med,* 13, 2486-2492.

Lipsskaia, L., Chemaly, E. R., Hadri, L., Lompre, A. M. & Hajjar, R. J. 2010. Sarcoplasmic reticulum $Ca^{(2+)}$ ATPase as a therapeutic target for heart failure. *Expert Opin Biol Ther*, 10, 29-41.

Liu, G.-X., B.-R. Choi, O. Ziv, W. Li, E. de Lange, Z. Qu and G. Koren (2012). "Differential conditions for early after-depolarizations and triggered activity in cardiomyocytes derived from transgenic LQT1 and LQT2 rabbits." *The Journal of Physiology* **590**(Pt 5): 1171-1180.

Liu, M., L. Gu, M. S. Sulkin, H. Liu, E. M. Jeong, I. Greener, A. Xie, I. R. Efimov and S. C. Dudley, Jr. (2013). "Mitochondrial dysfunction causing cardiac sodium channel downregulation in cardiomyopathy." *J Mol Cell Cardiol* **54**: 25-34.

Liu J, Xin L, Benson VL, Allen DG, Ju YK (2015). Store-operated calcium entry and the localization of STIM1 and Orai1 proteins in isolated mouse sinoatrial node cells. *Frontiers in physiology* 6: 69.

Lloyd-Jones, D. M., T. J. Wang, E. P. Leip, M. G. Larson, D. Levy, R. S. Vasan, R. B. D'Agostino, J. M. Massaro, A. Beiser, P. A. Wolf and E. J. Benjamin (2004). "Lifetime risk for development of atrial fibrillation: the Framingham Heart Study." *Circulation* **110**(9): 1042-1046.

Logantha, S. J., S. F. Cruickshank, E. G. Rowan and R. M. Drummond (2010). "Spontaneous and electrically evoked Ca^{2+} transients in cardiomyocytes of the rat pulmonary vein." *Cell Calcium* **48**(2-3): 150-160.

Lopez-otin, C., Blasco, M. A., Partridge, L., Serrano, M. & Kroemer, G. 2013. The hallmarks of aging. *Cell,* 153**,** 1194-217.

Lu, X., K. S. Ginsburg, S. Kettlewell, J. Bossuyt, G. L. Smith and D. M. Bers (2013). "Measuring Local Gradients of Intramitochondrial calcium in Cardiac Myocytes During Sarcoplasmic Reticulum Ca." *Circulation Research* **112**(3): 424.

Lukyanenko, V., A. Chikando and W. J. Lederer (2009). "Mitochondria in cardiomyocyte Ca^{2+} signaling." *Int J Biochem Cell Biol* **41**(10): 1957-1971.

Lyon, A. R., K. T. MacLeod, Y. Zhang, E. Garcia, G. K. Kanda, M. J. Lab, Y. E. Korchev, S. E. Harding and J. Gorelik (2009). "Loss of T-tubules and other changes to surface topography in ventricular myocytes from failing human and rat heart." *Proceedings of the National Academy of Sciences* **106**(16): 6854-6859.

Maack, C., S. Cortassa, M. A. Aon, A. N. Ganesan, T. Liu and B. O'Rourke (2006). "Elevated Cytosolic Na$^+$; Decreases Mitochondrial Ca^{2+} Uptake During Excitation-Contraction Coupling and Impairs Energetic Adaptation in Cardiac Myocytes." *Circulation Research* **99**(2): 172.

Malgaroli A, Milani D, Meldolesi J, Pozzan T (1987). Fura-2 measurement of cytosolic free Ca^{2+} in monolayers and suspensions of various types of animal cells. *The Journal of Cell Biology* 105: 2145.

Martin, V., Bredoux, R., Corvazier, E., Van Gorp, V., Kovàcs, T., Gélébart, P., and Enouf., J (2002). "Three novel Sarco/endoplasmic reticulum Ca^{2+}-ATPase (SERCA) 3 isoforms: EXPRESSION, REGULATION AND FUNCTION OF THE MEMBERS OF THE SERCA3 FAMILY." *J.Biol.Chem* **277**(27): 24442-24452.

Masani, F. (1986). "Node-like cells in the myocardial layer of the pulmonary vein of rats: an ultrastructural study." *Journal of Anatomy* 145: 133-142.

Matthews, G., Neher, E., Penner, R (1989). "Second messenger-activated calcium influx in rat peritoneal mast cells". *Journal of Physiology* 418: 105-130.

Mattiazzi, A., C. Mundiña-Weilenmann, L. Vittone, M. Said and E. G. Kranias (2006). "The importance of the Thr17 residue of phospholamban as a phosphorylation site under physiological and pathological conditions." *Brazilian Journal of Medical and Biological Research* 39: 563-572.

Mauvezin C, Ayala C, Braden CR, Kim J, Neufeld TP (2014). Assays to monitor autophagy in Drosophila. *Methods* 68**:** 134-139.

Maxwell, J. T. and L. A. Blatter (2012). "Facilitation of cytosolic calcium wave propagation by local calcium uptake into the sarcoplasmic reticulum in cardiac myocytes." *The Journal of Physiology* **590**(23): 6037-6045.

Mensah, M. Ezzati and C. J. Murray (2014). "Worldwide epidemiology of atrial fibrillation: a Global Burden of Disease 2010 Study." *Circulation* **129**(8): 837-847.

Mestre Prates, J. A., F. J. S. Garcia e Costa, A. M. R. Ribeiro and A. A. Dias Correia (2002). "Contribution of major structural changes in myofibrils to rabbit meat tenderisation during ageing." *Meat Science* **61**(1): 103-113.

Lin Y-K, Lin F-Z, Chen Y-C, Cheng C-C, Lin C-I, Chen Y-J, et al. (2010). Oxidative Stress on Pulmonary Vein and Left Atrium Arrhythmogenesis. *Circulation Journal* 74: 1547-1556.

Mogensen, U. M., Jhund, P. S., Abraham, W. T., Desai, A. S., Dickstein, K., Packer, M., Rouleau, J. L., Solomon, S. D., Swedberg, K., Zile, M. R., Kober, L., McMurray, J. J. V., Paradigm, H. F., Investigators, A. & Commitees 2017. Type of Atrial Fibrillation and Outcomes in Patients With Heart Failure and Reduced Ejection Fraction. *J Am Coll Cardiol,* 70, 2490-2500.

Morillo, C.A., Klein, G.J., Jones, D.L. and Guiraudon, C.M., 1995. Chronic rapid atrial pacing: Structural, functional, and electrophysiological characteristics of a new model of sustained atrial fibrillation. *Circulation*, **91**(5), pp. 1588-1595.

Mueller-Hoecker J., Beitinger F., Fernandez B., Bahlamann O., Assmann G., Troidl C., Dimomeletis I, Kaab S., Deindl E., 2008. Of rodents and humans: a light microscopic and ultrastructural study on cardiomyocytes in pulmonary veins. *Int.J.Med.Sci.* **5**(3), pp. 152-158.

Nalliah, C. J., T. W. Lim, E. Kizana, P. Qian, P. Kovoor, A. Thiagalingam, D. L. Ross and S. P. Thomas (2015). "Clinical significance of early atrial arrhythmia type and timing after single ring isolation of the pulmonary veins." *Europace* **17**(7): 1038-1044.

Nam SM, Kim JW, Yoo DY, Yim HS, Kim DW, Choi JH, et al. (2014). Physical exercise ameliorates the reduction of neural stem cell, cell proliferation and neuroblast differentiation in senescent mice induced by D-galactose. *BMC Neurosci.* 15.

Namekata, I., Y. Tsuneoka, A. Takahara, H. Shimada, T. Sugimoto, K. Takeda, M. Nagaharu, K. Shigenobu, T. Kawanishi and H. Tanaka (2009). "Involvement of the Na^+/Ca^{2+} Exchanger in the Automaticity of Guinea-Pig Pulmonary Vein Myocardium as Revealed by SEA0400." *Journal of Pharmacological Sciences* **110**(1): 111-116.

Nanayakkara, S., Hayowsky, M., Mariani, J., Van Emplel, V., Maeder, M. T., Vizi, D. & Kaye, D. M. 2017. Hemodynamic Profile of Patients With Heart Failure and Preserved Ejection Fraction Vary by Age. *J Am Heart Assoc*, 6.

Narath R, Ambros IM, Kowalska A, Bozsaky E, Boukamp P, Ambros PF (2007). Induction of senescence in MYCN amplified neuroblastoma cell lines by hydroxyurea. *Genes, Chromosomes and Cancer* 46: 130-142.

Narayan, S. M., M. R. Franz, P. Clopton, E. J. Pruvot and D. E. Krummen (2011). "Repolarization alternans reveals vulnerability to human atrial fibrillation." Circulation **123**(25): 2922-2930.

Narayan, S. M. e. a. (2002). "Alternans of Atrial Action Potentials During Atrial Flutter as a Precursor to Atrial Fibrillation." *Circulation* **106**(15): 1968-1973.

Nassal, M. M., X. Wan, K. R. Laurita and M. J. Cutler (2015). "Atrial SERCA2a Overexpression Has No Affect on Cardiac Alternans but Promotes Arrhythmogenic SR Ca^{2+} Triggers." *PLoS One* **10**(9): e0137359.

Nattel, S., B. Burstein and D. Dobrev (2008). "Atrial remodeling and atrial fibrillation: mechanisms and implications." *Circ Arrhythm Electrophysiol* **1**(1): 62-73.

Nattel, S. and M. Harada (2014). "Atrial remodeling and atrial fibrillation: recent advances and translational perspectives." *J Am Coll Cardiol* **63**(22): 2335-2345.

Neef, S., N. Dybkova, S. Sossalla, K. R. Ort, N. Fluschnik, K. Neumann, R. Seipelt, F. A. Schondube, G. Hasenfuss and L. S. Maier (2010). "CaMKII-dependent diastolic SR Ca^{2+} leak and elevated diastolic Ca^{2+} levels in right atrial myocardium of patients with atrial fibrillation." *Circ Res* **106**(6): 1134-1144.

Niemann B, Chen Y, Teschner M, Li L, Silber RE, Rohrbach S (2011). Obesity induces signs of premature cardiac aging in younger patients: the role of mitochondria. *Journal of the American College of Cardiology* 57: 577-585.

Nishida K, Taneike M, Otsu K (2015). The role of autophagic degradation in the heart. *Journal of molecular and cellular cardiology* 78: 73-79.

Nissim, T.B., Zhang, X., Elazar, A., Roy, S., Stolwijk, J.A., Zhou, Y., Motiani, R.K., Gueguinoi, M., Hempel, N., Hershfinkel, M., Gill, D.L., Trebak, M., Sekler, I. (2017). "Mitochondria control store operated Ca^{2+} entry through Na^{+} and redox signals" *The EMBO journal* 37: 797-815.

Nkuipoi-Kenfack, E., Schanstra, J. P., Bajwa, S., Pejchinovskki, M., Vinel, C., Dray, C., Valet, P., Bascands, J. L., Vlahou, A., Koeck, T., Borries, M., Bussch, H., Bechtel-Walz, W., Huber, T. B., Rudolph, K. L., Pich, A., Mischak, H. & Zurbig, P. 2017. The use of urinary proteomics in the assessment of suitability of mouse models for ageing. *PLoS One,* 12**,** e0166875.

Nottingham, F. (2010). "Diagnosis and treatment of atrial fibrillation in the acute care setting." *J Am Acad Nurse Pract* **22**(6): 280-287.

Okamoto, Y., M. Takano, T. Ohba and K. Ono (2012). "Arrhythmogenic coupling between the Na^{+}–Ca^{2+} exchanger and inositol 1,4,5-triphosphate receptor in rat pulmonary vein cardiomyocytes." *Journal of Molecular and Cellular Cardiology* **52**(5): 988-997.

Ou, B., Nakagawa, M., Kajimoto, M., Nobe, S., Ooie, T., Ichinose, M., Yonemochi, H., Ono, N., Shimada, T. & Saikawa, T. 2005. Heterogeneous expression of connexin 43 in the myocardium of rabbit right ventricular outflow tract. *Life Sci,* 77**,** 52-9.

Paes de Almeida, O., C. M. Bohm, M. de Paula Carvalho and A. Paes de Carvalho (1975). "The cardiac muscle in the pulmonary vein of the rat: a morphological and electrophysiological study." *J Morphol* **145**(4): 409-433.

Palty, R., W. F. Silverman, M. Hershfinkel, T. Caporale, S. L. Sensi, J. Parnis, C. Nolte, D. Fishman, V. Shoshan-Barmatz, S. Herrmann, D. Khananshvili and I. Sekler (2010). "NCLX is an essential component of mitochondrial Na^{+}/Ca^{2+} exchange." *Proceedings of_the National Academy of Sciences* **107**(1): 436-441.

Parameshwaran K, Irwin MH, Steliou K, Pinkert CA (2010). D-galactose effectiveness in modeling aging and therapeutic antioxidant treatment in mice. *Rejuvenation research* 13: 729-735.

Park, Joo-In., Jeong, Jin-Sook., Han, Jin-Yeong., Kim, Deok-In., Gao., Yan-Hao., Park, Sang-Chul., Rodgers., G.P., Kim, In-Hoo (2000). "Hydroyurea induces a senescence-like change of K562 human erythroleukemia cell." *J Cancer Res Clin Oncol* 126: 455-460.

Park, W. J. & Oh, J. G. 2013. SERCA2a: a prime target for modulation of cardiac contractility during heart failure. *BMB Reports,* 46, 237-243.

Patterson, E., R. Lazzara, B. Szabo, H. Liu, D. Tang, Y. H. Li, B. J. Scherlag and S. S. Po (2006). "Sodium-calcium exchange initiated by the Ca^{2+} transient: an arrhythmia trigger within pulmonary veins." *J Am Coll Cardiol* **47**(6): 1196-1206.

Periasamy, M., Bhupathy, P., and Babu, G. J. 2008. Regulation of sarcoplasmic reticulum Ca^{2+} ATPase pump expression and its relevance to cardiac muscle physiology and pathology. *Cardiovasc Res*, 77, 265-73.

Perez-Lugones, A., J. T. McMahon, N. B. Ratliff, W. I. Saliba, R. A. Schweikert, N. F. Marrouche, E. B. Saad, J. L. Navia, P. M. McCarthy, P. Tchou, A. M. Gillinov and A. Natale (2003). "Evidence of Specialized Conduction Cells in Human Pulmonary Veins of Patients with Atrial Fibrillation." *Journal of Cardiovascular Electrophysiology* **14**(8): 803-809.

Pearce RKB, Owen A, Daniel S, Jenner P, Marsden CD (1997). Alterations in the distribution of glutathione in the substantia nigra in Parkinson's disease. *Journal of Neural Transmission* 104: 661-677.

Pieri C, Recchioni R, Moroni F, Marcheselli F, Marra M (1994). Food restriction in female Wistar rats. VII. Mitochondrial parameters in resting and proliferating splenic lymphocytes. *Archives of Gerontology and Geriatrics* 19: 31-42.

Pieske, S. B., M. L. Maier, M. D. Bers and M. G. Hasenfuss (1999). "Ca^{2+} Handling and Sarcoplasmic Reticulum Ca^{2+} Content in Isolated Failing and Nonfailing Human Myocardium." *Circulation Research* **85**(1): 38-46.

Piquereau, J., Caffin, F., Novotova, M., Lemaire, C., Veksler, V., Garnier, A., Ventura-Clapier, R. & Joubert, F. 2013. Mitochondrial dynamics in the adult cardiomyocytes: which roles for a highly specialized cell? *Front Physiol,* 4, 102.

Priori, S. G. & Napotalino, C. 2005. Cardiac and skeletal muscle disorders caused by mutations in the intracellular Ca^{2+} release channels. *J Clin Invest,* 115**,** 2033-8.

Pritchard, T. J. and E. G. Kranias (2009). "Junctin and the histidine-rich Ca^{2+} binding protein: potential roles in heart failure and arrhythmogenesis." *J Physiol* **587**(Pt 13): 3125-3133.

Qin, N., R. Olcese, M. Bransby, T. Lin and L. Birnbaumer (1999). "Ca^{2+}-induced inhibition of the cardiac Ca^{2+} channel depends on calmodulin." *Proceedings of the National Academy of Sciences* **96**(5): 2435-2438.

Reiken, S., Wehrens, X. H., Vest, J. A., Barbone, A., Klotz, S., Mancini, D., Burkhoff, D. & Marks, A. R. 2003. Beta-blockers restore calcium release channel function and improve cardiac muscle performance in human heart failure. *Circulation,* 107**,** 2459-66.

Ressler, S., Bartkova, J., Niederegger, H., Bartek, J., Scharfetter-Kochanek, K., Jansen-Dürr, P., Wlaschek, M. (2006). "p16^{INK4A} is a robust in vivo biomarker of cellular aging in human skin." *Aging Cell* 5: 379-389.

Richards, M. A., J. D. Clarke, P. Saravanan, N. Voigt, D. Dobrev, D. A. Eisner, A. W. Trafford and K. M. Dibb (2011). "Transverse tubules are a common feature in large mammalian atrial myocytes including human." *Am J Physiol Heart Circ Physiol* **301**(5): H1996-2005.

Rietdorf, K., M. D. Bootman and M. J. Sanderson (2014). "Spontaneous, pro-arrhythmic calcium signals disrupt electrical pacing in mouse pulmonary vein sleeve cells." *PLoS One* **9**(2): e88649.

Rietdorf, K., S. Masoud, F. McDonald, M. J. Sanderson and M. D. Bootman (2015). "Pulmonary vein sleeve cell excitation-contraction-coupling becomes dysynchronized by spontaneous calcium transients." *Biochem Soc Trans* **43**(3): 410-416.

Rueckschloss, U., M. Villmow and U. Klockner (2010). "NADPH oxidase-derived superoxide impairs calcium transients and contraction in aged murine ventricular myocytes." *Exp Gerontol* **45**(10): 788-796.

Ruiz, A., E. Alberdi and C. Matute (2014). "CGP37157, an inhibitor of the mitochondrial Na^+/Ca^{2+} exchanger, protects neurons from excitotoxicity by blocking voltage-gated Ca2+ channels." *Cell Death &Amp; Disease* **5**: e1156.

Russell RC, Yuan HX, Guan KL (2014). Autophagy regulation by nutrient signaling. *Cell research* 24: 42-57.

Sag, C. M., Santos, C. X. & Shah, A. M. 2014. Redox regulation of cardiac hypertrophy. J Mol Cell Cardiol, 73, 103-11.

Sanderson, M. J. 2011. Exploring lung physiology in health and disease with lung slices. *Pulm Pharmacol Ther,* 24, 452-65.

Santulli, G., W. Xie, S. R. Reiken and A. R. Marks (2015). "Mitochondrial calcium overload is a key determinant in heart failure." *Proc Natl Acad Sci USA* **112**(36): 11389-11394.

Sato, D., Daniel C. Bartos, Kenneth S. Ginsburg and Donald M. Bers (2014). "Depolarization of Cardiac Membrane Potential Synchronizes Calcium Sparks and Waves in Tissue." *Biophysical Journal* **107**(6): 1313-1317.

Schotten (2009). "Distinct contractile and molecular differences between two goat models of atrial dysfunction: AV block-induced atrial dilatation and atrial fibrillation." *Journal of Molecular and Cellular Cardiology* 46(3): 385-394.

Schotten, U., H. Haase, D. Frechen, M. Greiser, C. Stellbrink, Jaime F. Vazquez-Jimenez, I. Morano, Maurits A. Allessie and P. Hanrath (2003). "The L-type Ca^{2+}-channel subunits α1C and β2 are not downregulated in atrial myocardium of patients with chronic atrial fibrillation." *Journal of Molecular and Cellular Cardiology* **35**(5): 437-443.

Schotten, U., S. Verheule, P. Kirchhof and A. Goette (2011). "Pathophysiological mechanisms of atrial fibrillation: a translational appraisal." *Physiol Rev* **91**(1): 265-325.

Shan, J., W. Xie, M. Betzenhauser, S. Reiken, B.-X. Chen, A. Wronska and A. R. Marks (2012). "Calcium Leak Through Ryanodine Receptors Leads To Atrial Fibrillation In Three Mouse Models of Catecholaminergic Polymorphic Ventricular Tachycardia." *Circulation research* **111**(6): 708-717.

Shanmugam, M., C. E. Molina, S. Gao, R. Severac-Bastide, R. Fischmeister and G. J. Babu (2011). "Decreased sarcolipin protein expression and enhanced sarco(endo)plasmic reticulum Ca^{2+} uptake in human atrial fibrillation." *Biochemical and Biophysical Research Communications* **410**(1): 97-101.

Shapira, AR., 2009. Catheter ablation of supraventricular arrhythmias and atrial Fibrillation. *Americal Family Physician,* **80**(10), pp. 1089-1094.

Sharma, M. R., P. Penczek, R. Grassucci, H.-B. Xin, S. Fleischer and T. Wagenknecht (1998). "Cryoelectron Microscopy and Image Analysis of the Cardiac Ryanodine Receptor." *Journal of Biological Chemistry* **273**(29): 18429-18434.

Shehab, A., M. Zubaid, A. S. Bhagavathula, W. A. Rashed, A. A. Alsheikh-Ali, W. AlMahmeed, K. Sulaiman, I. Al-Zakwani, A. AlQudaimi, N. Asaad, H. Amin and i. Gulf Survey of Atrial Fibrillation Events (2017). "Sex differences in management and outcomes of patients with atrial fibrillation in the Middle East: Gulf survey of atrial fibrillation events (Gulf SAFE)." *PLoS One* **12**(5): e0175405.

Shirakabe A, Ikeda Y, Sciarretta S, Zablocki DK, Sadoshima J (2016). Aging and Autophagy in the Heart. *Circulation research* 118**:** 1563-1576.

Shiroshita-Takeshita A, Schram G, Lavoie J, Nattel S (2004). Effect of Simvastatin and Antioxidant Vitamins on Atrial Fibrillation Promotion by Atrial-Tachycardia Remodeling in Dogs. *Circulation* 110: 2313.

Shou, W., B. Aghdasi, D. L. Armstrong, Q. Guo, S. Bao, M.-J. Charng, L. M. Mathews, M. D. Schneider, S. L. Hamilton and M. M. Matzuk (1998). "Cardiac defects and altered ryanodine receptor function in mice lacking FKBP12." *Nature* **391**(6666): 489-492.

Shukla, A. and A. B. Curtis (2014). "Avoiding permanent atrial fibrillation: treatment approaches to prevent disease progression." *Vasc Health Risk Manag* **10**: 1-12.

Skepper, J.N. and Naravatnam. V (1995). "Ultrastructural features of left ventricular myocytes in active and torpid harmsters compared with rats: a morphometric study." *Journal of Anatomy* 186: 585 - 592.

Smeazzetto, S., I. Schroder, G. Thiel and M. R. Moncelli (2011). "Phospholamban generates cation selective ion channels." *Physical Chemistry Chemical Physics* **13**(28): 12935-12939.

Smith MA, Zhu X, Tabaton M, Liu G, McKeel Jr DW, Cohen ML, et al. (2010). Increased Iron and Free Radical Generation in Preclinical Alzheimer Disease and Mild Cognitive Impairment. *Journal of Alzheimer's Disease* 19: 363-372.

Snetkov VA, Aaronson PI, Ward JPT, Knock GA, Robertson TP (2003). Capacitative calcium entry as a pulmonary specific vasoconstrictor mechanism in small muscular arteries of the rat. *British Journal of Pharmacology* 140**:** 97-106.

Soeller, C. and M. B. Cannell (1999). "Examination of the Transverse Tubular System in Living Cardiac Rat Myocytes by 2-Photon Microscopy and Digital Image Processing Techniques." *Circulation Research* **84**(3): 266-275.

Song, L. S., S. Guatimosim, L. Gomez-Viquez, E. A. Sobie, A. Ziman, H. Hartmann and W. J. Lederer (2005). "Calcium biology of the transverse tubules in heart." *Ann N Y Acad Sci* 1047: 99-111.

Song, Z., Christopher Y. Ko, M. Nivala, James N. Weiss and Z. Qu (2015). "Calcium-Voltage Coupling in the Genesis of Early and Delayed Afterdepolarizations in Cardiac Myocytes." *Biophysical Journal* **108**(8): 1908-1921.

Spach, M. S., R. C. Barr and P. H. Jewett (1972).
Stange, M., L. Xu, D. Balshaw, N. Yamaguchi and G. Meissner (2003). "Characterization of Recombinant Skeletal Muscle (Ser-2843) and Cardiac Muscle (Ser-2809) Ryanodine Receptor Phosphorylation Mutants." *Journal of Biological Chemistry* **278**(51): 51693-51702.

Stefansdottir, H., T. Aspelund, V. Gudnason and D. O. Arnar (2011). "Trends in the incidence and prevalence of atrial fibrillation in Iceland and future projections." *Europace* **13**(8): 1110-1117.

Suárez-Isla, B. A., J. J. Marengo, V. Irribarra and R. Bull (1990). Calcium Channels in Sarcoplasmic Reticulum Membranes Isolated from Skeletal Muscle. *Transduction in Biological Systems.* C. Hidalgo, J. Bacigalupo, E. Jaimovich and J. Vergara. Boston, MA, Springer US**:** 487-499.

Sueda, T., K. Imai, K. Orihashi, K. Okada, K. Ban and M. Hamamoto (2005). "Midterm results of pulmonary vein isolation for the elimination of chronic atrial fibrillation." *Ann Thorac Surg* **79**(2): 521-525.

Sugrue MM, Wang Y, Rideout HJ, Chalmers-Redman RME, Tatton WG (1999). Reduced Mitochondrial Membrane Potential and Altered Responsiveness of a Mitochondrial Membrane Megachannel in p53-Induced Senescence. B*iochemical and Biophysical Research Communications* 261: 123-130.

Sun, D. & Yang, F. 2017. Metformin improves cardiac function in mice with heart failure after myocardial infarction by regulating mitochondrial energy metabolism. *Biochem Biophys Res Commun,* 486, 329-335.

Sun, Q., M. Tang, J. Pu and S. Zhang (2008). "Pulmonary venous structural remodelling in a canine model of chronic atrial dilation due to mitral regurgitation." *Canadian Journal of Cardiology* **24**(4): 305-308.

Sun AY, Wang Q, Simonyi A, Sun GY (2010). Resveratrol as a Therapeutic Agent for Neurodegenerative Diseases. *Molecular Neurobiology* 41: 375-383.

Teh, A. W., J. M. Kalman, G. Lee, C. Medi, P. M. Heck, L. H. Ling, S. Kumar, S. J. Spence, J. B. Morton and P. M. Kistler (2012). "Electroanatomic remodelling of the pulmonary veins associated with age." *Europace* **14**(1): 46-51.

Terman A, Brunk UT (2004a). Aging as a catabolic malfunction. *The international journal of biochemistry & cell biology* 36**:** 2365-2375.

Terman A, Brunk UT (2004b). Lipofuscin. *The international journal of biochemistry & cell biology* 36**:** 1400-1404.

Terman A, Brunk UT (2005). The aging myocardium: roles of mitochondrial damage and lysosomal degradation. *Heart, lung & circulation* 14**:** 107-114.

Thijssen, V. L. J. L., J. Ausma, G. S. Liu, M. A. Allessie, G. J. J. M. van Eys and M. Borgers (2000). "Structural Changes of Atrial Myocardium During Chronic Atrial Fibrillation." *Cardiovascular Pathology* **9**(1): 17-28.

Timerman, A. P., E. Ogunbumni, E. Freund, G. Wiederrecht, A. R. Marks and S. Fleischer (1993). "The calcium release channel of sarcoplasmic reticulum is modulated by FK-506-binding protein. Dissociation and reconstitution of FKBP-12 to the calcium release channel of skeletal muscle sarcoplasmic reticulum." *Journal of Biological Chemistry* **268**(31): 22992-22999.

Tocchi, A., E. K. Quarles, N. Basisty, L. Gitari and P. S. Rabinovitch (2015). "Mitochondrial dysfunction in cardiac aging." *Biochimica et Biophysica Acta (BBA) - Bioenergetics* **1847**(11): 1424-1433.

Touchberry CD, Elmore CJ, Nguyen TM, Andresen JJ, Zhao X, Orange M*, et al.* (2011). Store-operated calcium entry is present in HL-1 cardiomyocytes and contributes to resting calcium. *Biochemical and biophysical research communications* 416**:** 45-50.

Townsley, M. I. (2012). "Structure and composition of pulmonary arteries, capillaries, and veins." *Compr Physiol* **2**(1): 675-709.

Trafford, A. W., Sibbring, G. C., Diaz, M. E. & Eisner, D. A. 2000. The effects of low concentrations of caffeine on spontaneous Ca release in isolated rat ventricular myocytes. *Cell Calcium,* 28**,** 269-76Tse, G. (2016). "Mechanisms of cardiac arrhythmias." *J Arrhythm* **32**(2): 75-81.

Tribulova, N., Szeiffova Bacova, B., Benova, T. & Viczenczova, C. 2015. Can we protect from malignant arrhythmias by modulation of cardiac cell-to-cell coupling? *J Electrocardiol,* 48, 434-40.

Tsuji, Y. and D. Dobrev (2013). "Safety and efficacy of vernakalant for acute cardioversion of atrial fibrillation: an update." *Vasc Health Risk Manag* **9**: 165-175.

Tsuneoka, Y., Y. Kobayashi, Y. Honda, I. Namekata and H. Tanaka (2012). "Electrical Activity of the Mouse Pulmonary Vein Myocardium." *Journal of Pharmacological Sciences* **119**(3): 287-292.

Turdi, S., Fan, X., Li, J., Zhao, J., Huff, A. F., Du, M. & Ren, J. 2010. AMP-activated protein kinase deficiency exacerbates aging-induced myocardial contractile dysfunction. *Aging Cell,* 9**,** 592-606.

Valdivia, H. H., J. H. Kaplan, C. R. E.-D. Graham and W. J. Lederer (1995). "Rapid Adaptation of Cardiac Ryanodine Receptors: Modulation by Mg^{2+} and Phosphorylation." *Science* **267**(5206): 1997-2000.

Van Der Velden, H. M., M. J. Van Kempen, M. C. Wijffels, M. Van Zijverden, W. Antoinette Groenewegen, M. A. Allessie and H. J. Jongsma (1998). "Altered pattern of connexin40 distribution in persistent atrial fibrillation in the goat." *Journal of_Cardiovascular Electrophysiology* **9**(6): 596-607.

Vanhooren, V. & Libert, C. 2013. The mouse as a model organism in aging research: usefulness, pitfalls and possibilities. *Ageing Res Rev,* 12**,** 8-21.

Van Petegem, F., F. C. Chatelain and D. L. Minor, Jr. (2005). "Insights into voltage-gated calcium channel regulation from the structure of the CaV1.2 IQ domain-Ca^{2+}/calmodulin complex." *Nat Struct Mol Biol* **12**(12): 1108-1115.

Venetucci, L. A., A. W. Trafford, S. C. O'Neill and D. A. Eisner (2007). "Na/Ca exchange: regulator of intracellular calcium and source of arrhythmias in the heart." *Ann N Y Acad Sci* **1099**: 315-325.

Verheule, S., E. Tuyls, A. van Hunnik, M. Kuiper, U. Schotten and M. Allessie (2010). "Fibrillatory Conduction in the Atrial Free Walls of Goats in Persistent and Permanent Atrial Fibrillation Clinical Perspective." *Circulation: Arrhythmia and Electrophysiology* **3**(6): 590.

Vest, J. A., X. H. Wehrens, S. R. Reiken, S. E. Lehnart, D. Dobrev, P. Chandra, P. Danilo, U. Ravens, M. R. Rosen and A. R. Marks (2005). "Defective cardiac ryanodine receptor regulation during atrial fibrillation." *Circulation* **111**(16): 2025-2032.

Vig M, Beck A, Billingsley JM, Lis A, Parvez S, Peinelt C, et al. CRACM1 Multimers Form the Ion-Selective Pore of the CRAC Channel. *Current Biology* 16: 2073-2079.

Voigt, N., N. Li, Q. Wang, W. Wang, A. W. Trafford, I. Abu-Taha, Q. Sun, T. Wieland, U. Ravens, S. Nattel, X. H. Wehrens and D. Dobrev (2012). "Enhanced sarcoplasmic reticulum Ca^{2+} leak and increased Na^{+}-Ca^{2+} exchanger function underlie delayed afterdepolarizations in patients with chronic atrial fibrillation." *Circulation* **125**(17): 2059-2070.

Wagenknecht, T., M. Radermacher, R. Grassucci, J. Berkowitz, H.-B. Xin and S. Fleischer (1997). "Locations of Calmodulin and FK506-binding Protein on the Three-dimensional Architecture of the Skeletal Muscle Ryanodine Receptor." *Journal of Biological Chemistry* **272**(51): 32463-32471.

Wakili, Reza., Voigt, Niels., Kääb, Stefan., Dobrev, Dobromir and Nattel, Stanley (2011). "Recent advances in the molecular pathophysiology of atrial fibrillation." *Journal of Clinical Investigations* **121**(8): 2955-2968.

Wang, C. and X. Wang (2015). "The interplay between autophagy and the ubiquitin-proteasome system in cardiac proteotoxicity." *Biochim Biophys Acta* **1852**(2): 188-194.

Wang, M., Peng, Y., Zheng, J., Zheng, B., Jin, X., Liu, H., Wang, Y., Tang, X., Huang, T., Jiang, P., Guan, Min-Xin (2016). "*A deafness-associated tRNAAsp mutation alters the m1G37 modification, aminoacylation and stability of tRNAAsp and mitochondrial function". Nucleic Acids Res* **44**:10974-10985.

Wang W, Li S, Dong HP, Lv S, Tang YY (2009). Differential impairment of spatial and nonspatial cognition in a mouse model of brain aging. *Life sciences* 85: 127-135.

Wehrens, X. H. T., S. E. Lehnart, F. Huang, J. A. Vest, S. R. Reiken, P. J. Mohler, J. Sun, S.Guatimosim, L.-S. Song, N. Rosemblit, J. M. D'Armiento, C. Napolitano, M. Memmi, S. G. Priori, W. J. Lederer and A. R. Marks (2003). "FKBP12.6 Deficiency and Defective Calcium Release Channel (Ryanodine Receptor) Function Linked to Exercise-Induced Sudden Cardiac Death." *Cell* **113**(7): 829-840.

Wohlgemuth, S. E., R. Calvani and E. Marzetti (2014). "The interplay between autophagy and mitochondrial dysfunction in oxidative stress-induced cardiac aging and pathology." *Journal of Molecular and Cellular Cardiology* **71**(Supplement C): 62-70.

Wongcharoen, W., Chen, Y. C., Chen, Y. J., Chen, S. Y., Yeh, H. I., Lin, C. I. & Chen, S. A. 2007. Aging increases pulmonary veins arrhythmogenesis and susceptibility to calcium regulation agents. *Heart Rhythm*, 4, 1338-49.

Wu, J., Z. Yan, Z. Li, X. Qian, S. Lu, M. Dong, Q. Zhou and N. Yan (2016). "Structure of the voltage-gated calcium channel Ca(v)1.1 at 3.6 A resolution." *Nature* **537**(7619): 191-196.

Xi, Q., Cheranov, S. Y. & Jaggar, J. H. 2005. Mitochondria-derived reactive oxygen species dilate cerebral arteries by activating Ca^{2+} sparks. *Circ Res,* 97**,** 354-62.

Xiao, B., C. Sutherland, M. P. Walsh and S. R. W. Chen (2004). "Protein Kinase A Phosphorylation at Serine-2808 of the Cardiac Calcium-Release Channel (Ryanodine Receptor) Does Not Dissociate 12.6-kDa FK506-Binding Protein (FKBP12.6)." *Circulation Research* **94**(4): 487.

Yamaguchi, N., L. Xu, D. A. Pasek, K. E. Evans, S. R. W. Chen and G. Meissner (2005). "Calmodulin Regulation and Identification of Calmodulin Binding Region of Type-3 Ryanodine Receptor Calcium Release Channel." *Biochemistry* **44**(45): 15074-15081.

Yang, K. C., Bonini, M. G. & Dudley, S. C., JR. 2014. Mitochondria and arrhythmias. *Free Radic Biol Med*, 71, 351-61.

Yang, X., Doser, T. A., Fang, C. X., Nunn, J. M., Janardhanan, R., Zhu, M., Sreejayan, N., Quinn, M. T. & Ren, J. 2006. Metallothionein prolongs survival and antagonizes senescence-associated cardiomyocyte diastolic dysfunction: role of oxidative stress. *FASEB J,* 20**,** 1024-6.

Yasuo I, Albert D, Fan L, Karen AW, Lionel B, Neil BR Resveratrol prevents oxidative stress-induced senescence and proliferative dysfunction by activating the AMPK-FOXO3 cascade in cultured primary human keratinocytes. *PLoS ONE* 10: e0115341.

Yeh, H. I., Y. J. Lai, S. H. Lee, S. T. Chen, Y. S. Ko, S. A. Chen, N. J. Severs and C. H. Tsai (2006). "Remodeling of myocardial sleeve and gap junctions in canine superior vena cava after rapid pacing." *Basic Res Cardiol* **101**(4): 269-280.

Yeo, E.J., Hwang, Y.C., Kang, C-M., Kim, I.H., Kim, D.I., Parka, J.S., Choy, H.E., Park, W.Y., Park, S.C. (2000). "Senescence-like changes induced by hydroyurea in human diploid fibroblasts." *Experimental Gerontology* 35: 553-571.

Zhai, Y., Wie, R., Liu, J., Wang, H., Cai, W., Zhao, M., Hu, Y., Wang, S., Yang, T., Liu, X., Yang, J., Liu (2017). "Drig-induced premature senescence model in human dental follicle stem cells." *Oncotarget* **8**(5): 7276-7293.

Zhang, X., Y. N. Tallini, Z. Chen, L. Gan, B. Wei, R. Doran, L. Miao, H.-B. Xin, M. I. Kotlikoff and G. Ji (2009). "Dissociation of FKBP12.6 from ryanodine receptor type 2 is regulated by cyclic ADP-ribose but not β-adrenergic stimulation in mouse cardiomyocytes." *Cardiovascular Research* **84**(2): 253-262.

Zhou, J., R. Olcese, N. Qin, F. Noceti, L. Birnbaumer and E. Stefani (1997). "Feedback inhibition of Ca^{2+} channels by Ca^{2+} depends on a short sequence of the C terminus that does not include the Ca^{2+}-binding function of a motif with similarity to Ca^{2+}-binding domains." *Proceedings of the National Academy of Sciences* **94**(6): 2301-2305.

Zhou, Q., Xiao, J., Jiang, D., Wang, R., Vembaiyan, K., Wang, A., Smith, C. D., Xie, C., Chen, W., Zhang, J., Tian, X., Jones, P. P., Zhong, X., Guo, A., Chen, H., Zhang, L., Zhu, W., Yang, D., Li, X., Chen, J., Gillis, A. M., Duff, H. J., Cheng, H., Feldman, A. M., Song, L. S., Fill, M., Back, T. G. & Chen, S. R. 2011. Carvedilol and its new analogs suppress arrhythmogenic store overload-induced Ca^{2+} release. *Nat Med,* 17, 1003-9.

Zhu, X., B. A. Altschafl, R. J. Hajjar, H. H. Valdivia and U. Schmidt (2005). "Altered Ca^{2+} sparks and gating properties of ryanodine receptors in aging cardiomyocytes." *Cell Calcium* **37**(6): 583-591.

Zitt C, Strauss B, Schwarz EC, Spaeth N, Rast G, Hatzelmann A, et al. (2004). Potent inhibition of Ca2+ release-activated Ca^{2+} channels and T-lymphocyte activation by the pyrazole derivative BTP2. *J Biol Chem* 279: 12427-12437.

Zorov, D. B., M. Juhaszova, Y. Yaniv, H. B. Nuss, S. Wang and S. J. Sollott (2009). "Regulation and pharmacology of the mitochondrial permeability transition pore." *Cardiovasc Res* **83**(2): 213-225.

Copyright

ELSEVIER LICENSE

TERMS AND CONDITIONS

Jan 11, 2018

This Agreement between Mr. Said Masoud ("You") and Elsevier ("Elsevier") consists of your license details and the terms and conditions provided by Elsevier and Copyright Clearance Center.

License Number 4265960823865

License date Jan 11, 2018

Licensed Content Publisher Elsevier

Licensed Content Publication Cell Calcium

Licensed Content Title The endoplasmic reticulum: a multifunctional signaling organelle

Licensed Content Author Michael J Berridge

Licensed Content Date November–December 2002

Licensed Content Volume 32

Licensed Content Issue 5-6

Licensed Content Pages 15

Start Page 235

End Page 249

Type of Use reuse in a thesis/dissertation

Portion figures/tables/illustrations

Number of figures/tables/illustrations 1

Formatboth print and electronic

Are you the author of this Elsevier article? No

Will you be translating? No

Original figure numbers Figure 6

Title of your thesis/dissertation The ultrastructural and abnormal calcium homeostasis in atrial myocytes and pulmonary vein sleeve cells during ageing

Expected completion date Jan 2018

Estimated size (number of pages) 300

Requestor Location Mr. Said Masoud

65 Grace Avenue

Milton Keynes, MK6 2XJ

United Kingdom

Attn: Mr. Said Masoud

Publisher Tax ID GB 494 6272 12

Total 0.00 GBP

Terms and Conditions